



UNIVERSIDAD DE CHILE
FACULTAD DE CIENCIAS FÍSICAS Y MATEMÁTICAS
DEPARTAMENTO DE FÍSICA

**SELF-ORGANIZATION INDUCED BY NONRECIPROCAL COUPLING IN
NONLINEAR SYSTEMS**

TESIS PARA OPTAR AL GRADO DE DOCTOR EN CIENCIAS, MENCIÓN FÍSICA

DAVID IGNACIO PINTO RAMOS

PROFESOR GUÍA:
Marcel Clerc Gavilán

MIEMBROS DE LA COMISIÓN:
Mustapha Tlidi
Ehud Meron
Ricardo Martínez García
Karin Alfaro Bittner

Este trabajo ha sido parcialmente financiado por:
Agencia Nacional de Investigación y Desarrollo (ANID)
Instituto Milenio de investigación en óptica (MIRO)

SANTIAGO DE CHILE
2023

RESUMEN DE LA TESIS PARA OPTAR
AL GRADO DE DOCTOR EN CIENCIAS,
MENCIÓN FÍSICA
POR: DAVID IGNACIO PINTO RAMOS
FECHA: 2023
PROF. GUÍA: Marcel Clerc Gavilán

**SELF-ORGANIZATION INDUCED BY NONRECIPROCAL COUPLING IN
NONLINEAR SYSTEMS**

**Autoorganización inducida por acoplamiento no
recíproco en sistemas no lineales**

La autoorganización es una propiedad exhibida por la materia viva y no viva, un fenómeno emergente del comportamiento colectivo y las interacciones de sistemas de muchos cuerpos. Las interacciones (o acoplamientos) entre los cuerpos pueden ser no recíprocas, lo que significa que en las interacciones por pares, el efecto de uno sobre el otro es diferente al inverso. En esta disertación, nos dedicamos a estudiar sistemas no lineales que exhiben acoplamiento no recíproco, particularmente las propiedades macroscópicas que podría inducir la no reciprocidad en el acoplamiento. Aprendimos que la heterogeneidad en los parámetros del sistema dinámico es relevante; por ello, también les dedicamos parte de esta tesis. Este documento está escrito en tres partes, cada una de las cuales consta de dos publicaciones en revistas revisadas por pares. La Parte I analiza un modelo prototípico en física no lineal, la ecuación de Frenkel-Kontorova cuando se somete a un acoplamiento no recíproco. Los frentes en estado inestable, las capas límite, los patrones autoensamblados y los frentes en estado estable se caracterizan por la no reciprocidad en el acoplamiento. Además, se brindan perspectivas experimentales y resultados preliminares, allanando el camino para otros estudios sobre acoplamiento no recíproco. La Parte II aborda la nucleación de diferentes estructuras no lineales (como defectos e interfaces) y cómo se ven afectadas por el acoplamiento no recíproco. La nucleación de vórtices se devela analizando cristales líquidos nemáticos y los defectos umbilicales que generan; estos vórtices también son equivalentes a dislocaciones en patrones. Los modelos de dinámica poblacional incorporan fácilmente acoplamiento no recíproco, y probamos nuestras predicciones en patrones de cobertura vegetal del norte de Chile, mostrando una distribución espacial de los defectos. Se emplean ideas similares para la dinámica de frentes hacia el estado estable nucleados a partir del ruido. Finalmente, en la parte III, exploramos el papel de la heterogeneidad en los parámetros, enfatizando los modelos de dinámica poblacional. En estos sistemas, la heterogeneidad tiene un origen ineludible. Incluyéndolo en los modelos, teóricamente podemos predecir el comportamiento de diferentes medidas realizadas sobre imágenes satelitales de patrones de cobertura vegetal. Se tienen en cuenta los diferentes modelos de evolución espaciotemporal de la biomasa presentes en la literatura, y el cálculo de las formas normales de la dinámica de la variedad central cerca de los puntos de bifurcación sirve como punto unificador para avanzar en la comprensión de estos sistemas complejos.

RESUMEN DE LA TESIS PARA OPTAR
AL GRADO DE DOCTOR EN CIENCIAS,
MENCIÓN FÍSICA
POR: DAVID IGNACIO PINTO RAMOS
FECHA: 2023
PROF. GUÍA: Marcel Clerc Gavilán

SELF-ORGANIZATION INDUCED BY NONRECIPROCAL COUPLING IN NONLINEAR SYSTEMS

Self-organization is a property exhibited by living and nonliving matter, an emerging phenomenon of the collective behavior and interactions of many-body systems. The interactions (or couplings) between the bodies can be nonreciprocal, meaning that in pairwise interactions, the effect of one over the other is different than the reverse one. In this dissertation, we are devoted to studying nonlinear systems exhibiting nonreciprocal coupling, particularly the macroscopic properties nonreciprocity in the coupling could induce. We learned that heterogeneity in the dynamical system parameters is relevant; thus, we also dedicate part of this dissertation to them. This document is written in three parts, each one consisting of two publications in peer-reviewed journals. Part I analyzes a prototypical model in nonlinear physics, the Frenkel-Kontorova equation when subjected to nonreciprocal coupling. Fronts into the unstable state, boundary layers, self-assembled patterns, and fronts into the stable state are characterized against the nonreciprocity in the coupling. Moreover, experimental perspectives and preliminary results are given, paving the way for other studies in nonreciprocal coupling. Part II addresses the nucleation of different nonlinear structures (such as defects and interfaces) and how they are affected by nonreciprocal coupling. Vortex nucleation is unveiled by analyzing nematic liquid crystals and the umbilical defects they generate; these vortices are also equivalent to dislocations in patterns. Population dynamics models easily incorporate nonreciprocal coupling, and we test our predictions in vegetation cover patterns from the north of Chile, showing a spatial distribution for the defects. Similar ideas are employed for the dynamics of fronts into the stable state nucleated from noise. Finally, in part III, we explore the role of heterogeneity in the parameters, emphasizing the population dynamics models. In these systems, the heterogeneity has an unavoidable origin. By including it in the models, we can theoretically predict the behavior of different measures performed on satellite images of vegetation cover patterns. The different biomass spatiotemporal evolution models present in the literature are taken into account, and the computation of the normal forms of the center manifold dynamic near the bifurcation points serves as a unifying point for advancing in understanding these complex systems.

*The scientist does not study nature because it is useful;
he studies it because he delights in it, and he delights in it because it is beautiful.*

Henri Poincaré

Acknowledgments

Esta tesis no sería posible sin el incommensurable amor de mi madre, padre, hermana, abuelos, abuelas, tíos, tías y más familiares. Agradezco a mi esposa Francisca por su paciencia eterna. Agradezco a mi amigo Mairon por creer en mí. Agradezco a mi maestro Marcel Clerc por mostrarme su pasión y compartirla conmigo, como también a mis compañeros que han recorrido este camino junto a mí. Agradezco a Sebastián su amistad y su entusiasmo por discutir toda idea.

El desarrollo de esta tesis fue apoyado financieramente por el Instituto Milenio de Investigación en Óptica (MIRO) a través de una beca de estudios de doctorado (2019-2020), como también por la Agencia Nacional de Investigación y Desarrollo (ANID) a través de la beca de doctorado nacional n° 21201484 (2020-2023).

Table of Content

Introduction	1
Objectives	2
Specific Objectives	2
Framework	4
Dynamical systems	4
Finite dimensional systems	4
Difference equations	4
Ordinary differential equations	5
Fixed points and stability	7
Bifurcations	9
Center manifold theorem	10
Normal forms of the center manifold dynamics	11
Infinite dimensional systems	19
The continuum limit	19
Reciprocal and nonreciprocal coupling	21
Partial differential equations	21
Integro-differential equations	22
Variational and non variational systems	22
Spatial instability	23
Normal forms of homogeneous solutions corrected by spatial coupling	24
Defects, patterns, and interfaces	28
Fronts	29
Fronts into the unstable state	30
Fronts into the stable state	32
Discreteness effects and the Peierls Navarro potential	35
Patterns	36
The stripe pattern	36
Isotropic environment	37
Anisotropic environment	37
The instabilities of the Ginzburg-Landau equation	39
Dislocation defect and its vortex structure in the phase	39
Interaction between vortices	40
Part I: Front-type nonlinear waves under nonreciprocal coupling	41
1. Nonreciprocal Coupling Induced Self-Assembled Localized Structures (Physical Review Letters 126 (19), 194102)	42

1.1. Supplementary materials	48
2. Giant boundary layer induced by nonreciprocal coupling in discrete systems (Communications in Nonlinear Science and Numerical Simulation 125, 107391)	54
Complements and perspectives on Part I	66
1. Nonreciprocal coupling effects on fronts into the stable state	66
The front position	66
The continuous profile characterizing the discrete front	67
The Peierls-Navarro potential revisited	67
2. The effect of fluctuations	71
Noise effects in a chain	71
3. Experimental perspectives	71
The liquid crystal light valve	72
The dynamics of the orientation field	74
Building a discrete grid of dynamical systems	74
Part II: Nucleation of defects and interfaces	76
3. Thermal Fluctuations Induced Emergence of Umbilical Defects in Nematic Liquid Crystal Cells (Nonequilibrium Thermodynamics and Fluctuation Kinetics. vol 208. pp 303-312)	77
4. Topological defects law for migrating banded vegetation patterns in arid climates (Science Advances 9 (31), eadf6620)	88
Complements and perspectives on Part II	100
1. Distribution of interface length in a nonreciprocally coupled Frenkel Kontorova lattice	100
The case of a lattice	100
Coarsening dynamics	100
2. Traveling patterns in liquid crystals	102
3. Non-oriented traveling patterns: traveling labyrinth	103
Part III: The effects of heterogeneity.	104
5. Vegetation covers phase separation in inhomogeneous environments (Chaos, Solitons & Fractals 163, 112518)	105
6. Effect of heterogeneous environmental conditions on labyrinthine vegetation patterns (Physical Review E 107 (5), 054219)	114
Complements and perspectives on Part III	124
1. Reduced equation from reaction-diffusion models in the pattern forming regime	124
Derivation from integrodifferential models	124
Derivation from reaction-diffusion models	125
2. Exact equivalence of vegetation models in specific cases	126
3. Heterogeneities in the regime of spots of vegetation	127

Conclusions	129
Bibliography	131

Index of Illustrations

2.1.	Fronts into the stable state obtained from numerical integration of Eq. 2.1. The three panels show the solutions $A_k(t)$ as a function of $z = k - x_0(t)$ at 20 seconds (simulation time) intervals. Parameters correspond to $\eta = 0.2$, $\epsilon = 1$, $D = 0.1$, $\alpha = -0.05$	67
2.2.	The continuous front profile obtained by collecting the solution points $(z, A_k(t))$. The left panel shows the profile around the position of the front, and the right insets show more detail up to the points forming the continuous function; 500 time snapshots were used to construct this figure. Parameters correspond to $\eta = 0.2$, $\epsilon = 1$, $D = 0.1$, $\alpha = -0.05$	68
2.3.	Velocity of the front as a function of the position $\dot{x}_0(x_0)$. The graph shows the plain truth, the implicit formula 2.13 using four terms, the average velocity, and the approximation to the average velocity from the continuum limit (corresponding to just the first term in each series of 2.13). Parameters correspond to $\eta = 0.2$, $\epsilon = 1$, $D = 0.1$, $\alpha = -0.05$	70
2.4.	Phase diagram of Eq. (2.14). Four regions could be differentiated by analyzing the order parameters corresponding to the domain walls' total and boundary layer sizes. Region I corresponds to the homogeneous, stable state. II shows permanent domain wall dynamics with thin boundary layers. In region III, the boundary layer enlarges drastically before the permanent domain wall dynamics. In region IV, stable self-assembled patterns can be observed. Continuous lines are a guide to the eye for the bifurcation places. Dashed lines correspond to analytical curves obtained from using the front into the unstable state velocity expression.	72
2.5.	Experimental setup in which nonreciprocal coupling is possible.	73
2.6.	Preliminar experimental results. a) shows the single cells induced. b) shows measures of the propagation velocity against the nonreciprocity parameter in a numerical prototypical model. Experimental measures are thanks to Manuel Díaz, Amaru Moya, and Pedro Aguilera, collaborators in this work.	75
4.1.	Dynamics of the nonreciprocally coupled Frenkel-Kontorova lattice. a) shows a snapshot of the dynamics in the absence of nonreciprocity. b) depicts how the phase wall size obeys a coarsening law in time for $\alpha = 0$. c) and d) exemplify values of intermediate nonreciprocity level α , where patterns can be observed despite fluctuations; here, the phase wall size is constant due to the periodicity of the self-assembled pattern. e) and f) illustrate how fluctuations can destabilize the pattern when high nonreciprocity creates permanent advected phase wall dynamics. The coarsening law of the $\alpha = 0$ case is observed with the change of variables $t \rightarrow i$	101

4.2.	Traveling patterns and dislocation dynamics in the LCLV. The upper panels show the numerical simulation results employing Eq. 2.15 with parameters $V_0/V_{FT} = 1.05$, $I_0 = 1$, $\alpha/\Gamma V_{FT} = 2.6$, $L = -1.5$, $\delta = 0.3$ (space and time units are such that $\tau = l = 1$). The bottom panels show the preliminary experimental measures courtesy of Pedro Aguilera, a collaborator in this part of the work.	102
4.3.	Traveling labyrinthine patterns in the integrodifferential model for population dynamics.	103
6.1.	Numerical characterization of solution branches with heterogeneous parameters. Panel a) illustrates the bifurcation diagram for a path in the mean aridity parameter depicted by the orange arrows, insets show different examples of the vegetation mosaics in the diagram. Panels b) and c) show the spatial characterization of the two branches of patchy patterns for the upper branch, which transit from a labyrinthine pattern to a patchy pattern. d) shows the lower branch that emerges as the aridity parameter decreases. Parameters are $\kappa = 0.6$, $d = 0.02$, $\gamma = 0.5$, $\alpha = 0.125$	128

Introduction

The analysis of nonlinear systems is at the heart of Classical Mechanics, a discipline where Poincaré opened a whole new realm of physics while studying the motion of the Sun, the Earth, and the Moon: nonlinear physics and chaos. This discipline, whose challenge lies in the impossibility to solve mathematically the dynamical system equations, saw its spring after the invention of computers that allowed scientists to observe and analyze the solutions of the system through numerical integration. The striking emergent phenomena nature exhibits could now be studied despite their complexity.

Not all natural systems, however, are well described by the Hamilton equations describing the motion of all particles. An effective description, including the dissipation and injection of energy processes that take place in the human timescale, is often more enlightening. In this limit, one can better understand the self-organized states that natural systems show. Phenomenon such as spatial-patterned states in skin fur coating [1], fluid dynamics convection [2], patterns and fronts in liquid crystal devices [3, 4], patterns in sand forced by wind in dunes and other localized structures in forced grains [5], and even large scale vegetation cover complex spatial structures [6], are well understood under the veil of nonlinear physics.

The emergent self-organized states these systems exhibit can have a multitude of microscopic origins; however, the relevant physical quantities behave with similar scalings near the birth of these states, the so-called *critical exponents* characterize each type of dynamical transition or *bifurcation*. In this dissertation, we analyze the bifurcations and self-organized states induced by nonreciprocal coupling among the participants of the dynamical systems. Nonreciprocal coupling occurs when the feedback an element imposes on its neighbor is not equivalent to the feedback the neighbor imposes on it. This type of coupling needs to be engineered, as the time-reversal symmetry of physics constrains interactions to be reciprocal. Nonreciprocity has been achieved in mechanic metamaterials using high nonlinearity [7] and robotic control [8]; in electric systems it can be achieved thanks to the operational amplifier couplers [9]; and in optics it could be observed when using translational optical feedback [10]. Linear systems with nonreciprocal coupling could display asymmetric standing wave modes, conducted amplification of perturbations, and even boundary or skin modes [11].

In this work, we will study the behavior that emerges from nonreciprocal coupling in nonlinear systems, extending what is known for the phenomenology observed in linear systems. To accomplish this, we consider the dynamics of an overdamped chain of coupled pendulums as our prototypical model, the Frenkel-Kontorova model. This model is sufficiently general, appearing in various physical contexts such as crystal dislocation motion, nonlinear oscillators, coupled short Josephson junctions, or electric circuits [12, 13]. Nonreciprocity is introduced in the couplers, breaking the space-reflection symmetry of the chain at mini-

mal order [8]. Nonlinear wave and boundary phenomena are characterized as a function of nonreciprocity, and we provide some perspectives on the effects of noise, which could induce the spontaneous creation of nonlinear structures such as fronts or defects. The concept of nonreciprocity can be extended further to continuous systems subjected to global or nonlocal coupling. With nonreciprocity and nonlinearity naturally arising in the dynamics of populations, we apply our ideas to patterns of vegetation cover in the north of Chile, confirming the predictions of the nonlinear theory in this context. Finally, we give our perspective on the effects the environmental heterogeneities, such as the topography (which modifies the coupling between the population), could have on these complex nonlinear systems.

This monograph describes the theoretical and numerical tools in the Framework chapter, which are used in the following six chapters, each consisting of an article or book chapter published under peer review. A brief introduction and future perspectives are given for these works. The final, general conclusions of the thesis work are found in the Conclusions chapter. The first two chapters are concentrated on the front propagation into the unstable state in nonreciprocally coupled systems. **Chapter 1** introduces the chain of nonreciprocally coupled pendulums, and the bifurcations of fronts into the unstable state are characterized, emphasizing a periodic self-assembled array of nonlinear structures. **Chapter 2** explores the effects of boundary conditions on the previously studied fronts, unveiling the formation of giant boundary layers. The following two chapters focus on the formation of nonlinear structures through noise or instabilities. **Chapter 3** Unveils the formation of vortices or domain walls under the effect of stochastic fluctuations, revealing the laws for their created number versus parameters. **Chapter 4** Applies the ideas of spontaneous formation of nonlinear structures, this time topological defects in patterns created through deterministic fluctuations of unstable modes, and the nonreciprocity in vegetation patterns interactions, to unveil a law for their number distribution in space. In the last part, the following two chapters focus on the heterogeneity affecting these nonlinear systems; they are similar to stochastic fluctuations but static in time. **Chapter 5** Introduces the heterogeneity of the environment in a general model of vegetation population evolution, which is derived from two different modeling perspectives available in the literature. **Chapter 6** Extends the previous study to patterns of the labyrinth type. In it, we show how heterogeneity can disarm the patterns in well-defined stages.

Objectives

The general objective of this thesis is to understand analytically and numerically the self-organized states and instabilities emerging from nonreciprocal coupling in nonlinear systems and to uncover the macroscopic variables that scale with the nonreciprocity parameters in damped oscillator chains and pattern-forming systems.

Specific Objectives

1. Perform extensive numerical simulations of the damped Frenkel-Kontorova chain under nonreciprocal coupling, making a sweep of the parameter space.
2. Create algorithms to capture the nucleus dynamics of the fronts into the unstable state observed under varying regimes of motion.

3. Analytically understand the different instabilities observed for the fronts into the unstable state occurring in the damped Frenkel-Kontorova chain emerging from the non-reciprocal coupling.
4. Test the robustness of the nonreciprocal coupling-induced phenomena in the Frenkel-Kontorova chain against boundary conditions and fluctuating forces.
5. Describe analytically the boundary layers arising for Dirichlet boundary conditions, employing techniques of difference equations (or maps).
6. Unveil how domain walls (or fronts into the stable state) nucleate due to fluctuations.
7. Analyze population dynamics models under nonlocal nonreciprocal coupling, corresponding to integrodifferential equations. Employing methods of linearization and weak nonlinear analysis.
8. Perform extensive numerical simulations of the population dynamic with nonreciprocal coupling models. Uncover the pattern formation regime and the emergent dynamical behaviors arising from nonreciprocity in the coupling.
9. Compare satellite images of pattern formations in *tillandsia landbeckii* species (proliferating in Chile's Atacama desert) with the predicted patterns in different regimes. Assess the status of the vegetation pattern and others.
10. Understand the origin of disorder in the vegetation patterns and amorphous cover, employing the idea of heterogeneities in the environment.

Framework

Dynamical systems

Throughout the text, we will be dealing with different types of *dynamical systems*. They correspond to abstract objects evolving in time; in physics, they often correspond to particles, molecules, rigid objects, and ensembles of any described by variables depending on time. A set of rules will dictate the variables' evolution. Generally, we encounter the dynamical systems classified according to the domains of the independent (often time) and dependent variable. They could be either discrete or continuous. Continuous time and variable dynamical systems are described by sets of *ordinary differential equations* (ODEs). A discrete-time evolution for a continuous variable is described by a *difference equation* (DE). Furthermore, we will refer to them as *finite dimensional* systems when the number of independent variables (the number of equations) is countable. The number of variables can become dense, describing a field, in which case we are addressing an *infinite dimensional system*; of this type, we will encounter *partial differential equations* (PDEs) and *integro-differential equations* (IDEs) [14]. It is important to keep in mind that infinite dimensional systems are often used as an approximation of our natural world (often a really good one), as ultimately, matter is made out of countable entities. Then, a mathematical relation between a finite and infinite dimensional system can be drawn: the *continuum limit*. However, one must take care, as not all the phenomena are translated from one system to another, and some can be lost. An example corresponds to the dynamics of a large number of identical masses arranged in a line, coupled with identical springs; the continuum limit allows us to quickly compute solutions employing a wave equation (PDE), giving waves satisfying a linear dispersion relation. Nevertheless, calculating with care in the original equations (the finite dimensional system) reveals a nonlinear dispersion relation [15]; a completely different curve.

Finite dimensional systems

Let us start by describing finite dimensional systems evolving according to the generalized time t (it can represent other independent variables, such as space, depending on the context). If the time changes continuously, we will deal with an ODE system; if it evolves at intervals, we will have a DE system. Denote the independent variables by $y_i(t)$, or use a vector notation $\mathbf{y}(t)$.

Difference equations

If time evolves at fixed intervals, then the dynamical system is described by the rules determining the next value (at the next time step) in terms of the information of the actual time step (and possibly the previous ones). They are often called *maps*, and the evolution rule has the form of a *recurrence relation*. Calling the time steps τ , they write

$$\mathbf{y}(t + \tau) = \mathbf{F}(\mathbf{y}(t), \mathbf{y}(t - \tau), \mathbf{y}(t - 2\tau), \dots, t; \mathbf{c}), \quad (0.1)$$

where \mathbf{c} is a vector containing fixed *control parameters* (for example, the mass of particles, the resistance of electrical elements, the intensity of an incoming light beam, etc.). A simple example would be the total population N of a species that produces offspring at precise intervals τ , assuming an offspring proportional to the population having it (rN) that adds to the actual population, the equation for the total population would be

$$N(t + \tau) = N(t) + rN(t).$$

If the recurrence relation is linear, we can find an analytic solution, in this case, replace $N(t) = N_0 a^t$ (where N_0 represents the initial population) and one is left with $a^\tau = (1 + r)$. Finally

$$N(t) = (1 + r)^{t/\tau} N_0.$$

If the offspring is less than the population producing it, then the population will go to zero at large times. Otherwise, it will increase. Note that the prediction is an unbounded increment of N over time; this is not physical. Obviously, we missed important aspects, such as an offspring that is a nonlinear function of the population producing it. Nonlinearities will render the problem non-solvable, but one will obtain phenomena not described otherwise [14].

Ordinary differential equations

A first order, first degree differential equation describes the rate of change of a variable in time according to a given function. The changes of each variable with respect to time are the components of the *field vector* $\mathbf{f}(\mathbf{y}, t)$; the system is said to be *autonomous* if it does not depend explicitly on time, otherwise it is *nonautonomous*. Then, the equation for the evolution of $\mathbf{y}(t)$ is

$$\frac{d\mathbf{y}}{dt} = \mathbf{f}(\mathbf{y}, t; \mathbf{c}). \quad (0.2)$$

This may be seen as a particular type of ODE. However, it covers most of the models found in the literature. Additionally, various natural systems can be described by the pondered balance between the n -th order derivatives of a variable, say, u

$$\mathcal{P}\left(u, \frac{du}{dt}, \frac{d^2u}{dt^2}, \dots, \frac{d^nu}{dt^n}; \mathbf{c}\right) = 0. \quad (0.3)$$

If \mathcal{P} is of first degree in the higher order derivative, one can always transform Eq. 0.3 to Eq. 0.2 by the changes of variables $d^k u / dt^k = y_{k+1}$ for $k = \{0, 1, 2, \dots, n - 1\}$. In the following, unless otherwise stated, we will assume $\mathbf{y} \in \mathbb{R}^n$ and consider the canonical inner product $\langle \mathbf{x} | \mathbf{y} \rangle \equiv \mathbf{x} \cdot \mathbf{y} = \sum_{i=1}^n x_i y_i$.

An example familiar to the reader is the Newton equation of motion, written explicitly for the position vector \mathbf{r} of a particle with mass m , subjected to a force \mathbf{F}

$$m \frac{d^2 \mathbf{r}}{dt^2} - \mathbf{F}(\mathbf{r}, \frac{d\mathbf{r}}{dt}, t) = 0.$$

Let $d\mathbf{r}/dt = \mathbf{v}$, then $d\mathbf{v}/dt = \mathbf{F}/m$, and the dynamical system is written explicitly as a first order one as

$$\frac{d}{dt} \begin{pmatrix} \mathbf{r} \\ \mathbf{v} \end{pmatrix} = \begin{pmatrix} \mathbf{v} \\ \mathbf{F}(\mathbf{r}, \mathbf{v}, t)/m \end{pmatrix}.$$

Linear ODEs can be solved by analyzing the matrix describing the linear equations, which we call the *Jacobian matrix* \mathbf{J}

$$\frac{d\mathbf{y}}{dt} = \mathbf{J}(t; \mathbf{c})\mathbf{y}. \quad (0.4)$$

The previous equations are not easy to solve, particularly when the Jacobian depends on time. In the simplified case of a constant Jacobian, a general solution could be drawn by inspection as

$$\mathbf{y}(t) = a_1 \mathbf{e}_1 e^{\lambda_1 t} + a_2 \mathbf{e}_2 e^{\lambda_2 t} + \dots + a_n \mathbf{e}_n e^{\lambda_n t}, \quad (0.5)$$

where the constants $\{a_k\}$ are determined by the initial condition of \mathbf{y} . The constants $\{\lambda_k\}$ are the eigenvalues of the Jacobian matrix, and $\{\mathbf{e}_k\}$ their corresponding eigenvectors; n is the dimension of \mathbf{y} . Special care must be taken when eigenvalues repeat or vanish, as these cases are not contained in Eq. 0.5. Note that, similar to the difference equations, we obtain indefinite growth or vanishing of variables for linear homogeneous (constant parameters) dynamics. This may or may not be a good model for the system we are describing. Again, nonlinearities would produce other behaviors at the cost of losing analytical solutions such as Eq. 0.5. An important question to ask oneself is whether solutions such as Eq. 0.5 exist and are unique; fortunately, under somewhat general conditions, they are. This is known as the *Picard-Lindelöf-Cauchy-Lipchitz* theorem; for it to hold, the vector field $\mathbf{f}(\mathbf{y}, t)$ must be continuous in t , and *Lipchitz continuous* in \mathbf{y} [16, 17] (intuitively, it must be continuous and have bounded distances between any pair of points). In general physical situations, problems are well defined and satisfy these conditions; however, tricky situations might hold for some interesting dynamical systems, see [17].

Solutions that can be reduced to explicit functions of time in terms of elementary functions, such as Eq. 0.5, are not general. The vector field will, in general, be nonlinear. Thus, general solutions do not exist. However, one may still obtain valuable information about the dynamical system without requiring the analytic solution. All the dynamics can be represented in the *phase space*, which is the space in which $\mathbf{y}(t)$ is represented as an n -dimensional vector. This position vector, parameterized on time, traces a trajectory in phase space for every initial condition given. Obtaining the form of the trajectory in phase space is a different problem than obtaining the analytical solution of the dynamical system (the trajectory parameterized on time), offering an alternative to analyze the dynamics. Sometimes, getting this trajectory in phase space (or at least some properties) can be enough for our purposes, as it describes the *qualitative* behavior of the solution.

In the rest of the section, we will focus on finite dimensional systems described by autonomous ODEs, as they are far more developed and familiar. Comments will be made on the difference equations, or nonautonomous counterparts whenever needed.

Fixed points and stability

One may ask if there exists a point in phase space for which, when reached, the dynamical system stops evolving. Such a point is called a *fixed point*. The condition for the system to stop evolving is $dy/dt = 0$; thus, a fixed point is also called an equilibrium point. The equation determining the fixed point \mathbf{y}_0 is

$$0 = \mathbf{f}(\mathbf{y}_0; \mathbf{c}). \quad (0.6)$$

Trajectories in phase space can not merge in finite time due to the existence and uniqueness theorem, and fixed points are for sure part of some solutions. Thus, fixed points are accessed on the limits $t \rightarrow \pm\infty$. Their presence or absence in phase space changes the orbits of dynamical systems. Not only points are *limit solutions*, cycles also exist. They correspond to closed curves in phase space fulfilling the property $\mathbf{y}(t+T) = \mathbf{y}(t)$ for all t and certain T called the period. Considering these trajectories reaching limit solutions and those generated by neighboring initial conditions, we gain insight into their *stability* depending on whether they move into or away from that limit solution.

Stability in the sense of Lyapunov. Given $dy/dt = \mathbf{f}(\mathbf{y})$. A solution $\mathbf{y}(t)$ is said to be uniformly stable if there exists a $\delta(\epsilon) > 0$ for every $\epsilon > 0$, such that any other solution $\mathbf{u}(t)$ for which $|\mathbf{y}(t_0) - \mathbf{u}(t_0)| < \delta(\epsilon)$, satisfies $|\mathbf{y}(t) - \mathbf{u}(t)| < \epsilon$ for all $t > t_0$. If no such $\delta(\epsilon)$ exists, then $\mathbf{y}(t)$ is said to be unstable [14].

This only means that nearby solutions remain arbitrarily close to the tested trajectory. Given this definition of stability, one can start to analyze the dynamics around fixed points and asses their type. Note that we can consider $\mathbf{y}(t) = \mathbf{y}_0$ a solution on the previous definition and classify fixed points into stable and unstable ones. Before we do so, it can be helpful to have the following theorem in mind

Lyapunov theorem of stability. Given $dy/dt = \mathbf{f}(\mathbf{y})$ and \mathbf{y}_0 a fixed point. If there exist a function $\mathcal{L}(\mathbf{y})$ in the neighborhood of \mathbf{y}_0 such that: i) $\mathcal{L}(\mathbf{y}_0) = 0$, $\mathcal{L}(\mathbf{y} \neq \mathbf{y}_0) > 0$, and ii) $\mathbf{f} \cdot \nabla \mathcal{L} \leq 0$. Then \mathbf{y}_0 is stable [14].

Functions $\mathcal{L}(\mathbf{y})$ are called *Lyapunov's functions*. Intuitively, note that $\dot{\mathcal{L}} = \nabla \mathcal{L} \cdot \frac{d\mathbf{y}}{dt} = \nabla \mathcal{L} \cdot \mathbf{f}$. Thus, $\dot{\mathcal{L}} \leq 0$, and the system evolves such that \mathcal{L} does not increase in value. In fact, we will reach the minimum of \mathcal{L} . Note that a simple way to create a system with these characteristics is to pick an \mathcal{L} function, say $\mathcal{L} = \mathbf{y} \cdot \mathbf{y}$, and consider $\mathbf{f} = -\nabla \mathcal{L}$. Such a system is said to be a *gradient system* or a *variational system* and is characterized by minimizing \mathcal{L} ; in such a system, we can learn everything about the fixed points by analyzing the Lyapunov's function landscape.

In a general problem, one could asses the stability of fixed points by finding the Lyapunov's functions; however, this may not be easy. We can further analyze the fixed points and

determine their stability by linearization. Let us expand around the fixed point \mathbf{y}_0 , that is, consider $\mathbf{y} = \mathbf{u} + \mathbf{y}_0$ in equation 0.2

$$\frac{d\mathbf{u}}{dt} = \left(\begin{array}{ccc} \partial f_1/\partial y_1 & \partial f_1/\partial y_2 & \dots \\ \partial f_2/\partial y_1 & \partial f_2/\partial y_2 & \dots \\ \dots & \dots & \dots \end{array} \right) \Big|_{\mathbf{y}_0} \mathbf{u} + \dots$$

equivalently one writes

$$\frac{d\mathbf{u}}{dt} = \nabla_{\mathbf{y}}\mathbf{f}(\mathbf{y}_0; \mathbf{c})\mathbf{u} + \dots \quad (0.7)$$

Where we have omitted the next terms in the Taylor expansion. We recognize that if $u \ll 1$, linear dynamics should describe the system fairly well around the fixed point. The linear equation will have a general solution similar to Eq. 0.5, and its behavior will be qualitatively determined by the sign of the Jacobian's $(\nabla_{\mathbf{y}}\mathbf{f}(\mathbf{y}_0; \mathbf{c}))$ eigenvalues. Whenever the real part of the eigenvalues are negative $\text{Re } \lambda_i < 0$ (for $i \in \{1, 2, 3, \dots, n\}$), an arbitrary initial condition close to the fixed point would converge to it; thus the point is *stable*. If some are positive, the fixed point would be *unstable*. This seems a reasonable approach; however, How is one sure that the remaining terms ignored on Eq. 0.7 are not relevant? This can be answered with the following theorem

Grobman-Hartman theorem. A hyperbolic fixed point is one whose Jacobian eigenvalues have nonvanishing real parts. Given $d\mathbf{y}/dt = \mathbf{f}(\mathbf{y})$ a continuous and at least one time differentiable vector field, namely, the nonlinear system. \mathbf{y}_0 an hyperbolic fixed point; and $d\mathbf{u}/dt = \nabla_{\mathbf{y}}\mathbf{f}(\mathbf{y}_0)\mathbf{u}$ the corresponding linear part of the system. Then, in a neighborhood of \mathbf{y}_0 , the nonlinear system is topologically equivalent to its linear part [17].

Topological equivalence of flows. Let two vector fields \mathbf{f} and \mathbf{g} producing the flows $\mathbf{y}_f(t; \mathbf{y}_i)$ and $\mathbf{y}_g(t; \mathbf{y}_i)$ (in other words, the collection of solutions for every initial condition \mathbf{y}_i). They are said to be equivalent if there exists a one-to-one mapping $\mathbf{h}(\mathbf{x})$ carrying the flow \mathbf{y}_f to \mathbf{y}_g such that $\mathbf{h}(\mathbf{y}_f(t; \mathbf{y}_i)) = \mathbf{y}_g(t; \mathbf{h}(\mathbf{y}_i))$. Moreover, they are said to be topologically equivalent if, in addition, the map \mathbf{h} and its inverse are continuous (\mathbf{h} is an *homeomorphism*) [16].

The theorem means that solutions on the linear part of the system can be continuously *deformed* to the actual solutions of the nonlinear system, preserving the direction (at least in a neighborhood around the fixed point). Thus, the linear analysis near a hyperbolic fixed point is enough to establish its stability type [17].

For example, consider a one dimensional damped linear oscillator satisfying Newton's equation with $F = -\mu v - \omega_0^2 x$. Clearly a fixed point corresponds to $(x_0, v_0) = (0, 0)$. Dynamics are already linear, so it is direct to write the eigenvalue equation

$$\left| \begin{pmatrix} -\lambda & 1 \\ -\omega_0^2 & -\mu - \lambda \end{pmatrix} \right| = \lambda(\lambda + \mu) + \omega_0^2 = 0.$$

Then,

$$2\lambda = -\mu \pm \sqrt{\mu^2 - 4\omega_0^2}.$$

We can see that for any value of ω_0^2 , if $\mu > 0$, both eigenvalues are negative, and the point

$(x_0, v_0) = (0, 0)$ is a stable fixed point. If $\mu < 0$, both eigenvalues are positive, and the fixed point would be unstable. One can note that the case $\mu = 0$ remains special; it is the point for which $\text{Re}\lambda_i = 0$ for some $i \in \{1, 2, 3, \dots, n\}$. At the same time, it defines a threshold in a control parameter for which a qualitative change in the phase space has occurred. Note that the Jacobian becomes singular at this threshold (at least one of its eigenvalues vanishes, then it becomes noninvertible). These singular properties define what is called a *bifurcation point*.

Bifurcations

The *control space* plays a major role in the theory of dynamical systems. It composes the space where the vector \mathbf{c} in Eq. 0.2 lays. We will refer to the dimension of the control space as the *codimension* c of our dynamical system. The reason is that, when computing fixed points, we have n equations corresponding to the dimension of the vector field. However, if one considers the control parameters variables, we have $n + c$ unknowns; the solutions are degenerated and parameterized by a vector of dimension c . As we saw in our previous example, changes may occur in the system when varying the control parameters. The term bifurcation was first employed by Poincaré [14, 18] when the number of fixed points changes in a system; one could generally say that

A bifurcation occurs any time the phase portrait is changed to a topologically nonequivalent portrait by a change of the control parameters [14].

When the number of fixed points changes, the previous condition holds. Whenever a fixed point changes stability, it continues to hold. Then, one has two clear approaches to studying bifurcations. Let us start analyzing fixed points. The equation for a fixed point \mathbf{y}_0 reads

$$0 = \mathbf{f}(\mathbf{y}_0; \mathbf{c}).$$

By solving this system, one could obtain the solutions $\mathbf{y}_0(\mathbf{c})$. Then, we may change the parameters in \mathbf{c} and analyze how the equilibrium changes. An important question is whether the solution exists and if it is continuous or not. If a discontinuity happens, a bifurcation may have occurred. To answer this, the implicit function theorem becomes useful, which we remember here

Implicit function theorem. Let $\mathbf{f}(\mathbf{y}, \mathbf{c}) = 0$ a system of n equations. Let $A \in \mathbb{R}^n$ and $B \in \mathbb{R}^c$ be regions that, for $\mathbf{y} \in A$ and $\mathbf{c} \in B$ the system has a solution, and the Jacobian in the first variable determinant does not vanish

$$\left| \begin{pmatrix} \partial f_1 / \partial y_1 & \partial f_1 / \partial y_2 & \dots \\ \partial f_2 / \partial y_1 & \partial f_2 / \partial y_2 & \dots \\ \dots & \dots & \dots \end{pmatrix} \right| \neq 0.$$

Then, there is a region C inside B such that for $\mathbf{c} \in C$ there is a unique solution

$$\mathbf{y} = \mathbf{g}(\mathbf{c}),$$

which is continuous in \mathbf{c} and satisfies $\mathbf{f}(\mathbf{g}(\mathbf{c}), \mathbf{c}) = 0$ [14].

This theorem warrants a *local* unique inversion of the problem (that is, find the fixed points in terms of the control parameters). However, it may hold in different regions; thus, multiple solutions are not forbidden. The solutions are continuous in \mathbf{c} ; then we refer to them as *branches* of solutions, as they draw a continuous path when moving the control parameters. From the point of view of the fixed points, a bifurcation may occur whenever these branches collide. If the continuous paths are still defined in the neighborhood of the bifurcation, the only condition that could be broken is the nonvanishing determinant of the Jacobian. Thus, at points for which $|\nabla \mathbf{f}(\mathbf{y}_0; \mathbf{c}_b)| = 0$, a bifurcation *may* have occurred at parameters \mathbf{c}_b ; verification by computing the higher order derivatives is needed for its assertion [14].

Now, let us return to the stability change of a fixed point past a bifurcation. As we mentioned earlier, considering initially a stable point, this would mean at least one eigenvalue crosses the imaginary axis as the parameters change. One can employ the implicit function theorem and convince oneself that eigenvalues $\lambda_i(\mathbf{c})$ vary continuously as \mathbf{c} changes (at least locally). Thus, at some critical value named the bifurcation point $(\mathbf{y}_0(\mathbf{c}_b), \mathbf{c}_b)$, one or various of the λ_i have vanishing real part. This is crucial, as, in this critical condition, the fixed point becomes nonhyperbolic. This means that the dynamics of a subspace of variables are determined by nonlinear terms, as well as the stability type of the fixed point. Considering the rest of the eigenvalues would have negative real parts, we expect that in the long time limit, only the dynamics of the zero eigenvalue subspace would be relevant. It is reasonable to ask oneself whenever the dynamics of the reduced subspace are general and describe bifurcations *universally*. One important mathematical result that moves in that direction corresponds to the *center manifold theorem*.

Center manifold theorem

For our purposes, a *manifold* corresponds to a space where one can locally define coordinates smoothly connected to their neighboring ones. For example, surfaces are submanifolds in \mathbb{R}^3 , as well as curves (*sub-* due to them having less dimension than the space containing them). Informally, any object for which you can impose a grid over it would be a manifold in our sense.

We mentioned that hyperbolic fixed points have neighboring dynamics topologically equivalent to the linear part of their dynamics. That is, the eigenvalues and eigenvectors play a crucial role in determining the flow. Eigenvectors, in particular, are tangent in the fixed point to a more general manifold, which we call the *unstable and stable manifolds* of the fixed point [17, 18] defined as follows

$$W_u(\mathbf{y}_0) = \{\text{all points traced by } \mathbf{y}(\mathbf{t}) \text{ such that } \mathbf{y}(\mathbf{t} \rightarrow -\infty) \rightarrow \mathbf{y}_0\} \quad (0.8)$$

$$W_s(\mathbf{y}_0) = \{\text{all points traced by } \mathbf{y}(\mathbf{t}) \text{ such that } \mathbf{y}(\mathbf{t} \rightarrow \infty) \rightarrow \mathbf{y}_0\} \quad (0.9)$$

In our previous example of an oscillator subjected to the force $F = -\mu v - \omega_0^2 x$, we found that for $\mu > 0$, the fixed point at the origin of the phase space (x, v) is stable; in this case, $W_s(\mathbf{y}_0)$ corresponds to the whole plane (x, v) and $W_u(\mathbf{y}_0)$ does not exist.

Now, at a nonhyperbolic fixed point, the system's flow has directions in phase space with nonexponential behavior (as the real part of some eigenvalue vanishes). This is predicted in the linear approximation. Moreover, the eigenvector corresponding to the eigenvalue with vanishing real part is tangent at the fixed point to a *center manifold* $W_c(\mathbf{y}_0)$, and the behavior of the flow in the center manifold is solely determined by the nonlinear terms; this is known as the *center manifold theorem* [17, 18]. Then, each subspace spanned by the eigenvectors associated with negative, positive, and vanishing eigenvalue real parts is tangent to the stable W_s , unstable W_u , and center W_c manifolds, respectively. The idea is to obtain an approximation of the dynamics at the center manifold thanks to changes of variables that produce the simplest possible equations. This procedure reveals the *normal form of the instability*, a unique equation (or set of equations) whose form depends on the Jacobian number of vanishing eigenvalues and symmetries of the system.

Normal forms of the center manifold dynamics

As mentioned earlier, the idea is to create a change of variables starting from the tangent eigenvectors as the initial term; then, one tries to obtain the center manifold coordinates systematically in a neighborhood of the fixed point. Different approaches can be found to obtain the change of variables; for example, see the summaries presented by Guckenheimer [18], or Arnold [17]. To be a normal form, the resulting equation should not be able to be simplified anymore by further changes or variables. In the following, we present a technique by Tirapegui et al. [19].

Let us start with the dynamical system $d\mathbf{y}/dt = \mathbf{f}(\mathbf{y}; \mathbf{c})$ whose linear part at the fixed point \mathbf{y}_0 , $d\mathbf{u}/dt = \nabla_{\mathbf{y}}\mathbf{f}(\mathbf{y}_0; \mathbf{c})\mathbf{u}$ is characterized by m eigenvalues with vanishing real part (and the rest negative, otherwise the unstable manifold would dominate) at the bifurcation point $\mathbf{c} = \mathbf{c}_b$. For simplicity we will describe the system with \mathbf{y}_0 at the origin, such that the system can be written as $d\mathbf{u}/dt = \nabla_{\mathbf{y}}\mathbf{f}(\mathbf{y}_0; \mathbf{c})\mathbf{u} + \mathbf{f}_{\text{N.L.}}(\mathbf{u})$ (remember that $\mathbf{u} = \mathbf{y} - \mathbf{y}_0$); then $\mathbf{f}_{\text{N.L.}}(\mathbf{u})$ represents the nonlinear part of the dynamical system (which will have typically a polynomial form after we have made the origin shift). Suppose one has written the system equations at the instability (or bifurcation) in the basis of (generalized) eigenvectors $\mathbf{Q} = (\mathbf{e}_1, \mathbf{e}_2, \dots, \mathbf{e}_n)$ (ordered by decreasing real part of their eigenvalue), that is, $\mathbf{A} = \mathbf{Q}\mathbf{y}$; Then, as we have vanishing real part of some eigenvalues, the equations will take the form of

$$\frac{d\mathbf{A}}{dt} = \mathbb{J}\mathbf{A} + \mathbf{f}_{\text{N.L.}}(\mathbf{A}), \quad (0.10)$$

where \mathbb{J} is a block diagonal matrix formed by Jordan blocks. Each type of instability produces a unique Jordan block (for example, a single eigenvalue vanishes, a pair of complex eigenvalues with vanishing real part, two single eigenvalues, two pairs of different complex eigenvalues, etc.); this is what allows the universal classification of instabilities according to normal forms. Of course, we will be interested in the first m equations. Moreover, we will be interested in the case for which we perturb the critical parameters such that $\mathbf{c} = \mathbf{c}_b + \epsilon$. This produces slight changes in the equation for \mathbf{A} that we generally write as

$$\frac{d\mathbf{A}}{dt} = \mathbb{J}\mathbf{A} + \mathbf{f}_{\text{N.L.}}(\mathbf{A}) + \mathbb{L}_\epsilon\mathbf{A} + \mathbf{f}_{\text{N.L.}\epsilon}(\mathbf{A}) + \mathbf{b}_\epsilon. \quad (0.11)$$

With the equation in this form, we will seek for a polynomial expansion of the first m

components of \mathbf{A} such that $A_i = \sum_k \sum_{l=0}^k A_i^{[k-l]} \epsilon_i^{[l]} \equiv \sum_k \sum_{l=0}^k A_i^{[k-l,l]}$ for $i = (1, 2, \dots, m)$; where $A^{[k,l]}$ means any monomial term composed of $(A_1, A_2, \dots, A_m, \epsilon_1, \epsilon_2, \dots)$ of order $k + l$, for example $\sqrt{2}A_1A_2$ is a term belonging to $A^{[2,0]}$, and $A_1A_2\epsilon_1 \cos 1$ belongs to terms $A^{[2,1]}$. This is motivated due to the fact that close to the instability and close to the fixed point, these variables should remain small.

Then, we have

$$\frac{dA_i}{dt} = \dot{A}_i^{[1,0]} + \dot{A}_i^{[0,1]} + \dot{A}_i^{[2,0]} + \dots = \sum_j (\mathbb{J}_{ij} + \mathbb{L}_{\epsilon ij}) \sum_k \sum_{l=0}^k A_j^{[k-l,l]} + \mathbf{f}_{\text{N.L.}}(\mathbf{A})_i + \mathbf{f}_{\text{N.L.}\epsilon}(\mathbf{A})_i + \mathbf{b}_{\epsilon i}.$$

Seeking to solve for $A_i^{[k,l]}$. The change of variables proposed and the structure of the operators form a hierarchy of equations where each subsequent term of the A_i series can be obtained from the previous ones by solving a linear problem. Note that one could separate

$$\mathbb{L}_\epsilon = \mathbb{L}_\epsilon^{[0,1]} + \mathbb{L}_\epsilon^{[0,2]} + \dots,$$

$$\mathbf{f}_{\text{N.L.}} + \mathbf{f}_{\text{N.L.}\epsilon} = \mathbf{f}_{\text{N.L.}}^{[2,0]}(A^{[1]}) + \mathbf{f}_{\text{N.L.}}^{[2,1]}(A^{[1]}, \epsilon^{[1]}) + \mathbf{f}_{\text{N.L.}}^{[3,0]}(A^{[1]}, A^{[2]}) + \dots,$$

and similarly for the rest of the terms. Then

$$\sum_j (\mathbb{J}_{ij}) A_j^{[k+1,l]} = -\dot{A}_i^{[k+1,l]} + \sum_p \sum_j \mathbb{L}_{\epsilon ij}^{[0,p]} A_j^{[k+1,l-p]} + \mathbf{f}_{\text{N.L.}}^{[k+1,l]}(A^{[1]}, \dots, A^{[k]}, \epsilon^{[1]}, \dots, \epsilon^{[l-1]}) + \mathbf{b}_\epsilon^{[k+1,l]}.$$

As $\mathbf{b}_\epsilon = \mathbf{b}_\epsilon^{[0,1]} + \mathbf{b}_\epsilon^{[0,2]} + \dots$ is a constant perturbation it only affects initial equations with $k + 1 = 0$ (for which $\mathbf{f}_{\text{N.L.}}^{[k+1,l]} = 0$). The first step corresponds to the linearized equations and the first-order parameter perturbations alone (these starting cases allow the iteration of the previous equation), reading

$$\mathbb{J}\mathbf{A}^{[0,1]} = -\dot{\mathbf{A}}^{[0,1]} + \mathbf{b}_\epsilon^{[0,1]}. \quad (0.12)$$

Note that the problems we are solving are of the type $\mathcal{A}\mathbf{x} = \mathbf{z}$. If the operator $\mathcal{A} : L_1 \rightarrow L_2$ (L_1, L_2 subspaces of \mathbb{R}^m), then, one must ensure that \mathbf{z} is in the image of \mathcal{A} . Imposing this condition will give an additional equation at each order of the hierarchy of equations; finally, the two unknowns $\dot{A}_i^{[k,l]}$ and $A_i^{[k,l]}$ can be unveiled systematically at each order. Finally, a scaling of the coefficients is proposed; the idea is that as the deviations from the bifurcation parameters remain small (at least $O(\epsilon)$), one has natural timescales which are used to construct a normal form independent of ϵ . We highlight that the method of Tirapegui et al. is characterized by providing a systematic approach to compute normal forms. This is because the linear problem to be solved at each order is the same (the operator does not change with subsequent orders of the hierarchy) and has the form 0.12. Tirapegui et al. provided the general solution of such a linear equation in [19], solving the problem of the computation of normal forms in any system.

The method is best illustrated with examples. Let us exhibit the calculations in two cases: a single vanishing eigenvalue and a pair of complex eigenvalues; they give rise to the *imperfect pitchfork* and *Andronov-Hopf* normal forms, respectively. To accomplish this, let us consider the physically relevant example of a one-dimensional generalized Van der Pol

oscillator described by

$$\ddot{x} - \mu(1 - x^2)\dot{x} - [(\epsilon - 1)x + \sin(x - \phi)] = 0,$$

where we have included the additional term $\sin(x - \phi)$ to play with an arbitrary nonlinearity in the equation. Note that $\mathbf{c} = (\mu, \epsilon, \phi)$. The equation defining the equilibria is

$$(\epsilon - 1)x + \sin(x - \phi) = 0,$$

and is easy to see that for $\phi = 0$, $(\dot{x}, x) = (0, 0)$ is an equilibrium of the system. Let us write $v = \dot{x}$ and we can write the system as

$$\frac{d}{dt} \begin{pmatrix} x \\ v \end{pmatrix} = \begin{pmatrix} 0 & 1 \\ \epsilon & \mu \end{pmatrix} \begin{pmatrix} x \\ v \end{pmatrix} + \begin{pmatrix} 0 \\ -\mu x^2 v + (-\phi - \frac{(x-\phi)^3}{3!} + \dots) \end{pmatrix}. \quad (0.13)$$

Analyzing the linear part, one finds eigenvalues

$$\lambda_{\pm} = \frac{\mu \pm \sqrt{\mu^2 + 4\epsilon}}{2}.$$

One realizes two separate things may occur. i) for any given $\mu < 0$ not necessarily small, we have a real eigenvalue (λ_+) which crosses the imaginary axis when $\epsilon = 0$. ii) for any given $\epsilon < 0$ not necessarily small, a pair of complex eigenvalues crosses the imaginary axis at $\mu = 0$. Note that both instabilities require fine-tuning only one parameter (ϵ in the first case and μ in the second case); thus, they are codimension one instabilities.

Let us first analyze the case i). Note that μ will be an arbitrary negative number, so let us employ dimensionless units $\tau = |\mu|t$ and $v = |\mu|v$ such that in equation $\mu = -1$. Then, we first separate the linear part as

$$\begin{pmatrix} 0 & 1 \\ \epsilon & -1 \end{pmatrix} = \begin{pmatrix} 0 & 1 \\ 0 & -1 \end{pmatrix} + \begin{pmatrix} 0 & 0 \\ \epsilon & 0 \end{pmatrix} \equiv \mathbf{J}_c + \mathbf{L}_\epsilon.$$

We compute the eigenvectors at the instability ($\epsilon = 0$), reading

$$\mathbf{v}_+ = \begin{pmatrix} 1 \\ 0 \end{pmatrix}, \quad \mathbf{v}_- = \begin{pmatrix} 1 \\ -1 \end{pmatrix}.$$

Finally, we construct the matrix of basis change $\mathbf{Q} = (\mathbf{v}_+, \mathbf{v}_-)$, and compute the matrices

$$\mathbb{J} = \mathbf{Q}\mathbf{J}_c\mathbf{Q}^{-1} = \begin{pmatrix} 0 & 0 \\ 0 & -1 \end{pmatrix}$$

and

$$\mathbb{L}_\epsilon = \mathbf{Q}\mathbf{L}_\epsilon\mathbf{Q}^{-1} = \begin{pmatrix} \epsilon & \epsilon \\ -\epsilon & -\epsilon \end{pmatrix}.$$

Also, the new variables

$$\mathbf{A} = \mathbf{Q} \begin{pmatrix} x \\ v \end{pmatrix} = \begin{pmatrix} x + v \\ -v \end{pmatrix} \equiv \begin{pmatrix} A_1 \\ A_2 \end{pmatrix},$$

and the constant perturbation

$$\mathbf{b}_\epsilon = \mathbf{Q} \begin{pmatrix} 0 \\ -\phi + \phi^3/3! + \dots \end{pmatrix}.$$

Finally, the problem we want to solve reads

$$\begin{aligned} \dot{\mathbf{A}} = \begin{pmatrix} 0 & 0 \\ 0 & -1 \end{pmatrix} \mathbf{A} + \begin{pmatrix} -A_2(A_1 + A_2)^2 + \frac{(A_1 + A_2)^2 \phi + (A_1 + A_2) \phi^2}{2} - \frac{(A_1 + A_2)^2}{6!} + \dots \\ -(-A_2(A_1 + A_2)^2 + \frac{(A_1 + A_2)^2 \phi + (A_1 + A_2) \phi^2}{2} - \frac{(A_1 + A_2)^2}{6!} + \dots) \end{pmatrix} \\ + \begin{pmatrix} \epsilon & \epsilon \\ -\epsilon & -\epsilon \end{pmatrix} \mathbf{A} + \begin{pmatrix} -\phi + \phi^3/3! + \dots \\ -(-\phi + \phi^3/3! + \dots) \end{pmatrix}. \end{aligned} \quad (0.14)$$

We start with the eigenvector associated with the vanishing eigenvalue as our initial guess (we denote its magnitude with A)

$$\mathbf{A} = A \begin{pmatrix} 1 \\ 0 \end{pmatrix} + \mathbf{A}^{[0,1]} + \mathbf{A}^{[1,1]} + \mathbf{A}^{[2,0]} + \mathbf{A}^{[2,1]} + \mathbf{A}^{[3,0]} + \dots \quad (0.15)$$

and the time derivative of this variable describing the central manifold (A), which we assume of the form

$$\dot{A} = \dot{A}^{[0,1]} + \dot{A}^{[1,1]} + \dot{A}^{[2,0]} + \dot{A}^{[2,1]} + \dot{A}^{[3,1]} + \dots \quad (0.16)$$

Replacing the previous ansatz in equation 0.14 results in a hierarchy of equations that we explicitly solve.

$O(A^{[0,1]})$:

$$\dot{A}^{[0,1]} \begin{pmatrix} 1 \\ 0 \end{pmatrix} = \mathbb{J} \mathbf{A}^{[0,1]} + \begin{pmatrix} -\phi \\ \phi \end{pmatrix}$$

Note that the image of \mathbb{J} corresponds to the vector $\mathbf{e}_2 = (0, 1)^T$ (where T denotes the transpose). Then, for the equation to have a solution, forcefully it is required that

$$\dot{A}^{[0,1]} = -\phi.$$

Then, the system has a solution given by

$$\mathbf{A}^{[0,1]} = \begin{pmatrix} 0 \\ \phi \end{pmatrix}.$$

$O(A^{[1,1]})$:

$$\dot{A}^{[1,1]} \begin{pmatrix} 1 \\ 0 \end{pmatrix} = \mathbb{J} \mathbf{A}^{[1,1]} + \begin{pmatrix} \epsilon & \epsilon \\ -\epsilon & -\epsilon \end{pmatrix} A \begin{pmatrix} 1 \\ 0 \end{pmatrix}.$$

The solutions are given by

$$\dot{A}^{[1,1]} = \epsilon A, \quad \mathbf{A}^{[1,1]} = \begin{pmatrix} 0 \\ -\epsilon A \end{pmatrix}.$$

$O(A^{[0,2]})$:

$$\dot{A}^{[0,2]} \begin{pmatrix} 1 \\ 0 \end{pmatrix} = \mathbb{J} \mathbf{A}^{[0,2]} + \begin{pmatrix} \epsilon & \epsilon \\ -\epsilon & -\epsilon \end{pmatrix} A \begin{pmatrix} 0 \\ \phi \end{pmatrix}.$$

The solutions are given by

$$\dot{A}^{[0,2]} = \epsilon \phi, \quad \mathbf{A}^{[0,2]} = \begin{pmatrix} 0 \\ -\epsilon \phi \end{pmatrix}.$$

$O(A^{[1,2]})$:

$$\dot{A}^{[1,2]} \begin{pmatrix} 1 \\ 0 \end{pmatrix} = \mathbb{J} \mathbf{A}^{[1,2]} + \begin{pmatrix} \epsilon^2 A + \frac{1}{2} A \phi^2 - 2A\epsilon\phi \\ -(\epsilon^2 A + \frac{1}{2} A \phi^2 - 2A\epsilon\phi) \end{pmatrix}.$$

The solutions are given by

$$\dot{A}^{[1,2]} = \epsilon^2 A + \frac{1}{2} A \phi^2 - 2A\epsilon\phi, \quad \mathbf{A}^{[1,2]} = \begin{pmatrix} 0 \\ -(\epsilon^2 A + \frac{1}{2} A \phi^2 - 2A\epsilon\phi) \end{pmatrix}.$$

$O(A^{[2,0]})$: At this order everything vanishes identically

$O(A^{[2,1]})$:

$$\dot{A}^{[2,1]} \begin{pmatrix} 1 \\ 0 \end{pmatrix} = \mathbb{J} \mathbf{A}^{[2,1]} + \begin{pmatrix} A^2 \phi / 2 \\ -A^2 \phi / 2 \end{pmatrix}.$$

The solutions are given by

$$\dot{A}^{[2,1]} = A^2 \phi / 2, \quad \mathbf{A}^{[2,1]} = \begin{pmatrix} 0 \\ -A^2 \phi / 2 \end{pmatrix}.$$

$O(A^{[3,0]})$:

$$\dot{A}^{[3,0]} \begin{pmatrix} 1 \\ 0 \end{pmatrix} = \mathbb{J} \mathbf{A}^{[3,0]} + \begin{pmatrix} -A^3 / 6 \\ -A^3 / 6 \end{pmatrix}.$$

The solutions are given by

$$\dot{A}^{[3,0]} = -A^3 / 6, \quad \mathbf{A}^{[3,0]} = \begin{pmatrix} 0 \\ A^3 / 6 \end{pmatrix}.$$

We stop here due to $A^3/6$ being the first term free of a parameter. We write the equation for A derived

$$\dot{A} = \epsilon\phi - \phi + \left(\epsilon + \frac{\phi^2}{2} - 2\epsilon\phi + \epsilon^2\right)A + \frac{\phi}{2}A^2 - A^3/6 + O(A^{[2,2]}, A^{[3,1]}, A^{[4,0]}, \dots).$$

Now, we apply the idea of scaling. Remember that we are close to the critical condition of bifurcation of the fixed point $(x, v) = (0, 0)$ of our original problem. Then, the parameters ϵ and ϕ are small (otherwise, our initial step has to be modified). Now, analyze the contribution of each term in the equation. The lowest contributions correspond to $-\phi + \epsilon A + \phi A^2/2 - A^3/6$, if all these terms were significant, it would indicate that $A^3 \sim \phi \sim \epsilon A \sim \phi A^2$; but if $\phi \sim A^3$, then $\phi A^2 \sim A^{[5]}$, which is a much higher order contribution. Finally, the scaling corresponds to $\epsilon \sim \phi^3/2$. We can formally provide an equation free of small parameters as follows. First, write $\epsilon = \delta\tilde{\epsilon}$ and $\phi = \delta^{\frac{3}{2}}\tilde{\phi}\sqrt{6}$, with $\delta \ll 1$; then, $A \equiv \delta^{\frac{1}{2}}\tilde{A}\sqrt{6} \sim \delta^{\frac{1}{2}}$. The linear term dictates the temporal evolution scale; we choose $\tau = \delta t$, and one has

$$\delta^{\frac{3}{2}}\frac{d\tilde{A}}{d\tau} = \delta^{\frac{3}{2}}\left(-\tilde{\phi} + \tilde{\epsilon}\tilde{A} - \tilde{A}^3\right) + O(\delta^4). \quad (0.17)$$

In the limit $\delta \rightarrow 0$ the equation is quantitatively correct. Let us write the equation with no tildes as follows

$$\dot{A} = -\phi + \epsilon A - A^3. \quad (0.18)$$

The previous equation is known as the *imperfect pitchfork* normal form. It is a codimension two equation, including a condition for instability and a condition for the birth of a hysteresis loop (known also as the birth of bistability) between asymmetric states. Equation 0.18 contains all the codimension one instabilities (except the Hopf instability), that is, it contains the *saddle node*, the *transcritical*, and *pitchfork* bifurcations. This equation describes the typical dynamics at the center manifold when a single eigenvalue crosses the imaginary axis. With a simple linear change of variables $A = A - A_0(\epsilon, \phi)$ it can be written in the equivalent form

$$\dot{A} = \eta A + \kappa A^2 - A^3,$$

which will appear continuously throughout chapters 4, 5, and 6 of this dissertation. It is much easier to see all the codimension one bifurcations in this form. Take $\kappa = 0$ and one recovers the pitchfork bifurcation. Consider only the neighborhood of $A = 0$ and one recovers the transcritical bifurcation. Simplify the equation for the equilibria by A and one is left with $\eta + \kappa A - A^2 = 0$, which exhibits a saddle node bifurcation at parameters $\kappa^2 + 4\eta = 0$.

Now, let us examine case ii), which produces the Andronov-Hopf normal form. Note that we will have oscillations in the center manifold whose frequency is arbitrary. In the case of complex eigenvalues crossing the imaginary axis, one needs to solve a slightly different linear problem at each order compared to the previous case; this is due to the arbitrary frequency of the linear solution appearing at each order, modifying the linear operator acting on the unknown function to be solved. Let us illustrate this by computing the normal form. First,

write the linear part as

$$\begin{pmatrix} 0 & 1 \\ \epsilon & \mu \end{pmatrix} = \begin{pmatrix} 0 & 1 \\ \epsilon & 0 \end{pmatrix} + \begin{pmatrix} 0 & 0 \\ 0 & \mu \end{pmatrix} \equiv \mathbf{J}_c + \mathbf{L}_\mu.$$

For negative epsilon we have the eigenvalues $\lambda_\pm = \pm i\sqrt{|\epsilon|}$. It will be convenient to write $\epsilon = -|\epsilon| = -\omega_0^2$ and rescale $v = \sqrt{|\epsilon|}v$. The problem reads

$$\frac{d}{dt} \begin{pmatrix} x \\ v \end{pmatrix} = \begin{pmatrix} 0 & \omega_0 \\ -\omega_0 & 0 \end{pmatrix} \begin{pmatrix} x \\ v \end{pmatrix} + \begin{pmatrix} 0 \\ \mu\omega_0 v - \mu\omega_0 x^2 v + (-\phi - \frac{(x-\phi)^3}{3!} + \dots) \end{pmatrix}. \quad (0.19)$$

The linear operator of the previous equation is the canonical block when a pair of eigenvalues crosses the imaginary axis. One can see that solutions $x = Ae^{i\omega_0 t} + c.c.$, $v = iAe^{i\omega_0 t} + c.c.$ satisfy the linear part. Then, it is proposed that

$$\begin{pmatrix} x \\ v \end{pmatrix} = \begin{pmatrix} 1 \\ i \end{pmatrix} A + \begin{pmatrix} 1 \\ -i \end{pmatrix} \bar{A} + \begin{pmatrix} x \\ v \end{pmatrix}^{[0,1]} + \begin{pmatrix} x \\ v \end{pmatrix}^{[1,1]} + \dots$$

and

$$\dot{A} = i\omega_0 A + \dot{A}^{[0,1]} + \dot{A}^{[1,1]} + \dot{A}^{[2,0]} + \dots$$

The equation for \dot{A} is obtained by conjugation of the previous expression. Inserting this expansions for the variables in the equations of motion yields a hierarchy of equations just as case i). However, the linear operator is a little different; the imaginary part of the eigenvalue ω_0 is not necessarily small, unlike the real part $\mu \ll 1$. Let us write the problem at the initial step $O^{[0,1]}$

$$\begin{pmatrix} 1 \\ i \end{pmatrix} \dot{A}^{[0,1]} + c.c. = \left[\begin{pmatrix} 0 & \omega_0 \\ -\omega_0 & 0 \end{pmatrix} - \mathbf{I} \left(i\omega_0 A \frac{\partial}{\partial A} - i\omega_0 \bar{A} \frac{\partial}{\partial \bar{A}} \right) \right] \begin{pmatrix} x \\ v \end{pmatrix}^{[0,1]} + \begin{pmatrix} 0 \\ -\phi \end{pmatrix}.$$

One can note a contribution $\mathbf{I} \left(i\omega_0 A \frac{\partial}{\partial A} - i\omega_0 \bar{A} \frac{\partial}{\partial \bar{A}} \right)$ acting on the elements of the vectors $(x \ v)^{[i,j]T}(A, \bar{A})$ (it repeats in all the equations of the hierarchy). We remind that A and \bar{A} are the vector amplitudes corresponding to each eigenvalue $\pm\omega_0$; that they are the conjugate one of the other (to ensure that the variables are real) is an additional constraint.

The action of the operation $A \frac{\partial}{\partial A}$ is better understood when introducing the inner product, considering $A = a_A + ib_A$

$$\langle f(A) | g(A) \rangle = \int \int e^{-a_A^2 - b_A^2} \bar{f}(A) g(A) da_A db_A.$$

Then, one can compute the following

$$\begin{aligned}
\langle f(A) | \frac{\partial}{\partial A} g(A) \rangle &= \int \int e^{-A\bar{A}} f(\bar{A}) \frac{\partial}{\partial A} g(A) da_A db_A, \\
&= \int \int \frac{\partial}{\partial A} \left[e^{-A\bar{A}} f(\bar{A}) g(A) \right] - \frac{\partial}{\partial A} \left[e^{-A\bar{A}} f(\bar{A}) \right] g(A) da_A db_A, \\
&= \int \int e^{-A\bar{A}} \bar{A} f(\bar{A}) g(A) da_A db_A, \\
&= \langle Af(A) | g(A) \rangle.
\end{aligned}$$

To obtain the third line we used the fact that $\partial/\partial A = \partial/\partial a_A - i\partial/\partial b_A$ and integrated directly.

We have obtained that $A = (\frac{\partial}{\partial A})^\dagger \equiv \hat{a}_A^\dagger$. The same can be formulated for the variable \bar{A} , obtaining $\bar{A} = (\frac{\partial}{\partial \bar{A}})^\dagger \equiv \hat{a}_{\bar{A}}^\dagger$. As the image of the operator acting over $(x \ v)^{[i,j]T}$ is not straightforward, we employ the Fredholm alternative; for a linear problem of the form $\mathcal{A}\mathbf{x} = \mathbf{z}$, we can find a solution if \mathbf{z} is in the image of \mathcal{A} , or alternatively, if \mathbf{z} is perpendicular to the kernel of \mathcal{A}^\dagger . In our case, the linear operator is

$$\mathcal{A} = \left[\begin{pmatrix} 0 & \omega_0 \\ -\omega_0 & 0 \end{pmatrix} - \mathbf{I} \left(i\omega_0 A \frac{\partial}{\partial A} - i\omega_0 \bar{A} \frac{\partial}{\partial \bar{A}} \right) \right].$$

Then, using that $(\hat{a}_A^\dagger \hat{a}_A)^\dagger = (\hat{a}_A^\dagger \hat{a}_A)$ one finds

$$\mathcal{A}^\dagger = \left[\begin{pmatrix} 0 & -\omega_0 \\ \omega_0 & 0 \end{pmatrix} + \mathbf{I} \left(i\omega_0 A \frac{\partial}{\partial A} - i\omega_0 \bar{A} \frac{\partial}{\partial \bar{A}} \right) \right].$$

One notes that

$$\left(i\omega_0 A \frac{\partial}{\partial A} - i\omega_0 \bar{A} \frac{\partial}{\partial \bar{A}} \right) A^m \bar{A}^n = i\omega_0(m-n)A^m \bar{A}^n,$$

and

$$\left[\begin{pmatrix} 0 & -\omega_0 \\ \omega_0 & 0 \end{pmatrix} + \mathbf{I} \left(i\omega_0 A \frac{\partial}{\partial A} - i\omega_0 \bar{A} \frac{\partial}{\partial \bar{A}} \right) \right] \begin{pmatrix} k_1 \\ k_2 \end{pmatrix} A^m \bar{A}^n = \begin{pmatrix} k_1 i\omega_0(m-n) - k_2 \omega_0 \\ k_1 \omega_0 + k_2 i\omega_0(m-n) \end{pmatrix}.$$

One easily finds the elements of the kernel by inspection. If $m-n=1$, then $k_2 = ik_1$ and k_1 is free. If $m-n=-1$, then $k_2 = -ik_1$; no more solutions exist, and we considered the most general nonlinear term formed by A and \bar{A} . Finally,

$$\text{Ker}(\mathcal{A}^\dagger) = \left\{ \begin{pmatrix} 1 \\ i \end{pmatrix} A|A|^m, \begin{pmatrix} 1 \\ -i \end{pmatrix} \bar{A}|A|^m \right\}.$$

In our initial step of the normal form computation, we find no elements in the kernel of \mathcal{A}^\dagger . One solves explicitly finding

$$\dot{A}^{[0,1]} = 0,$$

and

$$\begin{pmatrix} x \\ v \end{pmatrix}^{[0,1]} = \begin{pmatrix} -\frac{\phi}{\omega_0} \\ 0 \end{pmatrix}.$$

After straightforward calculations one finds the general normal form for an oscillatory instability, the Andronov-Hopf normal form

$$\begin{aligned} \dot{A} &= \epsilon A - cA|A|^2 + O(A^4), \\ \dot{\bar{A}} &= \bar{\epsilon}\bar{A} - \bar{c}\bar{A}|A|^2 + O(A^4). \end{aligned}$$

In our worked example, $\epsilon = \mu/2 + i\omega_0$ and $c = i/4$. Note that c is purely imaginary, thus solutions explode. This is due to the saturation mechanism of the equation $-\mu x^2 v$ being small, and thus negligible in the normal form computation. In reality, this term saturates the growing oscillations; if one wants to capture saturation, one should change $-\mu x^2 v \rightarrow -x^2 v$, then, $c \rightarrow 1 + i/4$ and solutions are well-behaved.

Infinite dimensional systems

When describing the dynamics of a continuous field, we will face infinite dimensional systems. This is due to the field being specified at each point of space; as space is dense, a dynamical system with a noncountable number of elements describes the field. Some entities are intrinsically a field, for example, electromagnetic fields. However, one can often think of infinite dimensional systems as idealizations of finite dimensional systems. This is the approach in this dissertation, constrained by the fact that infinite dimensional systems are not accessible in numerical studies (due to the finite information computers can process); we will always approximate fields by a discrete set of points. In other words, no matter if we are studying finite or infinite dimensional systems, numerical algorithms always correspond to finite dimensional ones; thus, they must be studied as such. A mathematical procedure that relates an infinite dimensional system with a finite counterpart is known as *the continuum limit*.

The continuum limit

Consider a finite dimensional system of a few variables describing the behavior of an individual object. For example, an oscillator. Imagine now that we have several of these objects, which may be identical or not (but generally described by the same set of variables), and they can interact. That is, we have a large collection of identical variables $\mathbf{y}_i(t)$ that we enumerate with i , an extended system. From here, we can construct several equations for a continuous variable $\mathbf{y}_i(t) \rightarrow \mathbf{y}(\mathbf{r}, t)$ depending mainly on: i) how do we arrange the identical objects, for example, we can arrange them in a line, in a square lattice, on a sphere, etc. ii) what is the form of the interactions.

One of the simplest choices is to consider linear interactions, arranging the objects in a regular grid. If the grid is one-dimensional, we refer to it as a *chain*. Then, the system would

read

$$\dot{\mathbf{y}}_i = \mathbf{f}_i + \mathbb{A} \begin{pmatrix} \mathbf{y}_1 \\ \mathbf{y}_2 \\ \cdot \\ \cdot \\ \cdot \end{pmatrix},$$

where \mathbb{A} is called the *adjacency matrix*. The element \mathbb{A}_{ij} dictates how the object in position i is affected by the object in position j . For a chain of nearest neighbor coupled objects, the matrix \mathbb{A} will be tri-diagonal. The diagonal is a term of self-interaction that normalizes the linear individual dynamics. The coupling is then characterized by the off-diagonal terms. Depending on whether the off-diagonal terms are symmetric, we classify the system as *reciprocally* or *nonreciprocally* coupled.

A continuum limit can be constructed by noting that the index of the individual objects can serve as a position. Then, let us say that the objects are separated by distances a in a regular grid (for simplicity). The grid will have a dimension depending on how many indexes are needed to map each point in it to three-dimensional space. This mapping takes the indexes i, j, \dots and constructs a position for each point $\mathbf{r} = \mathbf{r}(i, j, \dots)$. In the simplest case of a regular one-dimensional grid. $x = ia$. Thus, the continuous variable would be $\mathbf{y}_i(t) \rightarrow \mathbf{y}(x = ia, t)$. Finally, the coupling is approximated by operators on the continuous variable y ; one possibility is noticing that

$$\sum \mathbb{A}_{ik} \mathbf{y}_k(t) = \sum \mathbb{A}_{ik} \mathbf{y}(ak, t) = \mathbb{A}_{ii} \mathbf{y}(ia, t) + \mathbb{A}_{ii+1} \mathbf{y}(ia + a, t) + \mathbb{A}_{ii-1} \mathbf{y}(ia - a, t) + \dots (0.20)$$

And perform the approximations

$$\mathbf{y}(ia + ka) \equiv \mathbf{y}(x + ka) = \mathbf{y}(x) + ka \frac{\partial}{\partial x} \mathbf{y}(x) + \frac{k^2 a^2}{2!} \frac{\partial^2}{\partial x^2} \mathbf{y}(x) + \dots$$

A continuum equation is formally defined whenever in the limit of $a/a_0 \rightarrow 0$, equation 0.20 converges to something different than $\mathbf{y}(x) \sum_k \mathbb{A}_{ik}$; that is, some constants multiplying differential operators $\partial^k / \partial x^k$ survive the limiting process. a_0 is a characteristic distance to compare with the grid separation. This process is more straightforward whenever the adjacency matrix is sparse; then, operators have approximations in terms of a few points in the grid, such as

$$\begin{aligned} \frac{\partial}{\partial x} z(x = ia) &= \frac{z_{i+1} - z_{i-1}}{2a} + O(a^2), \\ \frac{\partial^2}{\partial x^2} z(x = ia) &= \frac{z_{i+1} - 2z_i + z_{i-1}}{a^2} + O(a^2), \end{aligned}$$

and other expressions which can be straightforwardly derived up to a desired accuracy in a .

Another convenient approximation whenever the adjacency matrix is not sparse corresponds to

$$\sum \mathbb{A}_{ik} \mathbf{y}_k(t) = \sum \mathbb{A}_{ik} \mathbf{y}(ak, t) \approx \frac{1}{a} \int dx' \mathbb{A}(x, x') \mathbf{y}(x'). \quad (0.21)$$

The adjacency matrix has been promoted to a continuous function of its indexes. When written in this form, we will refer to the coupling as nonlocal; this is due to Eq. 0.21 involving the whole field \mathbf{y} , the dynamic of a point of the field would depend on all the points. Compared to terms with differential operators, which are local.

Reciprocal and nonreciprocal coupling

We mentioned that depending on the properties of \mathbb{A} , we could call systems reciprocally or nonreciprocally coupled. The definition based on \mathbb{A} corresponds to the linear, one-dimensional (a chain) case. It is easy to note that in the chain, a stimulus (change of the variables) of the rightmost neighbors of an individual in position l has an effect that is equivalent (nonequivalent) to the effect produced by the same stimuli coming from the leftmost neighbors if the coupling is reciprocal (nonreciprocal).

This could be generalized to nonlinear interactions such that

$$\dot{\mathbf{y}}_i = \mathbf{f}_i + \sum_j \mathbf{f}_{ij}(\mathbf{y}_i, \mathbf{y}_j),$$

where we still have restricted ourselves to only pair-wise interactions. However, this will be enough for the purposes of the dissertation. Again, whenever $\mathbf{f}_{ij}(\mathbf{y}_i, \mathbf{y}_j) \neq \mathbf{f}_{ji}(\mathbf{y}_j, \mathbf{y}_i)$, the interaction will be said to be nonreciprocal. This time, the response to each stimulus can be nonlinear.

Considering the linear case (because of analytical solutions), one can readily see the enormous difference it yields when the adjacency matrix is symmetric or not. Symmetry warrants a complete set of eigenvectors spanning phase space and real eigenvalues, contrary to the case of an arbitrary matrix. Then, one could separate the adjacency matrix into a symmetric and anti-symmetric part. During this dissertation, we will refer to the symmetric part as the *reciprocal coupling part* and the anti-symmetric part as the *nonreciprocal coupling part*.

Nonreciprocal coupling is not natural at the fundamental level, as the time-reversal symmetry of the microscopic world restricts it. One is easily convinced by imagining a spring with markers at its two ends; a nonreciprocal spring (also called an *odd* spring [20, 21]) would show a displacement $d_{12}(x_{12})$ in the right end when displaced from the left a distance x_{12} , which will be different to a displacement $d_{21}(x_{21})$ on the left end when displaced from the right a distance x_{21} ; now, the time-reversed evolution of the process of applying x_{12} would require that $d_{21}(x_{21} = d_{12}) = x_{12}$, which is valid only if the spring answers reciprocally to stimuli. Passive mechanical elements that respond nonreciprocally have been obtained in a quasi-static regime [7], and nonreciprocal coupling in a dynamic regime has been constructed with active elements (robots) [8], which monitor the behavior of their neighbors and react prioritizing left (or right)-handed neighbors. Systems that actively consume energy and interact with their environments can be described with nonreciprocal couplings [11, 20].

Partial differential equations

If the adjacency matrix is sparse, that is, each element interacts with few others, it is probably that in the continuum limit, we will reach a partial differential equation for the field $\mathbf{y}(\mathbf{x}, t)$,

where $\mathbf{x} \in \mathbb{R}^d$, reading

$$\mathbf{P}_{pde}(\mathbf{y}, \frac{\partial}{\partial t}\mathbf{y}, \frac{\partial}{\partial x_1}\mathbf{y}, \dots, \frac{\partial}{\partial x_d}\mathbf{y}, \dots, \frac{\partial^2}{\partial x_1^2}\mathbf{y}, \dots, \frac{\partial^2}{\partial x_d^2}\mathbf{y}, \dots) = 0.$$

Such equations appear naturally in the standard descriptions of electromagnetic fields, the velocity fields of fluids, or the displacement fields of solids, to mention a few. Solution methods for these equations are scarce and situational. Linear equations can be solved by standard methods of separation of variables or basis decomposition. Nonlinear equations usually do not have solutions, and numerical methods are employed. In these numerical methods, a finite dimensional system (or a discretized equation) can be related to the partial differential equation, as mentioned earlier. Then, standard temporal solvers, such as the Runge-Kutta of fourth order algorithm, can be employed.

Integro-differential equations

A dense adjacency matrix would be best described by a kernel (or influence function, or pound function) over which we need to integrate to obtain the coupling. Previously, we illustrated the case of an adjacency matrix with constant coefficients, yielding a kernel $\mathcal{A}(x, x')$ independent of time. More general equations would also allow kernels to depend on space and time and include local operators (such as partial derivatives). Then, a general integro-differential equation would read

$$\mathbf{P}_{ide}(\mathbf{y}, \frac{\partial}{\partial t}\mathbf{y}, \frac{\partial}{\partial x_1}\mathbf{y}, \dots, \frac{\partial}{\partial x_d}\mathbf{y}, \dots, \frac{\partial^2}{\partial x_1^2}\mathbf{y}, \dots, \frac{\partial^2}{\partial x_d^2}\mathbf{y}, \dots, \int \mathcal{A}(\mathbf{x}, \mathbf{x}', t, t')\mathbf{P}(\mathbf{y}(\mathbf{x}', t')) d\mathbf{x}' dt', \dots) = 0.$$

Where $\mathbf{P}(\mathbf{y}(\mathbf{x}', t'))$ can be any function non necessarily linear. Such equations appear naturally in complex problems such as plasma physics and in general particle systems that can be described by Boltzmann equations for the phase space density; other physical examples include the Raman scattering effect in optical resonators [22].

Variational and non variational systems

The type of equations described previously have a structure that is not easy to address generally. Indeed, spatially extended systems (infinite dimensional systems) have much more richness of dynamical behaviors compared to the finite dimensional ones. Finite dimensional systems exhibit limit solutions, quasi-periodic orbits, and chaos. On the other hand, extended systems have qualitatively different complex states apart from chaos, such as turbulence, spatiotemporal intermittency, and spatiotemporal chaos (or extensive chaos), to mention a few.

Nevertheless, as in finite dimensional systems, there exists a variety of extended systems that asymptotically evolve to their fixed solutions (which can now be inhomogeneous in space), so-called *variational systems*. Consider an infinite dimensional dynamical system (for simplicity, consider a one-component field)

$$\frac{\partial}{\partial t}y = f(y, \frac{\partial}{\partial x}y, \dots).$$

If f can be obtained from a free energy functional (with suitable boundary conditions), the

system is said to be *variational*; then

$$f = -\frac{\delta G}{\delta y} = -\sum_k (-1)^k \frac{d^k}{dx^k} \left(\frac{\partial g}{\partial (\frac{\partial^k y}{\partial x^k})} \right), \quad G = \int g(y, \frac{\partial}{\partial x} y, \dots) dx.$$

And the Free energy G is always reduced by temporal evolution

$$\frac{dG}{dt} = \int \frac{\delta G}{\delta y} \frac{\partial y}{\partial t} dx = - \int \left(\frac{\partial y}{\partial t} \right)^2 dx.$$

Such a system will evolve to the minimum of the G functional, obtaining a stationary solution (independent of t). Differently, *nonvariational systems* do not have such a feature, and their dynamics could be permanent in time. Note that computing variational systems' equilibria is analogous to solving mechanical problems with an action function $S = G$ using the space variable instead of time. This applies to both partial differential and integro-differential equations; however, the formula of the functional derivative ($\delta G/\delta y$) in the latter case is not as simple as the one shown here (it can be computed with the standard methods of the calculus of variations).

Spatial instability

As in finite dimensional systems, branches of equilibrium solutions exist as a function of the control parameters. These branches suffer bifurcations in similar forms; now, spatially inhomogeneous profiles can unstabilize, too, giving rise to what is called *spatial instabilities*. Inhomogeneous solutions in equations governed by homogeneous drivings are intriguing, and the process of their formation is often referred to as *spontaneous symmetry breaking* [2].

A pioneer in studying patterns in dynamical systems is Alan Turing. Intrigued by the formation of forms, the *morphogenesis*, he established how two diffusing chemical reactants could generate periodic structures with an intrinsic wavelength depending on the reaction parameters. Spatial instabilities giving rise to intrinsic periodic patterns are often called *Turing instabilities*, and their theory is well developed in systems with homogeneous parameters (parameters that do not depend on space) [2, 23]. Consider a general system with general linear and nonlinear parts, replicate them N times in a regular grid, and couple them to their nearest neighbors linearly and reciprocally. In the continuum limit, that process leads to *diffusive* transport; that is, in the expansion of the adjacency matrix summation, only the second derivative term survives the limiting process. Such a general system would read (here we explicitly write a two-species system to maintain affordable calculations)

$$\frac{\partial}{\partial t} \begin{pmatrix} u \\ v \end{pmatrix} = \begin{pmatrix} \epsilon & 1 \\ \nu & -1 \end{pmatrix} \begin{pmatrix} u \\ v \end{pmatrix} + \begin{pmatrix} f_{N.L.u}(u, v) \\ f_{N.L.v}(u, v) \end{pmatrix} + \begin{pmatrix} D_u \nabla^2 u \\ D_v \nabla^2 v \end{pmatrix},$$

where we are employing time and variable units such that we can choose two coefficients of the linear part as one and minus one (we are assuming v linearly dissipates, without loss of generality). Now, this system has a right-hand side independent of the space variable \mathbf{r} explicitly. Ignoring the nonlinear terms, using the Fourier basis for the space dependence

representation seems useful. Indeed, one proposes that linearly

$$\mathbf{u}(\mathbf{r}, t) = \int \hat{\mathbf{u}}(\mathbf{k}, t) e^{i\mathbf{k}\cdot\mathbf{r}} d\mathbf{k},$$

where \mathbf{k} is known as the *wavevector*. Then, it follows from the equations of motion that

$$\int \frac{\partial}{\partial t} \hat{\mathbf{u}} e^{i\mathbf{k}\cdot\mathbf{r}} d\mathbf{k} = \int \left[\begin{pmatrix} \epsilon & 1 \\ \nu & -1 \end{pmatrix} - \mathbf{k}^2 \begin{pmatrix} D_u \\ D_v \end{pmatrix} \right] \hat{\mathbf{u}} e^{i\mathbf{k}\cdot\mathbf{r}} d\mathbf{k}.$$

We have a linear equation for each Fourier mode; this is the usefulness of the Fourier base in this type of problem. Whenever the linear part has inhomogeneous coefficients (they depend explicitly on the space coordinate), another base of space could be useful. Now, our linear problem has eigenvalues satisfying the equation

$$(\epsilon - D_u \mathbf{k}^2 - \lambda_{\mathbf{k}})(-1 - D_v \mathbf{k}^2 - \lambda_{\mathbf{k}}) = \nu.$$

A *Turing instability* may occur whenever the real part of an eigenvalue (or pair of complex eigenvalues) with a nonvanishing wavevector crosses the imaginary axis. If this happens, the amplitude of the *critical wavevector* (\mathbf{k}_c) and its neighbors start to grow exponentially, and the solution behaves as

$$\mathbf{u}(\mathbf{r}, t) = \int \hat{\mathbf{u}}(\mathbf{k}, t) e^{i\mathbf{k}\cdot\mathbf{r}} d\mathbf{k} \rightarrow \hat{\mathbf{u}}(\mathbf{k}_c, t_0) e^{i\mathbf{k}_c\cdot\mathbf{r} + \lambda_{\mathbf{k}_c} t},$$

which is a spatially periodic solution (period, or wavelength, equal to $2\pi/|\mathbf{k}_c|$) with an amplitude varying exponentially in time. To obtain the critical wavevector and the parameter conditions for a Turing instability, first, we look for local maxima of the $\text{Re}(\lambda_{\mathbf{k}}) \equiv \lambda(\mathbf{k})$ surface; then, we evaluate at such local maxima and require that the real part of the eigenvalue vanishes, reading

$$\nabla_{\mathbf{k}} \lambda|_{\mathbf{k}_c} = 0, \quad \lambda(\mathbf{k}_c) = 0.$$

We can apply these conditions to our example, giving the equation for the critical wavevector

$$\mathbf{k}_c(\mathbf{k}_c^2 - \frac{\epsilon D_v - D_u}{2D_v D_u}) = 0,$$

from where we can solve for $\mathbf{k}_c(D_u, D_v, \epsilon)$. The condition $\lambda(\mathbf{k}_c) = 0$ reads finally

$$\mathbf{k}_c^4(D_u, D_v, \epsilon) = -\nu - \epsilon,$$

defining the parameter values $(D_u, D_v, \epsilon, \nu)$ for which the instability occurs.

Normal forms of homogeneous solutions corrected by spatial coupling

From our previous discussion, one could ask oneself if there is a universal equation describing how the amplitude of the spatially periodic solution evolves; in principle, if one can restrict the spatial dynamics to only the critical mode, then we recover a finite-dimensional system, but what happens if a continuum of modes surges? In addition, one could ask which is the simplest infinite dimensional equation containing a Turing instability. To answer these questions, we need to modify the computation of normal forms to include spatially coupling terms.

First, note that $\mathbf{k} = 0$ corresponds to homogeneous perturbations; that is, for $\mathbf{k} = 0$, we recover a finite-dimensional system, and the application of the normal form calculation is straightforward. Then, spatial perturbations could be included by perturbatively moving away from this limit. Formally, consider that

$$\mathbf{u} = \int \hat{\mathbf{u}}(\mathbf{k}, t) e^{i\mathbf{k}\cdot\mathbf{r}} d\mathbf{k}.$$

Then, the spatial derivatives become

$$\frac{\partial^n}{\partial x_p^n} \mathbf{u} = \int (ik_p)^n \hat{\mathbf{u}}(\mathbf{k}, t) e^{i\mathbf{k}\cdot\mathbf{r}} d\mathbf{k}.$$

The spatial derivative of each Fourier mode drops a $(ik)^n$ factor. Varying the control parameters in an extended system, when linearized and written in an adequate spatial basis, allows for a great number of eigenvalues crossing the imaginary axis past a bifurcation; these are the spatial modes. If only a numerable number of eigenvalues is relevant, dynamics could be discretized to such few modes in a sort of *tight binding*-like procedure. Differently, if an infinite number of eigenvalues crosses the imaginary axis when moving the parameters, the system could be approximated by a partial differential equation; this is the case adopted from now as we are considering the Fourier basis in an infinite domain (in principle, after, we will impose boundary conditions).

We have our linearized problem giving the eigenvalues $\lambda = \lambda(\mathbf{k}, \mathbf{c})$, and there exist values for which $\nabla\lambda|_{\mathbf{k}_c} = 0$ (is a maximum) and $\lambda(\mathbf{k}_c, \mathbf{c}_c) = 0$. If $\mathbf{c} = \mathbf{c}_c + \delta\mathbf{c}$ we will have that $\lambda(\mathbf{k}) > 0$ for a narrow band of k modes, informally, $k_c - \delta k < k < k_c + \delta k$ will be the relevant modes at infinite time observations. The closer to the instability point, the narrower the band of unstable modes will be. This motivates the inclusion of $\delta\mathbf{k}$ as a small parameter in our expansions. Of course, this only makes sense when we explicitly write equations in the Fourier representation, but we will omit them, as they are not enlightening to write down; instead, it is natural to work in real space.

Let us derive the most general equation for a system exhibiting a Turing instability. Note that the intrinsic wavelength in our worked example corresponds to

$$\mathbf{k}_c^2 = \frac{\epsilon D_v - D_u}{2D_v D_u}.$$

Note that for any values of D_u , D_v , and ϵ , one can fine-tune ν to have a vanishing real part of the corresponding eigenvalue $\lambda(\mathbf{k}_c)$. In such a case, the Turing instability occurs at *finite wavelength*, and an equation for the *critical Fourier mode's amplitude* can be obtained; the resulting equations will be of the Hopf normal form type corrected with the spatial coupling leading to the so-called Ginzburg-Landau or Newell-Whitehead-Segel equation depending if we are under isotropic or anisotropic coupling [2, 23]. These equations will be addressed in the next section of this framework.

A different situation arises when the condition $\epsilon D_v - D_u = 0$ meets. The instability in this case occurs at *infinite wavelength*, that is, homogeneous solutions are perturbed by slowly varying functions of space (infinite wavelength) if $\mathbf{c} = \mathbf{c}_c + \delta\mathbf{c}$. Explicitly computing \mathbf{c}_b yields

the equations $\epsilon_c D_v = D_u$ and $\nu_c = -\epsilon_c$ for an *infinite wavelength Turing instability* (in our example with diffusive transport), note that we need to fine-tune at least two parameters to meet the two equations. Let $\epsilon = \epsilon_c + \epsilon_1$ and $\nu = -\epsilon_c + \nu_1$ with $|\epsilon_1| \ll \epsilon_c$ and $|\nu_1| \ll \epsilon_c$ ($\epsilon_c = D_u/D_v$ is an arbitrary positive number depending on the spatial coupling strength). Then, the system would read

$$\frac{\partial}{\partial t} \begin{pmatrix} u \\ v \end{pmatrix} = \begin{pmatrix} \epsilon_c & 1 \\ -\epsilon_c & -1 \end{pmatrix} \begin{pmatrix} u \\ v \end{pmatrix} + \begin{pmatrix} f_{N.L.u}(u, v) \\ f_{N.L.v}(u, v) \end{pmatrix} + \begin{pmatrix} D_u \nabla^2 u \\ D_v \nabla^2 v \end{pmatrix} + \begin{pmatrix} \epsilon_1 & 0 \\ \nu_1 & 0 \end{pmatrix} \begin{pmatrix} u \\ v \end{pmatrix}.$$

Fourier transforming the previous equation would yield

$$\frac{\partial}{\partial t} \begin{pmatrix} \hat{u} \\ \hat{v} \end{pmatrix} = \begin{pmatrix} \epsilon_c & 1 \\ -\epsilon_c & -1 \end{pmatrix} \begin{pmatrix} \hat{u} \\ \hat{v} \end{pmatrix} + \frac{1}{2\pi} \begin{pmatrix} \int f_{N.L.u}(u, v) e^{-i\mathbf{k}\cdot\mathbf{r}} d\mathbf{r} \\ \int f_{N.L.v}(u, v) e^{-i\mathbf{k}\cdot\mathbf{r}} d\mathbf{r} \end{pmatrix} + \begin{pmatrix} -\mathbf{k}^2 \hat{u} \\ -\mathbf{k}^2 \hat{v} \end{pmatrix} + \begin{pmatrix} \epsilon_1 & 0 \\ \nu_1 & 0 \end{pmatrix} \begin{pmatrix} \hat{u} \\ \hat{v} \end{pmatrix}. \quad (0.22)$$

Equivalently, one could write (u, v) as their Fourier representation and replace them in the equations of motion; one can note that nonlinearities in real space translate into convolutions in Fourier space, they remain nonlinear in the transformed fields \hat{u} and \hat{v} but nonlocal. Explicitly, for example in one dimension,

$$u^2 = \int \hat{u}(k) e^{ikx} dk \int \hat{u}(q) e^{iqx} dq = \int e^{ikx} \left[\int \hat{u}(q) \hat{u}(k-q) dq \right] dk.$$

Now that we have our equivalent problem in Fourier space, we can start computing the normal form. In addition to the small variables (A_1, A_2, \dots) (the magnitude of the variables describing the center manifold around the bifurcation point) and $\delta\mathbf{c}$ (the deviation of the critical parameters), we include the characteristic spatial variations $|\mathbf{k}| \equiv k$ as small. The ansatz needs to be modified by including an additional index describing the order of the solutions; that is, we use the notation $A^{[j,l,m]}$ for terms which are of order j in (A_1, A_2, \dots) , order l in $\delta\mathbf{c}$, and order m in k (the Fourier *wavenumber*). For example, a term of the form $\epsilon_1 A^2 \nabla^2 A$ would correspond to a $O^{[2,1,2]}$ term. Indeed, its Fourier representation reads (in one dimension for simplicity)

$$\begin{aligned} \epsilon_1 A^2 \nabla^2 A &= \epsilon_1 \int \hat{u}(k) e^{ikx} dk \int \hat{u}(q) e^{iqx} dq (-p^2) \int \hat{u}(p) e^{ipx} dp, \\ \epsilon_1 A^2 \nabla^2 A &= \epsilon_1 \int e^{ikx} \int \hat{u}(p) \hat{u}(q) \hat{u}(k-q-p) (-q^2) dq dp dk. \end{aligned}$$

One can note that writing it explicitly on the Fourier basis is cumbersome. Considering this, we start solving the problem 0.22. The linear order is easy to solve, proposing the expansions

$$\mathbf{A} = A \mathbf{v}_c + \mathbf{A}^{[1,1,0]} + \mathbf{A}^{[1,0,2]} + \mathbf{A}^{[2,0,0]} + \mathbf{A}^{[2,1,0]} + \mathbf{A}^{[3,0,0]} + \dots$$

where \mathbf{v}_c is obtained from the linear problem, and

$$\dot{\mathbf{A}} = \dot{A}^{[1,0,2]} + \dot{A}^{[1,1,0]} + \dot{A}^{[2,0,0]} + \dot{A}^{[2,1,0]} + \dot{A}^{[3,0,0]} + \dots$$

Remember that the last index in $A^{[j,l,m]}$ is formally defined only in the Fourier representation. Then, we will need the Fourier transforms of our new variables

$$\hat{\mathbf{A}} = \hat{A} \mathbf{v}_c + \hat{\mathbf{A}}^{[1,1,0]} + \hat{\mathbf{A}}^{[1,0,2]} + \hat{\mathbf{A}}^{[2,0,0]} + \hat{\mathbf{A}}^{[2,1,0]} + \hat{\mathbf{A}}^{[3,0,0]} + \dots$$

Terms $\hat{\mathbf{A}}^{[j,l,0]}$ do not depend on the wavenumber and thus represent the homogeneous contributions. At the linear order, $O^{[1,0,0]}$, one has

$$0 = \begin{pmatrix} \epsilon_c & 1 \\ -\epsilon_c & -1 \end{pmatrix} \mathbf{A} \mathbf{v}_c.$$

Which is solved for $\mathbf{v}_c = (1 \quad -\epsilon_c)^T$. At $O^{[1,1,0]}$ the equation reads

$$\dot{\mathbf{A}}^{[1,1,0]} \mathbf{v}_c = \begin{pmatrix} \epsilon_c & 1 \\ -\epsilon_c & -1 \end{pmatrix} \mathbf{A}^{[1,1,0]} + \begin{pmatrix} \epsilon_1 & 0 \\ \nu_1 & 0 \end{pmatrix} \mathbf{v}_c A.$$

We apply the condition for the previous linear equation to have a solution. It is clear that the image of the linear operator are the vectors $\mathbf{v}_I = (1 \quad -1)^T$. One imposes that

$$\dot{\mathbf{A}}^{[1,1,0]} \mathbf{v}_c - \begin{pmatrix} \epsilon_1 & 0 \\ \nu_1 & 0 \end{pmatrix} \mathbf{v}_c A \propto \begin{pmatrix} 1 \\ -1 \end{pmatrix}.$$

Then, $\dot{\mathbf{A}}^{[1,1,0]} - \epsilon_1 A \propto 1$ and $-\epsilon_c \dot{\mathbf{A}}^{[1,1,0]} - \nu_1 A \propto -1$. Equivalently, $\dot{\mathbf{A}}^{[1,1,0]} = (\epsilon_1 + \nu_1)A / (1 - \epsilon_c)$ and

$$\mathbf{A}^{[1,1,0]} = \begin{pmatrix} 0 \\ \frac{\epsilon_c \epsilon_1 + \nu_1}{1 - \epsilon_c} \end{pmatrix}.$$

From now, we will write only the terms relevant after the scaling. At order $O^{[1,0,2]}$ one has

$$\dot{\hat{\mathbf{A}}}^{[1,0,2]} \mathbf{v}_c = \begin{pmatrix} \epsilon_c & 1 \\ -\epsilon_c & -1 \end{pmatrix} \hat{\mathbf{A}}^{[1,0,2]} + \begin{pmatrix} -\mathbf{k}^2 D_u & 0 \\ 0 & -\mathbf{k}^2 D_v \end{pmatrix} \mathbf{v}_c A.$$

With solutions

$$\dot{\hat{A}} = \frac{D_u - \epsilon_c D_v}{1 - \epsilon_c} (-\mathbf{k}^2) \hat{A} = 0,$$

which vanishes due to the condition $k_c = 0$, and

$$\hat{\mathbf{A}}^{[1,0,2]} = \begin{pmatrix} 0 \\ \mathbf{k}^2 D_u \hat{A} \end{pmatrix}, \quad \mathbf{A}^{[1,0,2]} = \begin{pmatrix} 0 \\ -D_u \nabla^2 A \end{pmatrix}.$$

To continue computing explicitly, we choose the nonlinear terms $f_{N.L.u}(u, v) = \alpha u^2 - u^3$ and $f_{N.L.v}(u, v) = -uv$. At $O^{[2,0,0]}$ one finds

$$\dot{\mathbf{A}}^{[2,0,0]} \mathbf{v}_c = \begin{pmatrix} \epsilon_c & 1 \\ -\epsilon_c & -1 \end{pmatrix} \mathbf{A}^{[2,0,0]} + \begin{pmatrix} \alpha A^2 \\ \epsilon_c A^2 \end{pmatrix}.$$

With solutions

$$\dot{\hat{A}}^{[2,0,0]} = \frac{\alpha + \epsilon_c}{1 - \epsilon_c} A^2,$$

and

$$\mathbf{A}^{[2,0,0]} = \begin{pmatrix} 0 \\ \frac{\epsilon_c(1+\alpha)}{1-\epsilon_c} \end{pmatrix} A^2.$$

Similarly at $O^{[3,0,0]}$

$$\dot{A}^{[3,0,0]} \mathbf{v}_c = \begin{pmatrix} \epsilon_c & 1 \\ -\epsilon_c & -1 \end{pmatrix} \mathbf{A}^{[3,0,0]} + \begin{pmatrix} \alpha \\ \epsilon_c A^2 \end{pmatrix},$$

one finds the solution

$$\dot{A}^{[3,0,0]} = A^3 \left[\frac{-1}{1-\epsilon_c} - \frac{\epsilon_c(1+\alpha)}{(1-\epsilon_c)^2} \right].$$

After straightforward calculations one finds

$$\begin{aligned} \dot{A}^{[1,1,2]} &= \frac{D_v(\epsilon_c \epsilon_1 + \nu_1)}{(1-\epsilon_c)^2} \nabla^2 A, \\ \dot{A}^{[2,0,2]} &= \frac{D_u}{1-\epsilon_c} A \nabla^2 A + \frac{D_v \epsilon_c (1+\alpha)}{(1-\epsilon_c)^2} \nabla^2 (A^2), \\ \dot{A}^{[1,0,4]} &= \frac{-D_v D_u}{1-\epsilon_c} \nabla^4 A. \end{aligned}$$

Note that we have the equation

$$\begin{aligned} \dot{A} &= \frac{\epsilon_1 + \nu_1}{1-\epsilon_c} A + \frac{\alpha + \epsilon_c}{1-\epsilon_c} A^2 - \left[\frac{1}{1-\epsilon_c} + \frac{\epsilon_c(1+\alpha)}{(1-\epsilon_c)^2} \right] A^3 + \frac{D_v(\epsilon_c \epsilon_1 + \nu_1)}{(1-\epsilon_c)^2} \nabla^2 A \\ &\quad + \frac{D_u}{1-\epsilon_c} A \nabla^2 A + \frac{D_v \epsilon_c (1+\alpha)}{(1-\epsilon_c)^2} \nabla^2 (A^2) - \frac{D_u D_v}{1-\epsilon_c} \nabla^4 A + h.o.t. \end{aligned}$$

It is possible to find an scaling using the dummy parameter $\delta \ll 1$. Let $\epsilon_1 = -\nu_1 + \delta^2 \epsilon_2 (1-\epsilon_c)$, $\nu_1 = \delta \nu_1 (1-\epsilon_c) / D_v$, $\alpha = -\epsilon_c + \delta \alpha_1 (1-\epsilon_c)$, $A \sim \delta$, $\nabla \sim \mathbf{k} \sim \delta$, $\partial_t \sim \delta^2$. With this, the equation reads

$$\dot{A} = \epsilon_2 A + \alpha_1 A^2 - \frac{1+\epsilon_c}{1-\epsilon_c} A^3 + \nu_1 \nabla^2 A + \frac{D_u}{1-\epsilon_c} A \nabla^2 A + \frac{D_v \epsilon_c}{1-\epsilon_c} \nabla^2 (A^2) - \frac{D_u D_v}{1-\epsilon_c} \nabla^4 A + O(\delta).$$

The previous equation is known as the Lifshitz normal form [24], and it is the simplest pattern forming equation for an scalar field. This model is of codimension 3, as three parameters are fine-tuned to meet the critical conditions.

Defects, patterns, and interfaces

Extended nonlinear systems display a variety of behaviors. They are essential to understanding complex phenomena, such as the turbulent motion of fluid flows, which is captured by the Navier-Stokes equations, at least numerically. Thanks to the mapping of the *dynamic phase diagrams* classifying the behaviors of systems according to the parameter regions in which they are observed, one can make extended systems to operate in the regimes desired by the performer. The normal forms of the bifurcations provide great insight into the dynamics in the neighborhood of the critical points of parameter space, and the different regions of the phase diagram can be approximated analytically, thanks to them. Moreover, some normal forms are simple enough to allow the analytical computation of the solution of the nonlinear extended system, at least close to critical values from which one could use perturbation theory to explore the vicinity of parameters. These tools allow the description of several non-

linear phenomena under the same veil. In the following, we will describe the main nonlinear solutions of extended systems that will be researched throughout this dissertation: fronts and patterns.

Fronts

Fronts are solutions of an extended system (an infinite dimensional system) or arrays of coupled finite dimensional systems, that spatially connect two equilibria. For this reason, fronts are also called, depending on the context, phase walls, domain walls, propagation wave, or simply front into the stable (or unstable) state. The last name originates because fronts are solutions for which a position (or curve in higher dimensions) in space can be defined; therefore, they have a velocity. Fronts move, and as a consequence, they propagate an equilibrium state over the system. The equilibria connected through the front may not be spatially homogeneous; fronts between pattern solutions and even chaotic states can be defined [25]. In this dissertation, we will describe the effect nonreciprocal coupling has on fronts during chapters 1 and 2, but first, we need to understand the basic concepts of fronts. Depending on whether fronts propagate a stable state over a less stable state or over an unstable state, we classify them as *fronts into the stable state* or *fronts into the unstable state*, respectively. We will be able to analyze front dynamics employing the imperfect pitchfork normal form with diffusive transport (minimal reciprocal coupling with neighbors), reading

$$\frac{\partial}{\partial t}A = -\eta A + \kappa A^2 - A^3 + D\nabla^2 A. \quad (0.23)$$

This equation is generally obtained for coupled systems that suffer an instability of the homogeneous state, it is also known as the Landau-de Gennes equation. In our example leading to the Lifshitz normal form of the preceding section, we can obtain Eq. 0.23 if we do not ask the Turing instability at infinite wavenumber condition (which explicitly writes in the example $\nu = \nu_c = -D_u/D_v$), and instead let ν be an arbitrary number.

The difference between the two main types of front propagation relies on the properties of their velocity. Fronts into the unstable state are characterized by propagating over a region where the system is homogeneously in an unstable equilibrium; the perturbation of this unstable state due to the front profile is what drives the motion. Fronts into the stable state propagate over a region of homogeneous stable state variables; necessarily, the equilibrium being imposed after the front passes must be *more* stable than the previous state; this is what intuition dictates, but one must be able to define what is *more stable*, which is a difficult question for non-variational systems. Note that equation 0.23 is a variational system, for which

$$G = \int \left(\frac{\eta}{2}A^2 - \frac{\kappa}{3}A^3 + \frac{1}{4}A^4 + \frac{D}{2}(\nabla A)^2 \right) d\mathbf{r}.$$

Interestingly, if one includes a simple nonreciprocal coupling in the chain (for example, including a tridiagonal anti-symmetric matrix part in the adjacency matrix of the corresponding discrete system), G can cease to be a Lyapunov functional. We analyze this and its effects on the velocity propagation of fronts in the initial chapters and the perspectives of this dissertation.

Fronts into the unstable state

Let us start with equation 0.23 with parameters $\eta < 0$. This ensures that the equilibrium state $A_0 = 0$ is unstable against perturbations of any wavevector. Fronts into the unstable state are classified into two major types: pulled and pushed fronts [25]. Pulled fronts are characterized by a velocity determined by the linear dynamics around the unstable state; thus, they are *pulled* by the linear dynamics (from the state to be propagated). Pushed fronts have a velocity that is determined by the whole nonlinear system; thus, the parts where the front has already passed have an effect on the velocity; then, one says that the motion is *pushed* by the nonlinear dynamics (from the state propagated over the system). The one-dimensional problem $\partial A/\partial t = f(A) + \partial^2 A/\partial x^2$ (with $f(0) = 0$ and $f(1) = 0$ with $f'(0) > 0$ and $f'(1) < 0$) has been rigorously studied by Aronson and Weinberger [26], where they demonstrated that a rigid translating front profile has a speed v constrained by the limits

$$2\sqrt{f'(0)} \leq v < 2\sqrt{\sup\{f(A)/A\}},$$

where $f'(x)$ denotes the derivative of $f(x)$. The result can be obtained after lengthy calculations starting with the ansatz $A = u(x - vt)$ and the change of variables $p(u) = -\partial u/\partial z$ ($z = x - vt$). The lower bound for the velocity was found independently by Fisher [27] and Kolmogorov et al. [28] in 1937, studying the same model in different contexts ($f(A) = A(1 - A)$), in their case, the lower limit was exactly the velocity of the fronts propagating.

The lower limit is known as the linear spreading velocity and corresponds to the velocity of pulled fronts. The velocity of pushed fronts lies anywhere between the limits. It is interesting to note that a great variety of functions $f(A)$ with the boundary conditions mentioned have the property $\sup\{f(A)/A\} = f'(0)$, in that case, it is direct to establish the pulled nature of the front. Benguria and Depassier proposed a variational scheme to provide better bounds for the front speed [29–31] in the same problem studied by Aronson and Weinberger; essentially, one provides test functions that are operated and the result is after minimized with respect to some free parameter. The technique can help determine the exact or approximated speed of pushed fronts.

The equation studied by Aronson and Weinberger seems limiting at first glance, as more complex systems could also exhibit fronts, and the theory should be further developed in those cases. One answer lies in the normal form calculations, as any instability of the homogeneous state can be described by such equations. Similarly, patterns and oscillations have envelopes described by Andronov-Hopf normal forms corrected with diffusive coupling; thus, fronts between patterns can be similarly described with that equation. However, more complex situations might require the full set of equations far from the validity of the normal form computation. Indeed, one may be interested in the corrections to the front speed arising from non-diffusive transport mechanisms. A similar ansatz of a rigid moving front does not warrant the mathematical simplicity that the equation studied by Aronson and Weinberger offers; thus, the front speed computation for pushed fronts remains an open question. An extensive review of the pulled front speed properties and the experimental efforts to observe them is found in [25].

In chapters 1 and 2, we will encounter fronts into the unstable state of the pulled type. We present here the basics of the method for the computation of pulled front speed in PDE

models following [25]. First, consider a system described by

$$\frac{\partial}{\partial t} \mathbf{A} = \mathbf{f}(\mathbf{A}, \frac{\partial}{\partial \mathbf{x}} \mathbf{A}, \frac{\partial^2}{\partial \mathbf{x}^2} \mathbf{A}, \dots).$$

Let us assume that $\mathbf{A} = 0$ is an unstable equilibrium and corresponds to the initial state. One linearizes around the unstable equilibrium $\mathbf{A} = 0 + \mathbf{u}$, and the system will read generally

$$\frac{\partial}{\partial t} \mathbf{u} = \mathbf{f}_0 \mathbf{u} + \sum_k \mathbf{f}_{1k} \frac{\partial}{\partial x_k} \mathbf{u} + \mathbf{f}_{2k} \frac{\partial^2}{\partial x_k^2} \mathbf{u} + \dots$$

where $\mathbf{f}_0 = \partial \mathbf{f} / \partial \mathbf{A} |_{\mathbf{A}=0}$, $\mathbf{f}_{1k} = \partial \mathbf{f} / \partial (\partial \mathbf{A} / \partial x_k) |_{\mathbf{A}=0}$, etc. are matrix coefficients computed after making a simple Taylor expansion. Then, we analyze the problem after a Fourier transform, define

$$\mathbf{u} = \int \hat{\mathbf{u}}(\mathbf{k}, t) e^{i\mathbf{k} \cdot \mathbf{r}} d\mathbf{k}.$$

Then, the spatial part of the linear problem is transformed easily in an algebraic equation according to $\partial / \partial x_l = ik_l$, explicitly

$$\frac{\partial}{\partial t} \hat{\mathbf{u}} = \mathbf{f}_0 \hat{\mathbf{u}} + \sum_l \mathbf{f}_{1l} ik_l \hat{\mathbf{u}} + \mathbf{f}_{2l} i^2 k_l^2 \hat{\mathbf{u}} + \dots \equiv \mathbf{J}(\mathbf{k}) \hat{\mathbf{u}}$$

The solution to such an equation was discussed earlier in this Framework chapter and is obtained by computing the eigenvalues and eigenvectors of the matrix $\mathbf{J}(\mathbf{k})$. Let $\Psi_l(\mathbf{k})$ be the eigenvectors associated with the eigenvalues $\lambda_l(\mathbf{k})$, and $\hat{\mathbf{u}}(\mathbf{k}, t = 0) = \sum_l \hat{\mathbf{u}}_{0l} \Psi_l(\mathbf{k})$ the initial condition. Then, $\hat{\mathbf{u}}(\mathbf{k}, t) = \sum_l \hat{\mathbf{u}}_{0l}(\mathbf{k}) \Psi_l(\mathbf{k}) e^{\lambda_l(\mathbf{k})t}$. Finally, our linearized solution in real space is

$$\mathbf{u} = \int \sum_l \hat{\mathbf{u}}_{0l} \Psi_l(\mathbf{k}) e^{\lambda_l(\mathbf{k})t} e^{i\mathbf{k} \cdot \mathbf{r}} d\mathbf{k}.$$

Now, to have a front, we need to have a rigid-like movement of a profile connecting two different states. To obtain the equations for the velocity, let us transform to a coordinate system fixed with the front movement. Define $\xi = \mathbf{r} - \mathbf{v}t$. The phase factors in the last integral will read $\lambda_l(\mathbf{k})t + i\mathbf{k} \cdot \xi + i\mathbf{k} \cdot \mathbf{v}t$. Interested in the long time limits, one employs a stationary phase approximation to obtain the leading contribution to the integral, that is $\nabla_{\mathbf{k}} (\lambda_l(\mathbf{k}) + i\mathbf{k} \cdot \mathbf{v}) = 0$, or

$$\mathbf{v} = i \nabla_{\mathbf{k}} \lambda_l(\mathbf{k}).$$

If the solution is stationary in the co-moving reference frame, then exponential growth is forbidden. This gives the condition that

$$\text{Re}(\lambda_l(\mathbf{k}) + i\mathbf{k} \cdot \mathbf{v}) = 0.$$

These two equations determine both the complex wavenumber characterizing the front (its steepness and frequency of oscillations) and the propagation velocity. One can note that for more than one dimension, the notion of a front is diffused, as fronts are not characterized by a single point anymore, and thus the definition of velocity becomes an issue. The previous formulas need to be used with care only in quasi-one-dimensional dynamics of front propagation (fronts described by a single degree of freedom in space). For details on fronts in more than one dimension, see [23]. Another important aspect is which of the branches

of λ_l to use (for more than one field, we have more branches of eigenvalues); the answer lies in the stationary phase approximation, as we are looking at the infinite time limit, the biggest eigenvalue dominates. Thus, the highest linear spreading speed $v_l = v(\lambda_l)$ is the one selected [25].

Let us determine the linear spreading velocity of fronts in our general equation. Assume, for simplicity, that we are working in two spatial dimensions. The linearized dynamics around the unstable state $A = 0$ read

$$\frac{\partial}{\partial t} \hat{A} = (-\eta - D\mathbf{k}^2) \hat{A}.$$

Then, $\lambda(\mathbf{k}) = (-\eta - D\mathbf{k}^2)$, and the formulas for the velocity give

$$\mathbf{v} = -2Di \begin{pmatrix} k_x \\ k_y \end{pmatrix}, \quad -\eta - D\mathbf{k}^2 - \text{Im}k_x v_x - \text{Im}k_y v_y = 0.$$

Clearly, $\mathbf{k} \in \mathbb{C}$ for the velocity to be real. Moreover, its real part is zero. Then, $\mathbf{k} = (ik_x, ik_y)^T$. Write $k_x = k \cos \theta$ and $k_y = k \sin \theta$. Then, we have the equation

$$-\eta + Dk^2 - (k^2)2D = 0.$$

Giving $k = \sqrt{-\eta/D}$. Finally, the velocity of fronts propagating in the direction $\hat{\mathbf{r}} = (\cos \theta, \sin \theta)^T$ corresponds to

$$\mathbf{v} = 2\sqrt{-\eta D} \hat{\mathbf{r}}.$$

The speed is $v = 2\sqrt{-\eta D} = 2\sqrt{f'(A=0)D}$, which is the lower bound to the propagation speed of fronts in the problem of Aronson and Weinberger (note that they use dimensionless space units such that $D = 1$).

As a final remark, we note that the procedure is developed for PDEs, but is equally valid for coupled finite dimensional systems. One must take care that the wavenumber in Fourier space does not take values higher than the Nyquist frequency corresponding to $k_{Nyquist} = \pi/a$, with a the grid separation between the individual elements of the coupled system [25]. This technique is employed to compute the velocity of fronts into the unstable state affected by nonreciprocal coupling in the chain they exist during chapters 1 and 2.

Fronts into the stable state

These fronts result when two regions with different homogeneous stable states are connected through space in the dynamical system. The reaction and the transport will balance such that the front will move, propagating, typically, the most energetically favorable state. For this, we analyze our prototypical imperfect pitchfork normal form model before the saddle-node bifurcation that annihilates two equilibria, that is, we work for $\eta < \kappa^2/4$ in Eq 0.23. In this way, we have two homogeneous solutions, each one with its corresponding energy level given by the Lyapunov functional $G[A]$, giving the energies $G_1 = G[A_1]$ and $G_2 = G[A_2]$ (with A_1 and A_2 the respective homogeneous stable states). The equation used is intimately related to the ϕ^4 model in field theories [32]; this is due to the Lyapunov functional being analogous to the potential energy of a Lagrangian when promoting the first time derivative to a second one in the equations of motion (instead of overdamped dynamics, one considers conservative

dynamics). Thus, determining the ground and first excited states is a well-known problem and corresponds to the case of stationary fronts.

The problem of translating fronts between two stable states was first rigorously studied by Fife and McLeod [33] for the problem $\partial A/\partial t = f(A) + \partial^2 A/\partial x^2$ (with $f(0) = 0$ and $f(1) = 0$ with $f'(0) < 0$ and $f'(1) < 0$). Note that both states are stable, different from the problem Aronson and Weinberger studied. There, it was established that the direction of movement could be analyzed in terms of $f(A)$. First, consider a uniformly translating solution with velocity v writing $A = u(x - vt) \equiv u(z)$. The system transforms to $-vu'(z) = f(u) + u''(z)$, and one can multiply both sides by $u'(z)$ and integrate over all the domain. Considering that the front solution has a vanishing derivative at its ends (by definition, in the ends resides the homogeneous state), the velocity follows the expression

$$-v = \frac{\int f(u)u'(z)dz}{\int (u'(z))^2 dz}.$$

This has a slight difference with the procedure of Fife and McLeod, who directly integrate $-vu'(z) = f(u) + u''(z)$; their procedure is valid for monotonous fronts. Instead, we followed Pismen and Pomeau [23]. One notes that the sign of v is determined solely by the integral $\int f(u(z))u'(z)dz$. Moreover, if $f(u) = -dV/du$ with V a potential (or Lyapunov function for the local part), the expression is reduced further to

$$v \propto \int \frac{dV}{dz} dz = V(z \rightarrow \infty) - V(z \rightarrow -\infty).$$

Note that V acts as a free energy density. One says, then, that the front motion has a velocity proportional to the free energy density difference of the states it connects (say, the stable states 1 and 2 obtained by our imperfect pitchfork normal form). If the free energy density of both states is the same, we get $v = 0$. This situation is called the *Maxwell construction*, and we will refer as the *Maxwell point* to the point in parameter space for which it occurs.

An important problem is noted: the velocity is not explicitly obtained with this method. It corresponds to an *implicit* solution, as it depends at the same time on the front profile $u(z)$ via the integral $\int (u'(z))^2 dz$. One seeks a method to decouple the dynamics of the front evolution and the velocity. A perturbative scheme has been proposed to predict the relaxation dynamics of fronts connecting symmetric stable states in any dimension in [34, 35] and references therein. An extension of the method to predict the motion of the fronts due to an energy difference of the states is found in [23]; the technique is based on a perturbative approach close to the Maxwell point of some control parameter. In our model, the two equilibria become symmetric for $\kappa = 0$; in this case, the front is static, and we solve $0 = -\eta A - A^3 + D\nabla^2 A$. Again, we restrict the analysis to planar fronts, and it is easy to find that a solution corresponds to

$$A_{\text{kink}} = \sqrt{-\eta} \tanh\left(\hat{\mathbf{c}} \cdot (\mathbf{r} - \mathbf{c}_0) \sqrt{-\eta/D/2}\right).$$

The *kink* solution corresponds to a planar front in the direction $\hat{\mathbf{c}}$ and is a solution of the system for $\kappa = 0$. Note that the solution reflects the translation invariance of the system through the free parameter \mathbf{c}_0 , indicating the position of the front that can take any real

value and depends on the initial conditions. This solution offers a natural generalization for the case in which $\partial A/\partial t \neq 0$ (for parameters $\kappa \neq 0$), one promotes the position of the front \mathbf{c}_0 to be a function of time $\mathbf{c}_0 \rightarrow \mathbf{c}_0(t)$. Additionally, a correction to A_{kink} needs to be included; we intend to solve the problem

$$\begin{aligned} A &= A_{\text{kink}}(\mathbf{r} - \mathbf{c}_0(t)) + A^{[1]} + \dots \\ \dot{\mathbf{c}}_0 \cdot \hat{\mathbf{c}} &= v^{[1]} + v^{[2]} + \dots \\ \frac{\partial}{\partial t} A &= -\eta A + \kappa A^2 - A^3 + D\nabla^2 A. \end{aligned}$$

We assume we can write a series expansion for the profile and velocity, with the smallness defined by the closeness to the Maxwell point. Then, $|\kappa| \ll 1$ will be used as the parameter to define the hierarchy of equations. Replacing our ansatz in the equations of motion yields

$$\begin{aligned} -(v^{[1]} + v^{[2]} + \dots) \left(\frac{\partial A_{\text{kink}} + A^{[1]} + \dots}{\partial z} \right) &= -\eta(A_{\text{kink}} + A^{[1]} + \dots) + \kappa(A_{\text{kink}} + A^{[1]} + \dots)^2 - \\ &\quad (A_{\text{kink}} + A^{[1]} + \dots)^3 + D\nabla^2(A_{\text{kink}} + A^{[1]} + \dots). \end{aligned}$$

The terms $\kappa^{[0]}$ satisfy the equation automatically. Terms $\kappa^{[1]}$ yield

$$-v^{[1]} \frac{\partial A_{\text{kink}}}{\partial z} = (-\eta - 3A_{\text{kink}}^2 + D\nabla^2)A^{[1]} + \kappa A_{\text{kink}}^2.$$

Where we have defined $z = \hat{\mathbf{c}} \cdot (\mathbf{r} - \mathbf{c}_0)$. The last equation is linear; thus, to have a solution, we require that

$$-v^{[1]} \frac{\partial A_{\text{kink}}}{\partial z} - \kappa A_{\text{kink}}^2 \in \text{Image of } \mathcal{L} = (-\eta - 3A_{\text{kink}}^2 + D\nabla^2).$$

The image of the previous linear operator is not easy to obtain generally. Let us consider the inner product $\langle f(x)|g(x) \rangle = \int f^* g dx$; then, our previous statement is equivalent to

$$-v^{[1]} \frac{\partial A_{\text{kink}}}{\partial z} - \kappa A_{\text{kink}}^2 \perp \text{Ker}(\mathcal{L}^\dagger),$$

known as the Fredholm alternative. The kernel is easily found to be $\partial A_{\text{kink}}/\partial z$, then one finds

$$-v^{[1]} \int \left(\frac{\partial A_{\text{kink}}}{\partial z} \right)^2 dz = \kappa \int \frac{\partial A_{\text{kink}}}{\partial z} A_{\text{kink}}^2 dz.$$

Finally, one can compute the corrections to the speed up to the desired order. We note here that in our example

$$v^{[1]} = -\kappa \frac{\int (\partial A_{\text{kink}}/\partial z) A_{\text{kink}}^2 dz}{\int (\partial A_{\text{kink}}/\partial z)^2 dz} = -\kappa \sqrt{-\eta}^3 / (\sqrt{-\eta}^2 \sqrt{-\eta/D}) = -\kappa \sqrt{D}.$$

Notably, the free energy or the Lyapunov functional initially appeared fundamental to understanding the front motion. However, the procedure only requires an analytical solution for some particular parameters. Indeed, this method has been applied both to variational and nonvariational systems with perturbation techniques around an analytically obtained state

[36–38]. Fronts into the stable state and their properties are explored when the system is subjected to nonreciprocal coupling at the end of chapters 1 and 2, and their interaction with a heterogeneous environment (space-varying parameters) is analyzed in chapter five.

Discreteness effects and the Peierls Navarro potential

Until now, we have discussed the dynamics of fronts using PDEs, that is, infinite dimensional systems. One may ask if there are significant differences if one tries to make a similar analysis in the discrete counterpart of the equations. Let us continue to discuss our imperfect Pitchfork normal form, and write the corresponding discrete equation as

$$\dot{A}_i = -\eta A_i + \kappa A_i^2 - A_i^3 + \frac{D}{a^2}(A_{i+1} - 2A_i + A_{i-1}).$$

If $A_{i+1} = A(x+a) = A(x) + aA'(x) + a^2A''(x)/2 + \dots$, then the equation may be approximated by

$$\dot{A} = -\eta A + \kappa A^2 - A^3 + \frac{D}{a^2}\left(a^2 \frac{\partial^2 A}{\partial x^2} + \frac{2a^4}{4!} \frac{\partial^4 A}{\partial x^4} + \dots\right).$$

a is the grid separation, and we have assumed a chain for simplicity. Written in this form, we could use the parameter a as a control parameter; for $a \sim 1$, we see that all terms in the series are relevant and a continuum limit description is not appropriate. If $a \ll 1$, then the discrete equation has a simple PDE as a limit, corresponding to the diffusion equation we have used. Note that this limit is equivalent to having high coupling constants in the discrete system ($D/a^2 \rightarrow \infty$). Normalizing the distance to $a = 1$, we know that the PDE will approximate the discrete equation for $D \rightarrow \infty$.

Several systems are fundamentally discrete. However, a continuum limit approximation is often performed to obtain better analytical results. In doing so, some aspects of the dynamics can be lost. Particularly speaking of fronts, the major effect of the discrete grid is to induce *hopping dynamics* in the front position. That is, fronts move in an oscillatory fashion. Interestingly, the force inducing the oscillation is capable of stopping the front motion for a range of parameters around the Maxwell point, the *pinning region* [36], a phenomenon occurring in fronts into the stable state. The force inducing the oscillations supposes a potential wall the front position needs to overcome to propagate; this 'energy' is known as the *Peierls Navarro potential* studied in the dislocations of crystals (see [12] and references therein). Fronts into the unstable state show hopping dynamics also [39, 40], but pinning has not been reported. Explicitly, the velocity of fronts can be approximated by

$$v \approx v_0 + \Gamma \cos 2\pi x + \dots$$

v_0 is the average front speed, and Γ measures the intensity of the periodic force in the first harmonic approximation. This formula has been predicted approximating the grid with space-varying parameters and was fitted to numerical simulations of front motion into the unstable state with good results by Alfaro-Bittner et al. [39, 40]. In addition to the velocity, the front profile is also modified by the effect of the grid compared to fronts in the continuum limit. The problem of computing the analytical front shape has been addressed by Flach and Kladko [41] for stationary fronts, and the scaling behavior of the Peierls Navarro potential with parameters revisited in this perspective by Kladko et al. [12, 42]. At the end of chapters 1 and 2, we analyze the velocity of fronts into the stable state in a system under nonreciprocal

coupling; expressions for v_0 , Γ , and the rest of the series in terms of the original parameters are analyzed under a novel perspective.

Patterns

As we introduced earlier, two species interacting and being subjected to diffusive transport have a space-periodic solution with an intrinsic wavelength; the amplitude of this oscillation grows in time, according to the linear theory. This heterogeneous, space-periodic solution to the linearized equations can have an equilibrium amplitude thanks to nonlinear terms saturating the growth [2]. We showed how a general system could be reduced to the Lifshitz normal form for parameters close to an infinite wavelength Turing instability and an instability of the homogeneous state simultaneously. Then, without loss of generality, we can analyze patterns employing the equation

$$\frac{\partial A}{\partial t} = -\eta A + \kappa A^2 - A^3 - \nu \nabla^2 A - \nabla^4 A + bA \nabla^2 A + c(\nabla A)^2. \quad (0.24)$$

For $\kappa = b = c = 0$, the equation is known as the *Swift-Hohenberg* equation. Turing also discovered the equation independently, so it is fair to call it *Turing-Swift-Hohenberg* equation in general. Partially derived in describing the convection rolls in the Raileigh-Benard experiment by Swift and Hohenberg [43], it has become one of the most important equations in the study of nonlinear physics.

The stripe pattern

The Raileigh-Benard experiment consists of a heated plate covered with fluid and a second plate; for enough temperature difference between the plate and the upper boundary condition, the fluid starts to move, and one observes rolls in the surface; this is a consequence of the velocity field acquired past the instability. The word roll, or stripe, has an intuitive meaning only when speaking of scalar fields in two dimensions (such as the height of the fluid in the Raileigh-Benard experiment). We will generally call a pattern a *stripe pattern* if the periodic modulation occurs in a single, well-defined direction. This can be easily checked by analyzing the spatial Fourier transform of the system; if a single pair of wavevectors \mathbf{k}_c and $-\mathbf{k}_c$ dominate the spectrum, then one has a stripe structure in the pattern. This is not always the case, and will depend on the governing equation if the critical wavevectors (the wavevectors for which the eigenvalue crosses the imaginary axis) have some form of degeneration. For example, an *isotropic* system should be able to support any wavevector in the circle defined by $\lambda(\mathbf{k}_c) = 0$ (in other words, only the magnitude of \mathbf{k}_c is fixed, and its orientation is free); thus, a general initial condition would evolve to a solution consisting of a combination of a great number of wavevectors in the circle $\lambda(\mathbf{k}_c) = 0$. This situation leads to the observation of hexagons [2] and labyrinths [44], depending on the control parameters. In such an isotropic system, to observe a stripe pattern, one must start with an initial condition close to a stripe pattern. This is different in an *anisotropic* system, where it is possible that the condition $\lambda(\mathbf{k}_c) = 0$ is satisfied for just a few points \mathbf{k}_c ; then, pattern in such predisposed directions will form for any initial condition (at least containing the marginally unstable Fourier mode \mathbf{k}_c).

Isotropic environment

Equation 0.24 describes a variable in which the spatial coupling is *isotropic*. Any spatial rotation of the system leaves the equation invariant; equivalently, any system solution can be arbitrarily rotated and will still be a solution. Due to this property, when analyzing the linearized dynamics around $A = 0$, one gets

$$\lambda(\mathbf{k}) = -\eta + \nu\mathbf{k}^2 - \mathbf{k}^4.$$

The condition $\lambda(\mathbf{k}_c) = 0$ holds for a whole d -dimensional sphere shell in the space of wavevectors if $\eta = \eta_c = \nu/4$. All these eigenvalues with vanishing real parts should be considered when trying to reduce the dynamics to their central manifold. Writing

$$A = \int_{|\mathbf{k}|=k_c} B_{\mathbf{k}} e^{i\mathbf{k}\cdot\mathbf{r}} d\mathbf{k},$$

one wishes to compute whenever $|\eta - \eta_c| \neq 0$, thus, a thin d -dimensional spherical shell of wavevectors within a distance $|\mathbf{k} - \mathbf{k}_c| < \delta(\eta - \eta_c)$ interacts with the critical mode. The procedure becomes untraceable due to several resonances occurring (whenever the sum of different eigenvalues pondered with non-zero integer numbers equals zero [17]); these resonances are responsible for stabilizing hexagonal patterns (in two spatial dimensions), and quasi-crystals [2, 4]. Instead of the general case, it is easier to consider either $\eta = \eta_c$ only (thus, only obtaining the nonlinear part of the dynamics [17, 18]), or to reduce the relevant wavevectors considered in the expansion of the variable A . These procedures are depicted in [23] and references therein. Considering only a stripe pattern in the expansion for A in two dimensions gives the Newell-Whitehead-Segel equation, which can be used to further analyze the nonlinear behavior of the Raileigh-Benard convection rolls (most fluids are isotropic), for example, or other isotropic systems. In this dissertation, we will rather deal with anisotropic systems detailed below.

Anisotropic environment

The inclusion of nonreciprocal coupling will generally induce an imaginary part in the eigenvalues of the linearized dynamics; any spatial instability will have an oscillatory term, and the system evolves into nonlinear waves. If the nonreciprocal coupling is present, it could render an isotropic system to be anisotropic (the equations are not invariant to a simultaneous rotation of the coordinates and the nonreciprocity direction) [10, 45, 46]. In an anisotropic system, patterns and nonlinear structures will have preferred directions to form. For example, a linearized system with eigenvalues (in two dimensions)

$$\lambda(\mathbf{k}) = -\eta + \nu(k_x^2 - k_y^2) - \mathbf{k}^4$$

has only critical wavevectors $\mathbf{k}_c = \pm(\sqrt{\nu/2} \ 0)^T$ for $\eta = \eta_c = \nu/4$. One can readily see that such a system will try to form a stripe pattern in the x direction with wavenumber $\sqrt{\nu/2}$, reducing the dynamic to the center manifold of $\lambda(\mathbf{k}_c) = 0$ and computing the normal form will dictate if the pattern is stable or unstable, and how robust is against perturbations. To illustrate this procedure, consider a slight modification of our prototypical isotropic pattern

forming system 0.24 reading

$$\frac{\partial A}{\partial t} = -\eta A - A^3 - \nu \left(\frac{\partial^2 A}{\partial x^2} - \frac{\partial^2 A}{\partial y^2} \right) - \nabla^4 A.$$

It is important to note that the previous equation is merely of theoretical interest and used to illustrate the explicit computation of the normal form. A similar procedure in an applied problem of vegetation population dynamics in the north of Chile is developed in Chapter 4 of this dissertation.

Let $\eta = \eta_c + \eta_1$. One proposes

$$A = B e^{ik_c x} + \bar{B} e^{-ik_c x} + A^{[1,1,0]} + A^{[2,0,0]} + \dots,$$

and

$$\dot{B} = \dot{B}^{[1,1,0]} + \dot{B}^{[2,0,0]} + \dot{B}^{[1,0,2]} + \dots$$

At linear order one recovers

$$0 = \left(-\eta - \nu \frac{\partial^2}{\partial x^2} + \nu \frac{\partial^2}{\partial y^2} - \nabla^4 \right) B e^{ik_c x} + c.c.$$

We analyze the linear operator. Introducing the canonical inner product between functions

$$\langle f(x) | g(x) \rangle = \int \bar{f} g dx,$$

one easily sees that the linear operator is self-adjoint. Then, the kernel of the linear operator correspond to the functions $e^{\pm ik_c x}$. One can solve the hierarchy of equations giving

$$\begin{aligned} \dot{B}^{[1,1,0]} &= -\eta_1 B, \\ \dot{B}^{[3,0,0]} &= -3B|B|^2, \\ \dot{B}^{[1,0,2]} &= \nu \left(2 \frac{\partial^2 B}{\partial x^2} + \frac{\partial^2 B}{\partial y^2} \right). \end{aligned}$$

After rescaling the spatial coordinates, the resulting equation reads

$$\frac{\partial B}{\partial t} = -\eta_1 B - 3B|B|^2 + \nu \nabla^2 B + h.o.t.$$

The equation has a scaling near the Turing bifurcation point similar to the previous normal forms derived; the scaling reveals the slow time and spatial scales in which B evolves. In a more general pattern forming system (when including non variational terms) one generally arrives at the complex Ginzburg-Landau equation for the slowly varying complex amplitude of the pattern (it is the same equation, but with the parameters promoted to be complex numbers)

$$\frac{\partial A}{\partial t} = (\mu + i\omega)A - (1 + i\beta)|A|^2 A + (1 + i\alpha)\nabla^2 A. \quad (0.25)$$

This equation corresponds to a Hopf normal form when including spatial coupling. It de-

scribes a great variety of natural phenomena such as superconductors (when coupled to a vector potential), the dynamics of nematic liquid crystals, coupled oscillators such as hearth tissue, some fluid flows, and pattern envelopes, to mention a few [47].

The instabilities of the Ginzburg-Landau equation

How robust is a perfect pattern? Perfect patterns correspond to homogeneous solutions of the Ginzburg-Landau equation; in other systems, the 'translation' of the solutions of 0.25 to observable quantities depends on the original system from which one derives it. We analyze the instability of the homogeneous solutions, similar to what we did in the original set of equations; this procedure will reveal the *secondary instabilities* in the reduced equations. These secondary instabilities reveal the full behavior of the system in a small neighborhood of the critical point defined by $\lambda(\mathbf{c}_b) = 0$ (of the original system).

The Ginzburg-Landau equation in one and two dimensions displays a high variety of phenomena when $\beta \neq \alpha \neq 0$ [47]. This is due to the terms proportional to β and α being responsible to couple the phase and amplitude of the complex variable $A = |A|e^{i\phi}$. The simplest homogeneous solutions satisfy $0 = \mu - |A_0|^2$ and $\dot{\phi}_0 = \omega - \beta|A_0|^2$, it displays steady oscillations which frequency depends on the amplitude. Moreover, slow spatial modulations of these oscillations are also solutions; let $|A| = |A_0|e^{i\mathbf{k}\cdot\mathbf{r}} + c.c.$ and one finds $|A_0|^2 = \mu - \mathbf{k}^2$, $\dot{\phi}_0 = \omega - \beta|A_0|^2 - \alpha\mathbf{k}^2$. Analyzing perturbations around this state with $|A| = |A_0|e^{i\mathbf{k}\cdot\mathbf{r}} + |A_1|e^{i\mathbf{p}\cdot\mathbf{r}} + c.c.$ and $\phi = \dot{\phi}_0 t + \phi_1 e^{i\mathbf{p}\cdot\mathbf{r}} + c.c.$ reveals that a band of wavevectors around the homogeneous state $\mathbf{k}^2 < \mathbf{k}_E^2 = (1 + \beta\alpha)/(3 + 2\beta^2 + \beta\alpha)$ is stable provided that the Benjamin-Feir criterion $1 + \beta\alpha > 0$ is satisfied [47]. Solutions with wavevectors such that $\mathbf{k}^2 \geq \mathbf{k}_E^2$ are unstable. If $1 + \beta\alpha < 0$, all the solutions described until then are unstable. This curve divides the parameter space with a simple criterion, and much more others can be found in the literature; for a thorough review see [47]. Mostly all of the instability curves delimiting interesting phenomena such as defect turbulence, spatiotemporal intermittency, and others have been determined numerically due to their complexity [47]. We put emphasis on the defect turbulence state, which is characterized by constantly and homogeneously generating defects that are shortly annihilated [48]. Defects in the Ginzburg-Landau equation correspond to localized structures described in the next subsection.

Dislocation defect and its vortex structure in the phase

When describing a pattern via a complex amplitude, for example, $u = Ae^{i(kx+\phi)} + c.c.$, we need to consider that the amplitude A and the phase ϕ will not be homogeneous all the time. The pattern will not be a perfect periodic function in reality, and in general the functions A and ϕ will vary in space and time. One may ask, what happens when two patterns with a different value of ϕ encounter? Two patterns with different phase have stripes that does not match when concatenated side by side, inserting this as an initial condition to the governing equations will force the system to find a solution. In general, defects will form, and will *patch* the regions where the pattern can not be homogeneous. Stripes in a single direction display only one type of defect, *dislocations*. A dislocation occurs when, if following a stripe, one finds that the stripe divides in two, or merges with another stripe; they are very common to observe in the sand dunes. This situation described qualitatively has a very precise meaning for the fields A and ϕ . Circling a dislocation, the phase adds up $\pm 2\pi$ (due to one stripe, equivalently one wavelength, being inserted past the dislocation event); the phase is undefined at the core of the dislocation, and then, the amplitude vanishes. General

defects in the Ginzburg-Landau equation have the form (in polar coordinates) [47]

$$A(r, \theta, t) = R(r)e^{i(m\theta + \omega t + \psi(r))}.$$

R is the radial form of the defect, ψ their phase, and m their *winding number*. Extensive numerical observations reveal that only defects with winding number, or charge, equal to $|m| = 1$ are stable; defects with greater charge disarm into defects of $|m| = 1$ charge [47]. One can readily see that the phase $\phi = m\theta + \omega t + \psi$ changes by 2π whenever we enclose the defect moving from $\theta = 0$ to $\theta = 2\pi$. This property of the phase gives the name *vortex* to these solutions when $\omega = 0$, and *spirals* when $\omega \neq 0$.

Interaction between vortices

Whenever two defects coexist in two different regions of space, one expects them to interact. That is, the presence of one defect will affect the dynamic of the other. The interaction of two defects have been addressed by various authors, with a good summary of the attempts given in [47]. Some limits have been taken to simplify the calculations. Vortex solutions exist when $\omega = 0$, occurring in the limit $\beta = \alpha = 0$; their interaction is given by $v \log(v/v_0) \propto \pm 1/r$, where v is their radial velocity and r their separation distance. The case of spirals gives an weak exponential interaction whenever they have a well-developed regions of radial waves around them. Matsuoka and Nozaki [49] provide an interaction law for 'perturbed' vortices whenever the complex terms remain small $\beta \sim \alpha \ll 1$, which gives expressions similar to the interaction of vortices $v \log(v/v_0) \propto \pm 1/r$ with an additional tangential velocity component. Vortices of opposing charge attract (they interact with the minus sign of the previous equation), and annihilate if they come sufficiently close. For this reason, the behavior of an initial number of vortices as a function of time has been studied extensively, employing the interaction law and the simple argument that $N \propto \text{Volume} / \langle r_{12} \rangle^d$ (the number of vortices should scale with the total d-dimensional volume divided by the average volume a pair of vortices occupies), several authors have found behaviors $N \sim \log(t)/t$ in the two dimensional case [50–52], which is of crucial relevance to the case of stripe patterns and will be employed in chapter 4.

Part I: Front-type nonlinear waves under nonreciprocal coupling

Nonlinear wave phenomena are theoretically appealing. The break of the superposition principle that has allowed us to solve Mechanics and Electrodynamics superposing forces and fields to create new ones opens several questions about the dynamic of waves. Nonlinearity does not allow for superposition of solutions and creates unique ones; many of them have been studied employing a prototypical model: a chain of linearly coupled pendulums.

The chain of linearly coupled pendulums is described by an equation named the *Frenkel Kontorova* model. It does not only appear in coupled oscillators but also in the dynamics of crystal lattice atoms, coupled short Josephson junctions, and others [12]. This model also carries theoretical interest, particularly in the study of nonlinear waves. In the continuum limit, the *Frenkel Kontorova* model is called the *sine Gordon* equation, which allows for an impressive nonlinear superposition principle and is one of the few nonlinear extended equations for which all its solutions are known [53]; this is due to it being an integrable dynamical system. Breathers, kinks, and interactions between them represent nontrivial states in the sine Gordon model, and such solutions persist far from the continuum limit when the Frenkel Kontorova model has greater validity.

In the following two chapters, we will focus on the nonlinear wave of the dissipative kink type. Note that depending on the context, the same kind of nonlinear wave can have different names, such as *phase wall*, *front*, *domain wall*, *kink*, or *interface*, to mention a few. Its most important characteristic is that it corresponds to a solution connecting two different equilibrium states. In general, the region of transition between states occupies little space and can be described by position and velocity vectors; the same applies to systems in higher dimensions, and the dimension of the front increases accordingly. When subjected to nonreciprocal coupling between the elements of the chain, it is unknown what the result will be for these nonlinear waves. The continuum theory gives us some insight, and the phenomenon of nonlinear absolute-convective instability is expected; however, the effects of discreteness are to be unveiled when mixed with nonreciprocal coupling.

Chapter 1

Nonreciprocal Coupling Induced Self-Assembled Localized Structures (Physical Review Letters 126 (19), 194102)

Nonreciprocal coupling between elements of a chain is not trivial to obtain. Depending on the physical quantity that is coupled, one needs to engineer the system such that nonreciprocity arises in the equations describing the motion of such elements. Nonreciprocal coupling refers to the property that an element's effects on one neighbor are not equivalent to the effects that neighbor has on the element. Thus, if we are analyzing a system of oscillators, nonreciprocity appears if the mass matrix or the potential matrix of the dynamical system are non-symmetric [54]; when coupling electrical circuits, one would ask for a non-symmetric inductance matrix for nonreciprocal coupling to exist; in the realm of quantum mechanics, nonreciprocity would appear for non-symmetric Hamiltonians [8]. In all of these examples, for nonreciprocity to appear, it looks as if we are required to break the laws of physics. However, physics has effectively reproduced systems described by equations with nonreciprocal coupling employing techniques such as robotic control [8], high nonlinearity [7], chirality [21, 55], operational amplifiers in electrical circuits [9, 56], or spatiotemporal modulation [57], to mention a few. These generally require constant injection and energy dissipation for nonreciprocity to appear in a non quasi-static regime.

In the following article, we analyze further the dynamics of elastic nonreciprocal coupling, which has been achieved with robotic control [8] in the linear regime. We add a periodic on-site potential to each element, apart from the existing nonreciprocal elastic coupling reported there. The resulting system corresponds to a variation of the Frenkel Kontorova model, including now a nonreciprocal linear coupling between nearest neighbors. This allows us to explore the effect of nonreciprocal coupling on nonlinear waves using a prototypical model of nonlinear physics. We analyze the overdamped regime to avoid any divergence due to the permanent injection of energy nonreciprocal coupling drives into the system. In this regime, the front type of wave dominates the dynamics. We fully characterize the dynamics of the chain, describing the different instabilities fronts undergo due to nonreciprocal coupling. Strikingly, pattern formation is observed for enough nonreciprocity; the pattern is not of the Turing type and is self-assembled from alternating fronts into the stable state.

Nonreciprocal Coupling Induced Self-Assembled Localized Structures

D. Pinto-Ramos¹, K. Alfaro-Bittner^{2,3}, M. G. Clerc¹ and R. G. Rojas⁴

¹*Departamento de Física and Millennium Institute for Research in Optics, FCFM, Universidad de Chile, Casilla 487-3, Santiago, Chile*

²*Departamento de Física, Universidad Técnica Federico Santa María, Av. España 1680, Casilla 110V, Valparaíso, Chile*

³*Unmanned Systems Research Institute, Northwestern Polytechnical University, Xi'an 710072, China*

⁴*Instituto de Física, Pontificia Universidad Católica de Valparaíso, Casilla 4059, Valparaíso, Chile*



(Received 23 October 2020; accepted 22 March 2021; published 12 May 2021)

Chains of coupled oscillators exhibit energy propagation by means of waves, pulses, and fronts. Nonreciprocal coupling radically modifies the wave dynamics of chains. Based on a prototype model of nonlinear chains with nonreciprocal coupling to nearest neighbors, we study nonlinear wave dynamics. Nonreciprocal coupling induces a convective instability between unstable and stable equilibrium. Increasing the coupling level, the chain presents a propagative pattern, a traveling wave. This emergent phenomenon corresponds to the self-assembly of localized structures. The pattern wavelength is characterized as a function of the coupling. Analytically, the phase diagram is determined and agrees with numerical simulations.

DOI: [10.1103/PhysRevLett.126.194102](https://doi.org/10.1103/PhysRevLett.126.194102)

The dynamics of coupled oscillators have attracted the attention of physics since its dawn. Phenomena like synchronization [1], energy transfers from one oscillator to another [2], or wave propagation [3] are paradigmatic dynamical behaviors of coupled oscillators. In all the above examples, the oscillators are usually coupled with reciprocal elastic media. Namely, the elastic media are characterized by applying a force of equal magnitude and opposite direction to each of the coupled oscillators. Such dynamical behavior is known as Maxwell-Betti reciprocity [4–6]. Nonreciprocal behavior has been studied in diverse physical fields considering asymmetric, nonlinear, and/or nonreversible features in time. In optics, nonreciprocal responses have been observed in birefringent prisms [7], optomechanical resonators [8], and asymmetric cavities [9]. In acoustics, an emitter and a receiver can exhibit nonreciprocal behaviors in a resonant ring cavity biased by a circulating fluid [10]. A similar phenomenon is achieved for electrically driven nonreciprocity on a silicon chip [11]. Nonreciprocal behaviors for the propagation of electromagnetic waves have been accomplished through the application of magnetic fields [12,13], angular momentum [14], nonlinear coupling [15], and moving photonic crystals [16]. In active matter, nonreciprocal couplings are a rule rather than an exception [17,18]. Recently, through the use of mechanical metamaterials [19,20], nonreciprocal coupling elements have been built up. Namely, couplers that induce a force of different magnitude to the coupled elements. Chains with nonreciprocal couplings exhibit spatially asymmetric standing [21] and nonlinear waves [20]; likewise, localized disturbances tend to propagate more in one direction than another [6–19,21].

In this Letter, we investigate the nonreciprocal coupling effect on nonlinear waves. Based on a prototype model of a nonlinear chain, the dissipative Frenkel-Kontorova model with nonreciprocal coupling to nearest neighbors, a convective instability between unstable and stable steady state is observed. By increasing the level of nonreciprocity, the fronts between these states change from monotonous to nonmonotonous ones. Unexpectedly, beyond a certain nonreciprocity level, fronts become unstable and give rise to propagative patterns (traveling waves), which corresponds to the self-assembly of localized structures. The pattern wavelength is characterized as a function of the couplings. A similar phenomenon is observed in continuous models that include higher spatial derivatives (order four) [22], which accounts for the larger-range coupling and includes a characteristic length. This intrinsic length is the main ingredient of the Turing mechanism of patterns [23,24]. The extension of this phenomenon to discrete systems corresponds to a system coupled to first and second neighbors. It is expected to observe patterns as a result of the intrinsic length provided by more distant neighbors [23,24]. However, the presented pattern mechanism here with nonreciprocal coupling only includes interaction to nearest neighbors. Analytically, the phase diagram of the system is revealed, which shows an excellent agreement with numerical simulations.

Let us consider a dimensionless chain of $N + 1$ dissipative coupled pendulums (the dissipative Frenkel-Kontorova model with nonreciprocal coupling [25]):

$$\begin{aligned} \ddot{\theta}_i = & \omega^2 \sin \theta_i - \mu \dot{\theta}_i + (D - \alpha)(\theta_{i+1} - \theta_i) \\ & - (D + \alpha)(\theta_i - \theta_{i-1}), \end{aligned} \quad (1)$$

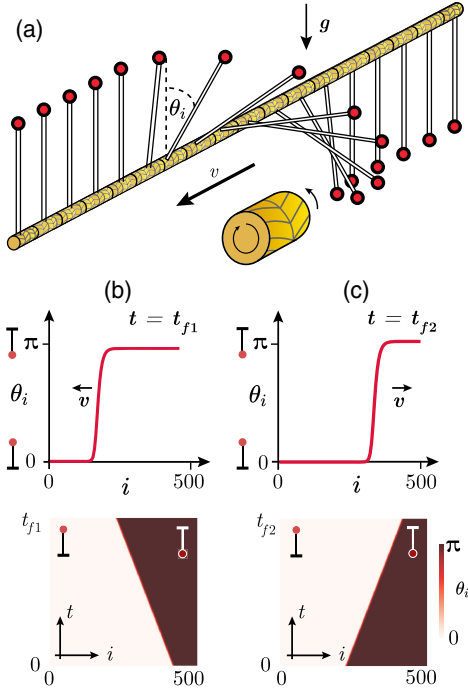


FIG. 1. Nonreciprocal coupled chain of pendulums and front propagation. (a) Schematic representation of a chain of pendulums coupled with a nonreciprocal material. $\theta_i(t)$ is the angle formed by the pendulum and the vertical axis in the i position at time t . Yellow cylinder accounts for a nonreciprocal metamaterial. Instantaneous profile and spatiotemporal evolution of π kink obtained for Eq. (2) with $\omega = 1$, $D = 4$, $\alpha = 1$ (b), and $\alpha = 2.5$ (c).

where $\theta_i(t)$ is the angle formed by the pendulum and the vertical axis in the i position at time t [cf. Fig. 1(a)]. ω and μ are the natural frequency and the damping coefficient of pendulums. D and α account for coupling elements that have different left-to-right and right-to-left linear responses. α accounts for the nonreciprocal coupling; when $\alpha = 0$, the chain has a reciprocal coupling. D stands for the linear deformation of an elastic material. α could account for the linear deformations of a rubber nonreciprocal torsion metamaterial [19] or a nonreciprocal robotic coupling [21]. Figure 1 shows a schematic representation of a chain of dissipative coupled pendulums. Note that $\theta_i = 0$ and $\theta_i = \pi$ describe the upside-down and upright pendulum, respectively. Equation (1) is of Lagrangian nature, which has the form

$$\mathcal{L} = \sum_i \left[\frac{\dot{\theta}_i^2}{2} - \omega^2 \cos \theta_i - \frac{D - \alpha}{2} (\theta_{i+1} - \theta_i)^2 \right] e^{\mu t} \Lambda^i,$$

where $\Lambda \equiv (D - \alpha)/(D + \alpha)$. Thereby, the dynamics of Eq. (1) is steered by a principle of least action. To figure out the nonreciprocal chain dynamics, we consider the overdamped limit of the dissipative Frenkel-Kontorova

model (see the Supplemental Material [26]). Then Eq. (1) can be approximated by

$$\dot{\theta}_i = \omega^2 \sin \theta_i + (D - \alpha)(\theta_{i+1} - \theta_i) - (D + \alpha)(\theta_i - \theta_{i-1}). \quad (2)$$

A similar model was proposed to study coupled Josephson junctions [29]. Two evident extended steady states correspond to the uniform upside-down and upright pendulums. To study the dynamics of nonlinear waves between these two states, we consider the boundary conditions being Dirichlet [$\theta_0(t) = 0$] and Neumann [$\theta_N(t) = \theta_{N-1}(t)$] on the left and right flank of the chain, respectively.

In the reciprocal limit $\alpha = 0$, considering all upside-down pendulums as an initial condition, slightly tilting a pendulum generates a nonlinear wave that propagates from the upright to the upside-down pendulums with a well-defined speed. This nonlinear wave is known as π kink [30]. The front speed is characterized by exhibiting a weakly oscillatory behavior [30,31]. π kinks are persistent in the presence of nonreciprocal coupling. Figure 1 shows the profile of a π kink wave and its respective spatiotemporal diagram. These diagrams were obtained by means of numerical simulations. All the numerical simulations presented were conducted by a fourth-order Runge-Kutta integration method. As a result of nonreciprocal coupling, the speed of the π kink decreases when α is increased. π kinks that invade the upside-down pendulums are observed in zone I of Fig. 2. The previous dynamical behaviors change when considering large enough α through an absolute convective instability [32]; the upside-down pendulums invade upright ones [see Fig. 1(c)]. These fronts are observed in zone II on the bifurcation diagram in Fig. 2.

To characterize the absolute convective instability, we use the same strategy presented in [30]. Let us introduce the ansatz $\theta_i(t) = A e^{k(i + \langle v \rangle t)}$ for the tail of the front to determine the average front speed $\langle v \rangle$, where k accounts for the front steepness. The average front speed $\langle v \rangle$ satisfies (see the Supplemental Material [26] for details)

$$\langle v(k) \rangle = \frac{\omega^2 - 2D}{k} + 2 \left[\frac{D \cosh(k) - \alpha \sinh(k)}{k} \right]. \quad (3)$$

Bounded disturbances induce fronts propagation into the unstable state with the minimum front speed v_{\min} as a function of the steepness, i.e., $v_{\min} = \langle v(k = k_c) \rangle$, $\partial_k \langle v(k = k_c) \rangle = 0$, and $\partial_{kk} \langle v(k = k_c) \rangle > 0$ [22]. The absolute convective instability corresponds when the minimum speed is zero [32]. Using this condition, we get

$$D = \frac{\alpha^2}{\omega^2} + \frac{\omega^2}{4}. \quad (4)$$

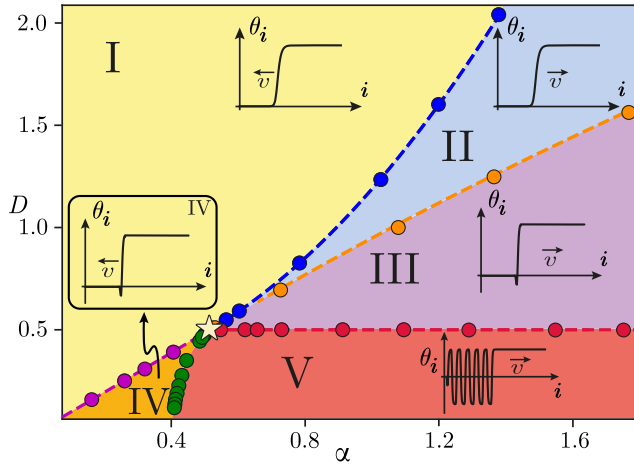


FIG. 2. Phase diagram of the overdamped Frenkel-Kontorova Eq. (2) with $\omega = 1$. In zone I, the upright pendulums invade the upside-down ones. This process is reversed in zone II. The blue curve, Eq. (4), is the analytical absolute convective instability between the upright and upside-down pendulums. The purple ($D = \alpha$) and orange curves account for the monotonous to nonmonotonous front transition, using Eq. (3). The star symbol (\star) accounts for the critical point ($\alpha = 1/2, D = 1/2$) where the critical curves converge. Red and green curves separate the localized structures' self-assembly region. The red curve was obtained using formula $D = 1/2$. The green curve is achieved through divergence of the self-assembly wavelength. All circles are obtained by means of numerical simulations.

Figure 2 shows the bifurcation diagram of the overdamped Frenkel-Kontorova model, Eq. (2). The dashed blue curve accounts for the previous expression. Notice that for large D coupling, the system is adequately described by the continuous limit, the dissipative sine-Gordon equation with advection, where the dynamic behaviors described above are expected. Surprisingly, as α increases further, the fronts exhibit a transition from monotonous to nonmonotonous fronts. Figure 3 shows the typical nonmonotonous front observed and its propagation. These fronts are observed in zones III and IV of the phase diagram shown in Fig. 2. In zone III (IV), the upside-down (upright) state propagates into the upright (upside-down) one. The transition of monotonous to nonmonotonous front is characterized by the fact that the speed curve $\langle v(k) \rangle$, Eq. (3), ceases to have a minimum, which becomes an inflection point. Indeed, the minimum is now in the complex plane of k , where the imaginary part corresponds to the spatial oscillations observed in the front profile (cf. Fig. 3). By imposing that $\langle v(k = k_c) \rangle$ stops having a minimum, we obtain

$$\frac{2D - \omega^2}{\operatorname{arctanh}\left(\frac{D}{\alpha}\right)} = 2\alpha \sqrt{1 - \left(\frac{D}{\alpha}\right)^2}. \quad (5)$$

For $D < \omega^2/2$, an explicit solution of the above transcendent equation is $D = \alpha$. Notice that this relationship corresponds

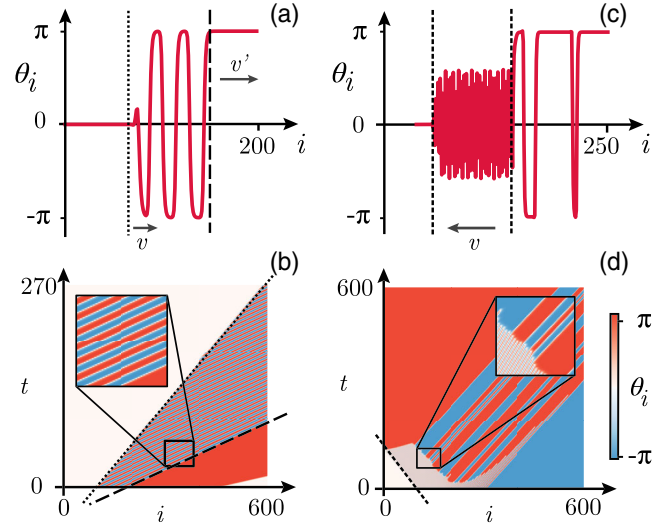


FIG. 3. Nonmonotonous fronts of the overdamped Frenkel-Kontorova Eq. (2) with $\omega = 1$. Profile (a) and spatiotemporal evolution (b) of a nonmonotonous front propagates from upside-down pendulums into upright ones for $D = 1$ and $\alpha = 1.25$. v and v' account for the speeds of different fronts. Profile (c) and spatiotemporal evolution (d) of a nonmonotonous front propagate from upright pendulums into upside-down pendulums for $D = 0.25$ and $\alpha = 0.325$.

to each oscillator being only coupled to its left neighbor. Furthermore, when $D < \alpha$, springs toward the right side are not of restoring nature, that is, their elastic constant is negative. The above is unacceptable for mechanical springs. However, this type of coupling can be achieved through the use of nonreciprocal robotic metamaterials [21]. For $D > \omega^2/2$, an explicit analytic expression is not accessible. Note that the curve obtained parametrically, Eq. (5), is slightly below the straight line $D = \alpha$. Figure 2 illustrates these curves by means of the purple and orange dashed lines, respectively. $D = \alpha = \omega^2/2$ is a critical point where the different transition curves converge, which is represented by a star in the phase diagram of Fig. 2. From nonmonotonous fronts where the upside-down pendulum state invades upright ones, unexpectedly, as D decreases, the emergence of a traveling wave is observed (see Fig. 4). Note that these patterns are characterized by connecting the vertical pendulum to itself. These propagative waves are observed in zone V on the phase diagram of Fig. 2. As α is increased or D is decreased, the wavelength of the propagative pattern λ decreases as illustrated in Fig. 4(c). To characterize the pattern emergence instability curve, we consider nonmonotonous fronts where upside-down pendulums invade upright ones. The average front speed $\langle v(k_c) \rangle$ is the global minimum as a function of steepness. Using the previous conditions in Eq. (3) after straightforward calculations (for details, see the Supplemental Material [26]), we obtain the relation $D = \omega^2/2$. The red dashed horizontal line in Fig. 2 outlines the wave instability curve. Increasing the number of

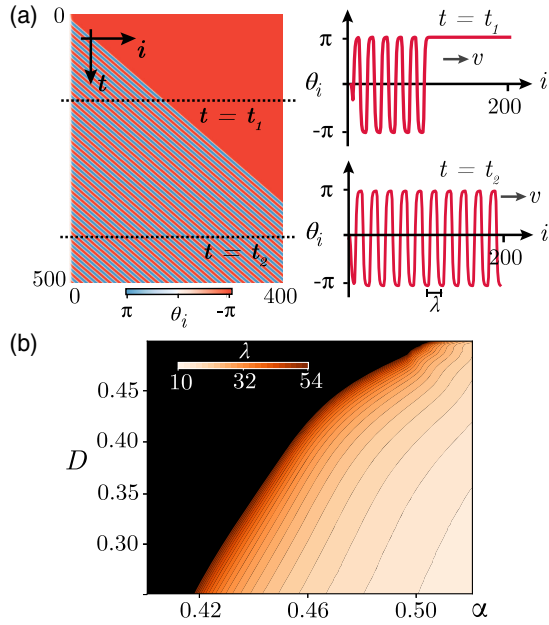


FIG. 4. Self-assembly of localized structures and the wavelength surface map for the overdamped Frenkel-Kontorova Eq. (2) with $D = 0.4$, $\alpha = 0.5$, and $\omega = 1$. (a) Spatiotemporal evolution and respective profiles in two instants of time, $t_1 = 120$ and $t_2 = 395$. v accounts for the traveling wave velocity. (b) Wavelength surface map for the D and α parameter space.

oscillators N close to the horizontal line, numerically, we observe that the wave exhibits a complex spatiotemporal dynamics. The origin and the characterization of the complex spatiotemporal behavior is in progress.

The transition between fronts and large wavelength waves (zones IV and V) cannot be obtained employing asymptotic analytical calculations due to its nonlinear nature. To determine this bifurcation, we numerically compute the curve of divergence of the pattern wavelength. Figure 2 illustrates this curve by means of green dots. Video in the Supplemental Material [26] illustrates the different observed nonlinear waves [33]. To shed light on the nature of the observed patterns, we perturb the periodic solution in a localized manner. The spatial oscillations with a length small enough compared to the pattern shrink and disappear, generating a hole in the pattern that propagates without deformation. In contrast, oscillations with a wavelength longer than the pattern, even several wavelengths, propagate as a localized state, a *pulse*. Figure 5 illustrates the scenario described above. A pattern made up of an extended periodic state is characterized by healing the disturbances and recovers the pattern characteristic wavelength [23,24]. However, patterns composed by the assembly of localized structures are characterized by exhibiting various wavelengths and configurations, depending on the initial condition [33]. When one regards a localized solution as an initial condition, it is propagated and advected. Because of the fixed boundary condition,

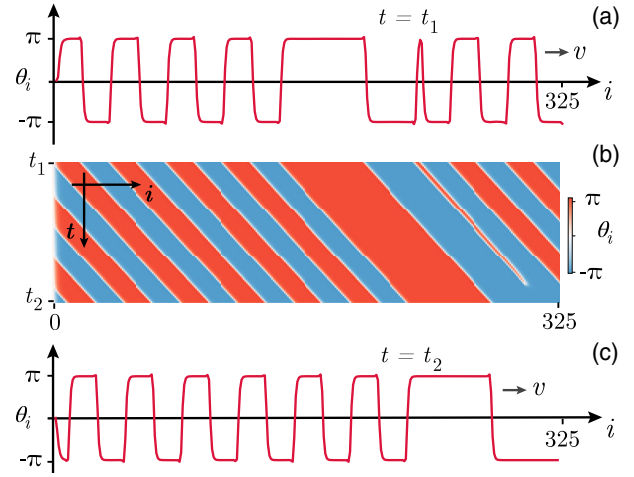


FIG. 5. Self-assembly of localized structures obtained for the overdamped Frenkel-Kontorova Eq. (2) with $D = 0.25$, $\omega = 1$, and $\alpha = 0.425$. (b) Spatiotemporal evolution of Eq. (2) with initial condition top panel (a) and final state bottom panel (c). v stands for the speed of the ensemble of localized structures.

localized structures of equal size begin to be emitted from the left flank, forming the propagative pattern. Therefore, the observed propagative pattern corresponds to a self-assembly of propagative localized structures (cf. Fig. 5).

The origin of the emergence of the observed pattern is that the front between the upright and upside-down pendulums has a well-defined periodic length when it tends to the fixed edge, left flank. This front profile engenders alternation of domains of the π and $-\pi$ states. Indeed, it locally generates a 2π kink gas. The interaction between these particle-type solutions is responsible for localized states [34]. Moreover, their interaction is characterized by exhibiting a family of localized solutions displaying a complex bifurcation diagram, a *collapsed snaking bifurcation*. Spontaneously from the left edge, there is an emission of localized solutions of one width. However, all localized solutions with greater width are observed (stable) when adequate initial conditions are considered.

When inertia is included, i.e., in the underdamped regime, the phenomena presented above persist. In fact, the phase diagram presented in Fig. 2 is slightly modified (for more details, see the Supplemental Material [26]).

In conclusion, based on a prototype model of a nonlinear oscillator chain with a nonreciprocal coupling to nearest neighbors, a convective instability between unstable and stable equilibrium is studied. By increasing the level of nonreciprocity coupling, fronts between these states exhibit a transition from monotonous to nonmonotonous fronts. Unexpectedly, as the level of nonreciprocity increases, fronts become unstable and give rise to propagative patterns with a wavelength controllable by coupling, which corresponds to self-assembly of localized structures. Analytically, the phase diagram of the system is revealed.

Because of the universal nature of the model under study, we expect that the presented findings are generic. Namely, we expect to observe the self-assembled localized structures in various nonlinear oscillators with nonreciprocal coupling. Josephson junctions, coupled with nonreciprocal robotic elements or computer-assisted coupling, are possible experiments that could display the proposed phenomena. In the case of considering large deformations of rubber nonreciprocal metamaterial, one would expect a nonreciprocal nonlinear coupling. The study of this type of coupling on the dynamics of waves is a work still in progress. In the continuous limit, the nonreciprocal coupling is only responsible for the absolute convective instability between fronts. Instead, the emergence of self-assembly of localized structures is a peculiar phenomenon of nonreciprocally coupled to nearest neighbor systems.

This work was funded by ANID-Millennium Science Initiative Program-ICN17_012. M. G. C. acknowledges financial support from the Fondecyt 1210353 project. D. P. R. acknowledges financial support from the ANID national Ph.D. scholarship 21201484.

-
- [1] A. Pikovsky, J. Kurths, M. Rosenblum, and J. Kurths, *Synchronization: A Universal Concept in Nonlinear Sciences*, Vol. 12 (Cambridge University Press, Cambridge, England, 2003).
- [2] J. P. Den Hartog, *Mechanical Vibrations* (Dover Publications, New York, 1985).
- [3] A. L. Fetter and J. D. Walecka, *Theoretical Mechanics of Particles and Continua* (Dover Publications, New York, 2003).
- [4] J. C. Maxwell, On the calculation of the equilibrium and stiffness of frames, *Philos. Mag. Ser. 5* **27**, 294 (1864).
- [5] E. Betti, Teoria della elasticita, *Il Nuovo Cimento* **7–8**, 158 (1872).
- [6] H. Nassar, B. Yousefzadeh, R. Fleury, M. Ruzzene, A. Alù, C. Daraio, A. N. Norris, G. Huang, and M. R. Haberman, Nonreciprocity in acoustic and elastic materials, *Nat. Rev. Mater.* **5**, 667 (2020).
- [7] L. Alekseeva, I. Povkh, V. Stroganov, B. Kidyarov, and P. Pasko, A nonreciprocal optical element, *J. Opt. Technol.* **70**, 525 (2003).
- [8] I. M. Mirza, W. Ge, and H. Jing, Optical nonreciprocity and slow light in coupled spinning optomechanical resonators, *Opt. Express* **27**, 25515 (2019).
- [9] P. Yang, X. Xia, H. He, S. Li, X. Han, P. Zhang, G. Li, P. Zhang, J. Xu, Y. Yang *et al.*, Realization of Nonlinear Optical Nonreciprocity on a Few-Photon Level Based on Atoms Strongly Coupled to an Asymmetric Cavity, *Phys. Rev. Lett.* **123**, 233604 (2019).
- [10] R. Fleury, D. L. Sounas, C. F. Sieck, M. R. Haberman, and A. Alù, Sound isolation and giant linear nonreciprocity in a compact acoustic circulator, *Science* **343**, 516 (2014).
- [11] H. Lira, Z. Yu, S. Fan, and M. Lipson, Electrically Driven Nonreciprocity Induced by Interband Photonic Transition on a Silicon Chip, *Phys. Rev. Lett.* **109**, 033901 (2012).
- [12] Z. Wang, Y. Chong, J. D. Joannopoulos, and M. Soljačić, Observation of unidirectional backscattering-immune topological electromagnetic states, *Nature (London)* **461**, 772 (2009).
- [13] F. D. M. Haldane and S. Raghu, Possible Realization of Directional Optical Waveguides in Photonic Crystals with Broken Time-Reversal Symmetry, *Phys. Rev. Lett.* **100**, 013904 (2008).
- [14] D. L. Sounas, C. Caloz, and A. Alù, Giant non-reciprocity at the subwavelength scale using angular momentum-biased metamaterials, *Nat. Commun.* **4**, 2407 (2013).
- [15] S. Lepri and G. Casati, Asymmetric Wave Propagation in Nonlinear Systems, *Phys. Rev. Lett.* **106**, 164101 (2011).
- [16] D.-W. Wang, H.-T. Zhou, M.-J. Guo, J.-X. Zhang, J. Evers, and S.-Y. Zhu, Optical Diode Made from a Moving Photonic Crystal, *Phys. Rev. Lett.* **110**, 093901 (2013).
- [17] M. Nagy, Z. Ákos, D. Biro, and T. Vicsek, Hierarchical group dynamics in pigeon flocks, *Nature (London)* **464**, 890 (2010).
- [18] F. Ginelli, F. Peruani, M.-H. Pillot, H. Chaté, G. Theraulaz, and R. Bon, Intermittent collective dynamics emerge from conflicting imperatives in sheep herds, *Proc. Natl. Acad. Sci. U.S.A.* **112**, 12729 (2015).
- [19] C. Coulais, D. Sounas, and A. Alù, Static non-reciprocity in mechanical metamaterials, *Nature (London)* **542**, 461 (2017).
- [20] L. Jin, R. Khajetourian, J. Mueller, A. Rafsanjani, V. Tournat, K. Bertoldi, and D. M. Kochmann, Guided transition waves in multistable mechanical metamaterials, *Proc. Natl. Acad. Sci. U.S.A.* **117**, 2319 (2020).
- [21] M. Brandenbourger, X. Locsin, E. Lerner, and C. Coulais, Non-reciprocal robotic metamaterials, *Nat. Commun.* **10**, 4608 (2019).
- [22] W. Van Saarloos, Front propagation into unstable states, *Phys. Rep.* **386**, 29 (2003).
- [23] L. M. Pismen, *Patterns and Interfaces in Dissipative Dynamics* (Springer Science & Business Media, New York, 2006).
- [24] M. Cross and H. Greenside, *Pattern Formation and Dynamics in Nonequilibrium Systems* (Cambridge University Press, Cambridge, England, 2009).
- [25] O. M. Braun and Y. S. Kivshar, *The Frenkel-Kontorova Model: Concepts, Methods, and Applications* (Springer Science & Business Media, New York, 2013).
- [26] See Supplemental Material, which includes Refs. [27,28], at <http://link.aps.org/supplemental/10.1103/PhysRevLett.126.194102> for detailed calculations and the inertia term effect. See video in the Supplemental Material [26]. The movie shows the different fronts and traveling waves exhibited by the dissipative Frenkel-Kontorova model with nonreciprocal coupling.
- [27] L. Jin, R. Khajetourian, J. Mueller, A. Rafsanjani, V. Tournat, K. Bertoldi, and D. M. Kochmann, Guided transition waves in multistable mechanical metamaterials, *Proc. Natl. Acad. Sci. U.S.A.* **117**, 2319 (2020).
- [28] S. H. Strogatz, *Nonlinear Dynamics and Chaos: With Applications to Physics, Biology, Chemistry and Engineering* (Addison-Wesley, Reading, MA, 1994).
- [29] E. Trias, J. J. Mazo, F. Falo, and T. P. Orlando, Depinning of kinks in a Josephson-junction ratchet array, *Phys. Rev. E* **61**, 2257 (2000).

1.1. Supplementary materials

The supplementary material of the article *Nonreciprocal Coupling Induced Self-Assembled Localized Structures (Art. 1)* includes the calculations of the Euler-Lagrange equations from the Lagrangian proposed to describe the chain under nonreciprocal coupling. The condition for the overdamped regime to be valid is discussed by employing an adimensionalization of the independent and dependent variables. Explicit computation of the phase diagram curves and the critical conditions using the linear spreading velocity theory [25] are presented. These critical conditions are recognized as points at which the derivatives of n -th order with respect to the front steepness vanish. Finally, an analysis of the effects the small terms neglected theoretically have on the phase diagram is given.

Supplementary Material for *Non-Reciprocal coupling induced self-assembled localized structures*

D. Pinto-Ramos¹, K. Alfaro-Bittner^{2,3}, M.G. Clerc¹, and R.G. Rojas⁴

¹*Departamento de Física and Millennium Institute for Research in Optics, FCFM, Universidad de Chile, Casilla 487-3, Santiago, Chile*

²*Departamento de Física, Universidad Técnica Federico Santa María, Av. España 1680, Casilla 110V, Valparaíso, Chile*

³*Unmanned Systems Research Institute, Northwestern Polytechnical University, Xi'an 710072, China*

⁴*Instituto de Física, Pontificia Universidad Católica de Valparaíso, Casilla 4059, Valparaíso, Chile*

1 The non-reciprocal Frenkel-Kontorova model

Non-linear waves are typical phenomena for coupled oscillators and coupled extended systems. The sine-Gordon equation and its discrete counterpart, the Frenkel-Kontorova model, play a relevant role in the understanding of these waves. These equations can model a coupled chain of pendula or coupled Josephson junctions, among others. The new physical metamaterials bring new horizons to coupled systems, since the coupling between the basic elements can now be non-reciprocal. Studies of waves have been done considering only the elastic non-reciprocal coupling between the basic elements (with no in-site potential) [1,2]. We propose studying the front waves considering a common in-site potential, modeling soft oscillators with non-reciprocal coupling. We refer to this model as the *non-reciprocal Frenkel-Kontorova model*, and it reads

$$\ddot{\theta}_i = \omega^2 \sin \theta_i - \mu \dot{\theta}_i + (D - \alpha)(\theta_{i+1} - \theta_i) - (D + \alpha)(\theta_i - \theta_{i-1}), \quad (1)$$

where ω is the natural frequency, μ is the dissipation coefficient, D is the elastic constant, and α measures the deviation from the reciprocal behavior. Note that in the limit $\alpha \rightarrow 0$, we recover the Frenkel-Kontorova equation. Likewise, in the continuous limit, α can be understood as a linear advection term. Note that the variable θ_i is measured with respect to the upside-down pendulum position.

1.1 A Lagrangian description

Let us consider the following Lagrangian

$$L(\theta_i) = \sum_i \left(\frac{\dot{\theta}_i^2}{2} - \omega^2 \cos \theta_i - \frac{D - \alpha}{2} (\theta_{i+1} - \theta_i)^2 \right) e^{\mu t} \left(\frac{D - \alpha}{D + \alpha} \right)^i. \quad (2)$$

Using the principle of least action, the Euler-Lagrange equations read

$$\frac{d}{dt} \left(\frac{\partial L}{\partial \dot{\theta}_k} \right) - \frac{\partial L}{\partial \theta_k} = 0. \quad (3)$$

To obtain this equation, one must determine

$$\frac{\partial L}{\partial \theta_k} = \left(\omega^2 \sin \theta_k + (D - \alpha)(\theta_{k+1} - \theta_k) \left(\frac{D - \alpha}{D + \alpha} \right)^k - (D - \alpha)(\theta_k - \theta_{k-1}) \left(\frac{D - \alpha}{D + \alpha} \right)^{k-1} \right) e^{\mu t}, \quad (4)$$

and

$$\frac{d}{dt} \left(\frac{\partial L}{\partial \dot{\theta}_k} \right) = \left(\ddot{\theta}_k + \mu \dot{\theta}_k \right) \left(\frac{D - \alpha}{D + \alpha} \right)^k e^{\mu t}. \quad (5)$$

Equating both terms, factoring $e^{\mu t}$ and $\left(\frac{D - \alpha}{D + \alpha} \right)^k$, the Euler-Lagrange equation reads (equation (1) of the main text)

$$\ddot{\theta}_k = \omega^2 \sin \theta_k - \mu \dot{\theta}_k + (D - \alpha)(\theta_{k+1} - \theta_k) - (D + \alpha)(\theta_k - \theta_{k-1}). \quad (6)$$

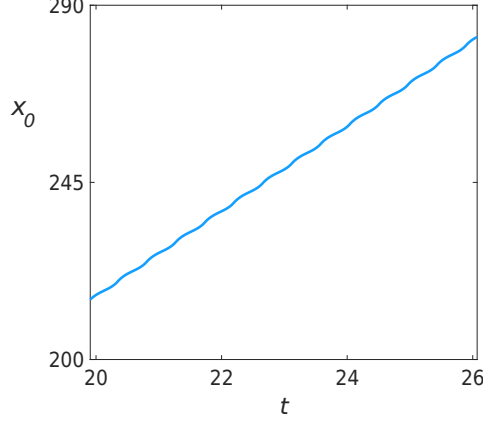


Figure 1: Hopping dynamics of a front. Temporal evolution of the front position $x_0(t)$ obtaining from Eq. (6) with $\omega = 1$, $\mu = 2$, $D = 0.04$, and $\alpha = 0$.

1.2 The overdamped limit

When the damping coefficient is large enough, one can rescale time to neglect the inertial term. Introducing $t \rightarrow \mu\tau$ equation (3) reads

$$\frac{1}{\mu^2}\ddot{\theta}_i = \omega^2 \sin \theta_i - \dot{\theta}_i + (D - \alpha)(\theta_{i+1} - \theta_i) - (D + \alpha)(\theta_i - \theta_{i-1}).$$

Note that τ has units of seconds squared. If μ is large enough ($\omega^2/\mu^2 \rightarrow 0$) [3], one can neglect the inertial term in the previous equation. Then, the system is described by the equation (*Overdamped non-reciprocal Frenkel-Kontorova*, equation (2) of the main text)

$$\dot{\theta}_i(\tau) = \omega^2 \sin \theta_i + (D - \alpha)(\theta_{i+1} - \theta_i) - (D + \alpha)(\theta_i - \theta_{i-1}). \quad (7)$$

In this equation, the analytical study is accessible. It is worth stressing that the phenomena reported are also present in the underdamped case.

2 Phase diagram

As $\alpha > 0$ (< 0), the solutions are advected towards the right (left) flank. Namely, π -kinks and 2π -kinks propagate with a speed that depends on the parameters. A disturbance of the unstable solution, $\theta_i = 0$, generates a π -kink, which propagates with the minimum speed determined by the asymptotic criterion [4]. Following the strategy presented in reference [4], as shown in Fig. 1, the fronts speed is not a constant. Rather it is oscillatory, with a characteristic period. Averaging the front speed during this period, one can find an *average speed* $\langle v \rangle$.

Let us consider the following ansatz for the asymptotic left tail of the front

$$\theta(i, t) \sim e^{k(i+vt)}(1 + f_{k,i}^T),$$

where $f_{k,i}^T(t)$ is a small oscillatory function, $f_{k,i}^T(t) \ll 1$, with period T and zero mean value. Inserting this ansatz in Eq. (7), we get

$$kv(1 + f_{k,i}^T) + \dot{f}_{k,i}^T = (\omega^2 - 2D + 2D \cosh k - 2\alpha \sinh k)(1 + f_{k,i}^T) + D(f_{k,i+1}^T - 2f_{k,i}^T + f_{k,i-1}^T) - \alpha(f_{k,i+1}^T - f_{k,i-1}^T). \quad (8)$$

Averaging over the period T , we obtain (equation (3) of the main text)

$$\langle v \rangle = \frac{\omega^2 - 2D + 2g(k)}{k}, \quad (9)$$

where $\langle v \rangle \equiv \int_t^{t+T} v(t') dt' / T$ is the average speed and $g(k) \equiv D \cosh k - \alpha \sinh k$. Note that this is equivalent to propose the following ansatz for the asymptotic left tail of the front $\theta(i, t) \sim e^{k(i+\langle v \rangle t)}$.

The minimal criterium of the speed asserts that the asymptotic speed of the front v is obtained when $v(k)$ is a minimum [5], so (from now we will drop the brackets)

$$\begin{aligned} \left. \frac{\partial v}{\partial k} \right|_{k^*} &= 0, \\ v_{min} &= v(k^*). \end{aligned} \tag{10}$$

2.1 I-II transitions

The curve that separates zone I from II corresponds to an absolute-convective instability. Hence, one can impose that $v = 0$ at this bifurcation. Using the relation

$$\partial_k(kv) = v + k\partial_k v = 2\partial_k g(k),$$

and imposing the conditions $\partial_k v = v = 0$, we get

$$\partial_k g(k)|_{k^*} = 0.$$

From this expression, it is obtained $k^* = \operatorname{arctanh}(\alpha/D)$. Replacing k^* in formula (9), we obtain

$$0 = \omega^2 - 2D + 2g\left(\operatorname{arctanh}\frac{\alpha}{D}\right).$$

Using $\cosh(\operatorname{arctanh} x) = 1/\sqrt{1-x^2}$ and $\sinh(\operatorname{arctanh} x) = x/\sqrt{1-x^2}$, the following expression describes the absolute-convective instability in the (D, α) plane

$$0 = \omega^2 - 2D + \frac{2D}{\sqrt{1 - (\frac{\alpha}{D})^2}} - \frac{2\alpha^2/D}{\sqrt{1 - (\frac{\alpha}{D})^2}} = \omega^2 - 2D + \frac{2D}{\sqrt{1 - (\frac{\alpha}{D})^2}} \left(1 - \left(\frac{\alpha}{D}\right)^2\right). \tag{11}$$

Simplifying this expression

$$\omega^2(\omega^2 - 4D) = -4\alpha^2,$$

and finally solving for D , it reduces to equation (4) of the main text

$$D = \frac{\omega^2}{4} + \frac{\alpha^2}{\omega^2}. \tag{12}$$

2.2 II-III and I-IV transitions

The transitions between these zones are characterized by the fact that the front changes from monotonous to non-monotonous, thus one study the threshold in which a real k can not satisfy $\partial_k v = 0$. This condition translates into looking for the point in which $\left. \frac{\partial^2 v}{\partial k^2} \right|_{k^*} = 0$ and simultaneously $\left. \frac{\partial v}{\partial k} \right|_{k^*} = 0$. Differentiating two times one has

$$\partial_k^2(kv) = 2\partial_k v + k\partial_k^2 v = 2g(k).$$

Imposing the conditions described above, one has $g(k^*) = 0$, this gives $k^* = \operatorname{arctanh}(D/\alpha)$. Using that also $\partial_k^2 v = v/k^2 - \partial_k v/k - 2\partial_k g(k)/k^2 + 2g(k)/k$, replacing formula (9) for v , and $\partial_k^2 v = \partial_k v = g(k^*) = 0$, we obtain the expression in the (D, α) plane

$$0 = \frac{\omega^2 - 2D}{k^*} - 2(D \sinh k^* - \alpha \cosh k^*). \tag{13}$$

Making use of $\cosh(\operatorname{arctanh} x) = 1/\sqrt{1-x^2}$, and $\sinh(\operatorname{arctanh} x) = x/\sqrt{1-x^2}$, after straightforward calculations this reduces to equation (5) of the main text.

$$\frac{2D - \omega^2}{\operatorname{arctanh}\left(\frac{D}{\alpha}\right)} = 2\alpha \sqrt{1 - \left(\frac{D}{\alpha}\right)^2}. \tag{14}$$

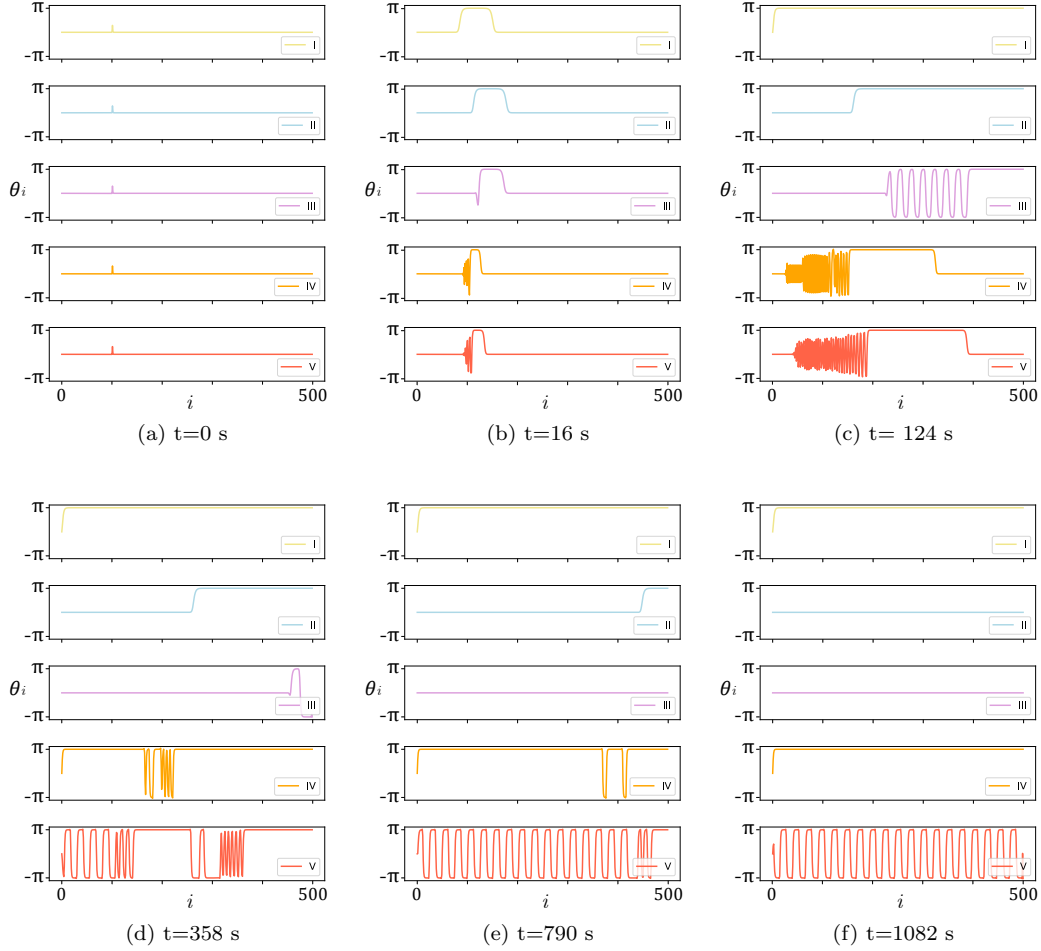


Figure 2: Nonlinear wave propagation of the overdamped Frenkel-Kontorova model with non-reciprocal coupling. Temporal evolution of different typical waves of the different zones of the phase diagram.

2.3 III-V transition

In this transition non-monotonous fronts present an absolute-convective instability, in which the front velocity changes its sign, so one can impose the same conditions as in the I-II transition. To obtain the relation, one must impose $\text{Im } v = 0$ for stability reasons. Then, one can obtain v_{min} with respect to k_r , proposing the ansatz for the asymptotic left tail of the front $\theta_i \sim e^{k(i+(v)t)+j\omega_k t}$, where $j \equiv \sqrt{-1}$, $k = k_r + jk_j$ is a complex parameter, and ω_k accounts for the oscillatory nature of the solution. The front speed satisfies

$$vk_r = \omega^2 - 2D + 2g(k_r) \cos k_j.$$

Imposing the condition of absolute-convective instability, $v = 0$ and $\partial_{k_r} v = 0$, we get

$$2\partial_{k_r} g(k_r) \cos k_j = 0.$$

Due to $\partial_{k_r} g(k_r) = 0$ is not satisfied in this region of the (D, α) plane, the only solution is $\cos k_j = 0$. Finally, imposing that the velocity vanishes and injecting $\cos k_j = 0$, the following relation is obtained

$$D = \frac{\omega^2}{2}. \quad (15)$$

2.4 IV-V transition

This transition curve could not be obtained by means of the asymptotic criterium. Therefore, we have numerically studied this transition. The instability emerges from the left flank and generates the propagative pattern.

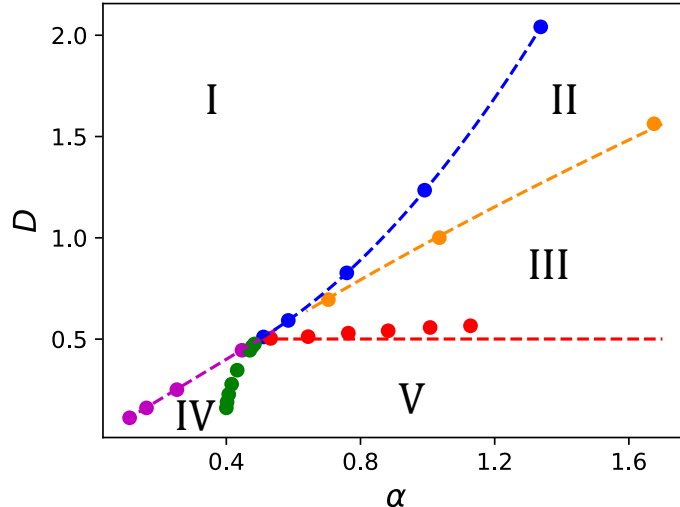


Figure 3: Bifurcation curves of the dissipative Frenkel-Kontorova model with non-reciprocal coupling for the underdamped case, for $\mu = 5$ and $\omega = 1$. The dashed lines are the bifurcation curves calculated on the overdamped case, dots represent numerical simulations in the underdamped case.

3 The phase diagram in the underdamped limit

3.1 Overdamped case

For the sake of simplicity of analytical analysis, in the main text, we have considered the overdamping limit of equation (1) and have determined its phase diagram depicted in figure 2 of the main text. The evolution of a perturbation, in each zone, is represented by the temporal sequence shown in Fig. 2. Likewise, we have added the supplemental video 1 showing an animation for the evolution of the different nonlinear waves.

3.2 Underdamped case

If the inertial term is not neglected in equation (1) of the main text, similar dynamic behaviors can be observed when the damping term is not small. When the damping is small, linear waves and interaction with nonlinear waves can change the dynamics presented. Taking $\mu = 5$ and $\omega = 1$, we obtain that the bifurcation curves shift slightly from their overdamped relative curves (see figure 3). It is important to note that using the same techniques presented above, the curve separating zones I and II is unchanged. The other instability curves have cumbersome mathematical expressions. Figure 3 shows the phase diagram of the dissipative Frenkel-Kontorova model with non-reciprocal coupling. The dashed curves account for the instabilities calculated on the overdamped case; dots stand for instability curves obtained by numerical simulations in the underdamped case. A slight shift is evident in the transition III-V curve.

4 References

- [1] M. Brandenbourger, X. Locsin, E. Lerner, and C. Coulais, *Non-reciprocal robotic metamaterials*, Nature Commun. **10**, 4608 (2019).
- [2] L. Jin, R. Khajetourian, J. Mueller, A. Rafsanjani, V. Tournat, K. Bertoldi, and D. M. Kochmann, *Guided transition waves in multistable mechanical metamaterials*, Proc. Natl. Acad. Sci. **117**, 2319 (2020).
- [3] S. H. Strogatz, *Nonlinear Dynamics and Chaos: With Applications to Physics, Biology, Chemistry and Engineering* (Addison-Wesley, Reading, MA, 1994).
- [4] K. Alfaro-Bittner, M. G. Clerc, M. A. García-Ñustes, and R. G. Rojas, *π -kink propagation in the damped Frenkel-Kontorova model*, EPL, **119**, 40003, (2017).
- [5] W. Van Saarloos, *Front propagation into unstable states*, Phys. Rep. **386**, 29 (2003).

Chapter 2

Giant boundary layer induced by nonreciprocal coupling in discrete systems (Communications in Nonlinear Science and Numerical Simulation 125, 107391)

Front solutions spatially connect two equilibrium states of the local entities forming the chain. Thus, these solutions break the homogeneity of space and usually acquire dynamics; for example, in variational systems, the front will move in a direction that reduces the system's free energy, ultimately leading to a homogeneous solution. However, one aspect to consider is the boundary conditions to which our system is subjected. If boundaries do not match with the equilibrium solution of the dynamical system at its bulk, they drive an inhomogeneous solution localized at the border connecting the bulk solution with the boundary condition constraint; namely, a *boundary layer* arises [58, 59].

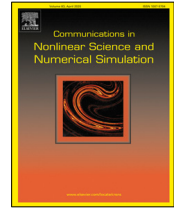
In the previous chapter, we employed boundary conditions favorable for forming fronts into the unstable state; at least one boundary was fixed at the unstable value of the variable under study, and the other is a free boundary. This particular choice (the fixed boundary) can be difficult to handle in experimental environments, as one usually has accuracy ranges for the tools. Even numerically, one is restricted by the finite memory of the computer trying to store the infinite information of the many real numbers describing the variables under study.

In this chapter, we analyze boundary layers arising when imposing fixed boundary conditions that have a mismatch with respect to the unstable homogeneous equilibrium value of the system. For exponentially small mismatch values, the apparent propagation of a front into the unstable state is observed; however, for systems with enough elements, one will observe the sudden detention of the front propagation, forming a *giant boundary layer*. The properties of these solutions as a function of the parameters are characterized, employing analytical expressions for the velocity of fronts to understand the phenomenon. The boundary layer size is analytically approximated employing map iteration techniques.



Contents lists available at ScienceDirect

Communications in Nonlinear Science and Numerical Simulation

journal homepage: www.elsevier.com/locate/cnsns

Research paper

Giant boundary layer induced by nonreciprocal coupling in discrete systems

D. Pinto-Ramos^{a,*}, K. Alfaro-Bittner^b, M.G. Clerc^a, R.G. Rojas^c^a Departamento de Física and Millennium Institute for Research in Optics, Facultad de Ciencias Físicas y Matemáticas, Universidad de Chile, Casilla 487-3, Santiago, Chile^b Universidad Rey Juan Carlos, Calle Tulipán s/n, 28933, Móstoles, Madrid, Spain^c Instituto de Física, Pontificia Universidad Católica de Valparaíso, Casilla 4059, Valparaíso, Chile

ARTICLE INFO

Article history:

Received 24 September 2022

Received in revised form 25 April 2023

Accepted 20 June 2023

Available online 25 June 2023

Keywords:

Nonreciprocal coupling

Front propagation

Boundary layer phenomena

Nonlinear discrete systems

ABSTRACT

Nonreciprocally coupled systems present rich dynamical behavior such as unidirectional amplification, fronts, localized states, pattern formation, and chaotic dynamics. Fronts are nonlinear waves that may connect an unstable equilibrium with a stable one and can suffer a convective instability when the coupling is nonreciprocal. Namely, a state invades the other one, and due to boundary conditions, the front stops and creates a boundary layer. Unexpectedly, in nonreciprocal coupled systems, we observe arbitrarily large boundary layers in the convective regime when the condition at the fixed edge does not match the equilibrium value. We analytically determine the boundary layer size using map iterations; these results agree with numerical simulations. On the other hand, if one of the boundary conditions matches the unstable equilibrium state, the boundary layer size diverges; however, due to the computer numerical truncation, it is finite in numerical simulations. Our result shows that, in nonreciprocally coupled systems, this mismatch in the boundary condition is relevant in controlling the boundary layer size, which exhibits a logarithm scaling with the mismatch value.

© 2023 Elsevier B.V. All rights reserved.

1. Introduction

It is a known matter that extended systems exhibit a boundary layer when two or more phases compete to dominate the system dynamics; they can originate from geometrical or topological aspects [1–3], forces driving different phases [1,3], or the boundary conditions [2,4], to mention a few. One example is nematic liquid crystal layers subjected to strong anchoring and electric fields. The elastic forces try to balance with the electrical ones leaving the mean orientation of molecules with a profile that connects two different states. A common example is the boundary layer of viscous flows passing through an obstacle or inside a pipe. The velocity profile needs to satisfy the no-slip condition and has to connect with the asymptotic flow far from the obstacle [4,5]. Both examples exhibit a thin (compared with the system size) boundary layer, in which the profile of the field has sharp changes near the edges of the respective system. Hence, the boundary layers are produced by imposing “uncomfortable” conditions at the boundaries. Note that boundary layers have different physical properties in comparison to the system bulk [4–6], such as the one exhibited by obstacles immersed in a flow, see Ref. [5]. In general, analytical solutions of boundary layers are not accessible, making therefore numerical simulations a useful tool to characterize them.

* Corresponding author.

E-mail address: david.pinto@ug.uchile.cl (D. Pinto-Ramos).

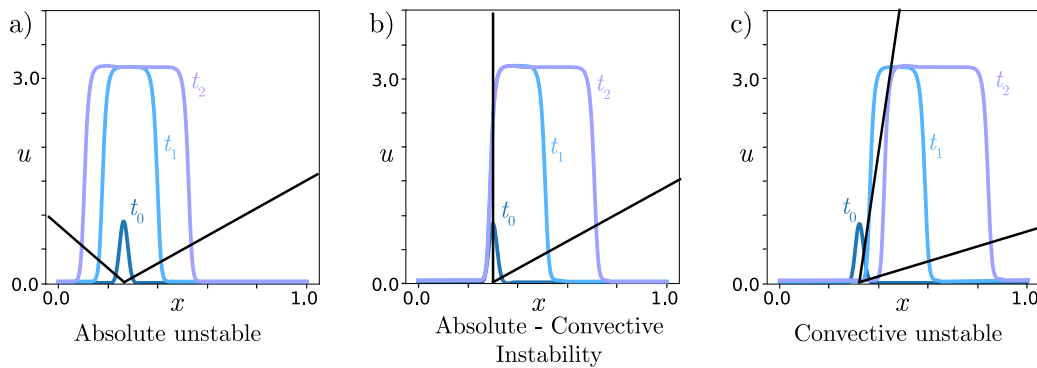


Fig. 1. Absolute-convective threshold. Panel (a) depicts the $u = 0$ as absolutely unstable; that is, perturbations propagate in both directions. Panel (b) shows the system in the absolute-convective instability threshold, where the left flank of the perturbation has exactly zero speed. Panel (c) illustrates the $u = 0$ state as convective unstable, where perturbations grow up and propagate towards the right flank.

A simple 1D scalar model to study the boundary layer is population propagation (when a fixed boundary condition is considered), particularly motivated by the spread of genes and diseases. This type of system is modeled by a simple reaction–diffusion equation known as the Fisher–Kolmogorov–Petrovskii–Piskunov equation (FKPP equation) [7,8]. This model is characterized by including the nonlinear response of the logistic model plus a diffusive transport process. Then, the system is characterized by having two equilibria, one stable ($u = 1$) and the other unstable ($u = 0$), where u accounts for the scalar field. In order to obtain a boundary layer, a fixed (Dirichlet) boundary condition must be considered. Note that the other flank boundary does not affect the above-mentioned boundary layer and, for example, can be considered as zero flow (Neumann). The edge with the fixed condition is settled to the unstable equilibrium value. When the system starts in the unstable state $u = 0$ and is locally disturbed, the emergence of two counterpropagating fronts moving towards the system edges are observed so that the stable state, $u = 1$, invades almost the entire system. These nonlinear waves are known as Fisher–Kolmogorov–Petrovskii–Piskunov fronts (FKPP fronts) [7–11]. Due to the fixed boundary condition at the border, a boundary layer is established between the unstable and stable state, and its size is proportional to the square root of the diffusion coefficient. The above scenario changes radically when one considers a drift or advection term in the direction towards the flank with zero flow. When the drift coefficient is small, the boundary layer is slightly modified; however, when this coefficient overcomes a critical value, the system exhibits an absolute–convective instability (triggered by the advection), and therefore the $u = 0$ state invades the system. In the latter case, the system does not present a boundary layer. Fixing a reference frame to the edges, for zero advection, the $u = 0$ state is said to be *absolute unstable*, meaning that perturbations over this state will propagate to the whole system, as seen in Fig. 1(a). On the other hand, for high enough advection, the $u = 0$ state will transit to be *convective unstable* at the absolute-convective instability threshold as seen in Fig. 1(b). Increasing further the advection, the propagation grows in a co-mobile frame, but in the edges reference frame, perturbations decay for infinite time, see Fig. 1(c).

The above-mentioned physical systems are described by continuous equations. However, this description fails to capture some phenomena observed in real systems. Note that real macroscopic systems can be approximated by continuous equations; nevertheless, they are intrinsically discrete. This means they are composed of a large – but finite – number of elements that can interact with each other. Likewise, numerical simulations of continuous descriptions are performed in discrete lattices. Surprisingly, the discrete nature of systems has measurable consequences on the macroscopic world, such as the dislocation dynamics observed in crystals that can only be explained by the Peierls–Nabarro potential [12], the front propagation in discrete systems presenting hopping dynamics [9,10,13], the dispersion of propagating waves [14], or the induction of localized structures [14], to mention a few. In the above examples, the physical principle of reciprocity governs the coupling between the elements, that is, each element that constitutes the system under study is symmetrically coupled to its neighbors [15]. Recently, different experiments have implemented nonreciprocal coupling, generally by breaking the spatial-reflection symmetry. As a consequence of the loss of this symmetry, in extended systems, one expects the perturbations to generate waves that favor specific directions of propagation. More precisely, nonreciprocal couplings are achieved by using rotating fluids [16], temporally modulated coupling elements [17,18], elastic metamaterials [19], or active robotic metamaterials [20].

The study of boundary layers has focused on continuous systems with various boundary conditions. To our knowledge, few systematic studies have been performed on boundary layers in discrete and nonreciprocal nonlinear systems. Moreover, recently it has been shown how nonreciprocal coupling in nonlinear coupled damped oscillators is responsible for convective instabilities, front modulation, and even pattern formation [21]. Our work aims to unveil the boundary layer formation on discrete systems and the nonreciprocal coupling effect on them based on two prototypical models. In the continuous limit, this kind of coupling is responsible for advection and may induce an absolute–convective instability [20,21]. Theoretically, we derive the condition for the convective instability of solutions connecting an unstable with a stable equilibrium in nonreciprocally coupled nonlinear systems. When the fixed boundary condition value mismatches

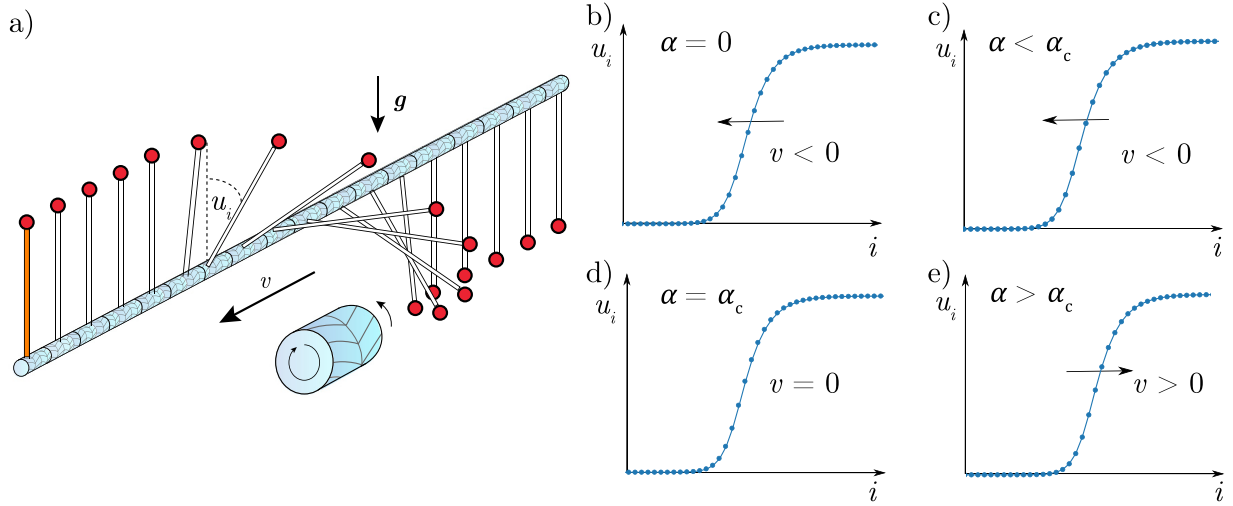


Fig. 2. Nonreciprocal Frenkel-Kontorova system. (a) Schematic representation of a chain of pendula with nonreciprocal coupling. The cylinder illustrates a nonreciprocal torsion spring. u_i accounts for the i th pendulum angle. This variable has its origin in the upside-down position. v stands for the speed of wavefront propagation. (b), (c), (d), and (e) illustrate the angle profile as a function of their index i and the effect of the nonreciprocal elastic coupling α on FKPP fronts. α_c accounts for the nonreciprocal critical elastic coupling that gives rise to absolute-convective instability.

with the unstable equilibrium, a boundary layer arises; otherwise, systems exhibit an absolute-convective instability. Unexpectedly, we observe arbitrarily large boundary layers; thus, we call them *giant boundary layers*. We propose a method to predict the boundary layer size based on a recurrence relation describing the equilibrium state that shows excellent agreement with the numerical findings. Our analysis illustrates the importance of the convective instability in FKPP fronts in determining the boundary layer size, where an abrupt shift of its size is observed at the instability. This instability creates two regimes, one where the boundary layer does not depend on the mismatch between the boundary condition and the unstable equilibrium value, and the other where a logarithmic law is obtained for the boundary layer size as a function of the boundary condition value.

2. Systems with nonreciprocal coupling

Two prototypical models that exhibit front propagation into an unstable state, *FKPP fronts*, are the Frenkel-Kontorova [12] and the Fisher-Kolmogorov-Petrovskii-Piskunov model [7,8]. The FKPP equation was proposed to model the spread of genes mutations and populations (see the textbook [22] and reference therein). The Frenkel-Kontorova model has been derived from several physical situations, including, for example, crystal lattices, torsion chain of pendula (cf. Fig. 2), coupled Josephson junctions, and coupled nonlinear oscillators [12]. In the previous examples, the coupling mechanism usually preserves the space reflection symmetry of the system; namely, they exhibit a reciprocal coupling [15]. Recently, several techniques, methods, and experiments have been developed to break the reciprocity and study the effect of nonreciprocal coupling [16,19,20,23]. Particularly, robotic metamaterials have been employed to explore energy propagation when space reflection symmetry is absent in linear oscillator chains. In these systems, it was shown that perturbations propagate asymmetrically [20], that is, waves are amplified in a preferred direction. Indeed, nonreciprocal coupling allows conducting of the energy in a desired direction. Furthermore, it led to the study of nonreciprocally coupled chains of nonlinear oscillators and front solutions in them [21]. To extend the understanding of nonreciprocal coupling and its effects, we analyze the overdamped discrete extended one-dimensional model given by

$$\dot{u}_i = f(u_i) + (D - \alpha)(u_{i+1} - u_i) - (D + \alpha)(u_i - u_{i-1}), \quad (1)$$

where $u_i(t)$ describes the variable under study for the i th element of the system, for example, the displacement of the i th oscillator with respect to its equilibrium, the population of a given specie in a specified region, or the phase of a given superconductor, to mention a few. α and D account for the nonreciprocal and reciprocal coupling strength, respectively. The chain consists of $(N+1)$ basic elements, which local dynamics is described by the nonlinear function or reaction term $f(u_i)$, and each element interacts with its nearest neighbors. The nonlinear functions that are considered in this work are $f(u_i) = \sin(u_i)$ (Frenkel-Kontorova nonlinearity) and $f(u_i) = u_i(1 - u_i)$ (Fisher-Kolmogorov-Petrovskii-Piskunov nonlinearity). Boundary conditions $u_0 = \epsilon$ (Dirichlet) and $u_{N+1} = u_{N-1}$ (zero flow) are imposed. Note that the transformation symmetry $i \leftrightarrow N - i$ is absent as a consequence of boundary conditions. Likewise, the reflection symmetry $i \pm 1 \rightarrow i \mp 1$ is absent when $\alpha \neq 0$.

It is worth noting that in Eq. (1), if one defines the coordinate $x = il_0$, where l_0 is the distance between the basic elements, the continuous limit appears as D and α go to infinity at the same time as l_0 vanishes, such that $D_{\text{diff}} \equiv Dl_0^2$ and $\alpha_{\text{adv}} \equiv 2\alpha l_0$ remain finite. With these assumptions, the coupling terms become a diffusive transport and a linear advection.

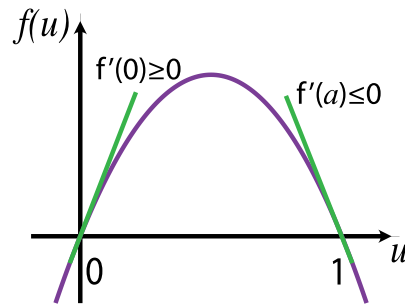


Fig. 3. Schematic representation of the local dynamics. Example of a reaction term $f(u)$ appearing in Eq. (1) as a function of u .

Note that the linear advection can be eliminated using a co-mobile reference frame for infinite systems. Despite the usefulness of the continuous limit to approximate the system solutions [20], we have recently proven that nonreciprocal coupling in discrete systems induces instabilities that are not present in their continuous limit [21].

Without loss of generality, one can choose two reference states such that $f(0) = 0, f'(0) > 0, f(a) = 0$, and $f'(a) < 0$, where $u_i = 0$ and $u_i = a$ are equilibria ($i = 0, 1, 2, \dots, N$). Fig. 3 depicts the typical reaction term under consideration. We assume that there exists a solution connecting both equilibria – a FKPP front – where $u_i = 0$ and $u_i = a$ are unstable and stable states, respectively. Fronts are particle-type solutions characterized by a position and core. In particular, the position is defined as the coordinate or index with the greatest spatial variation.

2.1. The overdamped Nonreciprocal Frenkel-Kontorova model

When $f(u_i) = \sin u_i$ and $\alpha = 0$ in Eq. (1), the model is known as the overdamped Frenkel-Kontorova model [12]. When inertia is not neglected, the Frenkel-Kontorova model naturally arises in a variety of systems such as crystal lattices, nonlinear oscillators, and Josephson junctions [12]. For large enough dissipation, a first-order equation can be written. Thus, the generalized overdamped Frenkel-Kontorova model with nonreciprocal coupling reads

$$\dot{u}_i = \sin u_i + (D - \alpha)(u_{i+1} - u_i) - (D + \alpha)(u_i - u_{i-1}). \tag{2}$$

A physical example is depicted in Fig. 2(a), which represents a chain of pendula where the upside-down and upright position corresponds to $u_i = 0$ and $u_i = \pi$, respectively. Note that the small cylinder illustrates a nonreciprocal coupling element and, at the border of the chain, the colored pendulum has a fixed position slightly different from zero. Moreover, note that we have swapped the usual equilibria for numerical convenience (commonly one finds in the literature $f(u_i) = -\sin u_i$, which is recovered with a linear transformation). Then, the mismatch boundary condition can read $u_0 = \epsilon$, with ϵ the deviation from the unstable equilibrium value. Fig. 2(b) and 2(c) show the typical FKPP front profile propagating to the left (into the unstable state) with speed $v(D, \alpha)$, corresponding to the absolute regime. Panel 2(d) shows a critical situation when the speed of the front is zero, i.e., the system exhibits an absolute convective–instability for a critical value of the nonreciprocal coupling parameter. Finally, panel 2(e) depicts the front in the convective regime, i.e., when the front propagation direction is reversed, spreading the zero equilibrium into the non-null state. Similar models to Eq. (2) can be found in the literature [21,24].

2.2. Nonreciprocal Fisher–Kolmogorov–Petrovskii–Piskunov model

When one considers $f(u_i) = u_i(1 - u_i)$ and $\alpha = 0$, Eq. (1) is known as the Fisher–Kolmogorov–Petrovskii–Piskunov model, originally written to describe combustion processes or the growth of a mutation in a population. It serves as a general model for population growth and saturation, being capable of describing the number of animals, bacteria, vegetation, and humans [22]. The generalization of the FKPP model that includes the nonreciprocal coupling is

$$\dot{u}_i = u_i(1 - u_i) + (D - \alpha)(u_{i+1} - u_i) - (D + \alpha)(u_i - u_{i-1}). \tag{3}$$

Similar equations can be found in [25–27], where nonreciprocal terms account for inhomogeneous food supply or external flows driving population movements, such as tides or winds.

3. Mean velocity of FKPP fronts

The calculation of the front propagation speed has been addressed in several continuous or discrete physical examples with various techniques [10,11]. The main difference between front propagation in continuous and discrete media is that in the former, the front speed is constant, whereas, in the latter, it is characterized by having hopping dynamics [28]. Here, we employ a similar method to determine the front mean velocity in discrete media following Refs. [10,21]. Considering

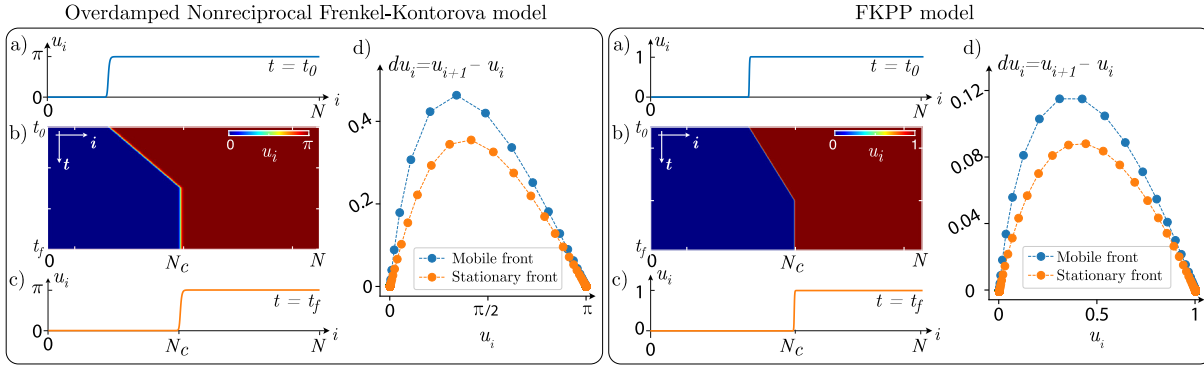


Fig. 4. Giant boundary layers in discrete systems. Examples of giant boundary layers of non-reciprocally coupled discrete systems, parameters $D = 1.5$ and $\alpha = 1.4$ for both the overdamped Nonreciprocal Frenkel-Kontorova model Eq. (2) and the Fisher-Kolmogorov-Petrovskii-Piskunov model Eq. (3). Panels (a) and (c) show the initial and final state of u_i . Panels (b) illustrate the spatiotemporal evolution of the system. (d) Phase portrait representation of the initial and final front profile.

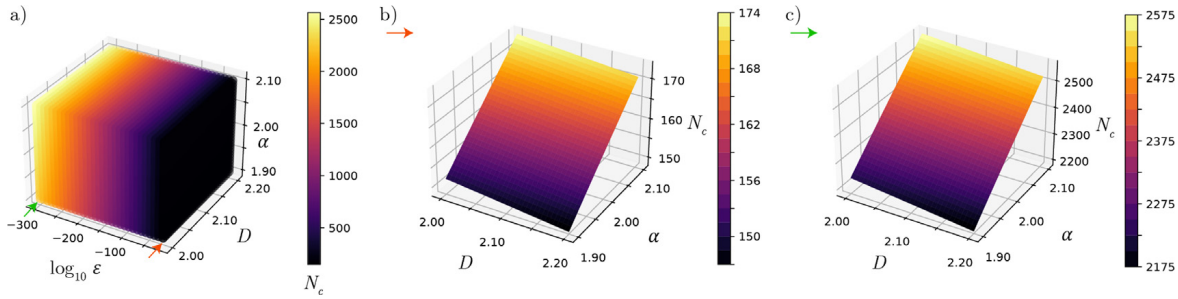


Fig. 5. Giant Boundary layer size characterization. (a) Boundary layer size N_c as a function of the parameters (D, α) and the boundary condition value ϵ for model Eq. (2). (b) and (c) show the dependence of N_c in different planes of constant ϵ value, corresponding to $\log_{10} \epsilon = -20$ and $\log_{10} \epsilon = -300$, respectively.

the ansatz $u_n \sim e^{k(n+\langle v \rangle t)}$ in Eq. (1)—where k and $\langle v \rangle$ correspond to the front steepness and mean velocity—after straightforward calculations, one obtains

$$\langle v(k) \rangle = \frac{f'(0) - 2D}{k} + 2 \left(\frac{D \cosh k - \alpha \sinh k}{k} \right), \tag{4}$$

where f' accounts for the derivative of the f function. For bounded perturbations, the front velocity $\langle v(k) \rangle$ tends to its minimum with respect to k , $\langle v \rangle_{min}$ [11]. Considering this $\langle v \rangle_{min}$, one can determine the critical parameter α_c for which the front changes its propagation direction. Namely, it suffers an absolute-convective instability at [21]

$$D = \frac{f'(0)}{4} + \frac{\alpha_c^2}{f'(0)}. \tag{5}$$

Note that for the models considered here, $f'(0) = 1$. Additionally, replacing the continuous limit approximations $D = D_{diff}/l_0^2$ and $\alpha = \alpha_{adv}/2l_0$ in the previous formula, one recovers the usual absolute-convective instability threshold in the continuous limit $\alpha_{adv} = 2\sqrt{D_{diff}f'(0)}$ [29], corresponding exactly to the speed of FKPP fronts in the continuum limit [30].

4. Numerical observations

Numerical simulations of Eqs. (2) and (3) were conducted using a Runge-Kutta of fourth order algorithm, with the aforementioned boundary conditions ($u_0 = \epsilon$ and $u_{N+1} = u_{N-1}$). Simulations are initialized with the initial condition $u_i = 0$ for $i = (2, 3, \dots, N)$ and $u_1 = 0.1$, corresponding to a small bounded perturbation near the left flank edge of the system. Surprisingly, the FKPP fronts propagation is frustrated due to the left boundary condition and the discrete nature of the system. Fig. 4 shows the failure for models Eqs. (2) and (3). We can see that the front propagates with a constant average speed and abruptly stops, frustrating its propagation. Let us denote the position where the front stops as N_c (the equilibrium front position), which corresponds to the boundary layer size. Note that the final profile of the front, i.e., its profile when the propagation stops, is different from the one it has while is propagating, see Figs. 4(d). A similar phenomenon is observed in the phase propagation of parametrically driven systems [31].

For $N > N_c$, the boundary layer size N_c is determined numerically by direct simulation of the dynamical system. Fig. 5(a) shows the boundary layer size in the parameter space (D, α, ϵ). Panels 5(b) and 5(c) show the (D, α) dependence

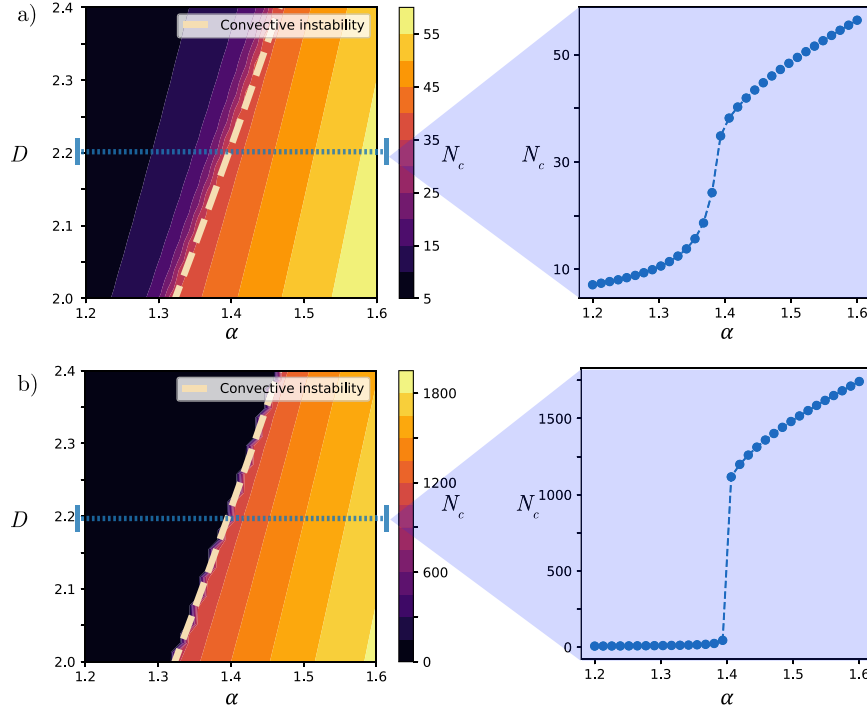


Fig. 6. Convective instability of FKPP fronts and boundary layer size. (a) and (b) exhibit the N_c dependence on parameters close to the convective instability of FKPP fronts characterized by $D = 1/4 + \alpha^2$. Insets show a horizontal cut where a change in behavior is observed at the instability. For (a), $\log_{10} \epsilon = -10$. For (b), $\log_{10} \epsilon = -320$.

for fixed values of ϵ corresponding to $\log_{10} \epsilon = -20$ and $\log_{10} \epsilon = -300$. Note that the phenomenon cannot be observed if $N < N_c$ because the boundary layer size would be greater than the system size, remaining unnoticeable.

We further study the region near the absolute-convective instability curve given by Eq. (5). One can observe that this bifurcation separates regions of small and large boundary layers depending on the boundary condition value, as seen in Fig. 6. The effect of the absolute-convective instability on boundary layer size is amplified when the boundary condition value ϵ goes to zero approaching the equilibrium value, as seen when comparing the insets of Figs. 6(a) and 6(b).

5. Equilibrium position of front-like solutions

To shed light on the steady states of the model Eq. (1), we use a method similar to the one used in Ref. [32]. This corresponds to solving the recurrence relation or map when one imposes the equilibrium condition $\dot{u}_i = 0$ and the boundary conditions. In our case, $u_0 = \epsilon$ is the initial condition for the map, and its recurrence relation reads

$$0 = f(u_i) + (D - \alpha)(u_{i+1} - u_i) - (D + \alpha)(u_i - u_{i-1}). \tag{6}$$

Note that the above equation corresponds to a bi-dimensional map [33]. In the case of $D = \alpha$, the map simplifies because equation (6) becomes a one-dimensional map. This corresponds to a unidirectional type of coupling, with only backward feedback being applied in the chain. Despite the particular parameter values, this limit illustrates in a simple way the equilibrium front position calculation N_c . In the unidirectional coupling limit, the map recurrence reads

$$u_i = u_{i+1} - \frac{f(u_{i+1})}{2D} \equiv g(u_{i+1}),$$

$$u_0 = \epsilon. \tag{7}$$

The value of N_c can be found iterating the map (7), and seeking the iteration step i^* in which the function $|u_{i^*}| - a/2$ changes its sign, where a corresponds to the non zero equilibrium value (cf. Section 2). As N_c rarely coincides with an element position of the discrete chain; we interpolate linearly $|u_{i^*}| - a/2$ between i^* and $i^* + 1$, then, one can find a continuous value of N_c looking for the zero of the interpolated function.

To iterate map (7) from an initial condition, one generally needs to numerically invert the relation to obtain the map $u_{i+1} = g^{-1}(u_i)$. To illustrate the method, we use the nonreciprocal FKPP model Eq. (3). In this case, one can obtain the recurrence relation analytically

$$u_{i+1} = \frac{1 - 2D + \sqrt{(1 - 2D)^2 + 8Du_i}}{2}. \tag{8}$$

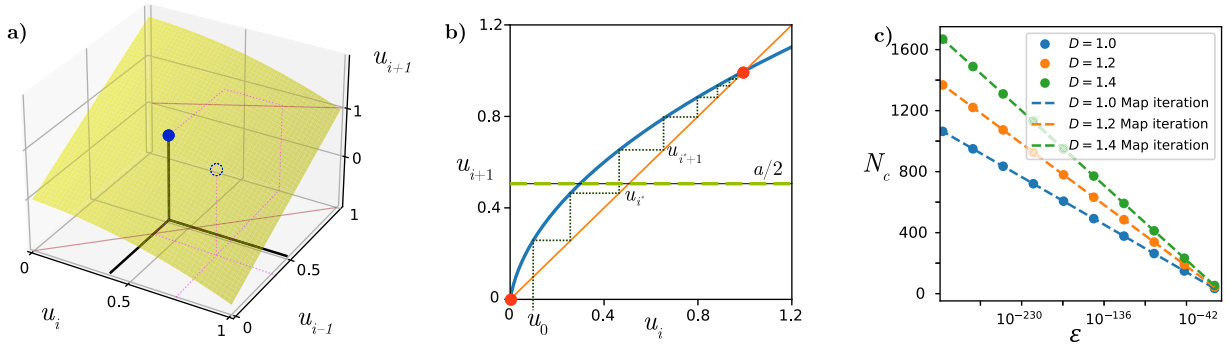


Fig. 7. Map iteration representation. Iterations of the resulting recurrence relation for the stationary solutions of the Nonreciprocal Fisher–Kolmogorov–Petrovski–Piskunov model (3). (a) Bi-dimensional map for $D = 0.6$ and $\alpha = 2$. (b) Unidirectional coupling case for $D = \alpha = 0.6$. u_0 value is the initial condition of the map, which corresponds to the boundary condition of the discrete equation. (c) Boundary layer size as a function of the mismatch ϵ for the unidirectional coupling case $D = \alpha$ for different values of D . Dots are the boundary layer size after equilibrium is reached in the numerical simulation of Eq. (3). Dashed lines are obtained from iterating map (8).

Fig. 7 shows the iteration of map (6) for the FKPP model, that is, $f(u_i) = u_i(1 - u_i)$. In particular, Fig. 7(a) shows the case when $\alpha \neq D$, corresponding to the bi-dimensional map where the dots exemplify a starting point (u_k, u_{k-1}) and its resulting value u_{k+1} . Fig. 7(b) illustrates the map iteration when $\alpha = D$. The unidirectional coupling case perfectly illustrates the fact that the heteroclinic orbit requires an infinite number of iterations, as predicted for $\epsilon = 0$ and, therefore, in agreement with the convective regime. For any other value of ϵ , the number of iterations to reach $u_i = 0.5$ ($a/2 = 0.5$ for FKPP model Eq. (3)) is finite, and can be determined numerically avoiding the singularity in the number of steps as one approaches fixed points. Finally, one can compare the results obtained for the boundary layer size N_c using direct numerical integration of the motion equations versus the map iteration approach, showing a perfect agreement as illustrated in Fig. 7(c).

6. Analytical approximation for N_c

A naive treatment of the problem suggests that (supported by its local linear dynamics and dimensional analysis) the time in which a perturbation $u = \epsilon$ reaches a $O(1)$ value corresponds to $\tau \sim -\log(\epsilon)$. This, together with a characteristic speed $v(D, \alpha)$ gives a characteristic length $L_c \sim -v(D, \alpha) \log(\epsilon)$. Indeed, for $\alpha > \alpha_c$ one can fit the boundary layer size obtained by direct numerical simulations with the formula

$$N_c(D, \alpha, \epsilon) = c(D, \alpha) - K(D, \alpha) \log(\epsilon). \tag{9}$$

The previous Eq. (9) is found by solving the linear dynamics of the map Eq. (6). To achieve this, one can define $p_i = u_i - u_{i-1}$ and solve equation (6) for u_{i+1} . Remind that most steps of the iteration occur around the fixed point $u = 0$ and, for this reason, we linearize the dynamics around this point, obtaining

$$p_i = u_i - u_{i-1}, \tag{10}$$

$$u_{i+1} = \frac{-f'(0)u_i + (D + \alpha)p_i}{D - \alpha} + u_i. \tag{11}$$

Replacing $p_i = Ab^i$, $u_i = Aqb^i$, and imposing $u_0 = \epsilon$, one finds

$$u_i = \epsilon b^i \equiv \begin{cases} \epsilon \left(\frac{D-1/2}{D-\alpha} - \sqrt{\left(\frac{D-1/2}{D-\alpha}\right)^2 - \frac{D+\alpha}{D-\alpha}} \right)^i & \text{if } \alpha_c < \alpha < D, \\ \epsilon \left(\frac{D-1/2}{D-\alpha} + \sqrt{\left(\frac{D-1/2}{D-\alpha}\right)^2 - \frac{D+\alpha}{D-\alpha}} \right)^i & \text{if } \alpha > D. \end{cases} \tag{12}$$

Then, replacing $i = N_c$ and $u_{N_c} = 1$ in Eq. (12) and solving for N_c (taking into account both signs of the different intervals), one obtains

$$N_c = -\frac{\log \epsilon}{\log b} \equiv -K(D, \alpha) \log \epsilon. \tag{13}$$

The previous relation allows obtaining the main features of N_c , that is, the logarithmic relation with ϵ and the constant of proportionality $K(D, \alpha)$. From here, one can deduce that the constant $c(D, \alpha)$ of Eq. (9) accounts for corrections to the linearized map approximation and the election of u_{N_c} . One can see from Fig. 8 that for $\alpha > \alpha_c$ the value of $c(D, \alpha)$ is a small constant. A perfect agreement between the predicted and numerically obtained values for $K(D, \alpha)$ is also seen.

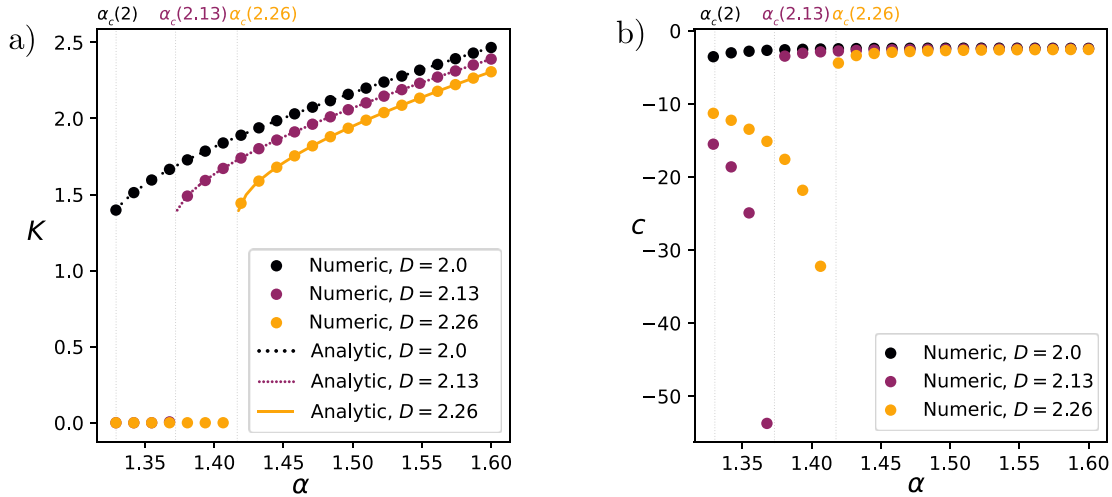


Fig. 8. Giant boundary layer analytic characterization. Values of the fitting constants K and c for the boundary layer size N_c from formula (9). Panels (a) and (b) show K and c as a function of α , respectively. Dots correspond to the numerically obtained values. Dashed lines are the analytical prediction of Eq. (13). The vertical gray lines highlight the value of $\alpha_c(D)$.

7. Contrast with boundary layers in reciprocally coupled systems

The theory developed in the previous sections predicts the boundary layer size of nonreciprocally coupled nonlinear systems for $\alpha > \alpha_c = \sqrt{f'(0)D - f^2(0)}/4$. Moreover, it is depicted how these boundary layers diverge in size in the limit as $\epsilon \rightarrow 0$, a phenomenon not observed in systems with reciprocal coupling. These systems exhibit boundary layers of finite size independently of the mismatch value ϵ . For $\epsilon \ll 1$, the effect of the mismatch is negligible, and the boundary layer size is mainly determined by the reciprocal coupling coefficient D . As mentioned earlier, in the continuum limit, the dependence of the boundary layer size on D_{diff} is a square root function, that is, $L_c \sim \sqrt{D_{diff}}$. Then, considering that $L_c = N_c l_0$ and $D_{diff} = D l_0^2$, it is straightforward to obtain that $N_c^{reciprocal} \sim \sqrt{D}$. To deduce the previous relationship analytically, we consider the continuum limit of Eq. (2) in the steady-state regime

$$0 = \sin u + D_{diff} \partial_{xx} u, \tag{14}$$

which is a Newton-type equation for a fictitious particle of equivalent mass D_{diff} , and it has a closed-form solution $u(x)$ even if we change the force-like term, $\sin u$, by another well-behaved function. Imposing the boundary condition $u(0) = \epsilon$ and, after straightforward calculations, the solution to Eq. (14) is

$$\Lambda(u) - \Lambda(\epsilon) = \sqrt{\frac{2}{D_{diff}}} x, \tag{15}$$

where $\Lambda(u) = \sqrt{2} \operatorname{arctanh}[\sin(u/2)]$. Defining the position of the boundary layer following the previous section, i.e., $u(L_c) = 1$ and replacing it in Eq. (15), one immediately obtains $L_c = \sqrt{D_{diff}[\Lambda(1) - \Lambda(\epsilon)]}/\sqrt{2}$. Note that this expression describes fairly well the boundary layer size N_c , despite it was calculated in the continuum limit. Hence, the ratio between the size of the boundary layers when $\alpha > \alpha_c$ and $\alpha = 0$ is

$$S \equiv \frac{N_c(\alpha, D, \epsilon)}{N_c^{reciprocal}(D, \epsilon)} = \sqrt{2} \frac{K(\alpha, D) \log \epsilon^{-1}}{\sqrt{D}[\Lambda(1) - \Lambda(\epsilon)]}. \tag{16}$$

Note that $\Lambda(1)$ is a constant of order one that changes for each model (different reaction functions f). It is easy to check that as $\epsilon \rightarrow 0$, then $S \rightarrow \infty$, i.e., there is a giant boundary layer. Additionally, S only grows with α because $K(\alpha, D)$ monotonically increases as function of it, see Fig. 8(a). Fig. 9 illustrates the dependence of $N_c^{reciprocal}(D, \epsilon)$ obtained by direct numerical simulations of Eq. (2). In particular, panel (a) shows the dependence $N_c^{reciprocal} \sim \sqrt{D}$ and panel (b) exhibits that the dependence on ϵ is negligible. Additionally, panels (c), (d), and (e) show boundary layers, with $\alpha = 0$, $\alpha < \alpha_c$, and $\alpha > \alpha_c$, respectively, in a chain of coupled pendula obtained numerically from Eq. (2). From this chart, one can see that for $\alpha < \alpha_c$, the boundary layer is composed of a few pendulums, contrasted with the case $\alpha > \alpha_c$ in which a counter-intuitively large number of pendulums form a giant boundary layer.

8. Discussion and perspectives

The results obtained in this work describe a phenomenon that is unavoidable numerically and experimentally. The observation of giant boundary layers arises when a system has the following three ingredients: individual (local) nonlinear

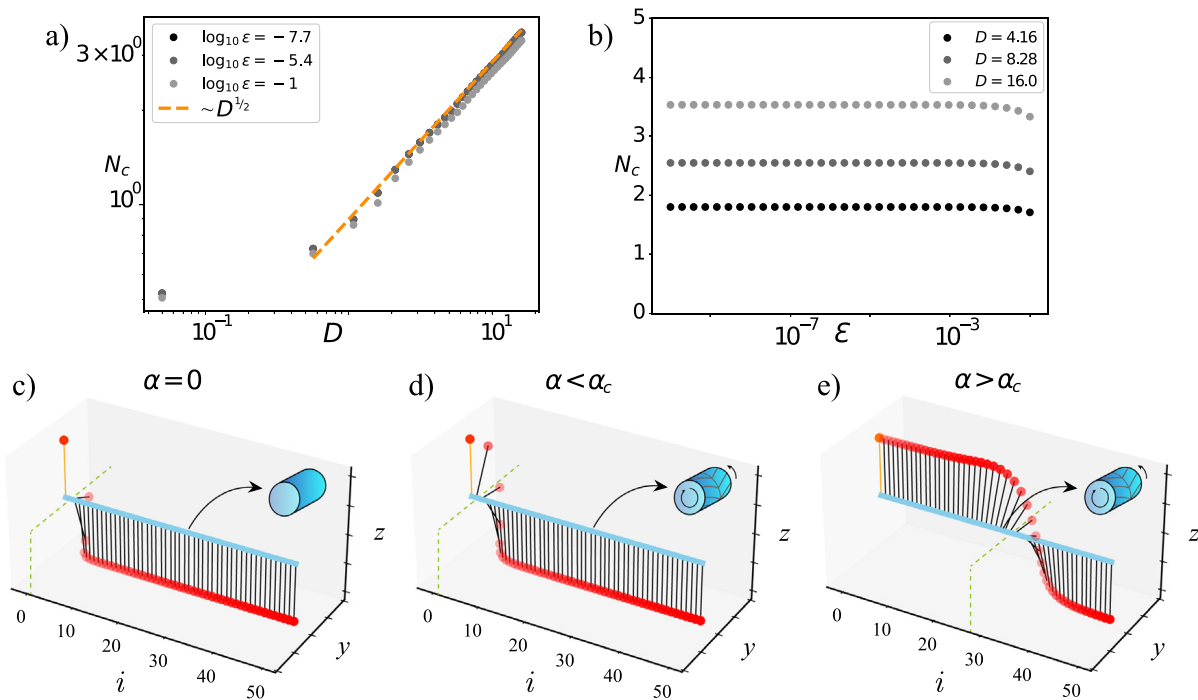


Fig. 9. Characterization of boundary layers in the reciprocal case and visual comparison with giant boundary layers. (a) and (b) illustrate the dependence of the boundary layer size in the reciprocal case on the parameters, $N_c(\alpha = 0, D, \epsilon) \equiv N_c^{\text{reciprocal}}(D, \epsilon)$. (c), (d), and (e) show a visual representation of the boundary layers in a chain of pendulums with data obtained from direct numerical integration of Eq. (2) with $D = 1$, $\epsilon = 10^{-3}$. α values are $\alpha = 0$, $\alpha = 0.5$, and $\alpha = 2$, respectively.

dynamics, nonreciprocal coupling, and boundary conditions. In particular, nonlinear dynamics and nonreciprocal coupling allow for front propagation and the absolute-convective instability. The latter generates counter-intuitive dynamics when $\alpha > \alpha_c$, allowing the propagation of upside-down pendulums over their intuitively rest state due to gravity. Moreover, if one considers particular boundary conditions, the giant boundary layer naturally arises.

Boundary conditions may be hard to handle in real-life situations. Furthermore, experiments are generally subjected to fluctuating drivers that may be stochastic or deterministic. These fluctuations can also be responsible for the formation of giant boundary layers even if a perfect match at the boundary is considered ($\epsilon = 0$). In this case, the boundary layer size is dynamic, i.e., it fluctuates around a mean value. The characterization of giant boundary layers subjected to fluctuations is a work in progress. Boundary layers are affected by the fluctuations, and also other downstream states generated by the nonreciprocal coupling, such as patterns [21].

Another aspect to have in mind is that, similar to what happens in experiments, boundary conditions can be challenging to handle in numerical simulations. Both experiments and simulations have finite accuracy in the relevant variables of the problem under study. Throughout this work, we highlight the numerical difficulties that can arise when handling arbitrarily small numbers (due to the finite representation of real numbers in computers). Moreover, the limit $\epsilon \rightarrow 0$ is not accessible, and its application to numerical simulation leads to wrong results (a finite-size giant boundary layer), where only the analytical theory enlightens the correct solution (an infinite-size boundary layer, or equivalently, the observation of the convective instability).

Finally, the implications that giant boundary layers could have in real systems are variable and difficult to visualize. The giant boundary layer composes a region in which the equilibrium states of the nonlinear systems are virtually swapped. The true equilibrium of the system is reached for the individual elements u_i only for $i > N_c$. For example, in the chain of pendulums, inside the giant boundary layer, there is stored potential energy that would release once the nonreciprocity is turned off; in the case of arrays of coupled Josephson junctions, the giant boundary layer would produce a steady current peaking at the boundary layer position. Finally, in the propagation of populations, the giant boundary layer connects large regions of negligible population with regions at full capacity. If the population modeled is a disease, a large portion of healthy individuals could be held inside the giant boundary layer thanks to nonreciprocity. Further development of nonreciprocal elements will unveil the impact of the naturally arising giant boundary layers.

9. Conclusions

Based on a theoretical and numerical study, we predict how “imperfections” in the value of boundary conditions induce the frustration of absolute-convective instability. This establishes a boundary layer whose size is determined with the map

iteration of the resulting equation for the equilibrium. These boundary layers are observed to use almost all of the space, even for small imperfections; thus, we call them giant boundary layers. The method proposed allows us to determine the giant boundary layer size or the mismatch in the boundary condition. Our findings show that this mismatch in the boundary condition for nonreciprocally coupled systems is relevant in controlling the boundary layer size. Moreover, the results are expected to hold for a great variety of discrete systems exhibiting *FKPP* fronts with broken spatial reflection symmetry.

We highlight that the difficulty of using computers to perform a numerical calculation is the finite resolution. The maps describing the equilibria of the systems cannot reach all the values in the real axis, making truncation errors. In other words, even if one initializes the system without mismatch at the boundary, in a finite number of steps, a boundary layer will appear in numerical simulations.

CRedit authorship contribution statement

D. Pinto-Ramos: Methodology, Formal analysis, Investigation, Writing – original draft, Writing – review & editing. **K. Alfaro-Bittner:** Conceptualization, Validation, Visualization, Writing – original draft, Writing – review & editing. **M.G. Clerc:** Conceptualization, Supervision, Writing – original draft, Writing – review & editing. **R.G. Rojas:** Supervision, Writing – original draft, Writing – review & editing.

Declaration of competing interest

The authors declare that they have no known competing financial interests or personal relationships that could have appeared to influence the work reported in this paper.

Data availability

Data will be made available on request.

Acknowledgments

D.P.-R. acknowledges the financial support of ANID National Ph.D. scholarship 2020-21201484. M.G.C. acknowledges the financial support of ANID-Millennium Science Initiative Program-ICN17_012 (MIRO) and FONDECYT project 1210353. R.G.R acknowledges DI INVESTIGACIÓN INNOVADORA INTERDISCIPLINARIA PUCV 2021 N° 039.409/2021. Nanoiónica: Un enfoque interdisciplinario. K.A.-B. thanks to URJC Grants n° 2023/00004/001M2978 and 2023/00005/016M3033.

References

- [1] Kamien RD, Selinger JV. Order and frustration in chiral liquid crystals. *J Phys: Condens Matter* 2001;13(3):R1–22.
- [2] Marić V, Giampaolo SM, Kuić D, Franchini F. The frustration of being odd: How boundary conditions can destroy local order. *New J Phys* 2020;22(8):083024.
- [3] Goodby JW, Slaney AJ, Booth CJ, Nishiyama I, Vuijk JD, Styring P, et al. Chirality and frustration in ordered fluids. *Mol Crystals Liquid Crystals Sci Technol A. Mol Crystals Liquid Crystals* 1994;243(1):231–98.
- [4] Schlichting H, Gersten K. *Boundary-layer theory*. Springer; 2016.
- [5] Prandtl L. Über Flüssigkeitsbewegung bei sehr kleiner Reibung. In: *Verhandl. III. Heidelberg*, Teubner, Leipzig: Internat. Math.-Kong.; 1904, p. 484–91, 1904.
- [6] Garratt JR. Review: The atmospheric boundary layer. *Earth-Sci Rev* 1994;37(1):89–134.
- [7] Fisher RA. The wave of advance of advantageous genes. *Ann Eugen* 1937;7(4):355–69.
- [8] Kolmogorov A, Petrovskii I, Piskunov N. A study of the equation of diffusion with increase in the quantity of matter, and its application to a biological problem. *Byul Moskovskogo Gos Univ* 1937;1:1–25.
- [9] Alfaro-Bittner K, Clerc MG, García-Ñustes MA, Rojas RG. π -Kink propagation in the damped Frenkel-Kontorova model. *Europhys Lett* 2017;119(4):40003.
- [10] Alfaro-Bittner K, Clerc MG, Rojas RG, García-Ñustes MA. Traveling wave into an unstable state in dissipative oscillator chains. *Nonlinear Dynam* 2019;98(2):1391–402.
- [11] Van Saarloos W. Front propagation into unstable states. *Phys Rep* 2003;386(2–6):29–22.
- [12] Braun OM, Kivshar YS. *The Frenkel-Kontorova model: concepts, methods, and applications*. Springer Science & Business Media; 2013.
- [13] Jara-Schulz G, Ferré MA, Falcón C, Clerc MG. Noise-induced kink propagation in shallow granular layers. *Chaos Solitons Fractals* 2020;134:109677.
- [14] Remoissenet M. *Waves called solitons: concepts and experiments*. Springer Science & Business Media; 2013.
- [15] Maxwell JC. On the calculation of the equilibrium and stiffness of frames. *Phil Mag Ser* 1864;27(182):294–9.
- [16] Nassar H, Yousefzadeh B, Fleury R, Ruzzene M, Alù A, Daraio C, Norris AN, Huang G, Haberman MR. Nonreciprocity in acoustic and elastic materials. *Nat Rev Mater* 2020;5:667–85.
- [17] Williamson IA, Minkov M, Dutt A, Wang J, Song AY, Fan S. Integrated nonreciprocal photonic devices with dynamic modulation. *Proc IEEE* 2020;108(10):1759–84.
- [18] Chen Z, Peng Y, Li H, Liu J, Ding Y, Liang B, Zhu X-F, Lu Y, Cheng J, Alù A. Efficient nonreciprocal mode transitions in spatiotemporally modulated acoustic metamaterials. *Sci Adv* 2021;7(45):eabj1198.
- [19] Coulais C, Sounas D, Alù A. Static non-reciprocity in mechanical metamaterials. *Nature* 2017;542(7642):461–4.
- [20] Brandenbourger M, Locsin X, Lerner E, Coulais C. Non-reciprocal robotic metamaterials. *Nature Commun* 2019;10(1):1–8.
- [21] Pinto-Ramos D, Alfaro-Bittner K, Clerc MG, Rojas RG. Nonreciprocal coupling induced self-assembled localized structures. *Phys Rev Lett* 2021;126:194102.

- [22] Murray JD. *Mathematical biology: I. An introduction*. 3rd ed.. New York, NY: Springer; 2002.
- [23] Souнас DL, Caloz C, Alù A. Giant non-reciprocity at the subwavelength scale using angular momentum-biased metamaterials. *Nature Commun* 2013;4(1):1–7.
- [24] Trias E, Mazo JJ, Falo F, Orlando TP. Depinning of kinks in a Josephson-junction ratchet array. *Phys Rev E* 2000;61(3):2257.
- [25] Nelson DR, Shnerb NM. Life and death near a windy oasis. *J Math Biol* 2000;41(1):1–23.
- [26] Cantrell RS, Cosner C, Lou Y. Movement toward better environments and the evolution of rapid diffusion. *Math Biosci* 2006;204(2):199–214.
- [27] Cosner C. Reaction-diffusion-advection models for the effects and evolution of dispersal. *Discrete Contin Dynam Syst* 2014;34(5):1701.
- [28] Clerc MG, Elías RG, Rojas RG. Continuous description of lattice discreteness effects in front propagation. *Phil Trans R Soc A* 2011;369(1935):412–24.
- [29] Chomaz JM. Absolute and convective instabilities in nonlinear systems. *Phys Rev Lett* 1992;69(13):1931.
- [30] Mollison D. Spatial contact models for ecological and epidemic spread. *J R Stat Soc Ser B Stat Methodol* 1977;39(3):283–313.
- [31] Clerc MG, Coulibaly S, Garcia-Ñustes MA, Zárata Y. Dissipative localized states with shieldlike phase structure. *Phys Rev Lett* 2011;107:254102.
- [32] Aubry S, Le Daeron PY. The discrete Frenkel-Kontorova model and its extensions: I. Exact results for the ground-states. *Physica D* 1983;8(3):381–422.
- [33] Ott E. *Chaos in dynamical systems*. Cambridge University Press; 2002.

Complements and perspectives on Part I

1. Nonreciprocal coupling effects on fronts into the stable state

Having analyzed fronts into the unstable state, we proceed to provide some perspectives in the case of fronts into the stable state. Consider our nonreciprocal Frenkel-Kontorova model discussed in part I, including a homogeneous forcing so the homogeneous states have different energies. Equivalently, restricting only to two stable equilibria (instead of the infinite ones of the Frenkel-Kontorova model), one can employ without loss of generality the imperfect pitchfork normal form coupled to nearest neighbors nonreciprocally, reading

$$\dot{A}_k = \eta + \epsilon A_k - A_k^3 + (D - \alpha)(A_{k+1} - A_k) - (D + \alpha)(A_k - A_{k-1}). \quad (2.1)$$

Similar to the methods in the continuum limit, one would like to find traveling solutions of the form $A_k(t) = A(k - x_0(t))$; but, as we already know, different to the continuum limit fronts solutions in a discrete grid will exhibit hopping dynamics. We make the surprising remark that the front shape $A_k(t)$ can be obtained from a continuous profile $A(z = k - x_0(t))$, provided its position is known. For different definitions of the position, a continuous profile $A(z)$ from which the state of the system cells $A_k(t)$ is obtained at all times. This will allow us to deduce an implicit formula for the velocity, which considers the hopping dynamics of the front, getting an expression for the velocity free of fitting parameters (implicitly depending on the front solution and the system parameters).

The front position

First, we define the position of the front. A straightforward definition is to set a threshold value A_T such that if $A_{i_0}(t) < A_T < A_{i_0+1}(t)$, then we define

$$x_0 = i_0 + \frac{A_T - A_{i_0}(t)}{A_{i_0+1}(t) - A_{i_0}(t)}. \quad (2.2)$$

This is just the continuous value x_0 at which the linear interpolated profile $A_i(t)$ reaches A_T . The front profile at different times as a function of $z = k - x_0(t)$ is seen in figure 2.1. One notices that the fronts do not translate as a rigid object. One can choose any value of A_T between the values of the equilibria. We selected $A_T = 0$ for simplicity.

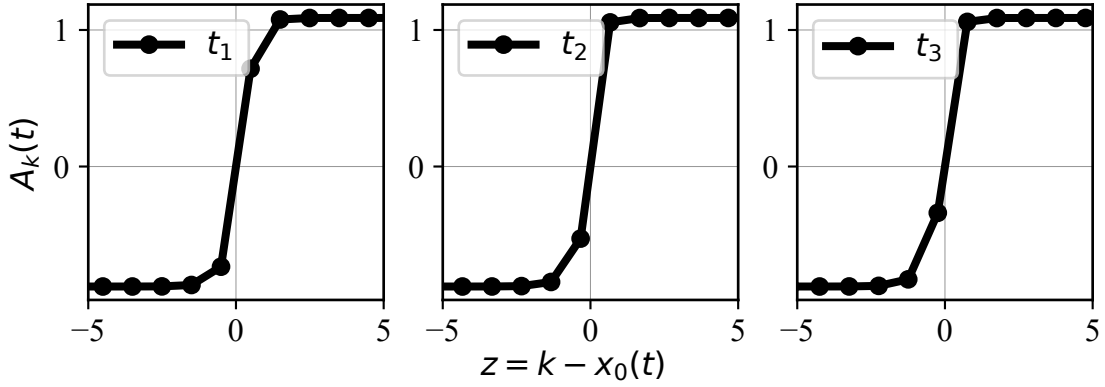


Figure 2.1: Fronts into the stable state obtained from numerical integration of Eq. 2.1. The three panels show the solutions $A_k(t)$ as a function of $z = k - x_0(t)$ at 20 seconds (simulation time) intervals. Parameters correspond to $\eta = 0.2$, $\epsilon = 1$, $D = 0.1$, $\alpha = -0.05$.

The continuous profile characterizing the discrete front

Surprisingly, if one collects several time snapshots of the points $(z, A_k(t))$, we notice that the cloud of points collected converges to a continuous function, as illustrated in figure 2.2. This fact allows for a formal change of variables in equation 2.1

$$\dot{A}_k(t) = -\dot{x}_0 A'(z).$$

We can convert the N equations (N is the number of cells composing the system) to the following expression

$$\begin{aligned} -\dot{x}_0 A'(z) &= (\eta + \epsilon A(z) - A^3(z)) + (D - \alpha)(A(z+1) - A(z)) - (D + \alpha)(A(z) - A(z-1)), \\ &= f(A(z)) + (D - \alpha)(A(z+1) - A(z)) - (D + \alpha)(A(z) - A(z-1)). \end{aligned}$$

It is important to note that the previous expression still composes N equations, as $z = k - x_0(t)$. We eliminate the spatial dependence multiplying by $A'(z)$ and summing over the N elements, then

$$-\dot{x}_0 = \frac{\sum_k (f(A(z)) + (D - \alpha)(A(z+1) - A(z)) - (D + \alpha)(A(z) - A(z-1))) A'(z)}{\sum_k (A'(z))^2}. \quad (2.3)$$

Since the profile $A(z)$ can be extracted from the numerical simulations, we can use the formula 2.3 to obtain the velocity exactly. To close the problem and obtain an explicit solution for $\dot{x}_0(t)$, we need to provide an analytical solution $A(z)$ for the continuous front profile. Solutions $A(z)$ are currently being explored, following methods similar to the ones proposed by Flach and Kladko [41].

The Peierls-Navarro potential revisited

We can explore the expression 2.3 further. One can note that the front profile $A(z = k - x_0(t))$ gives the same value if we consider the transformation $k \rightarrow k + 1$ and $x_0(t) \rightarrow x_0(t + \tau) = x_0(t) + 1$ for some τ . τ is the time the front position takes to advance one cell. Now, we need to consider expressions of the type $\sum_k^N A^m(z = k - x_0(t))$; for a fixed time t , we are

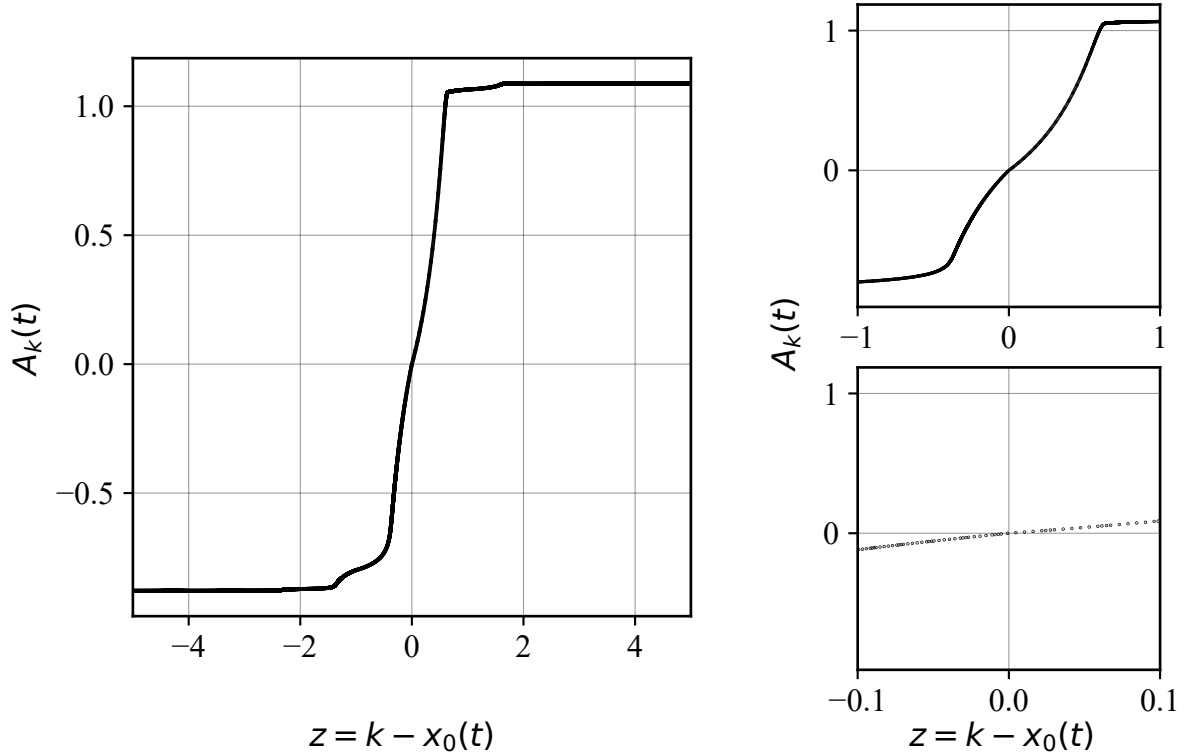


Figure 2.2: The continuous front profile obtained by collecting the solution points $(z, A_k(t))$. The left panel shows the profile around the position of the front, and the right insets show more detail up to the points forming the continuous function; 500 time snapshots were used to construct this figure. Parameters correspond to $\eta = 0.2$, $\epsilon = 1$, $D = 0.1$, $\alpha = -0.05$.

choosing N points from the continuous profile $A(z)$ and summing them. These N points will repeat (except by the two at the ends of the chain) again after the time τ , or equivalently, when a shift in one cell occurs. Then, the expression 2.3 can be either considered a periodic function of t (of period τ) or a periodic function of x_0 (of period one). This allows writing x_0 in a Fourier series representation; moreover, the numerator and denominator in Eq. 2.3 can be expressed in Fourier series separately. The denominator reads

$$\left(\sum_k A'(z)^2 \right) (x_0) = A_0 [A'(z)^2] + \sum_{n=1}^{\infty} \left(A_n [A'(z)^2] \cos(2\pi n x_0) + B_n [A'(z)^2] \sin(2\pi n x_0) \right) \quad (2.4)$$

Which we compactly write

$$\left(\sum_k A'(z)^2 \right) (x_0) = M_0 + \sum_n M_n. \quad (2.5)$$

The Fourier coefficients have interesting formulas reading

$$\begin{aligned}
A_n [A'(z)^2] &= \int_0^1 \left(\sum_{k=1}^N A'(z)^2 \right) \cos(2\pi k x_0) dx_0 \\
&= \sum_{k=1}^N \int_0^1 A'(z)^2 \cos(2\pi n x_0) dx_0 \\
&= \sum_{k=1}^N \int_{i-1}^i A'(z)^2 \cos(2\pi n(i-z)) dz \\
&= \int_0^N A'(z)^2 \cos(2\pi n z) dz,
\end{aligned} \tag{2.6}$$

and

$$\begin{aligned}
B_n [A'(z)^2] &= \int_0^1 \left(\sum_{k=1}^N A'(z)^2 \right) \sin(2\pi n x_0) dx_0 \\
&= - \int_0^N A'(z)^2 \sin(2\pi n z) dz.
\end{aligned} \tag{2.7}$$

They could be reduced to integrals of the continuous profile characterizing the front dynamic. Similar expressions follow for the numerator terms. The local term $f(A)$ contributes

$$\left(\sum_k f(A) A'(z) \right) (x_0) = A_0 [f(A) A'(z)] + \sum_{n=1}^{\infty} (A_n [f(A) A'(z)] \cos(2\pi n x_0) + \tag{2.8}$$

$$B_n [f(A) A'(z)] \sin(2\pi n x_0)). \tag{2.9}$$

Note that $A_0 [f(A) A'(z)] = -(V(z \rightarrow \infty) - V(z \rightarrow -\infty)) = -\Delta V$, with $V(A) = -\int^A f(x) dx$. The front speed has a contribution proportional to the free energy density, similar to fronts in the continuum limit; however, due to the grid, it has periodic contributions. Then, we compactly write

$$\left(\sum_k f(A) A'(z) \right) (x_0) = -\Delta V + \sum_n F_n(x_0). \tag{2.10}$$

One can compute the rest of the terms as follows

$$\begin{aligned}
D \int [A(z+1) + A(z-1) - 2A(z)] A'(z) dz &= 2D \int [(\cosh \partial_z - 1)A(z)] A'(z) dz \\
&= 2D \int \left(\left[\frac{1}{2!} \partial_z^2 + \frac{1}{4!} \partial_z^4 + \dots \right] A(z) \right) A'(z) dz \\
&= 2D \left[\frac{1}{2!} (A'(z))^2 \Big|_0^N - \frac{1}{4!} 2 (A''(z))^2 \Big|_0^N + \dots \right] \\
&= 0.
\end{aligned} \tag{2.11}$$

To obtain the last line, one uses the fact that the profile $A'(z)$ and its derivatives vanish at the ends of the front. Similarly

$$\begin{aligned}
\alpha \int [A(z+1) - A(z-1)] A'(z) dz &= 2\alpha \int ([\sinh \partial_z] A(z)) A'(z) dz \\
&= 2\alpha \int \left[A'(z) + \frac{1}{3!} A'''(z) + \dots \right] \partial_z u_F(z) dz \\
&= 2\alpha \int \left[(A'(z))^2 - \frac{1}{3!} (A''(z))^2 + \frac{1}{5!} (A'''(z))^2 - \dots \right] dz \\
&\equiv 2\alpha (M_0 + M_\alpha), \tag{2.12}
\end{aligned}$$

where $M_0 = \int (A'(z))^2 dz$ repeats in the denominator of equation 2.3. Then, we can write for equation 2.3 the following

$$-\dot{x}_0 = \frac{-\Delta V - 2\alpha(M_0 + M_\alpha) + \sum_{n=1} F_n(x_0)}{M_0 + \sum_{n=1} M_n(x_0)}. \tag{2.13}$$

We can compare what is obtained using implicit formula 2.13 using four terms in each summation with the plain truth of computing $\dot{x}_0(t)$ numerically in figure 2.3. What remains

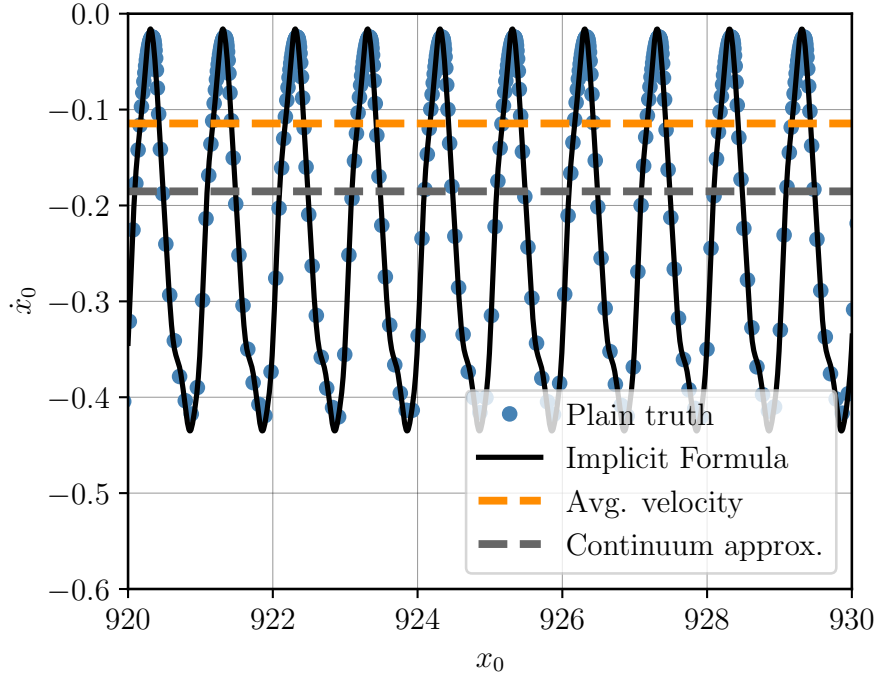


Figure 2.3: Velocity of the front as a function of the position $\dot{x}_0(x_0)$. The graph shows the plain truth, the implicit formula 2.13 using four terms, the average velocity, and the approximation to the average velocity from the continuum limit (corresponding to just the first term in each series of 2.13). Parameters correspond to $\eta = 0.2$, $\epsilon = 1$, $D = 0.1$, $\alpha = -0.05$.

an open question is to obtain an approximation or explicit solution to the continuous front profile $A(z)$ characterizing the discrete cells at all times. If that is possible, then the formula 2.13 would become explicit, and the velocity would be written as a function of the system parameters only (in this case η , ϵ , D , and α).

2. The effect of fluctuations

Up to now, we have studied deterministic systems. However, it is often realistic to include fluctuations that are approximately random. The idea that a fluctuating force acts on a particle is not new and comes down to Brown (who observed such a phenomenon on suspended particles) and Einstein (who revealed an explanation using statistical mechanics); see [60] and references therein. It models the several degrees of freedom we ignore when writing effective equations for the macroscopic world.

In general dynamical systems, the fluctuating terms do not necessarily refer to the ignored motion of microscopic particles, but can model other complex processes that produce small perturbations in timescales that are not relevant. To the terms that we allow to fluctuate *randomly*, we call them *noise* (in reality, the random process is an idealization, as a real random process would generate a discontinuous forcing and the dynamical system would not be well defined anymore). For example, noise terms are used to model the current fluctuations in several electrical components.

Noise effects in a chain

We analyze the effect of including noise terms in the dynamics of front propagation into the unstable state. For this, we propose the inclusion of *additive noise* to the overdamped nonreciprocal Frenkel Kontorova model introduced in chapter 1, reading

$$\dot{A}_k = \sin A_k + (D - \alpha)(A_{k+1} - A_k) - (D + \alpha)(A_k - A_{k-1}) + \sqrt{\Gamma}\xi_k(t). \quad (2.14)$$

The terms $\xi_k(t)$ are fluctuating functions that drive each cell independently and Γ is the noise intensity level. In our idealization of these random forces, we assume they have a Gaussian distribution and are delta-correlated in time, a *white noise* [60]. This means that there are not memory effects in the fluctuations. The same analysis could be performed with analogous models such as the imperfect pitchfork normal form nonreciprocally coupled 2.1. One readily notes that a fluctuating force driving each cell will rapidly put them out of their unstable equilibrium value, destroying the mechanism for propagating fronts into the unstable state. Indeed, fronts into the unstable state collapse; the dynamic is controlled by fronts into the stable state and the self-assembled pattern states already reported. The phase diagram is shown in figure 2.4, which can be compared to the one in the deterministic case reported in chapter 1. The phenomena displayed are types of *noise sustained structures*; they occur whenever an unstable state can be stabilized in the laboratory reference frame due to advective transport [61]. This condition coincides with the absolute-convective threshold; then, noise will constantly drive the system out of the convective unstable equilibrium, releasing different structures. At the same time, the fixed boundaries sustain that process permanently [61].

3. Experimental perspectives

A system available in the laboratory of robust phenomena at the physics department of the University of Chile can exhibit nonreciprocal coupling. There, coherent light from a laser interacts with a nematic liquid crystal in a planar cell (the $x - y$ plane) with planar boundary

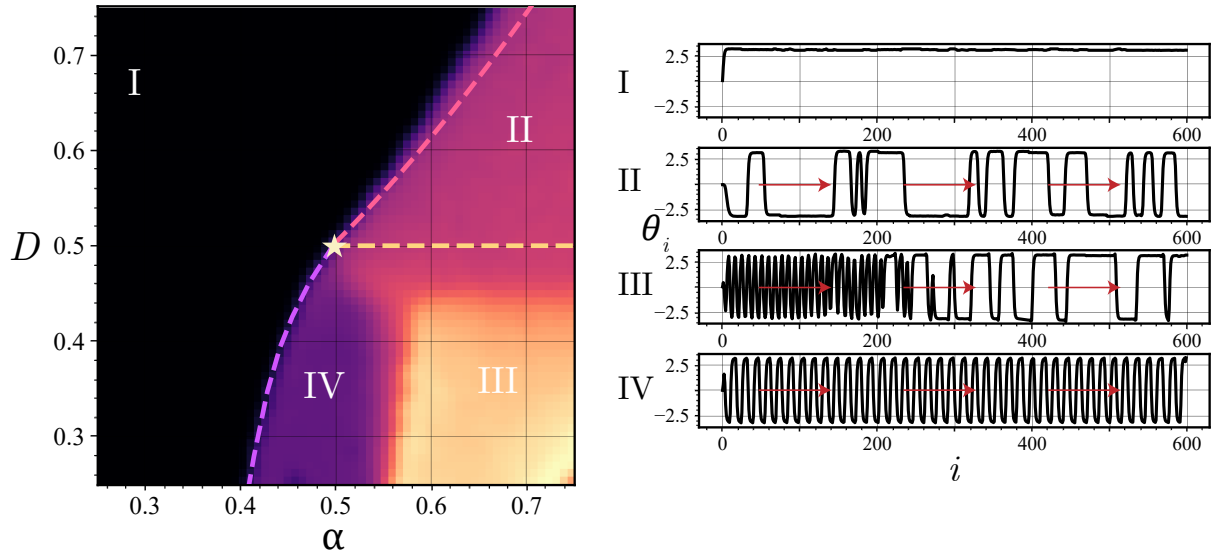


Figure 2.4: Phase diagram of Eq. (2.14). Four regions could be differentiated by analyzing the order parameters corresponding to the domain walls' total and boundary layer sizes. Region I corresponds to the homogeneous, stable state. II shows permanent domain wall dynamics with thin boundary layers. In region III, the boundary layer enlarges drastically before the permanent domain wall dynamics. In region IV, stable self-assembled patterns can be observed. Continuous lines are a guide to the eye for the bifurcation places. Dashed lines correspond to analytical curves obtained from using the front into the unstable state velocity expression.

conditions. The reflected light having a phase modulation due to the orientation of the liquid crystal molecules $\theta(x, y)$ is subjected to an optical path with different operations and later returned to force the liquid crystal cell, which we call the feedback beam. If the feedback beam suffers a translation or rotation $\delta \mathbf{r}$ in the transverse coordinates (x, y) to propagation, then, points (x, y) of the device will be coupled with points $(x, y) + \delta \mathbf{r}$ of the feedback beam, which is just a nonlinear transformation of the orientation field $\theta(x, y)$. When discretized, such a coupling is described by an adjacency matrix with a nonvanishing anti-symmetric part; thus, it corresponds to a nonreciprocal coupling.

The liquid crystal light valve

A scheme of the liquid crystal cell subjected to the laser beam and the feedback beam, called liquid crystal light valve (LCLV), is given in figure 2.5. A HeNe laser beam is collimated and passed through a spatial light modulator (SLM). This allows us to have the desired wavefront $\mathbf{E} \approx \mathbf{E}(x, y)e^{i(kz - \omega t)}$ dictated by what we program in the SLM. A polarizer beam splitter (PBS) selects a polarization direction for the *reading* light incoming from the left to the liquid crystal light valve (LCLV) device. At this stage, the device is subjected to a sinusoidal voltage difference V_0 between the plates. The effective electric field will realign the molecules of the liquid crystal in an average direction that we call the device axis (which at rest corresponds to the x direction). The nematic molecules correspond to a birefringent medium and is characterized by its ordinary and extraordinary refractive indexes n_o and n_e . The device axis is, on average (across the light propagation direction) tilted at an angle θ with respect to the axis x , which we let also vary in the transversal direction $\theta(x, y)$. At

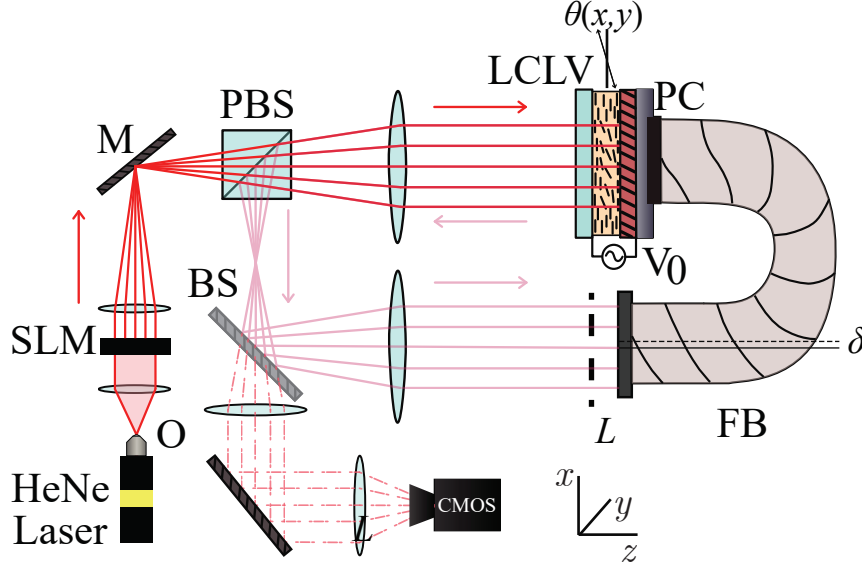


Figure 2.5: Experimental setup in which nonreciprocal coupling is possible.

the left end of the LCLV, the laser beam is divided into the ordinary and extraordinary beams, having different phase velocities; once crossing two times the device thickness d , they recombine and interfere according to the accumulated phase difference inside the birefringent medium. If we let

$$\mathbf{E}(x, y) = \begin{pmatrix} \cos \psi_1 \\ \sin \psi_1 \end{pmatrix}$$

describe the polarized beam (with a polarizer making an angle ψ_1 with x) coming at the left of the LCLV. Then, the beam will cross two times the thickness d of the LCLV, and the components will obtain a phase difference of $\beta = 2dk(n(\theta) - n_o)$. $n(\theta)$ is the effective refractive index reading [62, 63]

$$n(\theta) = \frac{\cos^2 \theta}{n_e} + \frac{\sin^2 \theta}{n_o}.$$

For small difference of the refraction indexes $\Delta n = n_e - n_o$, $n(\theta) \approx n_o + \Delta n \cos^2 \theta$. Then, $\beta = 2dk\Delta n \cos^2 \theta$ and

$$\mathbf{E}_{ref.}(x, y) = \begin{pmatrix} e^{-i\beta} \cos \psi_1 \\ \sin \psi_1 \end{pmatrix}$$

is the reflected beam that will enter again at the PBS. A portion of the reflected beam can pass the PBS up to the second beam splitter (BS), which continues through a lens and allows to image the light electric field at the LCLV in the plane marked with a dashed line. Lastly, it enters the feedback loop closed by the high-resolution optical fiber bundle (FB). This light corresponds to $\mathbf{E}_{ref.}$ passing through a second polarizer with angle $\psi_2 = \psi_1 - \pi/2$. The light in the image plane (dashed line in figure 2.5) has the form

$$\mathbf{E}_{im.}(x, y) = \begin{pmatrix} \cos^2 \psi_2 & \cos \psi_2 \sin \psi_2 \\ \cos \psi_2 \sin \psi_2 & \sin^2 \psi_2 \end{pmatrix} \begin{pmatrix} e^{-i\beta} \cos \psi_1 \\ \sin \psi_1 \end{pmatrix}.$$

The field $\mathbf{E}_{im.}(x, y)$ reaches the FB, which is translated with respect to the propagation axis a distance δ in the x direction. The FB may not necessarily be placed in the image plane; therefore, there is a distance L in which the beam is subjected to free propagation in space. Therefore, the electric field reaching the photoconductor, which we call the feedback field, is

$$\mathbf{E}_{feedback}(x, y) = e^{-i\frac{L}{2k}\nabla^2}\mathbf{E}_{im.}(x + \delta, y).$$

It is important to mention that we neglect all the retardation effects due to the negligible length of the total optical path.

The dynamics of the orientation field

One can see that the orientation field θ is related to the feedback field $\mathbf{E}_{feedback}$ via a complex transformation. We remind that θ is affected by the effective electric field inside the LCLV. When the feedback beam reaches the photoconductor (PC), the potential difference between the plates is modified, and the effective electric field the molecules perceive is

$$E_{eff} = \frac{\Gamma V_0}{d} + \frac{\alpha}{d} |\mathbf{E}_{feedback}|^2,$$

where α is a phenomenological constant describing the PC effect and Γ the impedance of the LCLV. We have assumed that the voltage frequency is much faster than the characteristic frequency response of the LCLV reorientation. A model for the orientation angle θ considering these arguments has been proposed [4, 24], we modify it to include the translation of the FB yielding a nonreciprocal coupling for the orientation field θ as follows

$$\tau \frac{\partial \theta}{\partial t} = l^2 \nabla^2 \theta - \theta + \frac{\pi}{2} \left(1 - \sqrt{\frac{\Gamma V_{FT}}{\Gamma V_0 + \alpha |e^{\delta \frac{\partial}{\partial x}} e^{-i\frac{L}{2k}\nabla^2} \mathbf{E}_{im.}|^2}} \right). \quad (2.15)$$

τ and l are characteristic time and length scales to be experimentally determined [4, 24, 64]. This equation is valid if the effective electric field inside the cell E_{eff} exceeds the Fréedericksz threshold E_{FT} . Otherwise the equation reads $\tau \partial_t \theta = l^2 \nabla^2 \theta - \theta$.

Building a discrete grid of dynamical systems

Employing the SLM, it is possible to shape the amplitude of the feedback beam (and the reading one). For example, one can create a circular mask to force only a small region of the LCLV to be illuminated. This can represent our singular cell, which exhibits bistability and thus fronts into the stable state can be analyzed. Then, we create an array of individual cells separated by enough distance such that perturbations can propagate between cells. Figure 2.6 illustrates this behavior. Panel a) shows the single cells created thanks to the SLM exhibiting bistability for the output light intensity versus the applied voltage, which show a controllable propagation velocity. Panel b) corresponds to the numerical propagation velocity of the stable state for the right and left ends using a prototypical model; nonreciprocal coupling becomes evident as the speeds of counter-propagating fronts are not equivalent. Work is being developed in deriving an effective discretized equation that accounts for the dynamics of the 'light cells' induced, see figure 2.6 a). Preliminary results show that a method similar to a tight binding reduction could be useful when considering the modulation produced by the SLM in the governing equations for θ . Then, applying the formulas derived for fronts into the stable state, we can gain insight into the result shown in figure 2.6 b); indeed, linear

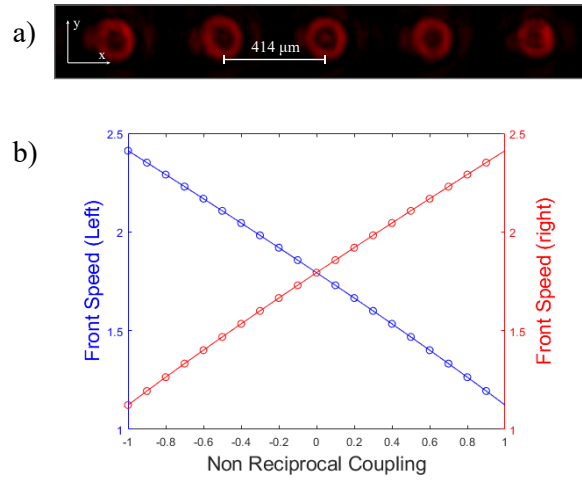


Figure 2.6: Preliminary experimental results. a) shows the single cells induced. b) shows measures of the propagation velocity against the non-reciprocity parameter in a numerical prototypical model. Experimental measures are thanks to Manuel Díaz, Amaru Moya, and Pedro Aguilera, collaborators in this work.

nonreciprocal coupling (δ) will produce a term $\dot{x}_0 \propto -\Delta V + \delta + \dots$, that would explain the linear behavior of the velocity. Efforts are being directed to develop the experiment.

Part II: Nucleation of defects and interfaces

The front solutions discussed until now break the homogeneity of space; thus, they are called *defects* in various contexts involving many particle or field theories. Defects are robust and require considerable energy (or effort) to destroy; however, they easily interact and annihilate with other appropriate defects in order to recover the homogeneity of space in the system. In one dimensional scalar fields, these defects are topological as they can not be destroyed with smooth transformations of the variable.

Think for example, in the fronts into the stable state we analyzed in the previous chapters. Forgetting about the boundary effects, in principle one can arrange the front in two ways: I) From left to right, we could connect the stable state, say u_1 , with the other stable state u_2 . II) From left to right, we could do the opposite and connect from u_2 to u_1 through space. These two fronts are equally valid, however they can be characterized by a special number which we call the *charge*. When analyzing the spatial variations of our order parameter (in the example we are talking about, u), we see that we can attribute a charge to each one according to $Q = \int_{-\infty}^{\infty} \partial_x u dx / |u_2 - u_1| = \pm 1$. The sign depends on which front we insert in the formula for Q , option I, or II.

The idea is simple, charge will be conserved. Starting with an homogeneous order parameter $Q = 0$; we can not create a front with charge $Q = 1$ without at the same time inducing the front with charge $Q = -1$. This simple idea has been widely generalized to higher dimensions and even defined in other parameter spaces apart from the configuration one [65]. Interestingly, in more than one dimension, this notion persists. To define the topological defect charge, we usually encircle the defect with an adequate surface, summing the order parameter variations [23].

Defects in general can be nucleated when quenching the system such that strong enough variations in the parameters could induce the formation of defect pairs. In the following chapters, we will analyze the formation of defects due to stochastic fluctuations in chains of bistable unit cells, as well as topological defects of the vortex type appearing in the description of the liquid crystal director tilt and the envelope function of patterns of vegetation biomass. In the latter example we develop a mathematical model including the natural nonreciprocal coupling among the vegetation biomass field participants and examine the response of vortices to this form of nonreciprocity in the coupling.

Chapter 3

Thermal Fluctuations Induced Emergence of Umbilical Defects in Nematic Liquid Crystal Cells (Nonequilibrium Thermodynamics and Fluctuation Kinetics. vol 208. pp 303-312)

Umbilical defects in nematic liquid crystals (NLC) correspond to singularities in the orientation of the nematic order director. They correspond to a natural system in which the topological defects of the vortex type arise. The system can be easily quenched thanks to a voltage applied across the NLC cell, and vortices are easily nucleated due to thermal fluctuations.

In this chapter, we study theoretically, numerically, and experimentally the nucleation of vortices in NLC cells. We compute the average number of vortices created as a function of the control parameters, experimentally corresponding to the voltage applied and the temperature of the cell. These trends are analytically deduced based on a linear theory around the post-quench unstable stable. Finally, a similar analysis is performed for defects in one-dimensional systems; a prototypical bistable chain analog to the previously introduced Frenkel Kontorova model is used for its generality and the presence of defects in it. The linear theory based on the quench of parameters produces fair results both for defects described by a one-dimensional scalar field, and a two-dimensional complex field.

Thermal Fluctuations Induced Emergence of Umbilical Defects in Nematic Liquid Crystal Cells



Esteban Aguilera, Marcel G. Clerc, David Pinto-Ramos, and Valeska Zambra

Abstract Optical vortices are equally relevant for their fundamental features as beams with topological properties and applications in image processing, telecommunications, optical tweezers, and quantum information. The interaction of light beams with umbilical defects in liquid crystal cells is a natural source of optical vortices. Here we investigate, experimentally and theoretically, the mechanisms of the matter vortices that appear in liquid crystal cells and establish statistical laws that govern them. Based on an adequate stochastic equation, the law for the number of nucleated vortices as a function of anisotropy, bifurcation parameter, and noise level intensity is set. Experimental results show a fair agreement with the theoretical findings.

1 Introduction

In the last decades, a great effort has been developed to understand spiral output light beams about their axis of propagation, *orbital angular momentum of light or optical vortex* [1–5]. These beams have a donut-like structure, that is, the beam intensity cancels out into the center, generating a phase singularity into the envelope. Around the point of zero intensity, the phase distribution forms an N -armed spiral, with N being the topological charge [2–6]. These optical vortices have aroused interest from both the fundamental and applied point of view. The photonic applications ranging from optical tweezers [7–9], enhancement of astronomical images [10], quantum computation [11], wavefront sensors [12], and data transmission [13]. From a fundamental point of view, the interchange of angular momentum between light and matter has attracted attention (see the collected articles [5] and references therein).

E. Aguilera · M. G. Clerc (✉) · D. Pinto-Ramos · V. Zambra
Departamento de Física and Millenium Institute for Research in Optics, Facultad de Ciencias Físicas y Matemáticas, Universidad de Chile, Casilla 487-3, Santiago, Chile
e-mail: marcel@dfi.uchile.cl

D. Pinto-Ramos
e-mail: david.pinto@ug.uchile.cl

© The Author(s), under exclusive license to Springer Nature Switzerland AG 2022
L. Brenig et al. (eds.), *Nonequilibrium Thermodynamics and Fluctuation Kinetics*,
Fundamental Theories of Physics 208,
https://doi.org/10.1007/978-3-031-04458-8_15

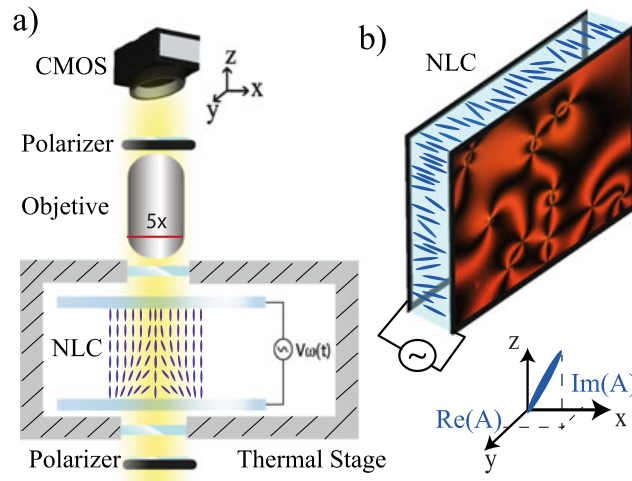


Fig. 1 Vortex nucleation in a nematic liquid crystal cell with homeotropic anchoring and negative dielectric anisotropic constant. **a** Schematic representation of the experimental setup. The rods are a schematic representation of the average orientations of molecules. **b** Snapshot of a vortex gas obtained in the nematic liquid crystal (NLC) cell. The lower inset is a schematic representation of the director and complex amplitude

Different methods have been used to generate optical vortices based on diffractive elements [14], deformable mirrors [15], holograms [16], spiral phase plates [17], nanostructured glass plates [18], and helical structures of liquid crystals [19–22]. In most of these methods, the light beam interacts with a material object which has a helicity. Hence, to control the optical vortex, it is important to have an adequate alignment between the light beam, the target, and the geometry of it. In the case of liquid crystals with photosensitive walls, the light induces a vortex in the matter (umbilical defect), with which interacts, generating an optical vortex [22–24]. These matter vortices are described by a nonlinear amplitude equation, the Ginzburg-Landau equation with real coefficients [24–26]. When a sufficiently large electric field is applied to a nematic liquid crystal cell with homeotropic anchoring and negative anisotropic dielectric constant, a gas of umbilical defects emerge (see Fig. 1). These defects later begin to be annihilated by pairs with opposite charges [27]. The emergence process and statistical rules that this phase singularity gas followed have not been established.

Using a liquid crystal cell with homeotropic anchoring and negative dielectric anisotropic constant under the effect of a transverse voltage allows us to study the statistical laws that govern the nucleation of vortices. Theoretically, based on a stochastic amplitude equation, the Ginzburg Landau equation with additive noise, we establish the law for the number of nucleated vortices as a function of anisotropy, bifurcation parameter, and intensity of the noise level. Experimental results show a qualitative agreement with the theoretical findings.

2 Experimental Setup

Nematic liquid crystals are nonlinear optical media [27, 28], composed by rod-like molecules that have a preferential orientational order but not a positional one. This state of matter shares features of solids and liquids, such as fluidity and birefringence. Introducing a liquid crystal inside a cell, that is, it is sandwiched between two confining layers, the molecules oriented according to anchoring conditions. Homeotropic anchoring is characterized by molecules that are oriented orthogonal to cell walls, as illustrated in Fig. 1. If the dielectric anisotropic constant of the liquid crystal is negative, when applying a vertical electric field, the molecules tend to orient orthogonal to it. This generates different domains connected by orientation defects or phase singularities, *matter vortices* [27]. Let us consider a 15 μm thick cell, (SB100A150uT180 manufactured by Instec), filled with nematic liquid crystal LC BYVA-01 (Instec) with dielectric anisotropy $\epsilon_a = -4.89$, birefringence $\Delta n = n_e - n_o = 0.1$, rotation viscosity $\gamma = 204$ mPas, splay and bend elastic constant, respectively, $K_1 = 17.65$ pN and $K_3 = 21.39$ pN. This sample is placed inside a thermal control chamber (Linkam LTS420), which in turn is inserted inside a microscope (Leica DM2700P), in between the crossed linear polarizers. The thermal control chamber allows precise control of the temperature of the liquid crystal cell. Likewise, cross-polarizer microscopy enables an efficient vortex detection methodology. Figure 1a shows a schematic representation of the experimental setup. To monitor the images a CMOS camera is connected to the microscope. A sinusoidal voltage with a frequency 100 Hz is applied to the sample.

Maintaining the temperature at 26 $^{\circ}\text{C}$, the voltage is turned on, the dynamics of vortex nucleation and annihilation are recorded. Figure 2a depicts the temporal evolution of the observed umbilical defects. To figure out vortex evolution, we have considered a voltage sweep between 9.0 Vpp and 30.0 Vpp. Likewise, keeping the voltage at 15 Vpp it is switched on and sweeping the temperature between 25 and 80 $^{\circ}\text{C}$, the dynamics of vortex nucleation is analyzed. From the chart in Fig. 2a, we infer that there is an abrupt process of vortex nucleation. The vortices are subsequently annihilated by pairs of opposite charges, generating a coarsening process characterized by a power law [29].

3 Theoretical Description

To shed light on the vortex nucleation mechanisms, theoretically, we consider the liquid crystal cell close to orientational instability, which is described by the stochastic Ginzburg-Landau equation [24–26]

$$\partial_t A = \mu A - |A|^2 A + \nabla^2 A + \delta \partial_{\eta, \eta} \bar{A} + \sqrt{T} \zeta(\mathbf{r}, t), \quad (1)$$

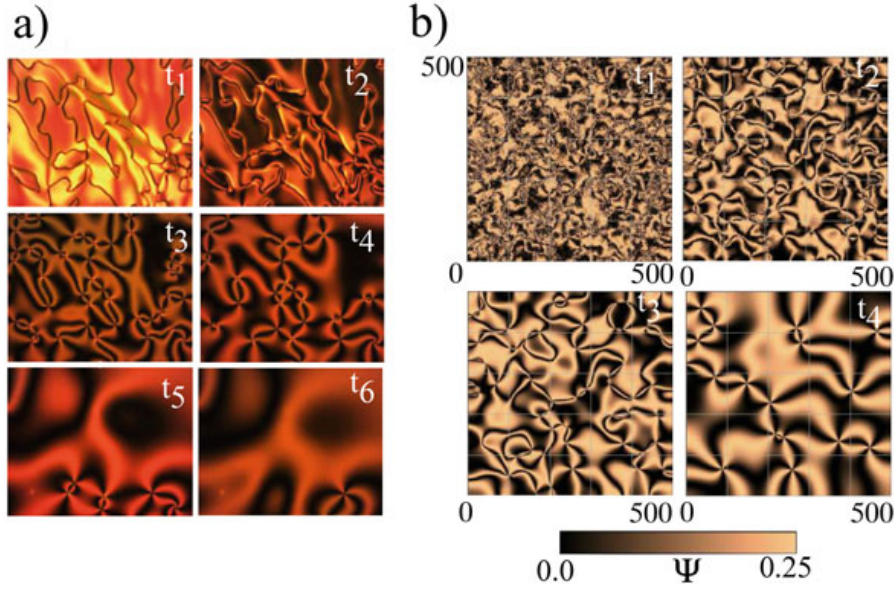


Fig. 2 Nucleation and evolution of umbilical defects in a liquid crystal cell driven by an electric field. **a** Experimental temporal evolution of the number of vortices as a function of time at fixed driven voltage of 15 Vpp, 100 Hz, and 26 °C. Right panel account for a temporal sequence of snapshots of the liquid crystal cell driven by an electric field and constant temperature ($t_1 < t_2 < t_3 < t_4 < t_5 < t_6$). **b** Numerical temporal sequence of polarized field $\Psi(\mathbf{r}, t) = \text{Re}(A)\text{Im}(A)$ obtained by the numerical simulations of the stochastic Ginzburg-Landau equation (1) with $\mu = 1.0$, $\delta = 0.0$, and $T = 0.01$

where the complex field $A(\mathbf{r}, t)$ accounts for the amplitude of the critical mode that describes the deviation of the molecular director with respect to the vertical direction. \bar{A} accounts for the complex conjugate of A . μ is the bifurcation parameter that is proportional to the voltage minus the critical Fréederickz voltage [24–26]. For a planar anchoring cell, the Fréederickz voltage has the analytical expression $V_{FT} \equiv 2\pi\sqrt{K_3/\epsilon_a}$. $\delta = K_1 - K_2/(K_1 + K_2)$ is the parameter that accounts for the anisotropy of the liquid crystal elastic constants. $\partial_\eta \equiv \partial_x + i\partial_y$ is a differential operator, note that the Laplacian operator satisfies $\nabla^2 = \partial_\eta\bar{\eta}$. $\zeta(\mathbf{r}, t)$ is a Gaussian white noise with zero mean value $\langle \zeta \rangle = 0$ and correlation $\langle \zeta(\mathbf{r}, t)\bar{\zeta}(\mathbf{r}', t') \rangle = \delta(t - t')\delta(\mathbf{r} - \mathbf{r}')$ and T accounts for the noise intensity level. The main sources of noise are inherent thermal fluctuations and electrical fluctuations on the applied voltage.

For $\mu \leq 0$, the Ginzburg-Landau Eq. (1) has a null solution $A = 0$ as a stable equilibrium, which corresponds to molecules that are not reoriented, *homeotropic state*. For $\mu > 0$, this state becomes unstable by means of a degenerate pitchfork bifurcation, giving rise to the appearance of vortices [26]. Figure 2b illustrates the emergence of vortices in model Eq. (1) as a result of stochastic fluctuations. As in the experiment, the uncontrollable fluctuations, noise, nucleates a large number of vortices that are subsequently annihilated by opposite pairs. Numerical simulations were implemented using a finite differences scheme in space that uses a centered

stencil of five grid points with Runge-Kutta order-4 algorithm, with a 500×500 points grid temporal step $dt = 0.0004$, and Neumann boundary conditions.

4 Vortices Nucleation Law

Numerically, we have monitored the number of vortices at a given instant as a function of the bifurcation parameter μ . Figure 3a summarizes the results found. From these charts, we infer that the number of vortices grows linearly with the bifurcation parameter. Likewise, we note that this behavior is not modified when we change the anisotropy δ . Experimentally, we have studied the number of umbilical defects in a given instant as a function of the voltage applied to the sample. We found that the number of defects grows with the voltage, which shows a qualitative agreement with the numerical results (cf. Fig. 3b). The defects emerge from the homeotropic state, due to the inherent fluctuations of the system. Hence, to understand the nucleation process, we approximate Eq. (1) by its deterministic linear part and consider the Fourier mode decomposition $A = A_k e^{\sigma t + i(k_x x + k_y y)}$, after straightforward calculations we get

$$\sigma = \mu - k_x^2(1 + \delta) - k_y^2(1 - \delta) \pm 2i\delta k_x k_y, \quad (2)$$

where $Re(\sigma)$ is the growth rate mode, k_x and k_y are wavenumber modes in the horizontal directions. $\sigma(k_x, k_y) > 0$ corresponds to unstable modes. Notice that white noise is characterized by excited in the same manner all modes. The boundary conditions and geometric dimensions of the system determine the wavenumbers of modes. For simplicity, if we consider periodic boundary conditions and a square domain wavenumbers take the form $k_x = 2\pi n/L$ and $k_y = 2\pi m/L$, where L is the size of the box and $\{n, m\}$ are integer numbers. The nodes of the spatial modes correspond to zeros of the amplitude; that is, these nodes correspond to phase singularities (vortex germ) for the modes. The mode with the maximum number of vortices (nodes) corresponds to $\sigma = 0$. To calculate this maximum number of vortices, we proceed by calculating the number of modes in one direction [$\sigma(n^c, k_y = 0) = 0$], then in the other [$\sigma(k_x = 0, m^c) = 0$], and finally we determine the maximum number of vortices (nodes) by

$$N = n^c m^c = \left(\frac{L}{2\pi}\right)^2 \frac{\mu}{\sqrt{(1 - \delta^2)}}. \quad (3)$$

Note that all other unstable modes have a similar expression (3) multiplied by a proper fraction. Hence, the number of vortices is proportional to the previous expression, in particular to the bifurcation parameter, which is consistent with what is observed numerically and experimentally (see Fig. 3). Likewise, we note that this result predicts that the number of vortices diverges when δ^2 tends to 1. This limit physically corresponds when one of the elastic constants diverges. This phenomenon is observed when there is a nematic-smectic transition ($K_2 \rightarrow \infty$) when the temper-

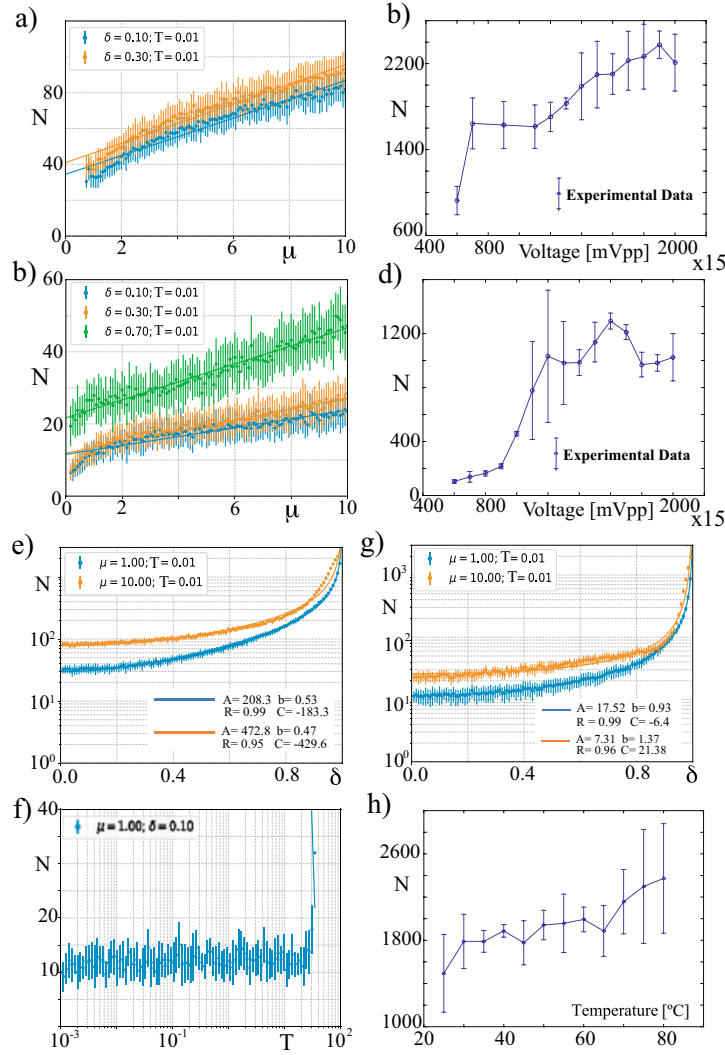


Fig. 3 The number of defects in a given instant as a function of the bifurcation parameter and noise level intensity. The number of defects obtained from numerical simulations of Eq. (1) with $\mu = 1.0$ at $t = 12$ (a) and $t = 60$ (b). The points with a bar account for mean value and standard deviation obtained after carrying out for each parameter 30 realizations. Number of umbilical defects as a function of the driven voltage at $t = 0.5$ s (c) and $t = 1.0$ s (d). The points with a bar account for mean value and standard deviation obtained after five experimental realizations. The number of defects in a given instant as a function of the anisotropic parameter δ , obtained from numerical simulations of Eq. (1) at $t = 12$ (e) and $t = 60$ (g). The points with a bar account for mean value and standard deviation obtained after carrying out for each parameter 20 realizations. The continuous curves were obtained using the fitting function $N = A/(1 - \delta^2)^b + C$. The simulations and fitting parameters are specified in insets. (f) The number of defects in a given moment as a function of the noise intensity level T . (h) Umbilical defects number as a function of the temperature after 1 s of applying voltage 15 Vpp. The points with a bar account for mean value and standard deviation obtained after carrying out 5 experimental realizations

ature is modified [30]. However, the liquid crystal under our study does not present this type of transition. The study of vortex nucleation near the nematic-smectic transition is in progress. Figure 3 shows the number of vortices at a given moment as a function of the anisotropy parameter δ . This result shows an excellent agreement with expression (3). To study its trend, we have used a more general fitting function of the form $N = A/(1 - \delta^2)^b + C$, which can take into account the nonlinear effects and errors of the vortex measurement method. From charts, Fig. 3e and g, note that the critical exponent b evaluated at higher times is dissimilar that predicted theoretically. This effect is due to the fact that nonlinear terms begin to play a non-negligible role. Experimentally, we cannot carry out a similar analysis since elastic anisotropy δ is determined by intermolecular interactions that we cannot control.

Formula (3) does not depend on the noise intensity level T . Indeed, the number of vortices (nodes) does not depend on the intensity of the noise, however, their presence is essential to stimulate unstable modes. Figure 3f shows that effectively the noise intensity level does not affect the number of vortices created. When the noise intensity is very large the linear theory is no longer valid and the vortices are no longer related to the linear modes (see Fig. 3f). To investigate experimentally fluctuations that are inherent to our system, we have estimated the number of vortices in a given moment as a function of temperature. Figure 3h summarizes the results found. We deduce that there is a tendency to increase the number of vortices with temperature. The increase in temperature has a double effect; on the one hand, it increases the thermal fluctuations and, in turn, modifies the elastic constants [30]. This last effect is responsible for the increase found in the number of vortices.

5 Noise Induced Emergence of One-Dimensional Defect

The above vortex creation mechanism should be a general defect creation mechanism not only valid in two dimensions. A simple dimensionless model of one-dimensional topological defects is the dissipative bistable model, which has the form [31, 32]

$$\partial_t u = \epsilon u - u^3 + \partial_{xx} u + \sqrt{T} \chi(t, x), \quad (4)$$

where $u(x, t)$ is a one-dimensional order parameter, ϵ is a bifurcation parameter, $\chi(x, t)$ is a Gaussian white noise with zero mean value $\langle \chi \rangle = 0$ and correlation $\langle \chi(x, t) \chi(x', t') \rangle = \delta(t - t') \delta(x - x')$ and T accounts for the noise intensity level.

The bistable model Eq. (4) is monostable for negative ϵ , where the equilibrium is $u = 0$. When the bifurcation parameter changes sign and becomes positive, the system exhibits a pitchfork bifurcation, giving rise to two equilibria $u = \pm\sqrt{\epsilon}$, bistable regime. In the latter regime, when inhomogeneous initial conditions are considered, it exhibits domain walls between these two equilibria. These domain walls are usually called kinks (u_k) or anti-kinks. Analytically these solutions have the form

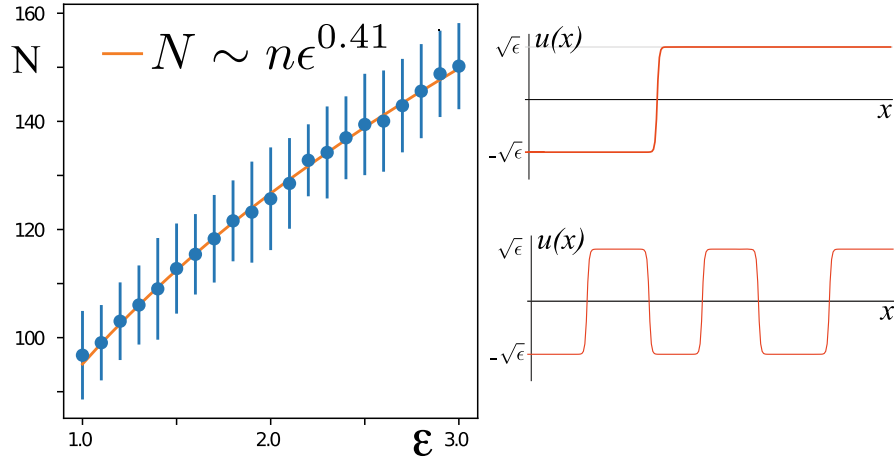


Fig. 4 Number of kinks in a given instant as a function of the bifurcation parameter ϵ obtained from numerical simulations of Eq. (5) with $T = 0.1$ at $t = 20$. The points with a bar account for mean value and standard deviation obtained after carrying out for each parameter 80 realizations. The continuous curves were obtained using the fitting function $N = n\epsilon^{0.41}$. The right panels account for a single kink and a kink gas, respectively

$$u_k(x) = \pm\sqrt{\epsilon} \tanh\left(\frac{\sqrt{\epsilon}}{2}(x - x_0)\right), \quad (5)$$

where x_0 accounts for the position of the wall, that is, $u_k(x = x_0) = 0$. Figure 4 shows a single kink and several kink-antikink interacting solutions obtained from numerical simulations of Eq. (4). These solutions are topological since the destruction of a kink employing continuous deformations can only be carried out through collision with an anti-kink.

When one starts from the null state, the fluctuations induce the emergence of kink and anti-kink solutions. Figure 4 shows how the number of kinks changes as a function of the bifurcation parameter. This chart shows that the number of kinks grows with the bifurcation parameter and has a power law. To understand this law, we use the same strategy used to understand vortex emergence. Then we linearize the dynamics around the zero value $u = 0$, which takes the form

$$\partial_t u = \epsilon u + \partial_{xx} u + \sqrt{T} \chi(t, x) \quad (6)$$

Introducing the ansatz $u = u_0 e^{ikx + \sigma t}$, in the above equation, one get $\sigma = \epsilon - k^2$. Hence, all unstable modes are in range $\{-\sqrt{\epsilon}, \sqrt{\epsilon}\}$. The unstable mode with the most spatial oscillations corresponds to $k = \sqrt{\epsilon} = 2\pi N/L$, where N is the number of domains or zeros of the critical mode. Then the number of domains satisfies the relation

$$N = \frac{L\sqrt{\epsilon}}{2\pi}. \quad (7)$$

Therefore, the number of defects or kinks grows with the square root of the bifurcation parameter. Figure 4 shows a good qualitative agreement. However, the

exponent is different. The possible origin of the difference between the exponent of analytical expression (7) and the numerical one (see Fig. 4) are nonlinearities and interactions of kinks and anti-kink that are neglected in the analytical expressions.

6 Conclusion and Remarks

Despite many studies of vortices for their fundamental properties associated with particles with topological properties and their interest in various technological applications such as telecommunications, image processing, and optical tweezers, the study of vortex nucleation in real physical systems had not been addressed to our knowledge. Based on linear theory and stochastic fluctuations, we can establish that the matter vortices are a consequence of the different excited unstable spatial modes. The above is summarized by formula (3) multiplied by a constant that accounts for the effect of all unstable modes. Therefore, we can establish that the number of vortices grows proportionally to the bifurcation parameter; it is inverse to the square of the elastic anisotropy and does not depend on the level of the noise intensity. Experimental observations show a qualitative agreement with theoretical findings. Vortices are an intrinsically nonlinear nature phenomenon; however, we show that the generic mechanism for creating vortices in nature is based on a simple linear theory of critical spatial modes.

Experimental imperfections, which give rise to heterogeneous parameters, can be a source of vortices. To understand the effect of heterogeneities is by modifying the linear problem to non-constant coefficients, which generates that the modes depend on these coefficients. The inclusion of this type of effect is in progress. Likewise, in the developed theory, we have considered no spatial and temporal correlation, white noise; however, the system may exhibit spatial correlations, which may be a consequence of the anisotropic elastic coupling of the liquid crystal. This type of correlation may be responsible for exciting some privileged unstable nodes, *stochastic resonance*. The inclusion of these phenomena can improve the simplified description presented.

Acknowledgements The authors thank Enrique Calisto, Michal Kowalczyk, and Michel Ferre for fructified discussions. MGC acknowledges financial support from ANID–Millennium Science Initiative Program–ICN17_012, Millennium Institute for Research in Optics and FONDECYT 1210353 project.

References

1. A. Sommerfeld, Lectures on theoretical physics, in *Optics*, vol. IV (Academic Press, New York, 1954)
2. J. Nye, M. Berry, Dislocations in wave trains. *Proc. R. Soc. Lond. A* **336**, 6–31 (1974)
3. L. Allen, M.W. Beijersbergen, R.J.C. Spreeuw, J.P. Woerdman, Orbital angular momentum of light and the transformation of Laguerre-Gaussian laser modes. *Phys. Rev. A* **45**, 8185 (1992)
4. M.S. Soskin, M.V. Vasnetov, in *Progress in Optics*, vol. 42, ed. by E. Wolf, (Elsevier, 2001), p. 219

5. L. Allen, S.M. Barnett, M.J. Padgett, *Optical Angular Momentum* (CRC Press, 2003)
6. L.M. Pismen, *Vortices in Nonlinear Fields* (Oxford Science, 1999)
7. D.G. Grier, A revolution in optical manipulation. *Nature* **424**, 810–816 (2003)
8. V.G. Shvedov, A.V. Rode, Y.V. Izdebskaya, A.S. Desyatnikov, W. Krolikowski, Y.S. Kivshar, Giant optical manipulation. *Phys. Rev. Lett.* **105**, 118103 (2010)
9. M. Padgett, R. Bowman, Tweezers with a twist. *Nat. Photonics* **5**, 343–348 (2011)
10. F. Tamburini, G. Anzolin, G. Umbriaco, A. Bianchini, C. Barbieri, Overcoming the Rayleigh criterion limit with optical vortices. *Phys. Rev. Lett.* **97**, 163903 (2006)
11. H.H. Arnaut, G.A. Barbosa, Orbital and intrinsic angular momentum of single photons and entangled pairs of photons generated by parametric down-conversion. *Phys. Rev. Lett.* **85**, 286–289 (2000)
12. K. Murphy, C. Dainty, Comparison of optical vortex detection methods for use with a Shack-Hartmann wavefront sensor. *Opt. Express* **20**, 4988–5002 (2012)
13. J. Wang, J.-Y. Yang, I.M. Fazal, N. Ahmed, Y. Yan, H. Huang, Y. Ren, Y. Yue, S. Dolinar, M. Tur, A.E. Willner, Terabit free-space data transmission employing orbital angular momentum multiplexing. *Nat. Photonics* **6**, 488–496 (2012)
14. V.Y. Bazhenov, M.V. Vasnetsov, M.S. Soskin, Laser beams with screw dislocations in their wavefronts. *JETP Lett.* **52**, 429–431 (1990)
15. R.K. Tyson, M. Scipioni, J. Viegas, Generation of an optical vortex with a segmented deformable mirror. *Appl. Opt.* **47**, 6300–6306 (2008)
16. J. Arlt, K. Dholakia, L. Allen, M.J. Padgett, The production of multiringed Laguerre-Gaussian modes by computer-generated holograms. *J. Mod. Opt.* **45**, 1231–1237 (1998)
17. M.W. Beijersbergen, L. Allen, H.E.L.O. van der Veen, J.P. Woerdman, Astigmatic laser mode converters and transfer of orbital angular momentum. *Opt. Commun.* **96**, 123–132 (1993)
18. M. Beresna, M. Gecevicius, P.G. Kazansky, T. Gertus, Radially polarized optical vortex converter created by femtosecond laser nanostructuring of glass. *Appl. Phys. Lett.* **98**, 201101 (2011)
19. D. Voloschenko, O.D. Lavrentovich, Optical vortices generated by dislocations in a cholesteric liquid crystal. *Opt. Lett.* **25**, 317319 (2000)
20. L. Marrucci, C. Manzo, D. Paparo, Optical spin-to-orbital angular momentum conversion in inhomogeneous anisotropic media. *Phys. Rev. Lett.* **96**, 163905 (2006)
21. E. Brasselet, N. Murazawa, H. Misawa, S. Juodkakis, Optical vortices from liquid crystal droplets. *Phys. Rev. Lett.* **103**, 103903 (2009)
22. R. Barboza, U. Bortolozzo, G. Assanto, E. Vidal-Henriquez, M.G. Clerc, S. Residori, Vortex induction via anisotropy stabilized light-matter interaction. *Phys. Rev. Lett.* **109**, 143901 (2012)
23. R. Barboza, U. Bortolozzo, G. Assanto, E. Vidal-Henriquez, M.G. Clerc, S. Residori, Harnessing optical vortex lattices in nematic liquid crystals. *Phys. Rev. Lett.* **111**, 093902 (2013)
24. R. Barboza, U. Bortolozzo, M.G. Clerc, S. Residori, E. Vidal-Henriquez, *Adv. Opt. Photonics* **7**, 635 (2015)
25. T. Frisch, S. Rica, P. Couillet, J.M. Gilli, Spiral waves in liquid crystal. *Phys. Rev. Lett.* **72**, 1471–1464 (1994)
26. M.G. Clerc, E. Vidal-Henriquez, J.D. Davila, M. Kowalczyk, Symmetry breaking of nematic umbilical defects through an amplitude equation. *Phys. Rev. E* **90**, 012507 (2014)
27. S. Chandrasekhar, *Liquid Crystals* (Cambridge University, New York, 1977)
28. L.M. Blinov, *Structure and Properties of Liquid Crystals* (Springer, New York, 2011)
29. V. Zambra, M.G. Clerc, R. Barboza, U. Bortolozzo, S. Residori, Umbilical defect dynamics in an inhomogeneous nematic liquid crystal layer. *Phys. Rev. E* **101**, 062704 (2020)
30. C. Chevallard, M.C. Clerc, Inhomogeneous Fréedericksz transition in nematic liquid crystals. *Phys. Rev. E* **65**, 011708 (2001)
31. J. Garcia-Ojalvo, J.M. Sancho, *Noise in Spatially Extended Systems* (Springer, New York, 1999)
32. D.A. Contreras, M.G. Clerc, Internal noise and system size effects induce nondiffusive kink dynamics. *Phys. Rev. E* **91**, 032922 (2015)

Chapter 4

Topological defects law for migrating banded vegetation patterns in arid climates (Science Advances 9 (31), eadf6620)

Once we have studied the topological defect of the vortex type regarding their nucleation, that is, how they born, we are left with the question of what happens with them later. The idea of the charge solves this problem quite easily. Since vortices are created from a solution with zero charge, once created defects of opposite charge will annihilate in pairs over time. This is a well studied problem [23], and interesting coarsening laws have been derived for the average length between defects over time [51, 52]. However, what happens with these defects if the elements forming them are subjected to nonreciprocal coupling is not entirely clear.

The following chapter explores migrating banded vegetation patterns, a system that can be described with equations where nonreciprocity in the interactions naturally arises. Oriented patterns are an alternative setup to study the dynamics of topological defects, since the dislocation type of defect corresponds to a phase singularity in the amplitude of the pattern envelope. The macroscopic effect of the modeled nonreciprocity among interactions is to produce the pattern to drift, or migrate in the context of living entities (however, we are not referring to moving plants, but a moving biomass field composed of plants of several ages). Thus, any topological defect in the pattern would move in the drift direction and directed out of the system. Interestingly, when considering appropriate boundary conditions, dynamical regimes in which topological defects are constantly created at the upstream boundary is observed. The constant creation on the boundary, followed by the annihilation dynamics on the comobile reference frame moving with the drift velocity, creates a unique imprint on the pattern, where the defects distribution in space is unveiled. This property is measured in three different vegetation patterns fulfilling the required constraints showing good agreement with the theory. Additionally, regimes for which defects create anywhere in the system are numerically predicted. These regimes act as different stages, possibly warning about the pattern condition when the biomass mortality increases due to environmental factors.



APPLIED PHYSICS

Topological defects law for migrating banded vegetation patterns in arid climates

D. Pinto-Ramos^{1*}, M. G. Clerc¹, M. Tlidi²

Self-organization and pattern formation are ubiquitous processes in nature. We study the properties of migrating banded vegetation patterns in arid landscapes, usually presenting dislocation topological defects. Vegetation patterns with dislocations are investigated in three different ecosystems. We show through remote sensing data analysis and theoretical modeling that the number of dislocations $N(x)$ decreases in space according to the law $N \sim \log(x/B)/x$, where x is the coordinate in the opposite direction to the water flow and B is a suitable constant. A sloped topography explains the origin of banded vegetation patterns with permanent dislocations. Theoretically, we considered well-established approaches to describe vegetation patterns. All the models support the law. This contrasts with the common belief that the dynamics of dislocations are transient. In addition, regimes with a constant distribution of defects in space are predicted. We analyze the different regimes depending on the aridity level and water flow speed. The reported decay law of defects can warn of imminent ecosystem collapse.

INTRODUCTION

Self-organization phenomena leading to spatially periodic patterns are observed in complex or nonlinear systems (1–5). Vegetation population dynamics provide puzzling and notable examples of spatially periodic structures, generically called vegetation patterns, formed by large-scale botanical organizations controlled by a non-equilibrium symmetry-breaking instability (6–13). The banded patterns, often called tiger bush (14), consist of dense vegetation bands alternating with sparsely covered or even bare soil, their wavelength ranges from decimeters to hundreds of meters. Banded vegetation patterns have probably been first reported by Macfadyen in the earlier fiftieth (15, 16). The spontaneous symmetry-breaking instability causes their formation even when the topography is flat (6). The presence of the slope causes the migrating banded patterns (6, 8, 12). They grow by a few decimeters each year in the opposite direction of the water flow (8, 12). Besides, a bibliography of empirical and scientific studies devoted to the origin of their formation and maintenance can be found in (6, 12, 17–20).

Most of the banded vegetation patterns observed in nature are disordered and present topological defects such as dislocations, as can be seen in Fig. 1. Dislocations in the banded vegetation patterns are indicated by red rings in the aerial photographs of Fig. 1. When two stripes join and transform into a single one, they form a defect called dislocation. Observations across large areas of numerous arid and semi-arid regions of Africa, Australia, America, and the Middle East show that topological defects are abundant. Banded vegetation is a well-documented issue that has been abundantly discussed and is by now fairly well understood. So far, however, the law governing the formation of such defects has neither been experimentally determined nor theoretically predicted.

Here, we establish a law governing the organization of dislocations. By analyzing satellite images taken from vast territories of the African and American continent, we show that the number of

dislocations obeys the formula $N \sim \log(x/B)/x$, where x is the coordinate in the opposite direction of water flow and B is a suitable constant. Theoretically, we have considered three different ecological approaches describing the dynamics of topological defects. All these models quantitatively support this deterministic law. Furthermore, these ecological models predict an additional dynamical regime where the number of dislocations remains constant. In addition to the slope, which is the source of dislocation propagation, we show that boundary conditions play an essential role in their permanent creation; defect generation from boundaries is a documented phenomenon in nonlinear physics that appears in several situations, the most common being the dynamics of viscous flows (21). Therefore, with a source of dislocations through the boundaries, the dynamics of these topological defects can be permanent rather than transient. This fact strongly contrasts with previous work where dislocation formation is considered a transient dynamic due to their mutual annihilation interaction, leading at long times to a perfectly ordered banded pattern free of defects (8). The permanent dynamics of defects is the process of pairs of dislocations being created at the boundary with opposite topological charges, and then they move with the pattern migration velocity (toward x) at the same time they interact, approaching each other until annihilation; the process is repeated in time in an unpredictable way. This complex permanent dynamic leaves an imprint in the dislocation number as a function of the x direction. We demonstrate how a decaying number of dislocations in space may be used as an early indicator of an ecosystem's potential collapse under harsh environmental conditions. We conclude by showing how the measure of the dislocation distribution in space can be used as a noninvasive tool for diagnosing ecosystem health. The ecosystem transition to bare soil is a much-studied issue in which spatial vegetation models play a crucial role (22–24). Our theory complements the understanding of ecosystem adaptability and resilience until now, as we consider the role of sloped topography and boundary conditions in the dynamics. The predicted law is supported by field observations and can be crucial for identifying and comprehending the

¹Departamento de Física and Millennium Institute for Research in Optics, FCFM, Universidad de Chile, Casilla 487-3, Santiago, Chile. ²Faculté des Sciences, Université Libre de Bruxelles, CP 231, Campus Plaine, B-1050 Bruxelles, Belgium.

*Corresponding author. Email: david.pinto@ug.uchile.cl

Copyright © 2023
The Authors, some
rights reserved;
exclusive licensee
American Association
for the Advancement
of Science. No claim to
original U.S. Government
Works. Distributed
under a Creative
Commons Attribution
License 4.0 (CC BY).

Downloaded from <https://www.science.org> on August 07, 2023

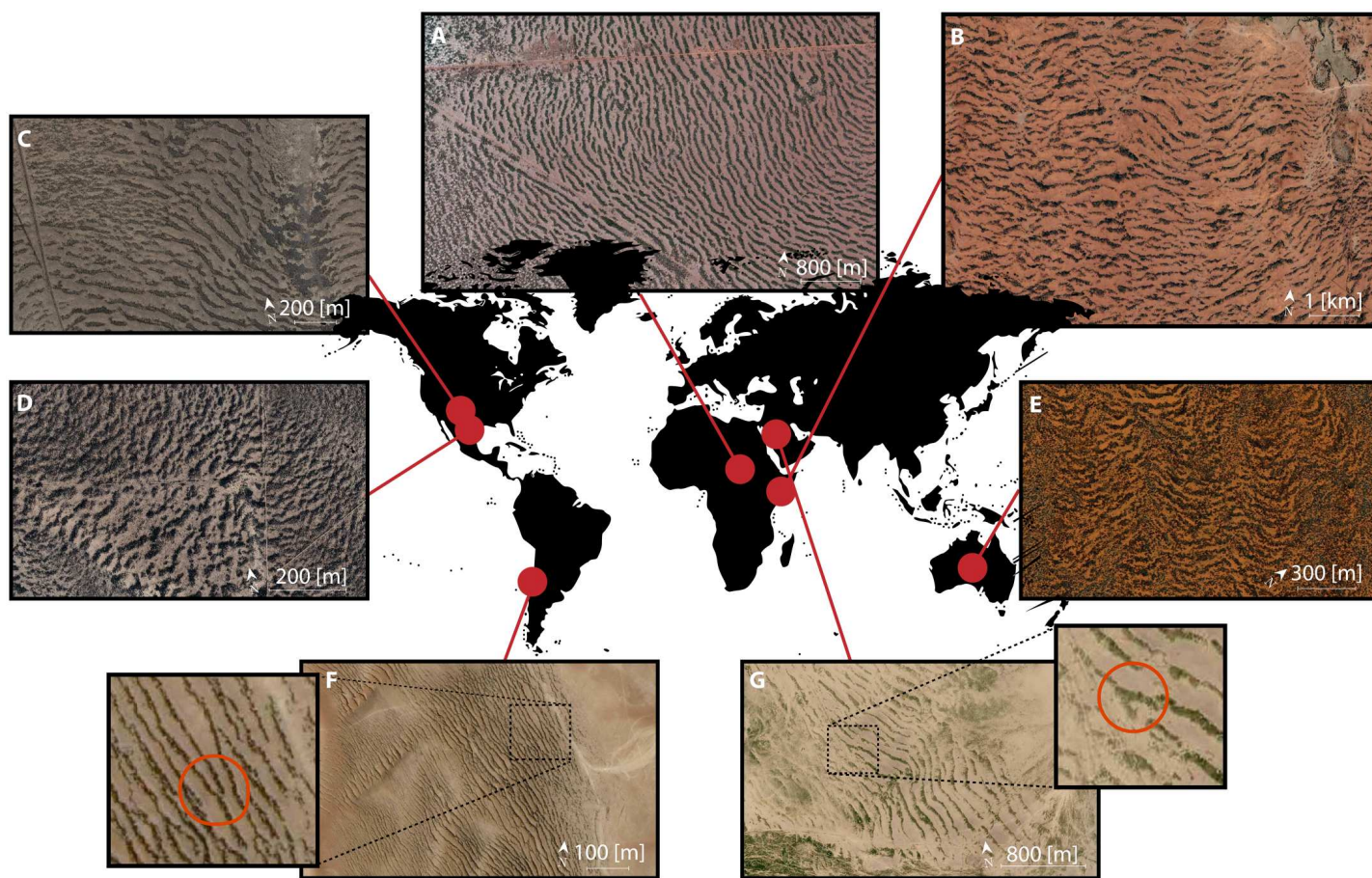


Fig. 1. Migrating banded vegetation patterns with dislocations observed in arid and semi-arid ecosystems on different continents. (A) Sudan 11° 9' N, 28° 16.5' E. **(B)** Somalia 8° 6.9' N, 47° 26.5' E. **(C)** United States 31° 2.5' N, 103° 5.5' W. **(D)** Mexico 28° 8.5' N, 104° 28' W. **(E)** Australia 23° 23' S, 133° 23.2' E. **(F)** Chile 20° 29.5' S, 70° 3.5' W. **(G)** Saudi Arabia 24° 19.8' N, 42° 55.2' E. Insets show dislocations indicated with red rings.

different spatiotemporal behaviors seen in complex systems other than ecological ones.

RESULTS

Remote sensing data analysis and the dislocation distribution decay law

To establish through field observation that the number of dislocations in the banded vegetation follows a logarithmic law, we perform an image analysis. Three regions of the world are considered: Chile, Sudan, and the United States. To do that, we use high-resolution satellite images obtained from the Google Earth software (<https://earth.google.com/web>), together with the elevation database SRTM (Shuttle Radar Topography Mission) with 1-arc sec resolution (25). First, we select and create an adequate mask of the region where banded vegetation patterns are settled on sloppy landscape as shown in the satellite images of Fig. 2 (A to C). Second, we extract the mean orientation of the elevation gradient (θ) over the selected region as illustrated by Fig. 2 (D to F). We assume that the mean orientation of the elevation gradient is parallel to x . In the case of the banded vegetation pattern in hyper-arid landscapes of Chile, the x variable decreases with height, as water comes from the East-to-West traveling fog (26, 27). This means that the water bubbles move uphill, and therefore, the vegetation pattern migrates

downhill. However, in arid landscapes of North America and Sudan, water is supplied by rainfall, and the x variable grows with height.

Once the x direction is defined, dislocation positions are marked. For the satellite images, because of the intrinsic fluctuations, the high anharmonicity, and the high variations in the wavelength in the banded vegetation, the dislocations could not be recognized with standard methods. To detect dislocations, we construct a skeleton of the banded vegetation pattern using the software for scientific image analysis Fiji (28) (see Materials and Methods section). This method allows us to identify the branch split points and the branch ends as points representing dislocations of the local pattern. The results are summarized in Fig. 2 (G to I).

Last, we select an area within the banded vegetation pattern in the plane (x, y) , and we define the dislocation number $N(x, y)$ over tiles of one wavelength side. Then, we average along the y direction. The obtained dislocation number $N(x)$ is plotted as a function of x/λ where λ is the wavelength of the banded vegetation pattern. Note that N is the expected number of dislocations in a λ^2 surface tile centered on the (x, y) plane. The results are shown in Fig. 3. In the hyper-arid landscape of Chile and Sudan and the United States arid landscapes, the number of dislocations $N(x)$ decreases with the x direction. From these results obtained from remote sensing observations, we can see that the spatial distribution

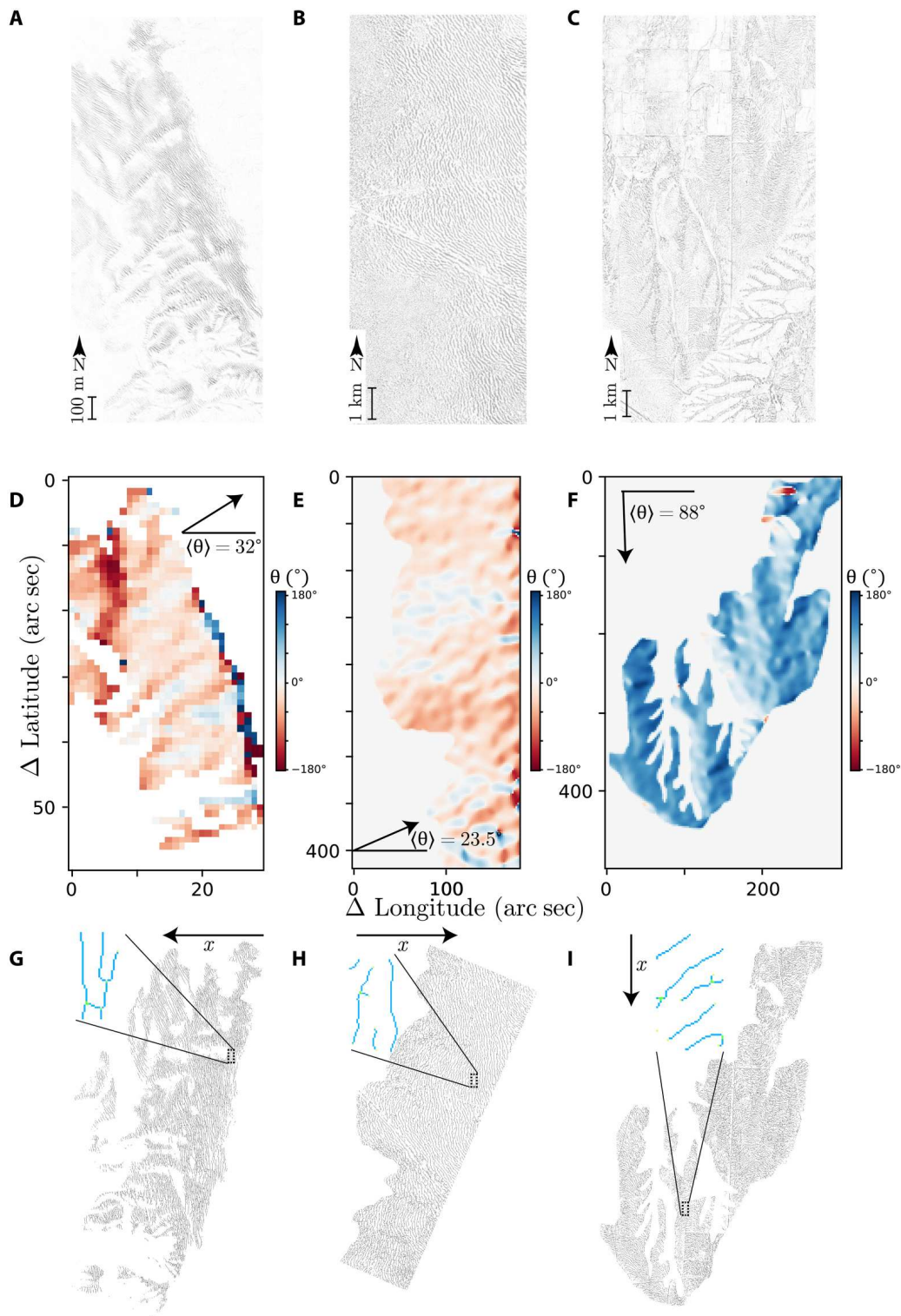


Fig. 2. Remote sensing analysis: Determination of the x direction and defect recognition with remote sensing data. (A to C) show the vegetation patterns in Chile $20^\circ 29.5' S$, $70^\circ 3.5' W$, Sudan $11^\circ 9' N$, $28^\circ 16.5' E$, and the United States $31^\circ 2.5' N$, $103^\circ 5.5' W$, respectively. (D to F) exhibit the direction of the steepest variation in the altitude over the region of interest. (G to I) illustrate the pattern's skeletons, and insets show the patterns dislocations highlighted.

Downloaded from <https://www.science.org> on August 07, 2023

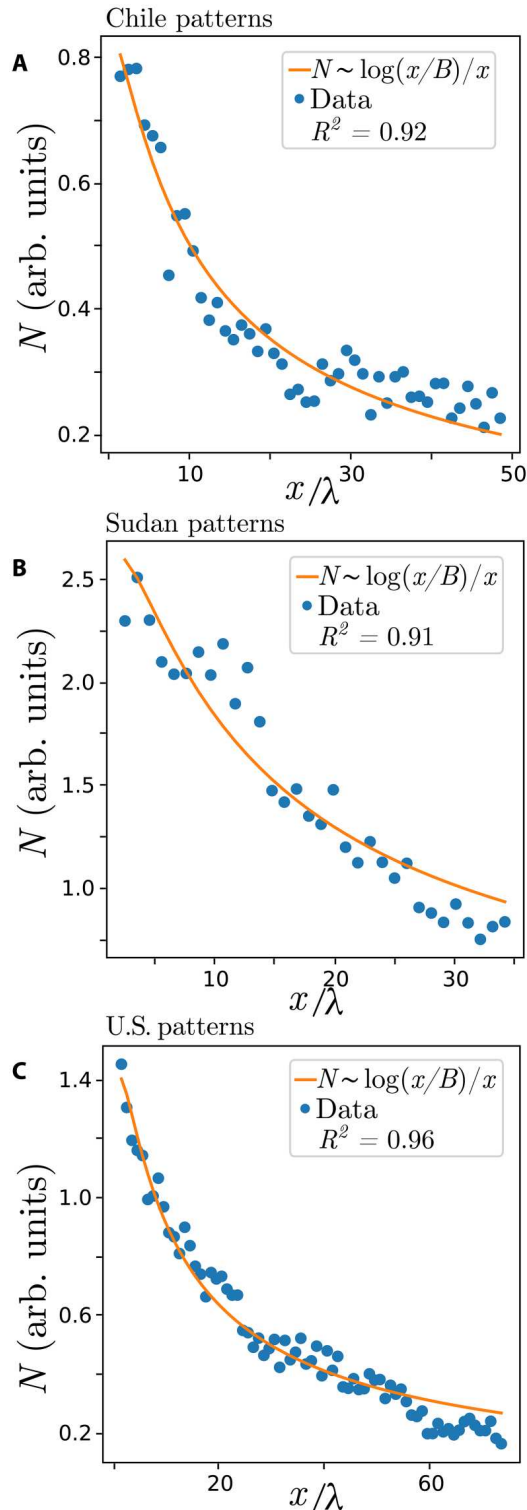


Fig. 3. Dislocation number decay law obtained from remote sensing analysis in Chile, Sudan, and U.S. landscapes. Circles account for observed data, and the orange curves represent the fits. (A to C) correspond to a $N(x) \sim \log(x/B)/x$ fit for patterns in Chile, Sudan, and the United States, respectively. Fit parameters in λ units are (A) $x_0 = -2.9$, $B = 1.2$, and $A = 2.7$; (B) $x_0 = -2$, $B = 1.5$, and $A = 10.6$; (C) $x_0 = -2.4$, $B = 1.3$, and $A = 5$. R^2 is the coefficient of determination of the fits.

of defects is not uniform. Their distribution depends on the sloped direction along which the water flows. The fit of the observations is indicated by continuous orange curves in Fig. 3. Unexpectedly, the $N(x) \sim \log(x/B)/x$ decay law fits well with the data obtained from Chile and Sudan. For the U.S. landscapes, the fit is excellent.

To understand the complex ecological phenomenon reported above and the role of the law dictating the number density of dislocations in space, mathematical modeling is indispensable. In the following subsections, we investigate the origin of the logarithm decay law through theoretical investigation and numerical simulations of three ecological models.

Theoretical modeling

To shed light on the observations of the previous section, we consider different standard approaches to explain biomass evolution. The dynamics of ecological systems are often described by either reaction-diffusion models that explicitly incorporate water transport or integrodifferential equations. The latter approach is grounded on nonlocal interactions associated with facilitative and competitive feedback and seed dispersion. Other models based on cellular automata have been first proposed (14) and also models based on environmental randomness (3, 29).

We consider the reaction-diffusion (8–11) and the integrodifferential approaches (6, 30). The later can be seen as a logistic equation with the abovementioned nonlocal interactions, i.e., the spatiotemporal evolution of the normalized biomass $b(\mathbf{r}, t)$, reads (30).

$$\partial_t b = m_f(1 - b)b - \mu m_c b + d\nabla^2 b \quad (1)$$

where $\mathbf{r} = (x, y)$ and t are the spatial coordinates and time, respectively. m_f and m_c account for facilitation and competition plant-to-plant feedbacks. The nonlocal contributions read $m_{f,c} = \exp[\chi_{f,c} \int \phi_{f,c}(\mathbf{r}')b(\mathbf{r} + \mathbf{r}', t)d\mathbf{r}']$, where $\phi_{f,c}(x, y) = \exp[-(x - x_{0f,0c})^2/2l_{fx,cx}^2 - y^2/2l_{fy,cy}^2]$ are ellipsoidal coupling kernels with a shift in x with respect to the origin of magnitude $x_{0f,0c}$. The facilitative and the competitive ranges are $l_{fx,cx}$ and $l_{fy,cy}$ for the x and y direction, and the feedback strengths are measured by $\chi_{f,c}$. The kernels $\phi_{f,c}$ introduce an anisotropy and break the reflection symmetry $x \leftrightarrow -x$. The last term of the right-hand side of Eq. 2 models the seed dispersion with diffusive coefficient d .

In the weak gradient approximation, one can derive from model Eq. 1 a simpler partial differential equation (see Materials and Methods for details) of the form

$$\partial_t b = \left(-\eta + \kappa b - \frac{b^2}{2}\right)b + p\nabla^2 b - b(\alpha\partial_x + \gamma\partial_x^2 + \partial_x^4)b \quad (2)$$

where α accounts for the translation parameter of the ellipsoidal kernel. The parameter η measures the decrease-to-growth rate ratio, called the aridity parameter. κ is the facilitation-to-competition strength difference, called the cooperativity parameter. γ is proportional to the difference of the squared competition-to-facilitation lengths and p plays the same role as d .

In addition to the integrodifferential and the weak-gradient models, we consider the water-biomass model describing the space-time evolution of the biomass (b) and water (w) density.

This model reads (10)

$$\begin{aligned} \partial_t b &= \left(\frac{\gamma w}{1+\sigma w} - \mu \right) b - b^2 + d \nabla^2 b \\ \partial_t w &= p - (1 - \rho b)w - w^2 b + \\ &\quad \nabla^2 (w - \beta b) - \alpha \partial_x (w - vb) \end{aligned} \quad (3)$$

The slope effect is accounted for in the term $\alpha \partial_x (w - vb)$, where α is the water speed, which flows opposite (in favor) to the x direction for $\alpha < 0$ ($\alpha > 0$). Because of the water absorption by plants, the biomass reduces the water advective transport mediated by the parameter v . The parameters γ and σ model the biomass production increase with water considering a saturable function, d models the seed dispersion, and μ accounts for mortality. The parameter p measures water input, ρ reduces the transpiration rate linearly with the biomass, and β models how plants affect water absorption by the soil.

Numerical simulations of the nonlocal model Eq. 1 with ellipsoidal translated kernels ($l_{f_x, c_x} \neq l_{f_y, c_y}$) display propagative banded patterns for small $x_{0f, 0c}$ values as shown in Fig. 4A. These results are obtained using Dirichlet boundary conditions with zero value in the flow direction edges ($b = 0$ for $x = 0$ and $x = s$, where s is the system size). Periodic boundary conditions are used in the y direction. Numerical simulations of all the models presented were conducted with a Runge-Kutta algorithm of fourth order for time integration and a finite difference scheme for space discretization.

As the translation parameter increases, the uniform banded patterns become unstable and the system generates permanent dislocations from the fixed edge $x = 0$, see Fig. 4B. Similarly, a permanent emission of defects can be sustained by environmental stochastic fluctuations (31).

The permanent dislocation dynamics are also obtained from the reduced model Eq. 2 (cf. Fig. 4, C and D) and the reaction-diffusion Eq. 3 (cf. Fig. 4, E and F). All models display a transition from a perfect traveling banded vegetation to a regime where dislocations are permanently emitted, as shown in Fig. 4. This transition occurs for $\alpha^* < \alpha$, the system asymptotically tends to a regular banded pattern as $x \rightarrow \infty$, cf. Fig. 5A(i), but with dislocations being created in the upstream boundary. The critical value α^* is the threshold for the boundary layer instability, and below this value, the number of dislocations is zero. The α^* parameter has no analytical expression and depends on the model considered. Hence, this parameter only is determined numerically. When dislocations are only created on the edge, numerical data follows

$$N(x) = \frac{A \log[(x - x_0)/B]}{(x - x_0)} \quad (4)$$

where A , B , and x_0 are the fit parameters. The number of dislocations $N(x)$ as a function of x is plotted in Fig. 5A(iii). This numerical result agrees with field observations using remote sensing image data analysis, as shown in the panels of Fig. 3. Table 1 summarizes the results of fitting law (4) to both observational and numerical data.

To understand analytically the origin of the logarithmic law, we perform a normal form analysis, which leads to the derivation of the well-known Ginzburg-Landau Eq. 9 (see Materials and Methods). Dislocations correspond to topological singularities in the phase of the Ginzburg-Landau equation (32–34). This reduction shows that in defect interaction, when the nonlinear phase correction β

is small, the length l between the defects decays according to the law $l^2 = t/\log(t)$ (35–37). Then if the system is advected with speed α , one can interchange the role of time for space using the relation $t = x/\alpha$. Hence, this characteristic length changes with distance as $l^2 = x/\alpha \log(x/\alpha)$. Likewise, the average number of defects in a given area Π is $N(x) = \Pi/l^2 = \Pi \alpha \log(x/\alpha)/x$. Again, the normal form analysis confirms the logarithmic law.

When, however, the advection parameter increases, i.e., large α , we identify a second transition where a permanent creation of dislocations occurs not only from the edge but also in the bulk, as shown in Fig. 5A(iv). This regime is well-known in nonlinear systems in general, and it is referred to as defects turbulence (32, 38). In this regime, the averaged dislocation number is constant $N(x) = c$ as a result of the continuous creation of defects in the bulk, see Fig. 5A(vi). This figure is obtained from numerical simulations of Eq. 2. The transition from nonturbulent to turbulent regime is also obtained from the Ginzburg-Landau Eq. 9, as shown in Fig. 5B.

The numerical analysis of ecological models indicates that by only measuring the number of dislocations in the pattern, one can infer if the semi-arid and arid ecosystems operate in the turbulent regime where $N(x) = c$ or in the nonturbulent regime where $N(x)$ obeys a logarithmic decay law. This law obtained from numerical simulations of the three models considered here is in good agreement with observations using remote sensing image analysis, as shown in the panels of Fig. 3. Therefore, the measure of the number of dislocations in the vegetation patterns and their spatial distribution can be used as a noninvasive tool for diagnosing the degree of complexity of arid landscapes and for identifying unexpected dynamical phenomena in ecological systems.

DISCUSSION

The transition between different regimes is investigated in terms of the speed of the water flows. We have shown that for a large speed, the ecosystem presents a turbulent behavior where the number of topological defects is constant. For a small value of the water flow speed, the number of defects decreases according to the logarithmic law. In what follows, we discuss the effect of the aridity level on dislocation formation. For this purpose, we fix the speed of the water flow and vary the aridity level. Figure 6 summarizes the different ecosystem operating regimes. For small aridity parameters, the system develops migrating banded pattern devoid of defects (cf. red curve). For a moderate level of aridity, the system exhibits a transition toward a turbulent regime where the number of dislocations is constant (see blue curve). However, for extreme aridity conditions, the system reaches a regime where the system undergoes self-organized dislocations with a logarithmic decay law (see yellow curve). Further increasing the aridity, the banded patterns exhibit a transition toward a state totally devoid of vegetation. Thus, for a given landscape with a homogeneous slope, the presence of a decaying number of dislocations can be an ecological indicator of imminent transition toward a bare state. This complements what is known about the catastrophic shift of ecosystems in flat topography, where different types of stationary patterns exist and where multistability of patterns with different wavelengths can be observed. The existence of many pattern branches permits the ecosystem to adapt to environmental changes, which allows a patterned ecosystem to survive past the tipping point compared to a

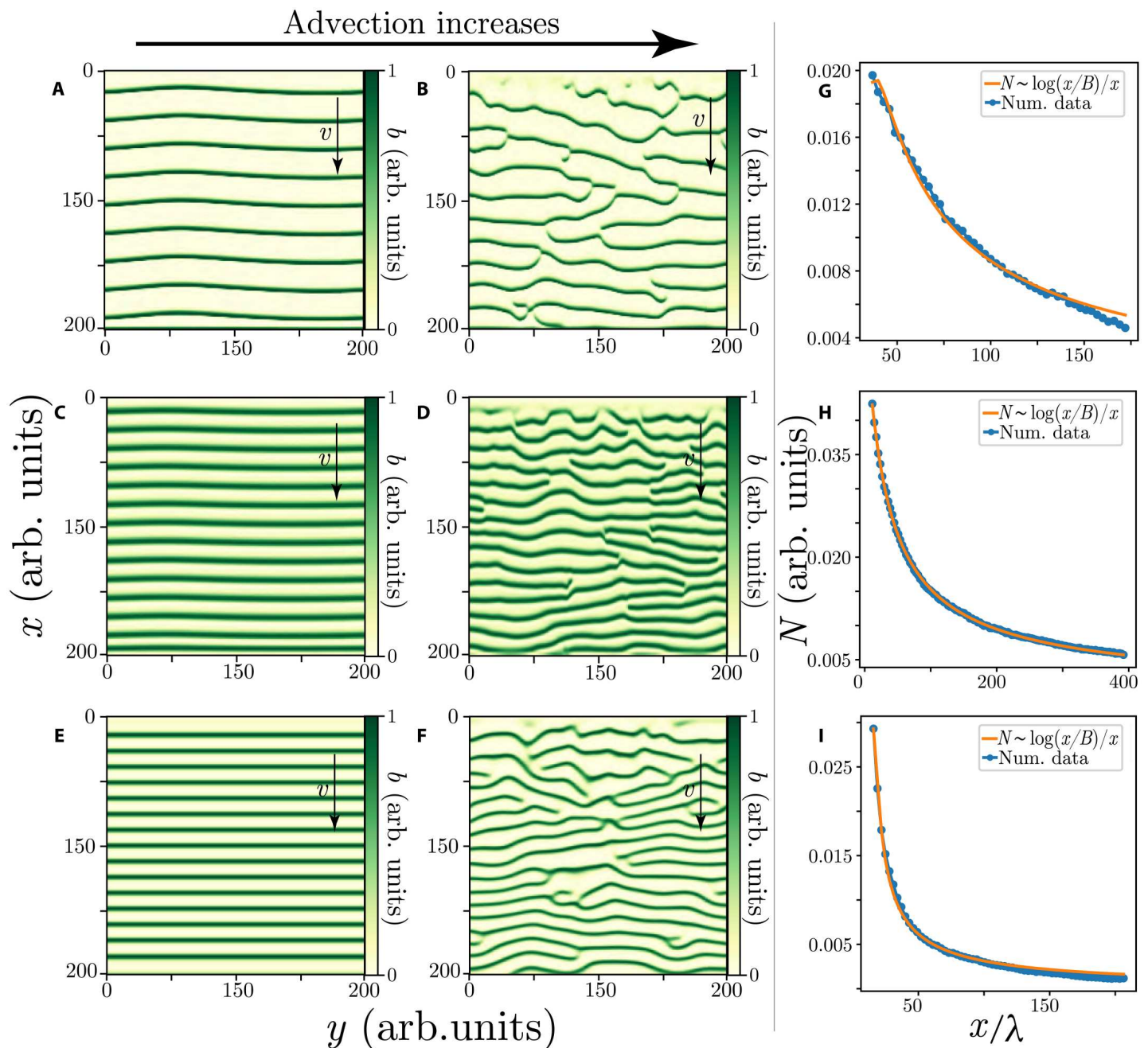


Fig. 4. Theoretical modeling of the dislocation decay law: Numerical simulations for three models of migrating banded vegetation patterns with different advection parameters. (A and B) correspond to the integrodifferential model Eq. 1. Parameters are $l_{fx} = l_{fy} = 0.5$, $l_{cx} = 2.2$, $l_{cy} = 0.3$, $\mu = 0.95$, $\chi_f = 2.8$, $\chi_c = 2.0$, $d = 0.01$, for (A) $x_{of} = -0.2$ and $x_{oc} = 0.1$, for (B) $x_{of} = -0.4$ and $x_{oc} = 0.8$. (C and D) show the weak gradient model Eq. 2, parameters are $\eta = -0.04$, $\kappa = 0.3$, $p = 0.05$, $\gamma = 1.9$, for (C) $\alpha = 0.4$, for (D) $\alpha = 1.0$. (E and F) represent the water-biomass model (3), parameters are $\gamma = 2.0$, $\sigma = 1.5$, $d = 0.1$, $\mu = 0.1$, $w_0 = 0.3$, $\rho = 0$, $\beta = 0$, $v = 4.0$, for (E) $\alpha = -1.4$, for (F) $\alpha = -2.0$. The right panels correspond to the respective number of dislocations $N(x)$ as a function of the propagation coordinate (x/λ) for each model in the regime of asymptotic uniform stripe patterns. Fit parameters in λ units are (G) $x_0 = 27.2$, $B = 4.1$, and $A = 0.2$ ($R^2 = 0.99$); (H) $x_0 = -7$, $B = 3.8$, and $A = 0.5$ ($R^2 = 1.0$); (I) $x_0 = 14.3$, $B = 0.7$, and $A = 0.06$ ($R^2 = 0.99$).

homogeneous ecosystem (22). However, once a gentle slope is introduced into the system, the advective effects of water flow must be taken into account for the stability analysis of patterns and other solutions of the system (39). This changes the stable pattern branches compared to a flat territory case. In addition, complex and turbulent-like dynamics can emerge as a consequence of the slope. These complex dynamical regimes have their own relative stability

compared to the different perfect migrating pattern regimes and homogeneous states. Multistability of the complex dynamical regimes and the perfect patterns can occur, as observed in Fig. 6, suggesting that in adaptation to change, ecosystems could transit to these complex regimes if in the presence of a sloped territory. Numerically, only the most stable branch of perfect patterns is accessible.

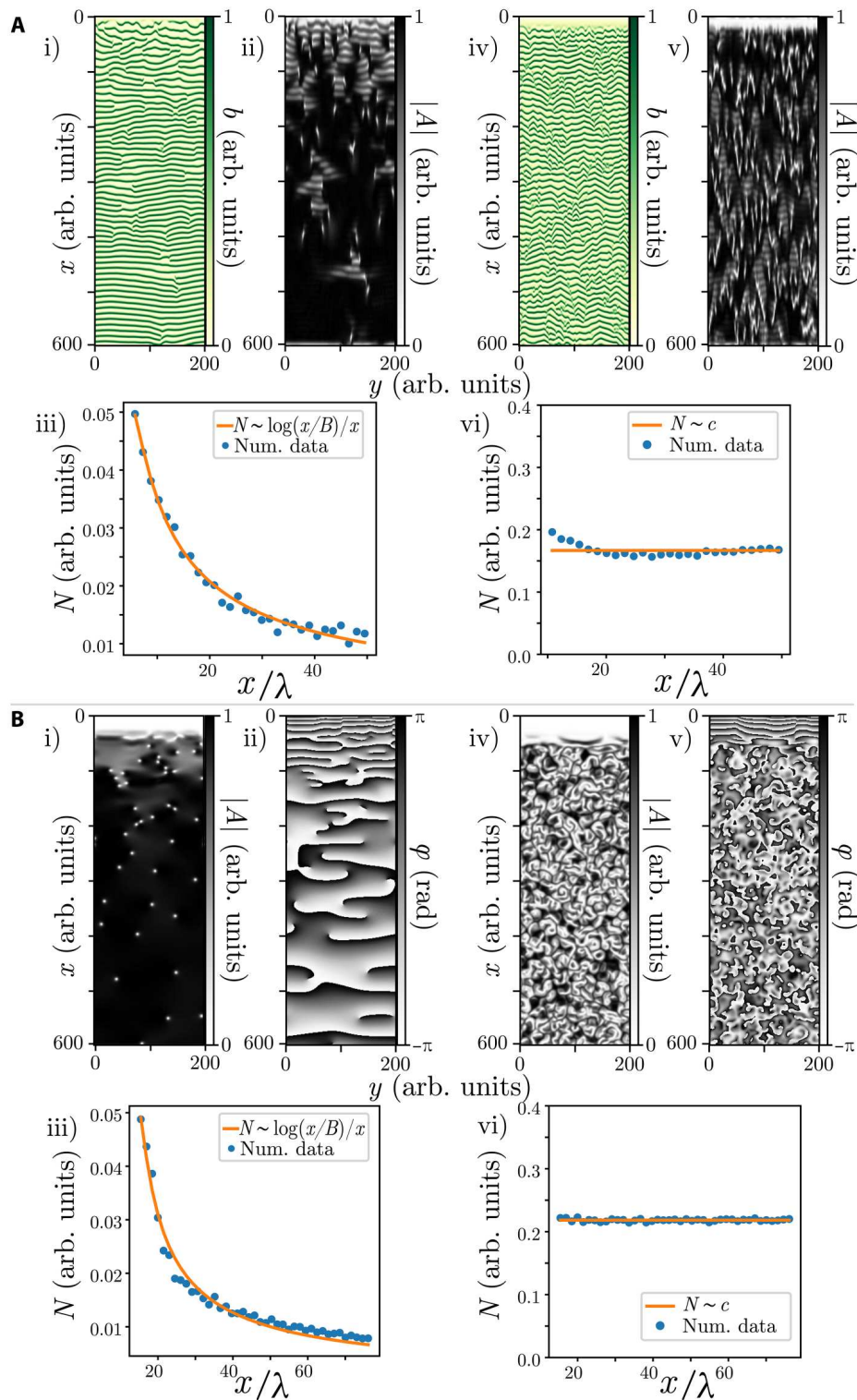


Fig. 5. Transition from nonturbulent to turbulent regime. (A) Numerical simulations of the weak gradient vegetation model Eq. 2. The real field, the amplitude of the banded pattern, and the defect number distribution. Parameters are $\eta = -0.04$, $\kappa = 0.3$, $p = 0.05$, $\gamma = 1.9$, for (i) and (ii) $\alpha = 1.0$, for (iv) and (v) $\alpha = 2.0$. (iii) and (vi) show the number of dislocations $N(x)$. (B) Numerical simulations of the complex Ginzburg-Landau Eq. 9. Parameters $\mu(x) = 1 - e^{-x/10}$, $\nu(x) = 10e^{-x/10}$, $\bar{\alpha} = 1.0$, for (i) and (ii) $\beta = 0.1$, for (iv) and (v) $\beta = 3.0$. (iii) and (vi) show the number of dislocations. Fit parameters in λ units are (A, iii) $x_0 = 2.7$, $B = 0.9$, and $A = 0.1$ ($R^2 = 0.99$); (B, iii) $x_0 = 13$, $B = 0.7$, and $A = 0.1$ ($R^2 = 0.98$). (A, vi) $c = 0.16$; (B, vi) $c = 0.21$

Table 1. Summary of the best fit for the decaying spatial distribution of dislocations for mathematical models and remote sensing image analysis. *A, B, and x_0 are the fit parameters of Eq. 4, and R^2 is the coefficient of determination for the respective fits.*

Mathematical models	A/λ	B/λ	x_0/λ	R^2
Eq. 1	0.2	4.1	27.2	0.99
Eq. 2	0.5	3.8	-7.0	1.0
Eq. 3	0.06	0.7	14.3	0.99
Remote sensing image analysis				
Chile	2.7	1.2	-2.9	0.92
Sudan	10.6	1.5	-2	0.91
United States	5	1.3	-2.4	0.96

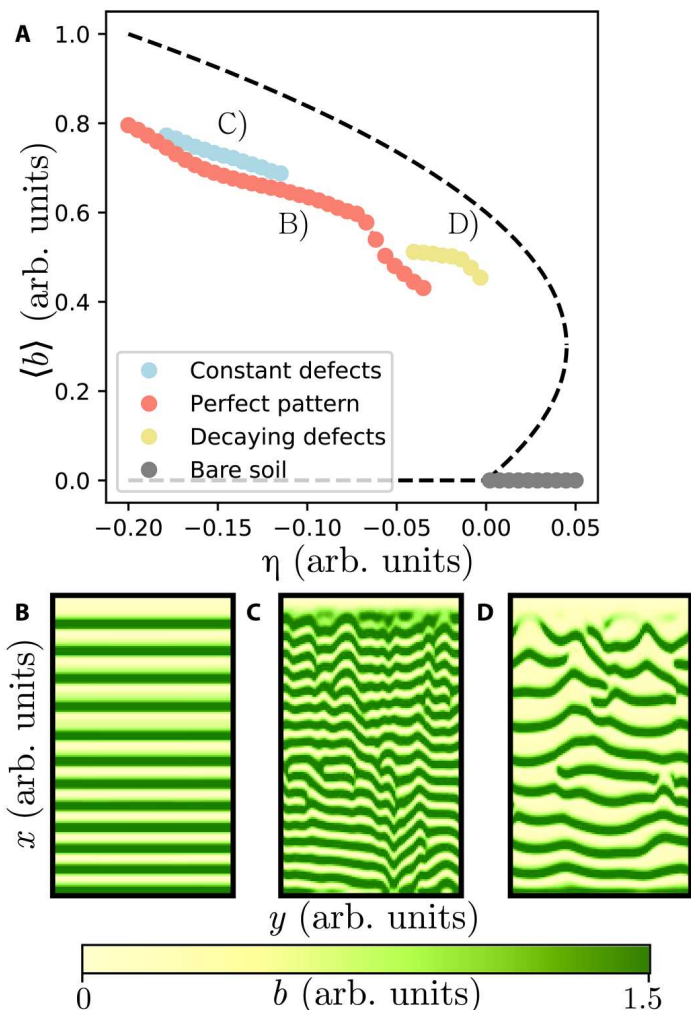


Fig. 6. Diagram of migrating banded vegetation pattern biomass as a function of the aridity parameter η . For Eq. 2, parameters $\kappa = 0.3, p = 0.05, \gamma = 2$, and $\alpha = 1$. (A) illustrates the mean biomass $\langle b \rangle$ at the steady states of the model when changing the aridity. (B) corresponds to the branch of perfect patterns $N(x) = 0$. (C) shows the turbulent-like behavior where $N(x) = c$. (D) represents the branch of asymptotic patterns, where $N(x) \sim \log(x/B)/x$.

Different stable branches of perfect patterns could be obtained from Eq. 9 analytically at the onset of pattern formation.

To summarize, we have investigated different transitions of migrating vegetation banded patterns: from zero defects, to constant, and to a decaying number of dislocations. We have shown analytically that the number of dislocations in space $N(x)$ obeys a $N(x) \sim \log(x/B)/x$ law. This formula is in good agreement with numerical simulations of the three ecological models and with remote sensing image data taken from three arid ecosystems of different continents. Furthermore, the dislocation law allows us to determine whether the self-organized response to the water scarcity of arid and semi-arid ecosystems favors uniform bands or ecological spatio-temporal complexity.

A usual approach to characterize the response of plants to changes in their environment is through studies of the plants themselves (local analysis). Characterizing dislocation distributions of migrating banded vegetation patterns (macroscopic analysis) opens a noninvasive diagnostic tool for determining the degree of aridity mediated by desertification and global warming processes. Likewise, a full characterization of the bifurcation diagram for models including reflection symmetry rupture and dislocations self-organization becomes relevant in designing conservation guidelines, preventing the further degradation of migrating patterned vegetation cover.

Last, the spatial distribution of defects is a consequence of their creation induced by the boundary condition and their annihilation through mutual interaction. The boundary induces inhomogeneities in the system. The inhomogeneous Ginzburg-Landau equation constitutes an ideal framework for investigating the dynamics of defects in banded vegetation patterns. It provides a unified and simple description containing the dynamics discussed. Thus, the analytical results can be easily extended to describe similar laws in other complex nonlinear spatially extended systems present in nature.

MATERIALS AND METHODS

Detailed derivation of the weak gradient model with advection

We look for an approximation to Eq. 1 of the main text, in the form of a partial differential Eq. 2. To account for anisotropy, we consider that the interaction ranges associated with facilitation and the competition $l_{cx,fx}$ and $l_{cy,fy}$ are different. We seek corrections to the steady states close to $\mu = 1$ and $b = 0$ that depend on time and space through the slow variables $T = \epsilon t, X = \epsilon^{1/8} x$, and $Y = \epsilon^{1/8} y$. We expand the parameters $\mu, \chi_{f,c}, l_{fx,fx}, x_{0c,0f}, d$, and the biomass b in terms of a small parameter ϵ ($\epsilon \ll 1$) that measures the distance from $\mu = 1$ as follows

$$\begin{aligned} \mu &= 1 + \epsilon\eta + \dots, \\ \chi_f &= 1 + \chi_c + \epsilon^{1/2}\kappa + \dots, \\ \chi_c &= \frac{l_{fx}^2}{l_{cx}^2 - l_{fx}^2} + \epsilon^{1/4}\chi_1 + \dots, \\ x_{0f} &= \epsilon^{3/8}\alpha_f + \dots, \quad x_{0c} = \epsilon^{3/8}\alpha_c + \dots, \\ l_{fy}^2 &= \epsilon^{1/4}\sigma_{fy}^2 + \dots, \quad l_{cy}^2 = \epsilon^{1/4}\sigma_{cy}^2 + \dots, \\ d &= \epsilon^{3/4}p + \dots, \quad b(t, x, y) = \epsilon b(T, X, Y) + \dots \end{aligned}$$

Introducing these scalings and the above expansions in Eq. 1, we then obtain a sequence of linear problems for unknown functions.

Downloaded from https://www.science.org on August 07, 2023

We analyze each problem and apply the solvability condition at each order. These conditions are automatically fulfilled at the orders $\epsilon^{1/2}$ and ϵ . By applying the solvability condition at the higher order inhomogeneous problem ($\epsilon^{3/2}$), we obtain the following partial differential equation for the biomass

$$\partial_T b = (-\eta + \kappa b - b^2/2)b + p\nabla^2 b - b(\alpha\partial_x + \gamma_x\partial_x^2 - \gamma_y\partial_y^2 + \Lambda\partial_x^4)b \tag{5}$$

where the coefficients are $\chi_0 = l_{fx}^2/(l_{cx}^2 - l_{fx}^2)$, $\alpha = \alpha_c\chi_0 - \alpha_f(1 + \chi_0)$, $\gamma_x = \chi_1(l_{cx}^2 - l_{fx}^2)$, $\gamma_y = \sigma_{fy}^2(1 + \chi_0) - \sigma_{cy}^2\chi_0$, and $\Lambda = 3l_{fx}^2 l_{cx}^2$.

Model Eq. 5 has different homogeneous steady states which are $b = 0$ and $b_0 = \kappa \pm (\kappa^2 - 2\eta)^{1/2}$. Note that the upper branch of b_0 is stable when $l_{cx} > l_{fx}$ and $\gamma_y > 0$. Otherwise, we need to consider higher ϵ orders in the equation. The condition $\gamma_y = 0$ will be used throughout the work, as it does not change the qualitative behavior of the system.

Introducing the scaling $X = 1/\Lambda^{1/4}X$ and $Y = 1/\Lambda^{1/4}Y$ and redefining $\alpha \rightarrow \alpha/\Lambda^{1/4}$, $\gamma_x \rightarrow \gamma/\Lambda^{1/2}$, and $p \rightarrow p/\Lambda^{1/2}$, we get Eq. 2.

Detailed derivation of the Ginzburg-Landau equation

Derivation of amplitude equation in the bulk

The amplitude equation obtained using a normal form analysis constitutes an adequate tool for understanding pattern formation. For the boundary conditions considered, the system creates a thin boundary layer next to the upstream edge of the system. The effect of this boundary layer can be neglected when focusing on regions far from the edges. Let us consider first the linear problem for a perturbation of the homogeneous stable state $u \ll 1$ as $b = b_0 + u$, where $b_0 = \kappa + \sqrt{\kappa^2 - 2\eta}$ is the homogeneous cover. Introducing this ansatz in Eq. 2 of the main text for the field b yields the linear problem

$$(\partial_t - L)u = 0$$

where the linear operator is defined as $L \equiv -\eta + 2\kappa b_0 - 3b_0^2/2 + p\nabla^2 - b_0(\alpha\partial_x + \gamma\partial_x^2 + \partial_x^4)$. Linear stability analysis for finite wavenumber k perturbations leads to the growth rate of modes $\lambda(k)$

$$\begin{aligned} \lambda(k) &= \text{Re}\lambda(k) + i\Omega(k) \\ &= -\eta + 2\kappa b_0 - \frac{3b_0^2}{2} - pk^2 - b_0(ia\kappa - \gamma k^2 + k^4) \end{aligned}$$

The conditions $\partial_k \text{Re}\lambda|_{k_c} = 0$ and $\text{Re}\lambda(k_c) = 0$ determine the critical wavenumber $k_c^2 = (b_c\gamma - p)/2b_c$ and the critical aridity parameter, which satisfies $-\eta_c + 2\kappa b_c - 3b_c^2/2 + b_c k_c^4 = 0$, where $b_c = \kappa + \sqrt{\kappa^2 - 2\eta_c}$. To obtain the amplitude equation for the critical mode, let us move slightly from the instability condition, using as the bifurcation parameter η , as $\eta = \eta_c + \epsilon$. Introducing the following expansion

$$b = b_0 + \epsilon^{1/2} A e^{ik_c x + i\Omega_c t} + \epsilon A^{[2]} + \epsilon^{3/2} A^{[3]} + \dots + c.c.$$

where $A \equiv A(X, Y, T)$ is the slowly varying envelope, with the scalings $X = \epsilon^{1/2}x$, $Y = \epsilon^{1/2}y$, $T = \epsilon t$, and the parameter $\Omega_c \equiv -b_c \alpha k_c$. $A^{[n]}$ accounts for the terms of order n in the amplitude A . At order ($\epsilon^{1/2}$), we obtain

$$(\partial_t - L_c)A e^{ik_c x + i\Omega_c t + \lambda(k_c)t} = 0$$

where

$$L_c = -\eta_c + 2\kappa b_c - \frac{3b_c^2}{2} + p\nabla^2 - b_c(\alpha\partial_x + \gamma\partial_x^2 + \partial_x^4)$$

At this order, the solvability condition is automatically satisfied. For the sake of simplicity, let us define $\hat{d} \equiv \alpha\partial_x + \gamma\partial_x^2 + \partial_x^4$ and $d(k) \equiv ia\kappa - \gamma k^2 + k^4$. Then, performing expansions, up to order ϵ , limiting to the case of small group velocities $v_g = \partial_k \Omega|_{k_c} \sim O(\epsilon^{1/2})$, we get

$$\begin{aligned} (\partial_t - L_c)A^{[2]} &= (\kappa - \frac{3}{2}b_c) (A^2 e^{2ik_c x + 2i\Omega_c t} + |A|^2 + c.c.) \\ &\quad - (A e^{ik_c x + i\Omega_c t} + c.c.) [Ad(k_c) e^{ik_c x + i\Omega_c t} + c.c.] \end{aligned} \tag{6}$$

To solve the linear problem, the following inner product is introduced

$$\langle f | g \rangle = \int_X^{X+\frac{2\pi}{k_c}} dx \int_T^{T+\frac{2\pi}{\Omega_c}} dt f^* g$$

valid over the periodic functions in space and time of period $2\pi/k_c$ and $2\pi/\Omega_c$. The kernel of the operator $(\partial_t - L_c)^\dagger$, defined as the solution of $(\partial_t - L_c)^\dagger \psi = 0$, corresponds to $\psi = e^{\pm i(k_c x + \Omega_c t)}$. Then, applying the solvability condition, we find

$$A^{[2]} = a_2 A^2 e^{2ik_c x} + b_2 |A|^2 + \bar{a}_2 \bar{A}^2 e^{-2ik_c x}$$

where

$$\begin{aligned} a_2 &= \frac{\kappa - 3/2b_c - d(k_c)}{2i\Omega_c - \lambda(2k_c)} \\ b_2 &= \frac{2\kappa - 3b_c - d(k_c) - d(-k_c)}{-\lambda(0)} \end{aligned}$$

Last, at order $\epsilon^{3/2}$, the solvability condition yields

$$\begin{aligned} \partial_T A &= \mu A + (a + i\beta)|A|^2 A \\ &\quad + D_x \partial_{XX} A + D_y \partial_{YY} A - ab_c \partial_X A \end{aligned} \tag{7}$$

with $\mu = (-1 + 2\kappa\partial_\eta b_0 - 3/2\partial_\eta b_0^2 + (\partial_\eta b_0)k_c^4 + b_c\partial_\eta k_c^4)|_{\eta_c}$, $(a + i\beta) = (2\eta_c - 3b_c)(b_2 + a_2) - 3/2 - a_2 d(2k_c) - a_2 d(-k_c) - b_2 d(k_c)$, $D_x = 4b_c k_c^2$, and $D_y = p$. This equation is the well-known Ginzburg-Landau equation with advection.

Boundary layer effect

To figure out the emission of dislocations from the boundary of the system in the regime of decaying number of dislocations, we need to consider the boundary layer effect arising from the Dirichlet boundary conditions. We use the method suggested in (40). For this purpose, we suppose that sufficiently near to the upstream edge, one can write

$$b = b_0 + \epsilon M(X)$$

where $M(X)$ is a function that helps to connect the population state $b = b_0$ with the nonpopulation state $b = 0$ at the boundary and satisfies $M(X) \rightarrow 0$ when $X \rightarrow \infty$. The analytical solution close to the boundary is not known. Qualitatively, $b(X)$ is a Monod function. On the basis of this nonuniform b , a modified amplitude equation is derived. Making straightforward calculations, one finds a similar amplitude equation compared to Eq. 7 but with inhomogeneous

linear terms

$$\partial_T A = [\mu + \mu_1(X) + iv(X)]A + (a + i\beta)|A|^2 A + D_x \partial_{XX} A + D_y \partial_{YY} A - \alpha b_c \partial_X A \quad (8)$$

where the parameters depend on $M(X)$ as

$$\mu_1(X) = (2\kappa - 3b_c + \gamma k_c^2 - k_c^4)M(X)$$

$$v(X) = \alpha k_c M(X)$$

Both terms are proportional to the slow inhomogeneity $M(X)$, so they asymptotically go to 0 as $X \rightarrow \infty$. Hence, one recovers the homogeneous Ginzburg-Landau Eq. 7. With the change of parameters and variables as $X = \sqrt{D_x}X$, $Y = \sqrt{D_y}Y$, $A = 1/\sqrt{-a}A$, $\beta = \beta/a$, and $\tilde{\alpha} = b_c \alpha / \sqrt{D_x}$, we get Eq. 9.

Amplitude equation description

The amplitude of migrating patterns A satisfies the complex Ginzburg-Landau equation with advection

$$\partial_t A = [\mu(x) + iv(x)]A - (1 + i\beta)|A|^2 A + \nabla^2 A - \tilde{\alpha} \partial_x A \quad (9)$$

The bifurcation parameter $\mu = \mu(x)$ and detuning $v = v(x)$ are inhomogeneous as a consequence of the boundary layer. For the sake of simplicity, we choose $M(x) \sim e^{-x}$, where $x = 0$ accounts for the position of the upstream edge, cf. Fig. 5B.

Note that similarly to ecological models described above, the amplitude Eq. 9 supports a permanent emission of dislocations from the upstream edge caused by the inhomogeneous character of μ and v . The modulus, the phase field, and the dislocation distribution for the nonturbulent and turbulent regimes are shown in Fig. 5B. Both defect number laws $N(x)$ are consistent with vegetation models' predictions.

Defect counting in numerical simulations

Reconstructing the analytical signal of the migrating vegetation patterns presented, dislocations are recognized as zeros of the amplitude field. This is achieved by the binarization process of the amplitude field and a particle detection algorithm, both available in the Fiji software (28). This software gives the position of all the particles (closed regions of zero amplitude) from which $N(x)$ is constructed. The permanent emission of dislocations enables us to compute $N(x)$. Using several snapshots of the time evolution for different initial conditions, the mean value of $N(x)$ is obtained. Note that dislocations start to be counted after the boundary layer region where they are created.

Remote sensing data analysis

Image treatment

Satellite images are processed with Fiji (28). Grayscale images are treated with a one-pixel width Gaussian blur to reduce inhomogeneities. Then, the subtract background algorithm with a rolling ball of a radius of 10 pixels is applied. Last, the image is binarized and a skeleton is constructed. Note that all the procedure is easily implemented with prebuilt Fiji functions.

SRTM data analysis

SRTM data are obtained from the public database (25). The netCDF4 files are analyzed in Python with the netCDF4 module. The height maps are given with one-arc sec resolution in both

the azimuthal and polar angles; thus, localizing the bounding coordinates of the regions of interest (with Google Earth software) allows obtaining the topography of the desired regions. Then, the gradient of the height map is calculated numerically to obtain the steepest direction at each point. Last, this direction is averaged over the region of interest, and the mean orientation (θ) is obtained. This angle is used to rotate the previously obtained skeletons, aligning the x direction (the steepest descent) with the horizontal or vertical axis. This allows for an efficient way to count dislocations.

Defect counting

One needs to consider that the region of interest to analyze is not rectangular as the ones obtained from numerical simulations. Thus, a density of defects is computed to consider irregularities in the region of interest boundaries. For example, consider that x and y are aligned with the i and j indices of the matrix representing the image, and then, for each j , we swept the i index in search of defects to construct a density $n(x, y)$. This is a binary function of (x, y) , with zero value if no dislocation is found and one if there is a dislocation. Their distance is measured from the boundary of the column analyzed, which is given by the mask of the region of interest. Note that for a single column j , there can exist several boundaries due to complex topography, if this is the case, subsequent intervals are treated as new columns. Last, we coarse grain the density in tiles of one wavelength sides and average over the y direction, obtaining $N(x)$.

REFERENCES AND NOTES

1. P. Glansdorff, I. Prigogine, *Thermodynamic theory of structure, stability and fluctuations* Wiley-Interscience, 1971.
2. M. C. Cross, P. C. Hohenberg, Pattern formation outside of equilibrium. *Rev. Mod. Phys.* **65**, 851–1112 (1993).
3. F. Borgogno, P. D'Odorico, F. Laio, L. Ridolfi, Mathematical models of vegetation pattern formation in ecohydrology. *Rev. Geophys.* **47**, RG1005 (2009).
4. J. D. Murray, *Mathematical biology: I. An introduction*. Springer Science & Business Media, 2007.
5. N. Akhmediev, A. Ankiewicz, *Dissipative Solitons: From Optics to Biology and Medicine* Lecture Notes in Physics, Springer-Verlag, Berlin, Heidelberg, 2008.
6. R. Lefever, O. Lejeune, On the origin of tiger bush. *Bull. Math. Biol.* **59**, 263–294 (1997).
7. O. Lejeune, M. Tlidi, A model for the explanation of vegetation stripes (tiger bush). *J. Veg. Sci.* **10**, 201–208 (1999).
8. C. A. Klausmeier, Regular and irregular patterns in semiarid vegetation. *Science* **284**, 1826–1828 (1999).
9. R. HilleRisLambers, M. Rietkerk, F. van den Bosch, H. H. Prins, H. de Kroon, Vegetation pattern formation in semi-arid grazing systems. *Ecology* **82**, 50–61 (2001).
10. J. von Hardenberg, E. Meron, M. Shachak, Y. Zarmi, Diversity of vegetation patterns and desertification. *Phys. Rev. Lett.* **87**, 198101 (2001).
11. T. Okayasu, Y. Aizawa, Systematic analysis of periodic vegetation patterns. *Prog. Theor. Phys.* **106**, 705–720 (2001).
12. V. Deblauwe, P. Couteron, J. Bogaert, N. Barbier, Determinants and dynamics of banded vegetation pattern migration in arid climates. *Ecol. Monogr.* **82**, 3–21 (2012).
13. I. Bordeu, M. G. Clerc, P. Couteron, R. Lefever, M. Tlidi, Self-replication of localized vegetation patches in scarce environments. *Sci. Rep.* **6**, 33703 (2016).
14. J. M. Thiery, J.-M. D'Herbès, C. Valentin, A model simulating the genesis of banded vegetation patterns in Niger. *J. Ecol.* **83**, 497–507 (1995).
15. W. A. Macfadyen, Soil and vegetation in British Somaliland. *Nature* **165**, 121–121 (1950).
16. W. A. Macfadyen, Vegetation patterns in the semi-desert plains of British Somaliland. *Geogr. J.* **116**, 199–211 (1950).
17. D. L. Dunkerley, K. J. Brown, Oblique vegetation banding in the Australian arid zone: Implications for theories of pattern evolution and maintenance. *J. Arid Environ.* **51**, 163–181 (2002).
18. J. A. Ludwig, B. P. Wilcox, D. D. Breshears, D. J. Tongway, A. C. Imeson, Vegetation patches and runoff-erosion as interacting ecohydrological processes in semiarid landscapes. *Ecology* **86**, 288–297 (2005).

19. D. L. Dunkerley, T. L. Booth, Plant canopy interception of rainfall and its significance in a banded landscape, arid western New South Wales, Australia. *Water Resour. Res.* **35**, 1581–1586 (1999).
20. J. E. G. W. Greenwood, The development of vegetation patterns in Somaliland Protectorate. *Geogr. J.* **123**, 465–473 (1957).
21. D. J. Tritton, *Physical Fluid Dynamics* Oxford University Press, New York, 1988.
22. M. Rietkerk, R. Bastiaansen, S. Banerjee, J. van de Koppel, M. Baudena, A. Doelman, Evasion of tipping in complex systems through spatial pattern formation. *Science* **374**, eabj0359 (2021).
23. P. Villa Martin, J. A. Bonachela, S. A. Levin, M. A. Muñoz, Eluding catastrophic shifts. *Proc. Natl. Acad. Sci. U.S.A.* **112**, E1828–E1836 (2015).
24. M. Scheffer, S. Carpenter, J. A. Foley, C. Folke, B. Walker, Catastrophic shifts in ecosystems. *Nature* **413**, 591–596 (2001).
25. NASA JPL (2013). NASA Shuttle Radar Topography Mission Global 1 arc second [Data set]. NASA EOSDIS Land Processes DAAC. Accessed 2022-09-03 from <https://doi.org/10.5067/MEaSUREs/SRTM/SRTMGL1.003>.
26. R. Pinto, I. Barria, P. A. Marquet, Geographical distribution of *Tillandsia lomas* in the Atacama Desert, northern Chile. *J. Arid Environ.* **65**, 543–552 (2006).
27. A. I. Borthagaray, M. A. Fuentes, P. A. Marquet, Vegetation pattern formation in a fog-dependent ecosystem. *J. Theor. Biol.* **265**, 18–26 (2010).
28. J. Schindelin, I. Arganda-Carreras, E. Frise, V. Kaynig, M. Longair, T. Pietzsch, S. Preibisch, C. Rueden, S. Saalfeld, B. Schmid, J.-Y. Tinevez, D. J. White, V. Hartenstein, K. Eliceiri, P. Tomancak, A. Cardona, Fiji: An open-source platform for biological-image analysis. *Nat. Methods* **9**, 676–682 (2012).
29. P. D'Odorico, F. Laio, L. Ridolfi, Patterns as indicators of productivity enhancement by facilitation and competition in dryland vegetation. *Eur. J. Vasc. Endovasc. Surg.* **111**, G03010 (2006).
30. M. Tlidi, R. Lefever, A. G. Vladimirov, "On vegetation clustering, localized bare soil spots and fairy circles" in *Dissipative Solitons: From Optics to Biology and Medicine*, N. Akhmediev and A. Ankiewicz, Eds. (Lecture Notes in Physics, Springer-Verlag, 2008), Vol. 751, Chap. 15.
31. M. G. Clerc, S. Coulibaly, F. Del Campo, M. A. Garcia-Nustes, E. Louvergneaux, M. Wilson, Recurrent noise-induced phase singularities in drifting patterns. *Phys. Rev. E.* **92**, 050902 (2015).
32. I. S. Aranson, L. Kramer, The world of the complex Ginzburg-Landau equation. *Rev. Mod. Phys.* **74**, 99–143 (2002).
33. L. Pismen, *Patterns and Interfaces in Dissipative Dynamics* Springer, Berlin, 2006.
34. D. Walgraef, *Spatio-temporal pattern formation: With examples from physics, chemistry, and materials science* Springer Science & Business Media, 2012.
35. C. Matsuoka, K. Nozaki, Vortex dynamics of the complex Ginzburg-Landau equation. *J. Physical Soc. Japan* **61**, 1429–1432 (1992).
36. B. Yurke, A. N. Pargellis, T. Kovacs, D. A. Huse, Coarsening dynamics of the XY model. *Phys. Rev. E* **47**, 1525–1530 (1993).
37. K. Kudo, Y. Kawaguchi, Coarsening dynamics driven by vortex-antivortex annihilation in ferromagnetic Bose-Einstein condensates. *Phys. Rev. A* **91**, 053609 (2015).
38. P. Coullet, L. Gil, J. Lega, Defect-mediated turbulence. *Phys. Rev. Lett.* **62**, 1619–1622 (1989).
39. J. M. Chomaz, Absolute and convective instabilities in nonlinear systems. *Phys. Rev. Lett.* **69**, 1931–1934 (1992).
40. W. Zimmermann, B. Painter, R. Behringer, Pattern formation in an inhomogeneous environment. *Eur. Phys. J. B.* **5**, 757–770 (1998).

Acknowledgments: We thank S. Echeverria-Alar for fruitful discussions. **Funding:** M.G.C. and D.P.-R. acknowledge the financial support of FONDECYT project 1210353 and Millennium Institute for Research in Optics (MIRO). D.P.-R. thanks the financial support of ANID by Beca Doctorado Nacional 21201484. M.T. is a Research Director at the Fonds National de la Recherche Scientifique (Belgium). The authors gratefully acknowledge the financial support of Wallonie-Bruxelles International (WBI). **Author contributions:** D.P.-R. and M.G.C. conceptualized and designed the study. D.P.-R. realized the theoretical and numerical analysis. M.G.C. and M.T. supervised the work. D.P.-R., M.G.C., and MT wrote, reviewed, and edited the text. **Competing interests:** The authors declare that they have no competing interests. **Data and materials availability:** All data needed to evaluate the conclusions in the paper are present in the paper.

Submitted 7 November 2022

Accepted 5 July 2023

Published 4 August 2023

10.1126/sciadv.adf6620

Complements and perspectives on Part II

1. Distribution of interface length in a nonreciprocally coupled Frenkel Kontorova lattice

Several solutions of nonlinear systems can be understood as *localized structures*, characterized by a position. These structures can coexist over a homogeneous solution and interact. We have devoted our attention to the vortex type of localized structure, which can be observed in homeotropic anchored nematic liquid crystal or any stripped pattern. The initial number of vortices created in a region starts to decrease according to a *coarsening* law; this may happen in the whole system, or in a co-mobile reference frame (in a system with advection, or equivalently, some form of nonreciprocal coupling).

We can develop similar analysis to front-type localized structures. We reported how one dimensional fronts into the stable state (or phase walls) are created from random initial conditions, unveiling the nucleated number of defects as a function of parameters in chapter 3. Here, we extend the study to fronts into the stable state in a discrete lattice; for this, we extend our prototypical overdamped nonreciprocal Frenkel Kontorova model to two spatial dimensions.

The case of a lattice

Instead of a chain, we analyze a lattice. The generalization to a lattice is direct and reads

$$\begin{aligned} \dot{A}_{ij} = & \sin A_{ij} + (D - \alpha)(A_{i+1j} - A_{ij}) - (D + \alpha)(A_{ij} - A_{i-1j}) \\ & + D_{\perp}(A_{ij+1} - A_{ij}) - D_{\perp}(A_{ij} - A_{ij-1}) + \sqrt{\Gamma}\xi_{ij}(t), \end{aligned} \quad (4.1)$$

where we have promoted $A_i \rightarrow A_{ij}$. D_{\perp} represents the transversal coupling to the chain (in the new direction introduced), and in principle, it could be a nonlinear function of A_{ij} . For simplicity we take $D_{\perp} = D$. Now, the solutions connecting the equilibrium states are curved fronts, and the front position is characterized by a curve instead of a single point. Interestingly, we can measure the average length of these fronts (or domain walls) $L \propto \langle \theta^2 \rangle \equiv \langle A_{ij}^2 \rangle$ as a function of space or time, and find that it exhibits coarsening dynamics as illustrated in figure 4.1.

Coarsening dynamics

We find characteristic exponents for the average front length as a function of space. This is due to their continuous emission at the boundaries and subsequent relaxation dynamics

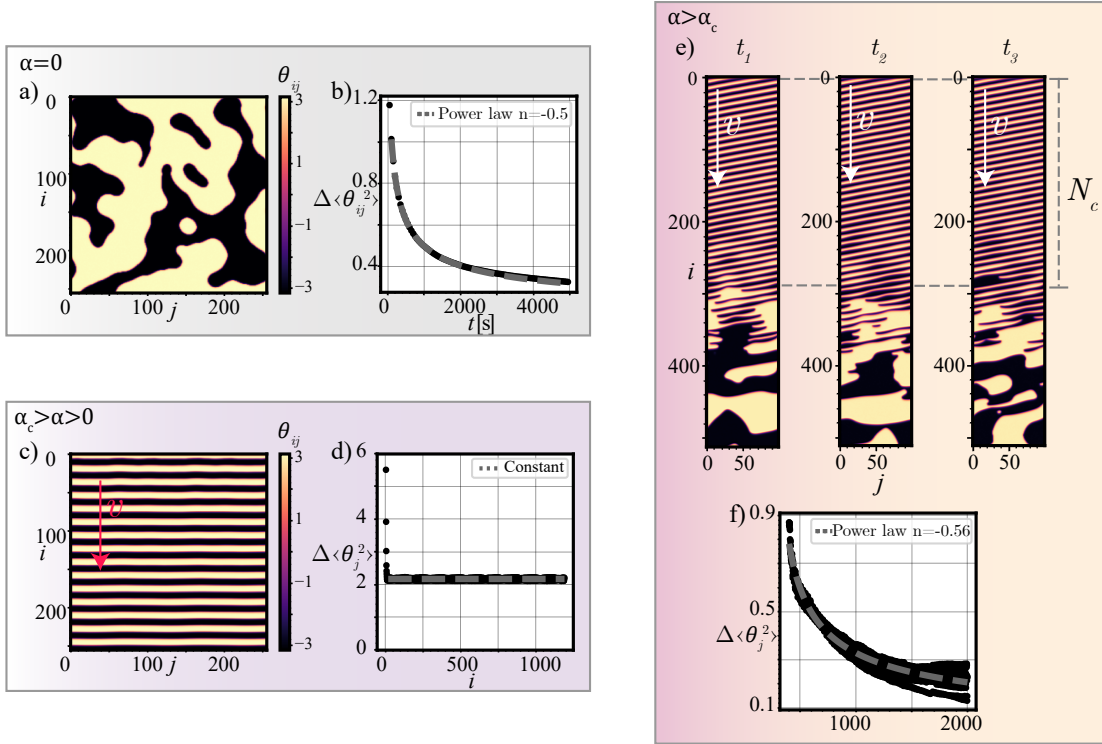


Figure 4.1: Dynamics of the nonreciprocally coupled Frenkel-Kontorova lattice. a) shows a snapshot of the dynamics in the absence of nonreciprocity. b) depicts how the phase wall size obeys a coarsening law in time for $\alpha = 0$. c) and d) exemplify values of intermediate nonreciprocity level α , where patterns can be observed despite fluctuations; here, the phase wall size is constant due to the periodicity of the self-assembled pattern. e) and f) illustrate how fluctuations can destabilize the pattern when high nonreciprocity creates permanent advected phase wall dynamics. The coarsening law of the $\alpha = 0$ case is observed with the change of variables $t \rightarrow i$.

while being drifted due to the nonreciprocity coupling effect. Panels a) and b) of figure 4.1 illustrate the case in the absence of nonreciprocal coupling, where one observes the relaxation dynamics of the front length evolving in time as $L \propto t^{-0.5}$; panels c) and d) show a state in which the self-assembled pattern dominates, and the front length remains constant both in time and in space; panels e) and f) show the general case, in which fronts will have a velocity proportional to the nonreciprocal coupling α (see the velocity of fronts into the stable state formulas) and continuously form at the boundaries, the almost linear relationship between each front point coordinate and time allows to understand the coarsening law exhibited this time in space $L \propto i^{-0.56}$ (which is obtained by replacing $i_{fronts} \approx \langle v_{fronts} \rangle t$ in the relaxation dynamics previously discussed). The work to analytically predict these behaviors is under development, employing ideas for the motion of curved fronts found in [23] together with the inclusion of nonreciprocal coupling in the dynamic.

2. Traveling patterns in liquid crystals

The distribution in space for dislocations in patterns reported in chapter 4 has strong numerical and theoretical evidence; however, the observations are available only for patterns virtually static in our timescale. To have a real-time observation of the dislocation dynamics, we employ the LCLV experiment described in part I of this dissertation. There, patterns can be easily observed. We can theoretically support this claim employing equation 2.15; linearizing around an homogeneous equilibrium state θ_0 and proposing a Fourier mode as an ansatz $\theta = \theta_0 + \theta_k e^{i\mathbf{q}\cdot\mathbf{r} + \lambda t}$ gives

$$\lambda(\mathbf{q}) = -1 - \mathbf{q}^2 l^2 + \frac{\pi}{4} \frac{(\Gamma V_{FT})^{1/2} i \beta \sin[2\theta_0]}{[\Gamma V_0 + 2\alpha (1 + \cos[\beta \cos^2 \theta_0])]^{3/2}} \left[\left(e^{-i\beta \cos^2 \theta_0} - 1 \right) e^{i(\delta q_x + L \mathbf{q}^2 / 2k)} - \left(e^{i\beta \cos^2 \theta_0} - 1 \right) e^{i(\delta q_x - L \mathbf{q}^2 / 2k)} \right].$$

It is easy to see that the previous equation has a preference in the x direction (the direction of nonreciprocity); it is in this direction that patterns with nonvanishing wavenumber will form. In reducing the dynamics to a center manifold to understand the development of the pattern, we note that the symmetries lead us to a Ginzburg-Landau type of equation. The situation is analogous to the one studied in chapter 4, and we can compare how defects distribute in space. Figure 4.2 exhibits the preliminary results.

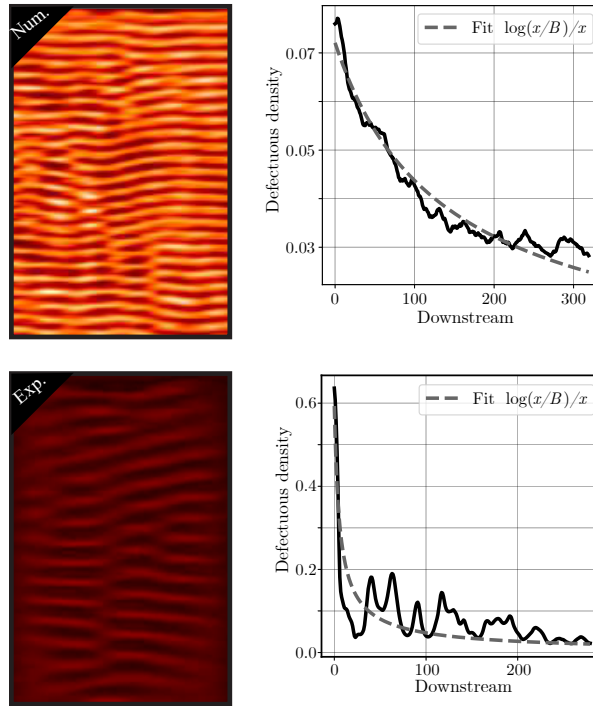


Figure 4.2: Traveling patterns and dislocation dynamics in the LCLV. The upper panels show the numerical simulation results employing Eq. 2.15 with parameters $V_0/V_{FT} = 1.05$, $I_0 = 1$, $\alpha/\Gamma V_{FT} = 2.6$, $L = -1.5$, $\delta = 0.3$ (space and time units are such that $\tau = l = 1$). The bottom panels show the preliminary experimental measures courtesy of Pedro Aguilera, a collaborator in this part of the work.

3. Non-oriented traveling patterns: traveling labyrinth

The question of the coarsening dynamics of defects can be extended even more. Having analyzed the phase wall dynamics and the dynamics of vortices when dynamical systems are subjected to nonreciprocal coupling, we ask which could be the effect in more complex nonlinear structures.

An interesting pattern exhibiting several defects is the *labyrinthine* pattern, rigorously described for the first time by Echeverria-Alar and Clerc [44]. Labyrinthine patterns exhibit dislocations, like striped patterns, but they also host disclinations, amplitude walls, and phase walls [23, 66]. All of them connect different stripe orientations. Due to them, the labyrinthine pattern is a rich place to analyze the dynamics of defects.

Unfortunately, a traveling labyrinth may be difficult to observe due to the fragility of the degeneracy of critical wavevectors, which is easily destroyed when including any nonreciprocal coupling. Numerical simulations of the integrodifferential model described in chapter 4 show a traveling labyrinth depicted in figure 4.3

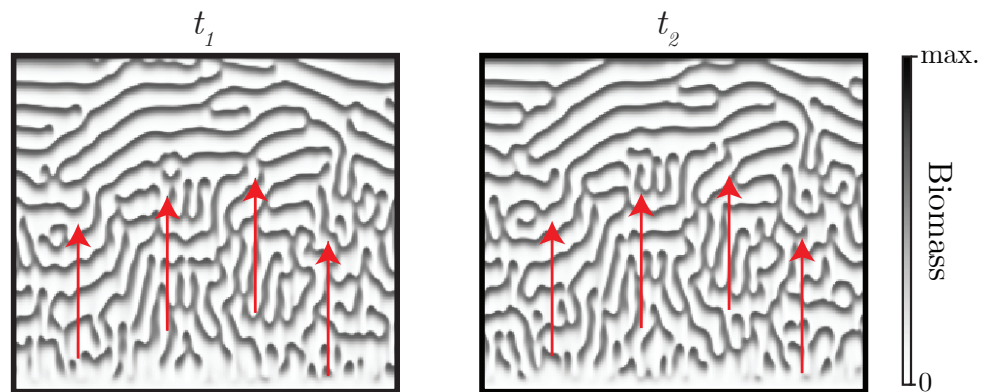


Figure 4.3: Traveling labyrinthine patterns in the integrodifferential model for population dynamics.

Part III: The effects of heterogeneity.

Heterogeneity in the parameters of systems can be unavoidable up to some threshold. Nothing is perfect, even in controlled environments. The vegetation patterns presented in the previous chapter are one system we analyzed in which heterogeneities are prominent. Plants are fundamentally different from each other in complex ways through genetics, with variety being favorable for plant development [67]; the soil is highly heterogeneous in density and nutrients, with topography playing a fundamental role [68–70]; soil moisture islands [71] provoke certain spatial regions to be favorable. One can readily see the effects of heterogeneity in patterns, such as the variations in wavelength inside single pattern patches, irregular boundaries of spots of vegetation, and high density variability.

Heterogeneities in the parameters can have various origins, as mentioned above. How to model them is another problem to tackle; one would need to consider other variables coupling to the biomass that evolve on timescales orders of magnitude slower; thus, they are virtually fixed variables varying in space only. However, the initial condition for such variables (that could or could not play a crucial role in determining the heterogeneity field) is unknown. Then, one needs to model them up to some degree. Imagine one starts with a random spatial distribution of a slow variable coupling to biomass, say, the soil infiltration rate of water; clearly, in real life, spatial correlations exist; thus, we implement simple rules to generate correlated distributions. One interesting question is whether these short-correlated heterogeneities can produce changes at the community level or not.

Here, we try to answer whether short-correlated random heterogeneities significantly affect the biomass density distribution predicted at equilibrium. We emphasize a reduced model covering two approaches proposed for biomass spatiotemporal evolution. The reduced equation derived is valid near a critical point of the corresponding dynamical systems, and it is obtained employing nonlinear changes of variables together with scale separation expansions. First, a regime of dissipative phase separation is studied, discerning the coarsening laws for the average biomass in time and the avoiding of catastrophic shifts. Second, the effects of heterogeneities on a pattern formation regime are analyzed, emphasizing the labyrinthine patterns observed in nature.

Chapter 5

Vegetation covers phase separation in inhomogeneous environments (Chaos, Solitons & Fractals 163, 112518)

The dynamic of population models is often described by logistic equations, which can be considered an empirical law capable of describing all sorts of populations over time [72]. The observation of spatial patterns in the distribution of vegetation biomass motivated the proposal of more involved mathematical models. Cellular automata models were first proposed [73]. Later, a mean-field theory defining a biomass density was proposed by Lefever and Lejeune in 1997 [74]; the model features nonlocal interactions of the density field modeling cooperative and competitive feedback. Similarly, a continuous theory based on reaction-diffusion equations coupling the biomass density field with the soil water density field was proposed by Klausmeier in 1999 [75] considering the advective transport of water in a single direction. Meron et al. proposed in 2001 [76] a more involved model considering diffusive transport in water as a first approximation and providing more realistic terms modeling the interaction. Later, in 2004, Gilad and Meron et al. [77] incorporated nonlocal interactions in reaction-diffusion models of water and biomass density. These pioneer works have motivated various models to be presented later, taking the perspective of nonlocal coupling, water-biomass coupling, or both [6, 78]. These models could display patterns. However, their high nonlinearities also allow for a bistability regime. A finite biomass density could coexist with the bare soil solution in these models, with interfaces mediating the spatial extent of these equilibria.

In this chapter, based on the observation of diverse heterogeneous distributions of biomass fields in satellite images, we develop a model from both a nonlocal and a reaction-diffusion system to describe the phenomenon of phase separation observed, where regions of homogeneous density arrange with the bare soil solution in various shapes. The usual theory of phase separation has well-studied asymptotic states which are not observed in this natural system. To reproduce the natural observations, we propose including heterogeneities in the system's parameters. This simple ingredient is capable of inducing in the mathematical model solutions various of the properties observed in actual observations. We also numerically analyze the coarsening dynamics of the average biomass density and how it could be affected by heterogeneities.



Vegetation covers phase separation in inhomogeneous environments

D. Pinto-Ramos^{a,*}, S. Echeverría-Alar^{a,1}, M.G. Clerc^{a,1}, M. Tlidi^{b,1}

^a Departamento de Física and Millennium Institute for Research in Optics, Facultad de Ciencias Físicas y Matemáticas, Universidad de Chile, Casilla 487-3, Santiago, Chile

^b Faculté des Sciences, Université libre de Bruxelles (ULB), CP. 231, 1050 Brussels, Belgium

ABSTRACT

Vegetation patterns in arid and semi-arid ecosystems as a self-organized response to resource scarcity is a well-documented issue. Their formation is often attributed to the symmetry-breaking type of instability. In this contribution, we focus on a regime far from any symmetry-breaking instability and consider a bistable regime involving uniformly vegetated covers and a bare state. We show that vegetation populations exhibit non-random two-phase structures where high biomass density regions are separated by sparsely covered areas or even bare soil. These structures are referred to as phase separation vegetation covers. We provide observations of this phenomenon in Gabon, Angola, Argentina, and Mexico. The inhomogeneities in environmental conditions are crucial to explain the origin of phase separation vegetation covers. We derive a simple equation from ecologically relevant models to explain various field observations. The bifurcation diagrams obtained from this model allow us to prove that inhomogeneity in the aridity parameter is a source of resilience for vegetation covers, avoiding collapsing towards a bare state. We characterize the natural observations and the equilibria from the model by using Fourier transform technique, spatial autocorrelation analysis, and size distribution of patches analysis.

1. Introduction

The fragmentation of landscapes and loss of biological production in drylands, which leads to desertification as a result of climate change and longer drought periods, is one of the world's most pressing environmental challenges. This fragmentation is typically accompanied by a non-equilibrium symmetry breaking instability, even when the topology of the landscapes is flat [1,2]. The patterns that emerge from the symmetry-breaking instability is generically called vegetation patterns. The 'tiger bush' is a well-known example that was first seen in the early 1940s thanks to the development of aerial photography [3]. Since this discovery, several modeling approaches have been proposed to explain the origin of these patterns, ranging from cellular-automata models [4], integrodifferential equations [1], reaction-diffusion equations [5–8], to spatially stochastic models [9, 10]. The later approach focuses on how environmental randomness can be used to create symmetry-breaking transitions that lead to the formation of vegetation patterns. Besides tiger bush other spatially periodic vegetation patterns have been reported such as hexagons [1,2,11,12], and labyrinths [2,12].

Vegetation patterns are not always periodic. They can be localized in space [13–17], found close to the symmetry-breaking instability. In [18,19], it is established how two well separated isolated patches interact in one- and two-dimensions. As one moves out from the patch center, the patch tail monotonically decays, whereas localized gaps have a damped oscillatory tail. Depending on how far apart the

gaps are, the interaction can be either attractive or repulsive [20]. Localized patches may exhibit a curvature instability that causes the self-replication phenomenon [21,22] or the emergence of arcs and spirals [23].

Nonperiodic vegetation patterns in a regime far from any symmetry-breaking instability can be observed in nature. These structures emerge spontaneously from random perturbations of the unstable homogeneous steady state that separates the two stable states forming a bistable system. This phenomenon is referred as phase separation. Growth of spatial domains of different phases whose dynamics is governed by power law in systems with conserved and nonconserved order parameters is a well documented issue [24–26]. This phenomenon has been studied in a variety of out-of-equilibrium systems, including polymer chemistry [27,28], material science [29], optical systems [30–33] and cell biology [34]. However, the topic of phase separation in ecosystems caused by environmental inhomogeneity has received little attention.

Examples of phase separation in ecosystems are shown in Fig. 1. These are satellite photos, retrieved from Google Earth software, of vegetation coverage in different regions. Near the African coast, the landscapes of Gabon (see Fig. 1a) and Angola (see Fig. 1b) show distinct patches of bare soil and planted areas of various sizes and forms. Scattered vegetated and non-vegetated areas are seen in the hilly regions of Argentina (see Fig. 1c) and Mexico (see Fig. 1d). It is seen that the vegetation distribution in all these places is inhomogeneous. Modeling

* Corresponding author.

E-mail address: david.pinto@ug.uchile.cl (D. Pinto-Ramos).

¹ David Pinto-Ramos, Sebastián Echeverría-Alar, Marcel G. Clerc, and Mustapha Tlidi contributed equally to the production of this work.

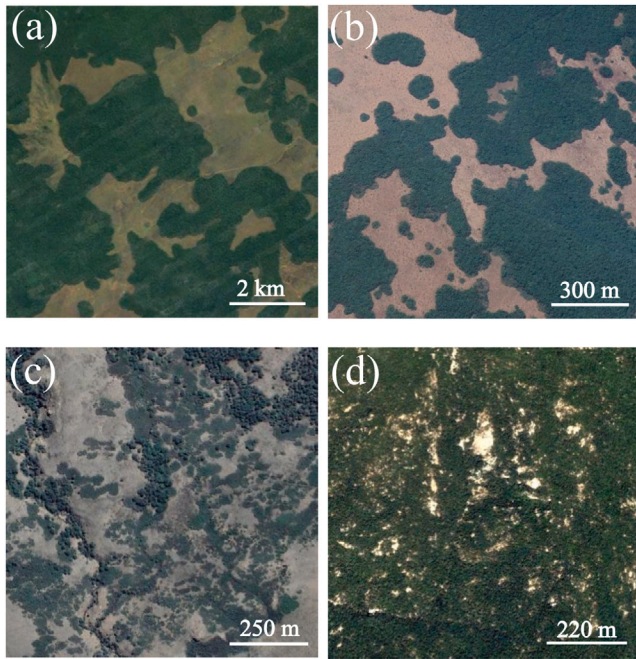


Fig. 1. Vegetation pattern phase separation. Top views of (a) Gabon, Africa ($2^{\circ} 44' 08.42''$ S, $10^{\circ} 12' 28.37''$ E), (b) Angola, Africa ($6^{\circ} 19' 39.10''$ S, $12^{\circ} 35' 25.98''$ E), (c) Argentina, South America ($40^{\circ} 58' 17.21''$ S, $71^{\circ} 16' 03.76''$ O), and (d) Mexico, North America ($29^{\circ} 04' 25.99''$ N, $110^{\circ} 11' 19.27''$ O).

approaches in vegetation ecosystems do not exhibit heterogeneous non-periodic self-organization as equilibrium. The spatial characterization of such vegetation states and the transitions between them have not been explored.

We propose a unified description for non-homogeneous and non-periodic vegetation covers, vegetation pattern phase separation. We show that the inhomogeneous vegetation covers are equilibrium states of the ecosystem under inhomogeneous environment. We demonstrate how the inclusion of inhomogeneities in the parameters plays a crucial part in explaining the wide range of distinct observed equilibria. We observe that the vegetation spatial organization is characterized by a power-law distribution in Fourier space and an exponential decay in the spatial correlation. Finally, a power law for the early temporal evolution of the total biomass is numerically inferred.

Following an introduction, Section 2 shows the characterization of the spatial self-organization of the satellite images in Fig. 1. In Section 3, we present a straightforward Fisher–Kolmogorov–Petrovskii–Piskunov (FKPP) type model with inhomogeneous environmental conditions and explore the dynamics of phase separation vegetation covers. The study of equilibria and the coarsening dynamics of homogeneous states are discussed in Sections 4 and 5, respectively. In Section 5.2, we examine how the coarsening dynamics are impacted by an inhomogeneous environment by avoiding collapse to the bare state. The paper is concluded in Section 6. A detailed derivation of the FKPP equation from the generic interaction redistribution model and the reaction–diffusion water and biomass model is included in the Appendix section.

2. Spatial characterization of field observations

To characterize vegetation phase separation patterns shown in Fig. 1, we evaluate their Fourier spectrum and their spatial autocorrelation. The results are shown in Fig. 2, where the Fourier spectrum $|F(q)|^2$, as a function of the radial wavevector q , is depicted in Fig. 2(a₁, b₁, c₁, d₁). All satellite images taken from Gabon, Angola, Argentina, and Mexico unexpectedly possess a power-law decaying tail connecting

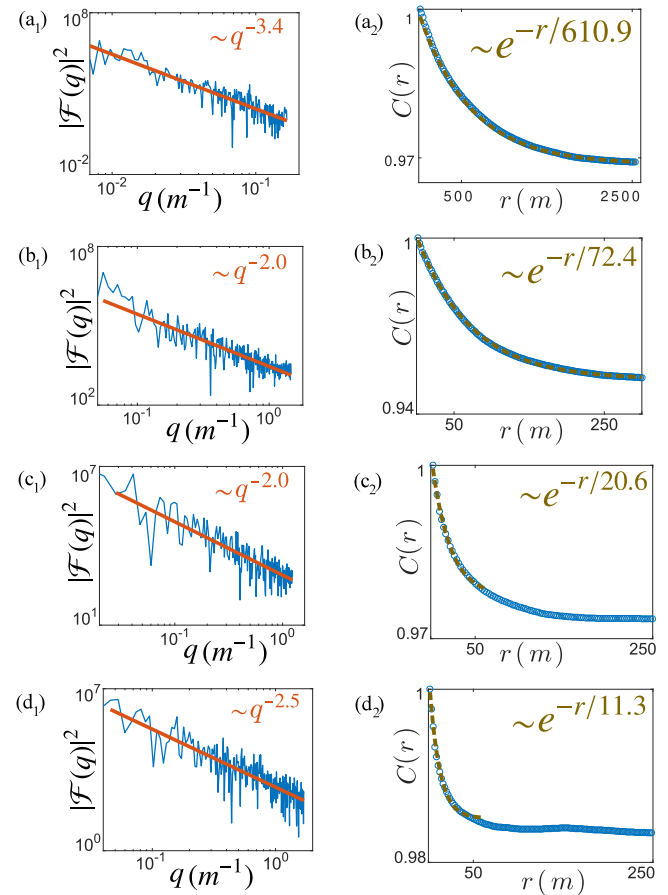


Fig. 2. Fourier spectra and spatial autocorrelations. The blue dots and the blue lines represent the real data from the vegetation images of Fig. 1. (a₁, b₁, c₁, and d₁) correspond to the Fourier spectrum of Gabon, Angola, Argentina, and Mexico vegetation patterns, respectively. The red line in the Fourier space illustrates the power-law behavior of the tail in the radial direction q . The exponents range from 2.0 to 3.4. The R^2 values of the linear fittings are (a₁) 0.79, (b₁) 0.77, (c₁) 0.69, and (d₁) 0.70, respectively. (a₂, b₂, c₂, and d₂) are autocorrelations corresponding to Gabon, Angola, Argentina, and Mexico vegetation patterns, respectively. The characteristic correlation lengths l are (a₂) $l = 610.9$ m, (b₂) $l = 20.6$ m, (c₂) $l = 11.3$ m, and (d₂) $l = 72.4$ m. They are obtained by fitting the exponential law $Be^{-r/l}$ to the real data, where B is a positive constant. The R^2 value of all the exponential fittings is 0.99. (For interpretation of the references to color in this figure legend, the reader is referred to the web version of this article.)

a range of spatial scales in the wavevector space. In this figure, the linear fitting is indicated by red line. At the very least, this eliminates the possibility of a wavelength selection process leading to the formation of periodic vegetation patterns. Besides, each vegetation photograph of Fig. 1 is accompanied by spatial autocorrelation function $C(r)$ as a function of a distance r [see Fig. 2(a₂)]. The vegetation structures have a spatial autocorrelation characterized by an exponential decay behavior until an asymptotic value is reached. Up until great distances, Gabon shown in Fig. 2(a₂) and Angola shown in Fig. 2(b₂) exhibit an exponential behavior. At small distances, the exponential decay is truncated in Argentina and Mexico as shown in Fig. 2(c₂) and Fig. 2(d₂), respectively. The exponential decay is represented by fitting curves of the form $\sim e^{-r/l}$ of the autocorrelation data [see brown dashed lines in panels of Fig. 2(a₂, b₂, c₂, d₂)]. The correlation length is denoted by l , which describes the local vegetation pattern phase-separation of a well defined mean patch size. In fact, a closer look at the vegetation covers in Fig. 1 reveals nonperiodic behavior, leaving aside the explanation of spontaneous symmetry-breaking mechanisms.

The Fourier spectra together with spatial autocorrelations indicated that the vegetation patterns observed in Africa and America reported in

Fig. 1 do not emerge spontaneously from symmetry-breaking instability but rather from phase separation mechanism. Independent of the region of the planet, and type of soil and vegetation (bushes, patches, shrubs, trees), we observe a power-law in Fourier space and an exponential decay of the autocorrelation function. In the next sections, we introduce a model and provide an explanation to the field observations.

3. Phase separation dynamics for biomass

We adopt a continuous time and space description of the biomass density $b(x, y, t)$ at space coordinates $\mathbf{r} = (x, y)$ and time t . Theory of vegetation patterns based on the non-local FKPP equation has been reported in [35–37]. In this contribution, we consider the paradigmatic local FKPP [38,39] model equation describing the population dynamics of individuals with the inclusion of small inhomogeneities in the growth parameter

$$\partial_t b = -\left(\eta + \sqrt{\Gamma} \xi(\mathbf{r})\right) b + \kappa b^2 - b^3 + D \nabla^2 b. \quad (1)$$

This simple model is derived from the nonlocal FKPP equation, and from reaction–diffusion water biomass model (see the Appendix). The parameter η measures the linear growth ($\eta < 0$) or decay ($\eta > 0$) of vegetation population. η increases as the aridity of the environment increases; κ measures the net effect of facilitative versus competitive interactions, and b^3 is the nonlinear saturation. The last term describes diffusion with coefficient D and $\nabla^2 = \partial_{xx} + \partial_{yy}$ is the bidimensional laplacian operator. The degree of aridity described by the parameter η of an environment is related with on-site evapotranspiration process [40]. A spatial distribution of this process can arise naturally due to different type of soil, diverse plant groups, and topographic variations [41]. The function $\xi(\mathbf{r})$ models these environmental inhomogeneities and Γ measures the intensity of them.

Let us briefly recall that Eq. (1) can be stated in gradient form

$$\partial_t b = -\frac{\delta F}{\delta b}, \quad F \equiv \int d\mathbf{r} \left(\eta(\mathbf{r}) \frac{b^2}{2} - \kappa \frac{b^3}{3} + \frac{b^4}{4} + \frac{D}{2} (\nabla b)^2 \right), \quad (2)$$

where $\eta(\mathbf{r}) = \eta + \sqrt{\Gamma} \xi(\mathbf{r})$. Then, it is well-known that the system Eq. (1) will reach an equilibrium minimizing the potential F .

In what follows, we focus on the effects of independent inhomogeneities in space. In this case, the function $\xi(\mathbf{r})$ is generated by a delta-correlated gaussian random process of zero mean. In the absence of inhomogeneities, i.e., $\Gamma = 0$, the model for vegetation Eq. (1) was derived from ecologically relevant models (see the Appendix). It has also been derived from a variety of physical systems, including liquid crystals [42], flame combustion [43], fiber Kerr resonators [44], passive Kerr cavity [45], and electrical circuits [46], to mention a few.

Eq. (1) for $\Gamma = 0$ supports domain walls [47] (or bistable fronts) separating the two stable equilibrium states $b_{h1} = (\kappa + \sqrt{\kappa^2 - 4\eta})/2$ and $b_{h2} = 0$. One important aspect of equilibria, is that for positive values of κ there exist a tipping – or saddle node – point at $b_s = \kappa/2$ and $\eta_s = \kappa^2/4$. As one crosses the critical aridity $\eta = \eta_s$, this bifurcation, which is defined by the annihilation of two equilibria, causes dramatic changes in the system [48], well documented as catastrophic shift in ecology.

The dynamics of Eq. (1) in the simple case of homogeneous environmental conditions, is characterized by front propagation. Straightforward calculations lead to a propagation speed of the fronts proportional to the difference of energy of the homogeneous states. Neglecting the curvature effects for the domain propagation, the speed of walls reads (see the textbook [47] and reference therein)

$$v_{walls}(b_{h1} \rightarrow b_{h2}) \equiv v_0 \propto F(b_{h2}) - F(b_{h1}), \quad (3)$$

$$F(b) \equiv \eta \frac{b^2}{2} - \kappa \frac{b^3}{3} + \frac{b^4}{4}. \quad (4)$$

In homogeneous environmental conditions where η is a constant, the dynamics leads to either a uniform vegetated cover or a state totally

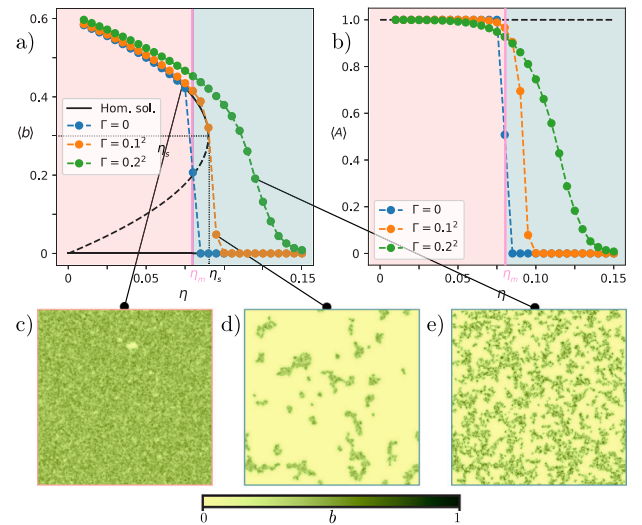


Fig. 3. The bifurcation diagram of Eq. (1) for parameters $\kappa = 0.6$ and $D = 0.1$, showing the different behaviors for different Γ values. (a) Bifurcation diagram for the averaged biomass $\langle b \rangle$. (b) Bifurcation diagram for the area fraction $\langle A \rangle$. (c), (d) and (e) show examples of the different equilibria exhibited in the bifurcation diagram. (For interpretation of the references to color in this figure legend, the reader is referred to the web version of this article.)

devoid of vegetation. This approximation cannot explain the wide range of vegetation patterns depicted in Fig. 1. It is then necessary, to include inhomogeneities in the environmental conditions, such as the aridity, which will explain the field observation as we will see in the next section.

4. Equilibrium states analysis

In this section, we discuss equilibria of Eq. (1) first in the homogeneous parameter $\Gamma = 0$ case, and then when $\Gamma \neq 0$, considering both delta-correlated and spatial correlated inhomogeneities.

4.1. Homogeneous case $\Gamma = 0$

Starting from random initial conditions $b_i(\mathbf{r}, 0)$ around the unstable vegetated state, one can introduce the averaged biomass $\langle b \rangle \equiv \sum_{i=1}^N \int d\mathbf{r} b_i(\mathbf{r}, T) / NL^2$, where N is the number of realizations and T is the time to reach equilibrium. $\langle b \rangle$ exhibits an abrupt change when increasing the aridity parameter η as shown by the blue dotted curve in Fig. 3(a). There exist a single point called the Maxwell point and denoted by $\eta = \eta_m$, where front solutions of Eq. (1) are stationary, i.e., when the two stable homogeneous steady states have the same energy. For $\eta < \eta_m$, b_{h1} has the lowest free energy density, whereas for $\eta > \eta_m$, $b_{h2} = 0$ is the preferred state. Figs. 3(b) illustrates the bifurcation diagram for the mean biomass $\langle b \rangle$ and the biomass area fraction $\langle A \rangle \equiv \sum_{i=1}^N \int d\mathbf{r} A_i(\mathbf{r}, T) / NL^2$, respectively. The latter is defined using the binarized biomass field A_i for different initial conditions b_i as

$$A_i(\mathbf{r}, T) \equiv \begin{cases} 1 & \text{if } b_i(\mathbf{r}, T) \geq b_s = \kappa/2, \\ 0 & \text{if } b_i(\mathbf{r}, T) < b_s = \kappa/2. \end{cases} \quad (5)$$

The biomass area fraction corresponding to the case $\Gamma = 0$ is indicated by the blue dotted curve in Fig. 3(b). Without inhomogeneities, numerical simulations of Eq. (1) for a long time evolution, reach either a uniform cover state or a state totally devoid of vegetation. These equilibrium biomass covers correspond to an area fraction one or zero in Fig. 3(b), respectively. Therefore, vegetation patterns and phase separation vegetation covers are excluded in this case.

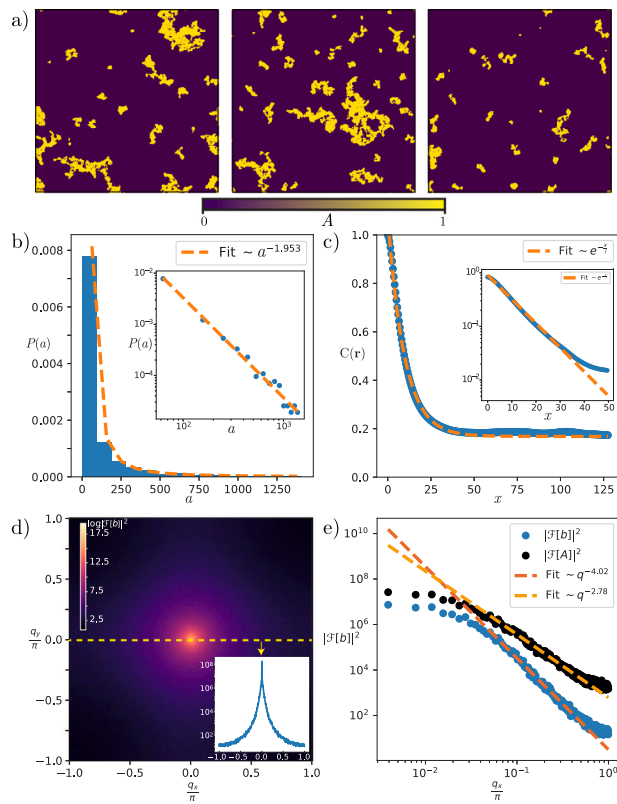


Fig. 4. Statistical analysis of a low area fraction equilibrium for parameters $\kappa = 0.6$, $D = 0.1$, $\eta = 0.95$, and $\Gamma = 0.01$. (a) Examples of equilibrium A fields. (b) Probability density of patch area $P(a)$ with a power law fit and its logarithmic scale graph in the inset. (c) Autocorrelation function of the b field, showing an exponential fit and a semi logarithmic scale graph in the inset. (d) Averaged absolute value of the Fourier transform of b in semi logarithmic scale (for contrast purposes). (e) Logarithmic scale graph for the tail of the Fourier transform with power law fits for the A and b fields. (For interpretation of the references to color in this figure legend, the reader is referred to the web version of this article.)

4.2. Inhomogeneous $\Gamma \neq 0$ and non-correlated $\xi(\mathbf{r})$ case

When the aridity parameter is inhomogeneous $\Gamma \neq 0$, numerical simulations of Eq. (1), using different random initial conditions and different realizations of $\xi(\mathbf{r})$, show there is no abrupt change in the mean biomass for large enough Γ . Fig. 3(a) show this smooth transition (see orange and green curves). In this case, the transition is rather continuous avoiding a catastrophic shift in the ecosystem.

Contrarily to the homogeneous case, the system can reach phase separation vegetation covers as shown in Figs. 3(c, d, e). Now, the system is characterized by the coexistence of disordered patches of vegetation and bare soil. According to the bifurcation diagram in Fig. 3(b), equilibrium biomass covers can have an area fraction other than zero or one. Note that states with low area fraction ($\langle A \rangle \ll 1$) are found above the Maxwell point ($\eta > \eta_m$) (cf. Figs. 3(d) and 3(e)). However, states with high area fraction ($1 - \langle A \rangle \ll 1$) are only found below the Maxwell point ($\eta < \eta_m$), as shown in Fig. 3(c).

Inhomogeneities can prevent plants from collapsing to bare ground. It is important to notice that even for entirely uncorrelated inhomogeneities, one can recognize the spatial structures seen in vegetation (see Fig. 1), and predicted by the FKPP Eq. (1). One can identify the location and size of patches by using ImageJ software [49], which has been applied to the field A . Fig. 4(a) shows examples of the field A for different realizations of the numerical simulations. It is interesting to note that the probability distribution of patch sizes $P(a)$, where a is the area of a biomass patch, follows a power law as shown in Fig. 4(b). This $P(a)$ behavior is in line with some measurement for small patch

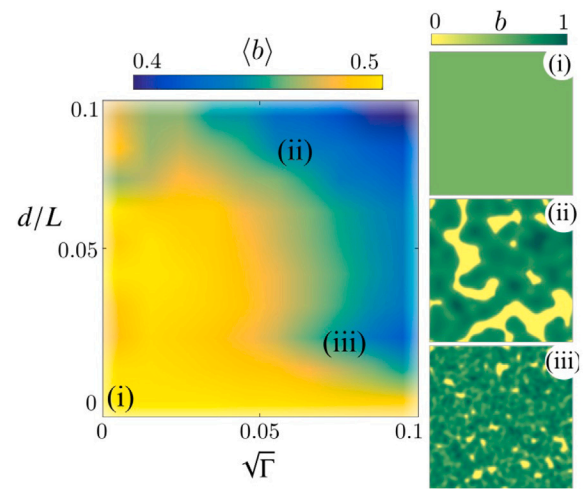


Fig. 5. Steady state averaged biomass $\langle b \rangle$ from Eq. (1) with spatially correlated inhomogeneities. The surface-plot show the average biomass $\langle b \rangle$ for different values of the intensity $\sqrt{\Gamma}$ and the degree of correlation d/L of the inhomogeneities. d is the correlation length of the $\xi(\mathbf{r})$ function, obtained by fitting an exponential law to the autocorrelation $C(r)$ of $\xi(\mathbf{r})$, and L is the size of the simulation box. All the correlated $\xi(\mathbf{r})$ were created with the reaction-diffusion process ($\epsilon = 0.1$). (i) $d/L = 0$ and $\sqrt{\Gamma} = 0$, (ii) $d/L = 0.03$ and $\sqrt{\Gamma} = 0.08$, and (iii) $d/L = 0.08$ and $\sqrt{\Gamma} = 0.07$ correspond to different equilibria obtained in Eq. (1). The biomass b is normalized to 1 in the three insets. (For interpretation of the references to color in this figure legend, the reader is referred to the web version of this article.)

sizes that have been documented in the literature [50]. In addition, as shown in Figs. 4(d) and 4(e), the tails of the Fourier transform of the $b_i(\mathbf{r}, T)$ and $A_i(\mathbf{r}, T)$ fields both follow a power law, typical of complex systems [51,52]. This Fourier space structure translates into a well-defined correlation function with an exponential decay for equilibrium states produced by the model Eq. (1), as shown in Fig. 4(c). We compare the outcomes of numerical simulations of the model equation with the satellite photos provided in Fig. 1 thanks to these straightforward analysis tools.

4.3. Inhomogeneous $\Gamma \neq 0$ and correlated $\xi(\mathbf{r})$ case

In what follows, we address the problem of considering the effects of inhomogeneities that are spatially correlated. To have spatially correlated inhomogeneities, let us consider an initial delta correlated function $\xi(\mathbf{r})$, to go through a simple reaction-diffusion process

$$\partial_s \xi(\mathbf{r}) = -\epsilon \xi(\mathbf{r}) + \nabla^2 \xi(\mathbf{r}), \quad (6)$$

where ϵ is a positive relaxational constant, and s parametrizes the evolution of $\xi(\mathbf{r})$. We extract different temporal stages of this evolution. In this way, we obtain inhomogeneity functions with a degree of spatial correlation, which is characterized by the dimensionless parameter d/L . d is the correlation length and L is the system size. After, we normalize the correlated functions $\xi(\mathbf{r}, s)$ between $[-1, 1]$ in order to control the inhomogeneities in Eq. (1) with the inhomogeneity level intensity Γ . Fig. 5 shows the averaged biomass $\langle b \rangle$ from Eq. (1) for different values of the inhomogeneity intensities Γ and correlation lengths d of the inhomogeneities $\xi(\mathbf{r})$. When increasing d , $\langle b \rangle$ decreases (see insets (ii) and (iii) in Fig. 5) in comparison to the homogeneous case shown in the inset (i) of Fig. 5. This is related to the coherent patches of bare soil that can coexist with the vegetated state thanks to incorporating a correlated inhomogeneity function $\xi(\mathbf{r})$. The addition of the spatial correlation can capture more smooth vegetation distributions, which are comparable to the satellite images of Gabon and Angola (cf. Figs. 1(a) and 1(b), respectively).

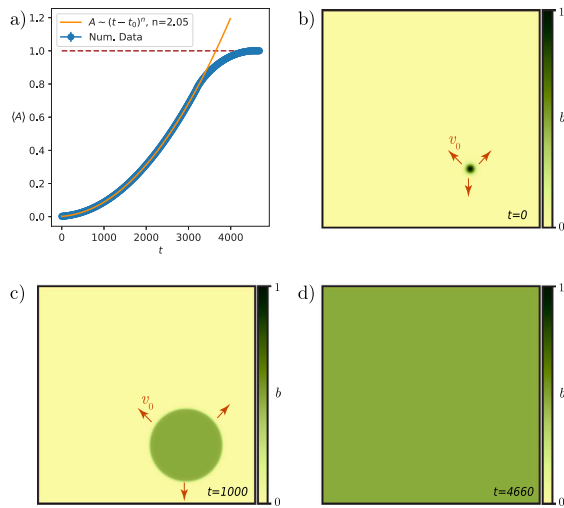


Fig. 6. Biomass propagation in homogeneous landscape. (a) The blue dots are the temporal evolution of the area cover for numerical simulations of Eq. (1), with parameters $\kappa = 0.6$, $D = 0.1$, $\eta = 0.02$, and $\Gamma = 0$. The orange indicates the theoretical prediction from Eq. (9). (b), (c), and (d) are different stages of propagation, showing that homogeneous conditions favor circular patches and full cover at equilibrium. (For interpretation of the references to color in this figure legend, the reader is referred to the web version of this article.)

5. Coarsening dynamics

In the last section, we analyze the early temporal evolution of the biomass density field $b(x, y, t)$ that leads to the equilibrium states discussed previously.

5.1. Coarsening in homogeneous environment

From the front or wall speed Eq. (3), one can infer the temporal evolution for the total cover of the biomass b as depicted in Fig. 6(a). For this, consider that a localized portion of vegetation (patch) is placed on bare ground $b = 0$, as shown in Fig. 6(b). Then, the interface propagates, as seen in Figs. 6(c) and 6(d), with an approximated speed of v_0 (see Section 3 and Eq. (3)). Thus, the characteristic size of the patch increases linearly with time t as

$$\langle L_{patch} \rangle \sim v_0 t. \tag{7}$$

Then, it is straightforward to introduce the total biomass and the area of a patch A_{patch} by

$$b_{total} \sim b_{h1} \langle L_{patch} \rangle^2 \equiv b_{h1} \langle A_{patch} \rangle. \tag{8}$$

From this, one can easily see that

$$\langle A_{patch} \rangle \sim t^n, \tag{9}$$

with $n = 2$. The previous expression is valid for a single patch in space neglecting curvature effects. Otherwise, front interactions and curvature effects alter the simple dynamics of the front. Fig. 6 (a) shows perfect agreement with this simple theory by fitting Eq. (9) to the numerical data.

More interesting is the natural nucleation of multiple patches after an initial perturbation. Initializing the system with random initial conditions, small deviations from the critical exponent $n = 2$ are expected due to multiple patch nucleation, as seen in Figs. 7(a) and (b) for early times. Figs. 7(c) to 7(f) show the temporal evolution of the nucleation of patches. Note that as one gets closer to the Maxwell point, the interaction between walls becomes stronger, and we expect larger deviations from the naive exponent $n = 2$. Unexpectedly, a crossover between exponents $n = 2$ and $n = 3$ is observed for low area fractions $\langle A \rangle$ with the former dominating the early time dynamics.

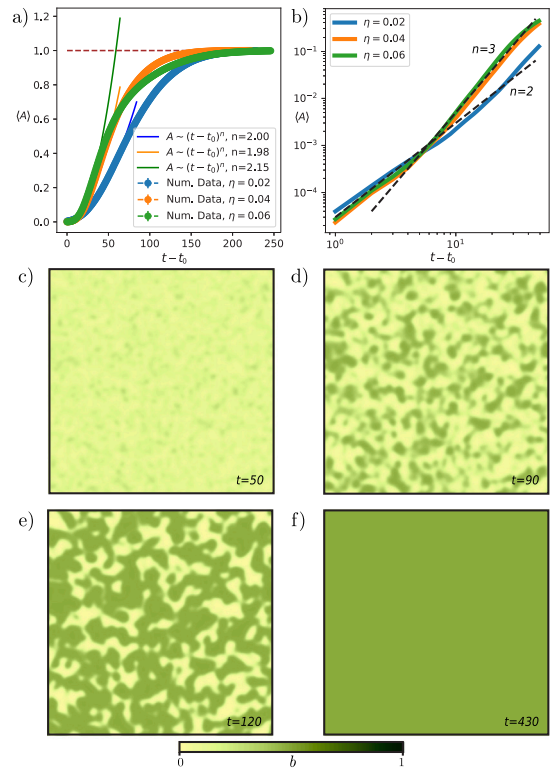


Fig. 7. Temporal dynamics of multiple patch growth in homogeneous landscape. (a) and (b) exhibit the temporal dynamics following power laws in time for the vegetation area cover, calculated from numerical simulation data of Eq. (1) with parameters $\kappa = 0.6$, $D = 0.1$, and $\Gamma = 0$. (c), (d), (e) and (f) show different stages of temporal evolution with coarsening dynamics. (For interpretation of the references to color in this figure legend, the reader is referred to the web version of this article.)

5.2. Coarsening in an inhomogeneous environment

In the case $\Gamma \neq 0$, fronts can suffer from a pinning phenomenon [53], explaining the amorphous shapes we can observe as equilibrium states. Pinning phenomenon has been studied in several fields of physics, appearing naturally in discrete systems such as crystal lattices [54], and pattern forming systems [55]. Spatially modulated parameters could also induce pinning phenomenon as observed in liquid crystal devices [56] or granular media [57].

For the temporal dynamics, fronts will be highly coupled to the external inhomogeneities imposed, putting in doubt the validity of Eq. (7). Surprisingly, coarsening dynamics for low area fractions were observed, although with a different exponent n compared with the homogeneous case, as seen in Fig. 8.

One can see that inhomogeneities increase the characteristic exponent for the area cover growth, from $n = 2$ to $n = 4$. Indeed, it is observed that inhomogeneities dramatically accelerate evolution towards the equilibrium state, reaching an almost full cover approximately fifty times faster compared to the homogeneous case $\Gamma = 0$ case.

6. Conclusions

We have reported satellite photos showing phase separation vegetation covers, obtained from Google Earth software in different landscapes of Africa and America. We have characterized vegetation phase separation patterns by establishing their Fourier spectra and spatial autocorrelations. We have demonstrated that these patterns, independent of the plant involved and the type of soil in which they are observed, exhibit a generic power-law in Fourier space and exponential decay of the autocorrelation function. Thanks to this investigation, we were able

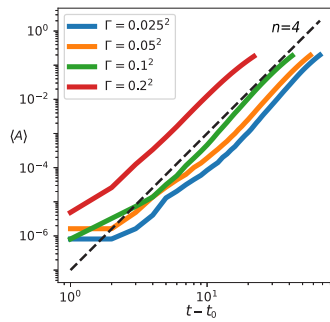


Fig. 8. Effect of inhomogeneities on early temporal evolution. The area cover of vegetation shows a different exponent for its temporal dynamics, from numerical simulations of Eq. (1) with delta correlated $\xi(\mathbf{r})$, parameters $\kappa = 0.6$, $D = 0.1$, $\eta = 0.02$. (For interpretation of the references to color in this figure legend, the reader is referred to the web version of this article.)

to rule out the symmetry-breaking mechanism caused by the formation of periodic vegetation patterns.

We have derived a simple equation, the local FKPP, as a paradigm for the studying of population dynamics, from the generic interaction redistribution model, and the reaction–diffusion water and biomass model. We have demonstrated that environmental inhomogeneities are necessary to account for the phase separation patterns observed in vegetation. Numerical simulations for a long time evolution showed that the model Eq. (1) without inhomogeneities cannot support phase separation vegetation covers.

Simple static indicators such as patch size distributions, spatial Fourier transform analysis, and correlation functions analysis reveal the presence of inhomogeneities. Additionally, we propose dynamical indicators given by the coarsening power-law exponents for the early time evolution of vegetation covers.

More importantly, inhomogeneities are shown to be a source of resilience for vegetation covers. We demonstrated that enough inhomogeneities allowed to avoid collapsing towards a bare state, shedding light on mechanisms to preserve arid ecosystems from the global warming process and long drought periods.

Declaration of competing interest

The authors declare that they have no known competing financial interests or personal relationships that could have appeared to influence the work reported in this paper.

Data availability

Data will be made available on request.

Acknowledgments

D.P.-R. acknowledges the financial support of ANID National Ph.D. scholarship, Chile 2020-21201484. M.G.C. acknowledges the financial support of ANID-Millennium Science Initiative Program-ICN17_012 (MIRO), Chile and FONDECYT, Chile project 1210353. S.E.-A. acknowledges the financial support of ANID National Ph.D. scholarship, Chile 2020-21201376. M.T. is a Research Director at Fonds de la Recherche Scientifique FNRS.

Appendix

A.1. Nonlocal FKPP model

The nonlocal FKPP model for vegetation population reads [20,35]

$$\partial_t b = b(1 - b)m_f(\mathbf{r}) - \mu b m_c(\mathbf{r}) + D m_D(\mathbf{r}), \quad (10)$$

$$m_{f,c} = \exp(\chi_{f,c}) \int d\mathbf{r}' \phi_{f,c}(\mathbf{r}') b(\mathbf{r} + \mathbf{r}'), \quad (11)$$

$$m_D = \int d\mathbf{r}' \phi_D(\mathbf{r}') [b(\mathbf{r} + \mathbf{r}') - b(\mathbf{r})], \quad (12)$$

where b corresponds to the biomass density field, following a logistic growth depending on the neighboring biomass with m_f . Mortality has a base rate μ enhanced by competition feedback through m_c . The seed dispersion is described by the last term in the rhs of Eq. (10). The nonlocal terms Eqs. (11) and (12) correspond to a weighted sum of the biomass with kernels $\phi_{f,c,D}(\mathbf{r}')$. These kernels are decaying functions of the distance between interacting plants, and are assumed to be radially symmetric. They model facilitative (f), competitive (c), and seed dispersion (D) processes. The strength of the competitive and facilitative interactions are χ_f and χ_c , respectively. Whereas D is the intensity of seed dispersion.

We perform a weak nonlinear analysis in Eq. (10). First, note the critical parameter $\mu = \mu_c = 1$ at which the bare soil state $b = 0$ changes its stability. The curve defining the non-trivial homogeneous equilibria is $0 = (1 - b) \exp(\chi_f b) - \mu \exp(\chi_c b)$, and has two positive solutions for $\chi_f - \chi_c \geq 1$. These solutions collapse to the $b = 0$ state at $\chi_f - \chi_c = 1$ and $\mu = \mu_c$. Let us explore the vicinity of the onset of bistability by introducing a small parameter ϵ ($\epsilon \ll 1$) that describes the distance from criticality as

$$\mu = \mu_c + \epsilon^2 \eta, \quad (13)$$

$$\chi_f - \chi_c = 1 + \epsilon \kappa. \quad (14)$$

A linear analysis of Eq. (10) around $b = 0$ with finite wavevector perturbation $b = A \exp(i\mathbf{q} \cdot \mathbf{r} + \lambda t)$ leads to the characteristic equation $\lambda(\mathbf{q}) = 1 - \mu + D(\hat{\phi}_D(\mathbf{q}) - 1)$, where $\hat{\phi}_D(\mathbf{q})$ is the Fourier transform of $\phi_D(\mathbf{r})$. Remembering that the kernels are normalized, it follows that $\hat{\phi}_{f,c,D}(\mathbf{q} = 0) = 1$. Moreover, as the kernels are radially symmetric the expansion for large wavelength perturbation reads $\hat{\phi}_D(\mathbf{q}) \approx 1 + \partial_{q_x q_x} \hat{\phi}_D(\mathbf{0}) q^2 / 2 + \dots$, having at dominant order the band of unstable modes $\Delta q^2 = (\mu - 1) / (D \partial_{q_x q_x} \hat{\phi}_D(\mathbf{0}) / 2) \sim \epsilon^2$. Then, we propose the ansatz

$$b = \epsilon A(T = \epsilon^2 t, \mathbf{R} = \epsilon \mathbf{r}) + \epsilon^2 W^{[2]} + \epsilon^3 W^{[3]} + \dots, \quad (15)$$

where $W^{[n]}$ correspond to nonlinear corrections of order ϵ^n . Additionally, we expand the integral terms, provided that the kernels in Eqs. (11) and (12) decay faster than an exponential, as

$$\int d\mathbf{r}' \phi_{f,c,D}(\mathbf{r}') b(\mathbf{r} + \mathbf{r}') \approx b(\mathbf{r}) + \frac{\nabla^2 b}{4} \int d\mathbf{r}' \phi_{f,c,D}(\mathbf{r}') \mathbf{r}'^2 + \dots$$

By replacing this expansion and Eqs. (13), (14), (15) in Eq. (10) a hierarchy of equations at different orders in ϵ are found. Orders ϵ and ϵ^2 satisfy automatically the solvability condition, and at ϵ^3 order we get the equation

$$\partial_T A = -\eta A + \kappa A^2 - A^3 / 2 + D_e \nabla^2 A, \quad (16)$$

where

$$D_e = \frac{D}{4} \int d\mathbf{r}' \phi_D(\mathbf{r}') \mathbf{r}'^2. \quad (17)$$

In this way, with a renaming and scaling of variables and parameters in Eq. (16), we recover the local FKPP Eq. (1).

A.2. Water and biomass model

Another popular approach to explain the vegetation pattern formation proposed in the literature is based on water transport [5–8]. When biomass and water interact, vegetation ecosystems can be modeled by a pair of coupled reaction–diffusion equations. A general approach when considering sloped territory was provided in [5]. A model considering the possible bistability between bare soil and populated state reads [58]

$$\begin{aligned}\partial_t b &= b(1-b)w(1+\gamma b)^2 - \mu b + D\nabla^2 b, \\ \partial_t w &= p - w - \sigma b w(1+\gamma b)^2 + \nabla^2 w.\end{aligned}\quad (18)$$

Where b and w correspond to the biomass and ground water density fields, respectively. γ characterizes the increase of biomass production with water consumption. The parameter μ represents the mortality rate and D accounts for the dispersal by seeds. The parameter p models the mean water input to the system, and σ weights the water lost by consumption of the biomass.

We can derive a normal form equation for long wavelength perturbations near the onset of bistability. Let us consider the linear dynamics around the bare soil state as $(b, w) = (0, p) + \delta A \vec{v} \exp(i\mathbf{q} \cdot \mathbf{r} + \lambda t)$, with $\delta A \ll 0$, the jacobian reads

$$J = \begin{pmatrix} p - \mu - Dq^2 & 0 \\ -\sigma p & -1 - q^2 \end{pmatrix}, \quad (19)$$

which has eigenvalues $\lambda_s(q) = -1 - q^2$ and $\lambda_u(q) = p - \mu - Dq^2$. The eigenvalue λ_u can change of sign at $\mu_c = p$ and the equilibrium point changes its stability. The corresponding band of unstable modes is $\Delta q^2 = (p - \mu)/D$. thus, close to the instability of the bare soil solution $p = \mu$, slow spatial variations domain the dynamics ($\Delta q^2 \rightarrow 0$). We use a multiple time–space scale analysis to establish a simple normal form model Eq. (1). We choose a small parameter ϵ which measure the distance from the critical point $p = \mu$ as

$$p = \mu - \epsilon^2 \eta, \quad (20)$$

then, $\Delta q^2 \sim \epsilon^2$. The non-trivial homogeneous equilibria read $w_1 = \mu / [(1-b)(1+\gamma b)^2]$ and $w_2 = p / [1 + \sigma b(1+\gamma b)^2]$. The onset of bistability condition reads $\partial_b w_1|_{b=0} = \partial_b w_2|_{b=0}$, giving the critical relation $\sigma_c = 2\gamma - 1$. Thus, we perturb around this condition as

$$\sigma = 2\gamma - 1 - \epsilon \kappa. \quad (21)$$

To perform a weak nonlinear analysis, we consider the ansatz

$$\begin{pmatrix} b \\ w \end{pmatrix} = \begin{pmatrix} 0 \\ p \end{pmatrix} + \epsilon A(T, \mathbf{R}) \vec{v}_1 + \epsilon^2 \vec{W}^{[2]} + \epsilon^3 \vec{W}^{[3]} + \dots \quad (22)$$

where the slow time scale is $T = \epsilon^2 t$, and the space scale is $\mathbf{R} = \epsilon \mathbf{r}$. We insert the previous expressions for b and w , and expansions Eqs. (20), (21) in Eq. (18), and solve the linear problems for the unknown functions $\vec{W}^{[n]}$ corresponding to nonlinear corrections of order ϵ^n .

At order ϵ , one has

$$0 = \begin{pmatrix} 0 & 0 \\ -\sigma_c p & -1 \end{pmatrix} A \vec{v}_1, \quad (23)$$

which gives the eigenvector at instability

$$\vec{v}_1 = \begin{pmatrix} 1 \\ -\sigma_c p \end{pmatrix}. \quad (24)$$

At order ϵ^2 , one finds

$$0 = \begin{pmatrix} 0 & 0 \\ -\sigma_c p & -1 \end{pmatrix} \vec{W}^{[2]} + A^2 \begin{pmatrix} 0 \\ -\sigma_c p \end{pmatrix}, \quad (25)$$

which is solved for

$$\vec{W}^{[2]} = A^2 \begin{pmatrix} 0 \\ -\sigma_c p \end{pmatrix}. \quad (26)$$

Finally, at order ϵ^3 , we get the following linear inhomogeneous problem

$$\begin{aligned}\vec{v}_1 \partial_T A &= \begin{pmatrix} 0 & 0 \\ -\sigma_c p & -1 \end{pmatrix} \vec{W}^{[3]} + A \begin{pmatrix} -\eta \\ 0 \end{pmatrix} + p A^2 \begin{pmatrix} \kappa \\ 0 \end{pmatrix} + \\ & p A^3 \begin{pmatrix} -3\gamma^2 \\ -\sigma_c(\gamma^2 - 2\gamma\sigma_c - \sigma_c) \end{pmatrix} + \nabla^2 A \begin{pmatrix} D \\ -\sigma_c p \end{pmatrix}.\end{aligned}\quad (27)$$

Introducing the inner product $\langle \vec{f} | \vec{g} \rangle \equiv \sum_i f_i g_i$, we search for the kernel of the adjoint of the linear operator acting on $\vec{W}^{[3]}$, which is

$$v^* = \begin{pmatrix} 1 \\ 0 \end{pmatrix}.$$

Then, for a linear problem of the form $Ax = b$, solutions exist whenever $(\ker(A^\dagger)|b) = 0$. Applying the solvability condition to solve Eq. (27), we get

$$\partial_T A = -\eta A + p \kappa A^2 - 3\gamma^2 p A^3 + D \nabla^2 A. \quad (28)$$

By a renaming and scaling of variables and parameters, we recover the local FKPP Eq. (1).

References




- [1] Lefever R, Lejeune O. On the origin of tiger bush. *Bull Math Biol* 1997;59(2):263–94.
- [2] Lejeune O, Tlidi M. A model for the explanation of tiger bush vegetation stripes. *J Veg Sci* 1999;10:201–8.
- [3] Macfadyen W. Vegetation patterns in the semi-desert plains of British somaliland. *Geogr J* 1950;116(4/6):199–211.
- [4] Thiery J, d’Herbès J-M, Valentin C. A model simulating the genesis of banded vegetation patterns in Niger. *J Ecol* 1995;497–507.
- [5] Klausmeier CA. Regular and irregular patterns in semiarid vegetation. *Science* 1999;284(5421):1826–8.
- [6] HilleRisLambers R, Rietkerk M, van den Bosch F, Prins HH, de Kroon H. Vegetation pattern formation in semi-arid grazing systems. *Ecology* 2001;82(1):50–61.
- [7] von Hardenberg J, Meron E, Shachak M, Zarmi Y. Diversity of vegetation patterns and desertification. *Phys Rev Lett* 2001;87(19):198101.
- [8] Okayasu T, Aizawa Y. Systematic analysis of periodic vegetation patterns. *Progr Theoret Phys* 2001;106(4):705–20.
- [9] D’Odorico P, Porporato A, Runyan CW. *Dryland ecohydrology*. Vol. 9. Springer; 2006.
- [10] D’Odorico P, Laio F, Ridolfi L. Patterns as indicators of productivity enhancement by facilitation and competition in dryland vegetation. *J Geophys Res Biogeosciences* 2006;111(G3).
- [11] Lejeune O, Tlidi M, Lefever R. Vegetation spots and stripes: dissipative structures in arid landscapes. *Int J Quantum Chem* 2004;98(2):261–71.
- [12] Rietkerk M, Boerlijst MC, van Langevelde F, HilleRisLambers R, de Koppel Jv, Kumar L, et al. Self-organization of vegetation in arid ecosystems. *Amer Nat* 2002;160(4):524–30.
- [13] Lejeune O, Tlidi M, Couteron P. Localized vegetation patches: a self-organized response to resource scarcity. *Phys Rev E* 2002;66(1):010901.
- [14] Rietkerk M, Dekker SC, De Ruiter PC, van de Koppel J. Self-organized patchiness and catastrophic shifts in ecosystems. *Science* 2004;305(5692):1926–9.
- [15] Vladimirov A, Lefever R, Tlidi M. Relative stability of multipeaked localized patterns of cavity solitons. *Phys Rev A* 2011;84(4):043848.
- [16] Fernandez-Oto C, Tlidi M, Escaff D, Clerc M. Strong interaction between plants induces circular barren patches: fairy circles. *Phil Trans R Soc A* 2014;372(2027):20140009.
- [17] Clerc MG, Echeverria-Alar S, Tlidi M. Localised labyrinthine patterns in ecosystems. *Sci Rep* 2021;11(1):1–12.
- [18] Berríos-Caro E, Clerc MG, Escaff D, Sandivari C, Tlidi M. On the repulsive interaction between localised vegetation patches in scarce environments. *Sci Rep* 2020;10(1):1–8.
- [19] Tlidi M, Berríos-Caro E, Pinto-Ramo D, Vladimirov A, Clerc MG. Interaction between vegetation patches and gaps: A self-organized response to water scarcity. *Physica D* 2020;414:132708.
- [20] Tlidi M, Lefever R, Vladimirov A. On vegetation clustering, localized bare soil spots and fairy circles. In: *Dissipative solitons: from optics to biology and medicine*. Springer; 2008, p. 1–22.
- [21] Bordeu I, Clerc MG, Couteron P, Lefever R, Tlidi M. Self-replication of localized vegetation patches in scarce environments. *Sci Rep* 2016;6(1):1–11.
- [22] Tlidi M, Bordeu I, Clerc MG, Escaff D. Extended patchy ecosystems may increase their total biomass through self-replication. *Ecol Indic* 2018;94:534–43.
- [23] Tlidi M, Clerc M, Escaff D, Couteron P, Messaoudi M, Khaffou M, et al. Observation and modelling of vegetation spirals and arcs in isotropic environmental conditions: dissipative structures in arid landscapes. *Phil Trans R Soc A* 2018;376(2135):20180026.

- [24] Domb C. Phase transitions and critical phenomena. Elsevier; 2000.
- [25] Allen SM, Cahn JW. A microscopic theory for antiphase boundary motion and its application to antiphase domain coarsening. *Acta Metall* 1979;27(6):1085–95.
- [26] Meron E. Pattern formation in excitable media. *Phys Rep* 1992;218(1):1–66.
- [27] Flory PJ. Thermodynamics of high polymer solutions. *J Chem Phys* 1942;10(1):51–61.
- [28] Bates FS. Polymer-polymer phase behavior. *Science* 1991;251(4996):898–905.
- [29] Wang Z, Gao K, Kan Y, Zhang M, Qiu C, Zhu L, et al. The coupling and competition of crystallization and phase separation, correlating thermodynamics and kinetics in OPV morphology and performances. *Nature Commun* 2021;12(1):1–14.
- [30] Tlidi M, Mandel P, Lefever R. Kinetics of localized pattern formation in optical systems. *Phys Rev Lett* 1998;81:979–82.
- [31] Tlidi M, Mandel P, Le Berre M, Ressayre E, Tallet A, Di Menza L. Phase-separation dynamics of circular domain walls in the degenerate optical parametric oscillator. *Opt Lett* 2000;25(7):487–9.
- [32] Tlidi M, Le Berre M, Ressayre E, Tallet A, Di Menza L. High-intensity localized structures in the degenerate optical parametric oscillator: comparison between the propagation and the mean-field models. *Phys Rev A* 2000;61(4):043806.
- [33] Gomila D, Colet P, Oppo G-L, San Miguel M. Stable droplets and growth laws close to the modulational instability of a domain wall. *Phys Rev Lett* 2001;87(19):194101.
- [34] Boeynaems S, Alberti S, Fawzi NL, Mittag T, Polymenidou M, Rousseau F, et al. Protein phase separation: a new phase in cell biology. *Trends Cell Biol* 2018;28(6):420–35.
- [35] Lefever R, Turner JW. A quantitative theory of vegetation patterns based on plant structure and the non-local F-KPP equation. *C R Méc* 2012;340(11–12):818–28.
- [36] Dornelas V, Colombo EH, López C, Hernández-García E, Anteneodo C. Landscape-induced spatial oscillations in population dynamics. *Sci Rep* 2021;11(1):1–11.
- [37] Piva G, Colombo E, Anteneodo C. Interplay between scales in the nonlocal FKPP equation. *Chaos Solitons Fractals* 2021;153:111609.
- [38] Fisher RA. The wave of advance of advantageous genes. *Ann Eugen* 1937;7(4):355–69.
- [39] Kolmogorov AN. A study of the equation of diffusion with increase in the quantity of matter, and its application to a biological problem. *Moscow Univ Bull Math* 1937;1:1–25.
- [40] Middleton N, Thomas D. World atlas of desertification. Arnold, Hodder Headline, PLC; 1997.
- [41] Mauser W, Schädlich S. Modelling the spatial distribution of evapotranspiration on different scales using remote sensing data. *J Hydrol* 1998;212:250–67.
- [42] De Gennes P-G, Prost J. The physics of liquid crystals. (83). Oxford University Press; 1993.
- [43] Clavin P. Dynamic behavior of premixed flame fronts in laminar and turbulent flows. *Prog Energy Combust Sci* 1985;11(1):1–59.
- [44] Coen S, Tlidi M, Emplit P, Haelterman M. Convection versus dispersion in optical bistability. *Phys Rev Lett* 1999;83:2328–31.
- [45] Odent V, Tlidi M, Clerc MG, Glorieux P, Louvergneaux E. Experimental observation of front propagation in a negatively diffractive inhomogeneous Kerr cavity. *Phys. Rev. A* 2014;90:011806.
- [46] Murray JD. *Mathematical biology: I. an introduction*. third ed.. New York, NY: Springer; 2002.
- [47] Pismen LM. *Patterns and interfaces in dissipative dynamics*. Springer Science & Business Media; 2006.
- [48] Strogatz SH. *Nonlinear dynamics and chaos: with applications to physics, biology, chemistry, and engineering*. CRC Press; 2018.
- [49] Abramoff MD, Magalhães PJ, Ram SJ. Image processing with ImageJ. *Biophotonics Int* 2004;11(7):36–42.
- [50] Maestre FT, Escudero A. Is the patch size distribution of vegetation a suitable indicator of desertification processes? *Ecology* 2009;90(7):1729–35.
- [51] Bak P. *How nature works: the science of self-organized criticality*. Springer Science & Business Media; 1996.
- [52] Sornette D. *Critical phenomena in natural sciences: chaos, fractals, selforganization and disorder: concepts and tools*. Springer Science & Business Media; 2006.
- [53] Clerc M, Falcon C, Tirapegui E. Additive noise induces front propagation. *Phys Rev Lett* 2005;94(14):148302.
- [54] Braun OM, Kivshar YS. *The Frenkel-Kontorova model: concepts, methods, and applications*. Springer Science & Business Media; 2013.
- [55] Pomeau Y. Front motion, metastability and subcritical bifurcations in hydrodynamics. *Physica D* 1986;23(1–3):3–11.
- [56] Alfaro-Bittner K, Castillo-Pinto C, Clerc MG, González-Cortés G, Jara-Schulz G, Rojas RG. Front propagation steered by a high-wavenumber modulation: Theory and experiments. *Chaos* 2020;30(5):053138.
- [57] Jara-Schulz G, Ferré MA, Falcón C, Clerc MG. Noise-induced kink propagation in shallow granular layers. *Chaos Solitons Fractals* 2020;134:109677.
- [58] Meron E. *Nonlinear physics of ecosystems*. CRC Press Boca Raton, FL; 2015.

Chapter 6

Effect of heterogeneous environmental conditions on labyrinthine vegetation patterns (Physical Review E 107 (5), 054219)

Labyrinthine patterns are complex structures that show all the wavevectors of a given modulus in a non-coherent combination; this describes a disordered pattern in general. However, they can be characterized as labyrinths in a strict sense provided that, locally (when looking at windows with a size of the order of the pattern's wavelength), the pattern observed corresponds to the stripe type [44]. Focusing on models of vegetation pattern formation, we try to extend the labyrinth definition and characteristics when it is subjected to heterogeneities, which could produce windows in the pattern not fulfilling the labyrinth criteria. To perform this, we numerically analyze a reduced equation of pattern formation derived from two different models of vegetation biomass spatiotemporal evolution. An extension to define the labyrinthine pattern theoretically is proposed based on the structure factor of the pattern. Depending on the intensity and correlation length of the parameters inhomogeneity, the pattern could retain its structure or become either an *imperfect labyrinth* or a *disordered self-organized state*.

Effect of heterogeneous environmental conditions on labyrinthine vegetation patternsS. Echeverría-Alar ¹, D. Pinto-Ramos ¹, M. Tlidi,² and M. G. Clerc ¹¹*Departamento de Física and Millennium Institute for Research in Optics, FCFM, Universidad de Chile, Casilla 487-3, Santiago, Chile*²*Faculté des Sciences, Université libre de Bruxelles (U.L.B), CP 231, 1050 Brussels, Belgium*

(Received 31 August 2022; revised 4 April 2023; accepted 24 April 2023; published 23 May 2023)

Self-organization is a ubiquitous phenomenon in Nature due to the permanent balance between injection and dissipation of energy. The wavelength selection process is the main issue of pattern formation. Stripe, hexagon, square, and labyrinthine patterns are observed in homogeneous conditions. In systems with heterogeneous conditions, a single wavelength is not the rule. Large-scale self-organization of vegetation in arid environments can be affected by heterogeneities, such as interannual precipitation fluctuations, fire occurrences, topographic variations, grazing, soil depth distribution, and soil-moisture islands. Here, we investigate theoretically the emergence and persistence of vegetation labyrinthine patterns in ecosystems under deterministic heterogeneous conditions. Based on a simple local vegetation model with a space-varying parameter, we show evidence of perfect and imperfect labyrinthine patterns, as well as disordered vegetation self-organization. The intensity level and the correlation of the heterogeneities control the regularity of the labyrinthine self-organization. The phase diagram and the transitions of the labyrinthine morphologies are described with the aid of their global spatial features. We also investigate the local spatial structure of labyrinths. Our theoretical findings qualitatively agree with satellite images data of arid ecosystems that show labyrinthinelike textures without a single wavelength.

DOI: [10.1103/PhysRevE.107.054219](https://doi.org/10.1103/PhysRevE.107.054219)**I. INTRODUCTION**

Self-organization is a universal feature of out-of-equilibrium systems and is of common occurrence in many fields of nonlinear science [1–4]. The spontaneous emergence of self-organized dissipative structures out of a homogeneous state has been observed in many out-of-equilibrium systems, including biology, chemical reaction-diffusion systems, fluid mechanics, nonlinear optics, and laser physics [1–3]. On the one hand, these systems are subjected to a balance between a nonlinear effect and a transport or a spatial coupling process. On the other hand, they are subjected to a continuous injection and dissipation of energy. The balance between these processes triggers the emergence of dissipative structures with an intrinsic macroscopic scale [2,5,6], which corresponds to a spontaneous symmetry-breaking instability. Over the past decades, extensive research has been done to understand the origins of simple patterns, such as stripes, hexagons, and squares, from a theoretical point of view [2,7]. However, nontrivial symmetry patterns, i.e., labyrinths, have gotten little attention due to their complicated structure, rich in spatial defects [8,9]. Recently, an attempt to characterize this ubiquitous phenomenon has introduced a quantitative definition of *ideal* labyrinthine patterns [10], which satisfy the following: (i) the disordered patterns are characterized globally by a powdered ring Fourier spectrum, and (ii) the spatial structures are described locally by a single wave mode. The *ideal* adjective refers to labyrinths with a single dominant characteristic wavelength, which are observed in controlled physical contexts, e.g., ferrofluids, chemical reactions, cholesteric liquid crystals, block copolymers, metal nanosurfaces, and ferroelectric thin films [11–16].

Self-organized structures arise in plant ecology, where stressed vegetation biomass can self-organize when resources, such as water or nutrients, are limited [17–24]. Under these arid conditions, the plant community displays coherent distributions, which are maintained by facilitative and competitive processes involving plants and the environment [18]. These distributions, whose wavelengths range from centimeter to kilometer scales, are frequently referred to as vegetation patterns. Starting from a uniform cover, as the aridity level is increased, the first pattern that appears consists of a periodic spatial distribution of gaps followed by labyrinths and then spots. This generic sequence has been predicted using various pattern-forming ecological models. The first paper that discusses the sequence was [19] in 1999. Later on, the sequence was analyzed from reaction-diffusion models in 2001 [20] and 2002 [21]. The sequence gaps-stripes/labyrinths-spots as a function of the aridity has been empirically studied in an arid region of Sudan [24]. There, the term labyrinth was used to describe disordered vegetation bands in a flat surface [20–25]. Besides periodic, other aperiodic and localized vegetation patterns have been reported [26–31]. Well-documented localized vegetation patterns are the fairy circles [32–39]. Localized vegetation patterns can exhibit curvature instabilities leading either to the self-replication phenomenon [40,41], or the formation of arcs and spirals [42]. Other alternative hypotheses for the spatial structure of vegetation self-organization have been explored, such as random patterns and power-law distributions of patch sizes [43,44].

In ecological systems, the presence of spatial and/or temporal heterogeneities may influence the self-organization of plant communities. The causes of heterogeneities are frequently related to variations in interannual precipitation,

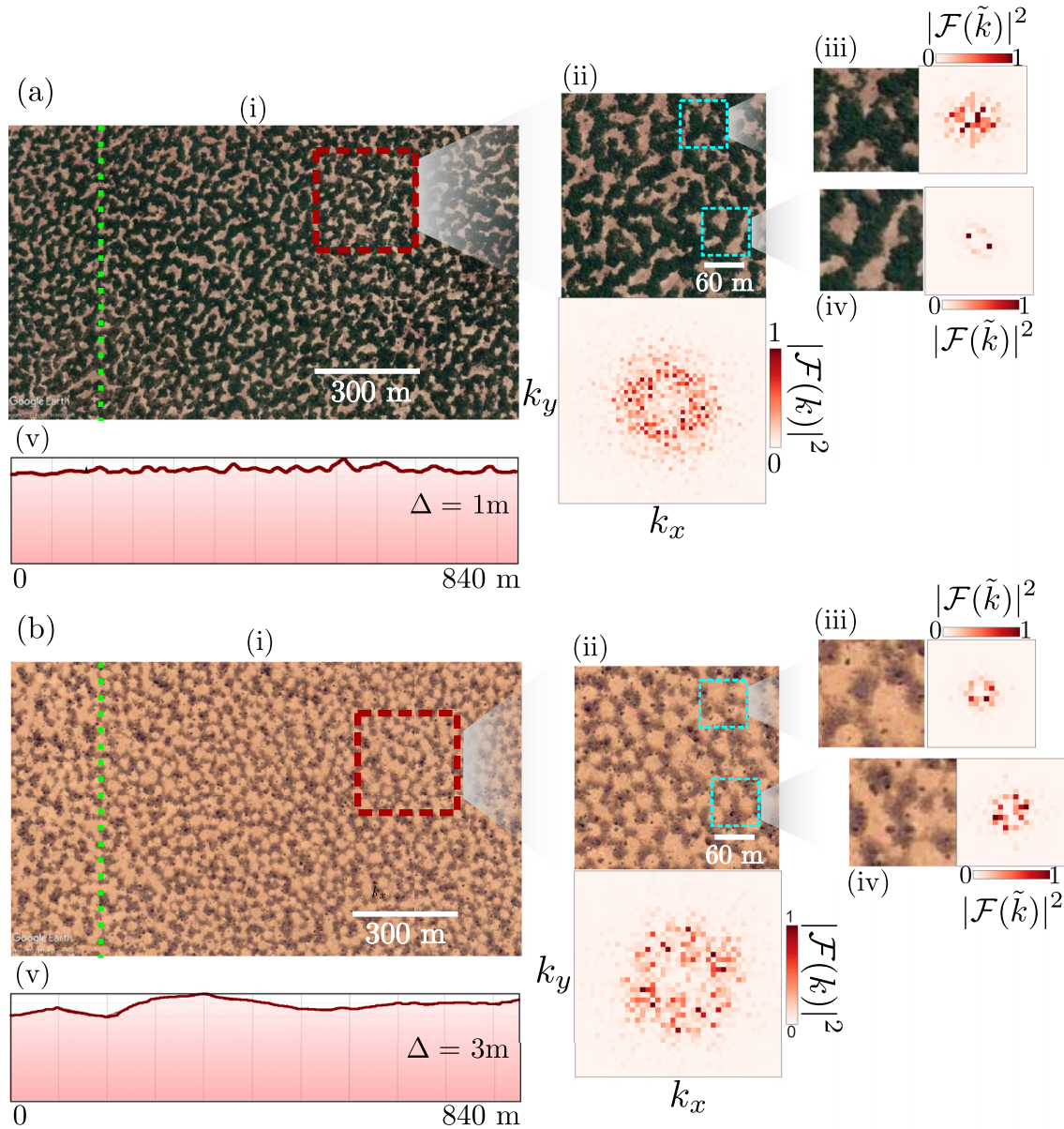


FIG. 1. Satellite images of vegetation labyrinths. Self-organization of vegetation observed in (a)(i) Niger ($12^{\circ}27'50.58''$ N $3^{\circ}18'30.76''$ E) and (b)(i) Sudan ($11^{\circ}18'26.07''$ N $27^{\circ}57'58.62''$ E). The (ii) insets display a zoom of images in (i) and are characterized by their Fourier transform $|\mathcal{F}(k)|^2$. The (iii) and (iv) insets are local regions of the images in (ii) accompanied by their local Fourier transforms $|\mathcal{F}(\tilde{k})|^2$. The (v) insets correspond to elevation profiles along the green dotted lines in (i). The value of Δ indicates the difference between the maximum and the minimum height. The vegetation snapshots and elevation profiles were retrieved from Google Earth Pro software.

occurrences of fire, topographic changes, grazing, soil depth distribution, and soil-moisture islands [22,45–49]. It makes sense to infer that one or more of the aforementioned heterogeneities control the irregularities in vegetation patterns (see the labyrinthine structures in Fig. 1). In the majority of the ecological mathematical models, these heterogeneous effects are not included, resulting in far too ideal vegetation patterns, or are approached by stochastic processes in time [46,47,49,50] or space [51]. To our knowledge, the role of deterministic heterogeneities in forming different labyrinthine-like vegetation patterns and controlling their possible transitions has not been addressed. Understanding the conditions under which heterogeneous labyrinths arise is

relevant from an ecological perspective as it sheds light on the self-organization of vegetation in isotropic real ecosystems (Fig. 1). Furthermore, the study of these types of vegetation self-organization can contribute to the discussion on how heterogeneities in arid or semiarid systems can avoid catastrophic shifts [27,51,52], which corresponds to abrupt transitions between a vegetated cover and bare soil, by establishing irregular vegetation mosaics.

In this article, we investigate theoretically the role of deterministic heterogeneities in shaping labyrinthine-like vegetation patterns as equilibria in arid and semiarid landscapes. For this purpose, we use a well-established model for vegetation biomass, where the effects of heterogeneities are modeled

as spatial variations around a mean aridity parameter. The heterogeneities are controlled by their intensity and degree of correlation. Different equilibria are numerically observed after the temporal evolution of the biomass. These vegetation patterns are characterized by their structure factor and their spatial Fourier transform at a global and local scale. These tools allow us to differentiate between perfect and imperfect labyrinths, and disordered self-organization. We construct a phase diagram and show that a minimum intensity level and/or degree of correlation are needed to observe imperfect labyrinthine patterns. This equilibrium qualitatively resembles the labyrinthine patterns observed in nature (Fig. 1). Finally, we discuss a possible implementation of our classification in natural landscapes.

II. LABYRINTHINELIKE PATTERNS IN ECOSYSTEMS

It is crucial to identify whether plants have structures resembling labyrinths to assess if they fulfill the definition of a labyrinth proposed recently [10]. Figures 1(a i) and 1(b i) show two examples of labyrinthine self-organized structures in Niger and Sudan, respectively. These vegetation images can be characterized by their Fourier spectrum at different scales as shown in insets (ii), (iii), and (iv) of Fig. 1. The insets (ii) exhibit the disordered feature of the self-organization at a global scale. The Fourier transform is nearly isotropic and highly scattered, involving several wave vectors (powderlike ring spectrum). The insets (iii) and (iv) of Fig. 1 show the spatial behavior at a local scale. The local Fourier transforms do not show a dominant single wave vector pair structure. Specifically, two diametrically opposed peaks are not visible in the local two-dimensional Fourier transform, and more complex structures are exhibited. As a result, neither the landscapes of Niger nor of Sudan meet the criteria for a perfect labyrinthine pattern [10]. We attribute the departure from the ideal pattern to the presence of heterogeneities in the regions shown in Fig. 1. The insets (v) in Figs. 1(a) and 1(b) display the topographic variations of the terrain in Niger and Sudan, respectively. Indeed, the topography is a source of spatial heterogeneity for the vegetation local self-organization [53–55]. In the following, we suppose that these topographic fluctuations affect the resource distribution on the Niger and Sudan landscapes.

III. THEORETICAL MODELING APPROACH

We choose to model the emergence of vegetation patterns from the perspective of symmetry-breaking instabilities of homogeneous covers in arid or semiarid environments [18]. Particularly, we use an interaction-redistribution approach for plant community behavior, where the biomass density $c = c(\mathbf{r}, t)$ at space point $\mathbf{r} = (x, y)$ and time t evolves following a logistic equation that includes nonlocal interactions of the biomass [33]:

$$\partial_t c = c(1 - c)M_f(\mathbf{r}) - \mu c M_c(\mathbf{r}) + DM_d(\mathbf{r}). \quad (1)$$

The first term on the right-hand side (rhs) of Eq. (1) models the rate at which biomass increases and eventually saturates. The nonlocal function $M_f(\mathbf{r}) = \exp[\chi_f \int d\mathbf{r}' \phi_f(\mathbf{r}', L_f)c(\mathbf{r} + \mathbf{r}')] accounts for interactions facilitating growth, regulated by$

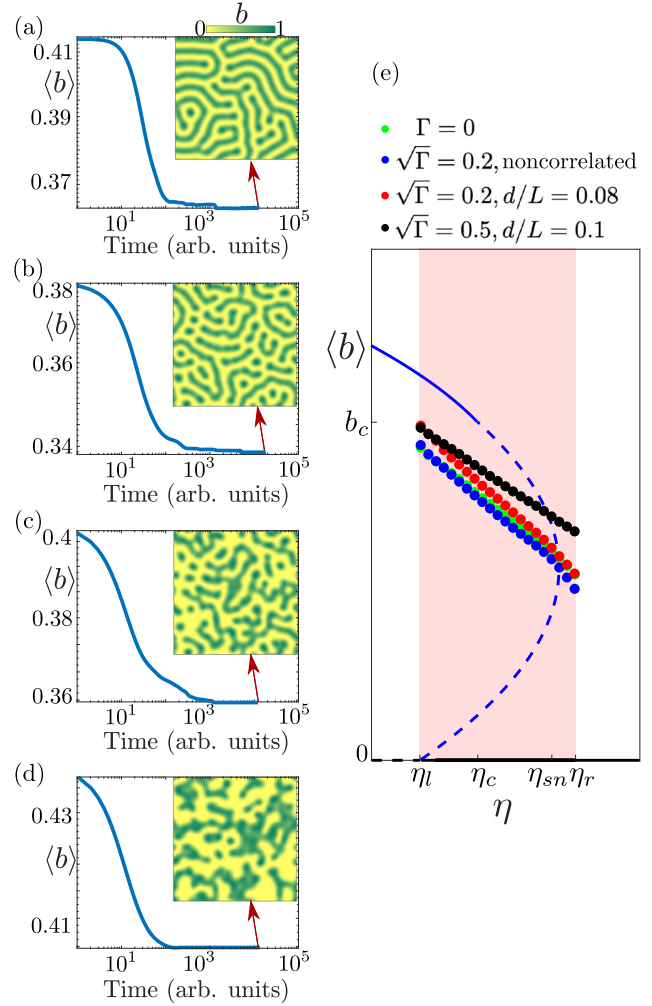


FIG. 2. Equilibrium patterns of Eq. (2) in a square domain of size $L = 240$ (arb. units) with $\kappa = 0.6$, $\nu = 0.011$, $\gamma = 0.5$, and $\alpha = 0.125$. The temporal evolutions of the spatially averaged biomass $\langle b \rangle$ are displayed for the (a) homogeneous case $\Gamma = 0$, and the inhomogeneous cases $\Gamma \neq 0$ considering both (b) noncorrelated and (c),(d) correlated heterogeneities. The insets show the respective equilibria. (e) Bifurcation diagram of Eq. (2). The black lines correspond to the bare state and the blue curves account for the uniform vegetated state in the homogeneous case $\Gamma = 0$. The continuous (broken) lines indicate that these analytical solutions are stable (unstable). In the shaded region, limited by η_l and η_r , the labyrinthine patterns in homogeneous conditions are stable. In this subfigure, $\langle b \rangle$ is the mean value over 30 random initial conditions around b_+ .

an intensity χ_f . These effects are controlled by the kernel function ϕ_f , whose range of influence is of the order of the plant's aerial structure L_f . The second term on the rhs of Eq. (1) represents the biomass death processes. $M_c(\mathbf{r}) = \exp[\chi_c \int d\mathbf{r}' \phi_c(\mathbf{r}', L_c)c(\mathbf{r} + \mathbf{r}')] accounts for interactions enhancing biomass decay with an intensity χ_c . The parameter μ is a measure of the mortality-to-growth rate ratio of plants in the absence of interaction with others, which can be seen as resource scarcity or aridity [18,56]. This negative feedback acts over distances of the order of the root length L_c with an intensity χ_c and is controlled by the kernel function$

ϕ_c . A cooperative measure of the ecological system can be introduced as $\chi_f - \chi_c$. The last term in Eq. (1) incorporates seeds dispersion with a diffusion parameter D , where $M_d(\mathbf{r}) = \int d\mathbf{r}' \phi_d(\mathbf{r}') [c(\mathbf{r} + \mathbf{r}') - c(\mathbf{r})]$, and $\phi_d(\mathbf{r}')$ accounts for the biomass transport between positions \mathbf{r} and \mathbf{r}' .

The integrodifferential equation (1), close to the double limit of nascent bistability (between uniform vegetation cover and bare soil) and the symmetry-breaking instability of the uniform cover, can be reduced to a partial differential equation. The reduced model reads [19,33]

$$\partial_t b = -\eta b + \kappa b^2 - b^3 + (v - \gamma b) \nabla^2 b - \alpha b \nabla^4 b, \quad (2)$$

where $b = b(\mathbf{r}, t)$ is the state variable associated to the biomass density close to nascent bistability. The parameters η and κ are the deviations of the aridity and cooperativity critical parameters, respectively. v and γ are linear and nonlinear diffusion coefficients, respectively. The last term is a nonlinear hyperdiffusion controlled by α . The parameters $\{v, \gamma, \alpha\}$ depend on the strength of the competitive feedback, the seed's diffusion, and the shape of the kernels ϕ_f , ϕ_c , and ϕ_d [30]. The model equation (2) has three homogeneous states: the bare state $b = 0$ [black line in Fig. 2(d)] and $b_{\pm} = (\kappa \pm \sqrt{\kappa^2 - 4\eta})/2$ [blue line in Fig. 2(d)]. The b_{\pm} equilibria are connected by a saddle-node bifurcation at $\eta_{\text{sn}} = \kappa^2/4$ with κ positive. The uniform solution b_- is always unstable. For small aridity, the vegetated state b_+ is stable. When the aridity is increased the uniform cover suffers a spatial instability. This spatial instability with critical wavelength $\lambda_c = 2\pi\sqrt{2\alpha/(\gamma - v/b_c)}$ occurs at $\eta \equiv \eta_c$, where η_c satisfies the implicit condition $4\alpha b_c^2(2b_c - \kappa) = (\gamma b_c - v)^2$ with $b_c \equiv b_+(\eta_c)$. Hence, the homogeneous cover b_+ is unstable to patterns within the range $\eta_c \leq \eta \leq \eta_{\text{sn}}$ [see Fig. 2(d)]. By fixing the parameters $\{\kappa, v, \gamma, \alpha\}$ in Eq. (2), labyrinthine patterns are stable within the aridity range $[\eta_l, \eta_r]$ as shown in Fig. 2(d).

To model the effect of heterogeneities in the labyrinths of Eq. (2), in principle, we must promote all parameters to be spatially dependent; that is, one should consider five functions $[\eta(\mathbf{r}), \kappa(\mathbf{r}), \alpha(\mathbf{r}), v(\mathbf{r}), \gamma(\mathbf{r})]$, which makes the theoretical and numerical studies cumbersome. To shed light on the effect of heterogeneities in the labyrinthine patterns, we promote the aridity parameter to be spatially dependent $\eta(\mathbf{r})$ and keep the other parameters homogeneous. Hence, in the following analysis, we focus on the model equation (2) with heterogeneous aridity $\eta(\mathbf{r}) = \eta + \sqrt{\Gamma} \xi(\mathbf{r})$, where η accounts for the mean aridity. This average value is inside the aridity range $[\eta_l, \eta_r]$. $\xi(\mathbf{r})$ models the spatial variations with zero mean value $\langle \xi(\mathbf{r}) \rangle = 0$ and intensity level Γ . The heterogeneities $\xi(\mathbf{r})$ can be spatially independent (delta correlated) or correlated. To obtain a spatially correlated function $\xi(\mathbf{r})$ characterized by a correlation length d , we consider a relaxation diffusive process with a random initial condition, which evolves until a given time [57]. Note that the results presented below are qualitatively similar if all parameters are spatially dependent.

IV. RESULTS

Let us introduce the spatially averaged biomass $\langle b \rangle \equiv \int_0^L \int_0^L b(\mathbf{r}, t) dx dy / L^2$, where L^2 is the system size. The charts

in the left panel of Fig. 2 show the temporal evolution to equilibrium for $\langle b \rangle$ according to Eq. (2) starting from the vegetated state b_+ in the symmetry-breaking regime $\eta_c \leq \eta \leq \eta_{\text{sn}}$. Figure 2(a) corresponds to the homogeneous case, $\Gamma = 0$, exhibiting an ideal labyrinthine pattern. Figure 2(b) represents the noncorrelated spatial variations, while Figs. 2(c) and 2(d) show the spatially correlated cases. In these cases, the striped structure of the labyrinthine pattern becomes locally distorted. Figure 2(e) shows the bifurcation diagram of Eq. (2). The labyrinthinelike patterns (dotted plots) are characterized by their averaged biomass $\langle b \rangle$. The green dotted curve indicates a branch of an ideal labyrinthine pattern when $\Gamma = 0$, which is stable in the range $\eta_l \leq \eta \leq \eta_r$. By increasing the aridity level, the labyrinth exhibits a transition to a mosaic of localized spots at $\eta > \eta_r$. When decreasing the aridity parameter, the labyrinthine pattern becomes clusters of hexagonal gaps at $\eta < \eta_l$ [31]. The blue dotted curve represents the stable branch of a vegetation pattern when $\Gamma \neq 0$ and ξ is noncorrelated. The red and black dotted curves are the stable branches of labyrinthinelike patterns under correlated heterogeneous conditions. We note that the impact of heterogeneities in the averaged biomass is not always strong [see red and blue dots in Fig. 2(e)]. Thus, other types of spatial tools are needed to understand and differentiate the labyrinthinelike equilibria of Eq. (2).

To characterize labyrinthine equilibria under homogeneous ($\Gamma = 0$) and heterogeneous ($\Gamma \neq 0$) conditions, we consider first the aridity distributions depicted in Fig. 3, and next we concentrate on the biomass densities $b_{\text{eq}}(\mathbf{r})$ shown in Fig. 4. We analyze the spatial structure of these aridities and biomass equilibria employing the Fourier transform amplitude $|\mathcal{F}(\mathbf{k})|^2 = |\int g(\mathbf{r}) e^{i\mathbf{k}\cdot\mathbf{r}} dx dy|^2$ and the structure factor $S(k) = \int_{-\pi}^{\pi} |\mathcal{F}(\mathbf{k})| k d\theta$, where $\mathbf{k} = (k \cos \theta, k \sin \theta)$, and $g(\mathbf{r})$ can be either $b_{\text{eq}}(\mathbf{r})$ or $\eta(\mathbf{r})$. The homogeneous and noncorrelated heterogeneous aridity distributions are characterized by a delta and a noisy flat $|\mathcal{F}(\mathbf{k})|^2$, respectively [see Figs. 3(a) and 3(b)]. The spatially correlated aridities have a nontrivial $S(k)$ shape associated with their coherent distribution [cf. Figs. 3(c) and 3(d)].

Let us now have a look at the biomass densities $b_{\text{eq}}(\mathbf{r})$ displayed in the top panels of Fig. 4. These equilibria are obtained by numerical simulations of the model equation (2) in square boxes. The spatial profiles of the aridity $\eta(\mathbf{r})$ used in these numerical simulations are the same as those in Fig. 3. Under homogeneous conditions, the biomass density exhibits a *perfect* labyrinthine pattern. The corresponding spectrum and the structure factor are shown in Fig. 4(a). From this figure, we see that the spectrum has a powdered ringlike shape and the structure factor presents a well-defined peak at $k = k_c$ [see Fig. 4(a)]. The finite width in the structure factor is attributed to the defects size and local variations of the wavevector [9]. The powdered ringlike shape indicates no preferred direction since the system is isotropic in the (x, y) plane. The full width at half maximum of $S(k)$ for the labyrinth in Fig. 4(a) is $w \approx 0.15k_c$. It is obtained by fitting a Lorentzian squared curve to the structure factor [58,59]. We define $w_h = k_c \pm w/2$ as the characteristic wavevector range of the perfect labyrinthine pattern, which emerges from a symmetry-breaking instability in Eq. (2). Figure 4(b) shows an equilibrium in the case of $\Gamma \neq 0$ and delta-correlated $\xi(\mathbf{r})$.

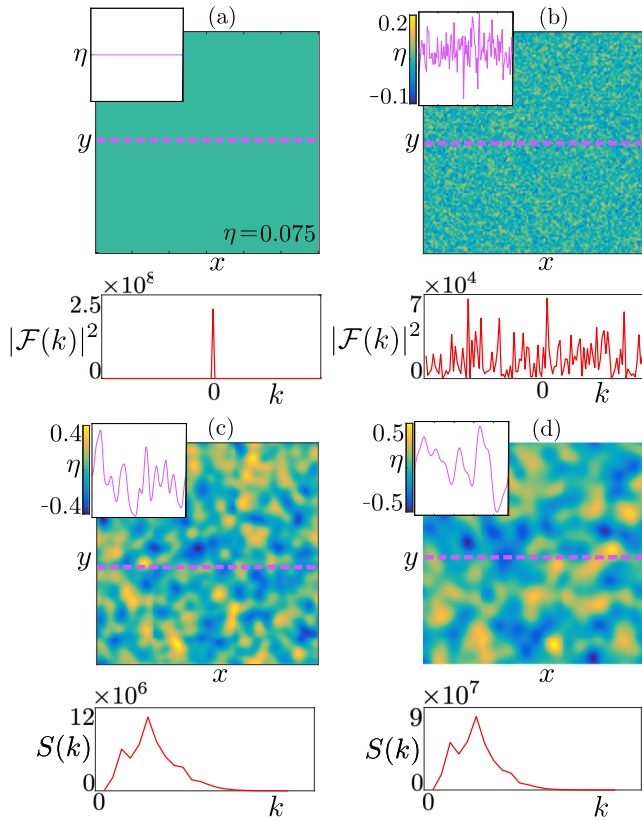


FIG. 3. Spatial distributions of the aridity parameters $\eta(\mathbf{r}) = \eta + \sqrt{\Gamma}\xi(\mathbf{r})$ with $\eta = 0.075$. In the top panels, the aridity distributions are shown. The insets correspond to an arbitrary one-directional cut represented by dashed pink lines. The lower panels illustrate the spatial structure of the distributions by their Fourier transform amplitude $|\mathcal{F}(\mathbf{k})|^2$ or structure factor $S(k)$. Other parameters are (a) $\Gamma = 0$; (b) $\sqrt{\Gamma} = 0.2$, $d/L = 0$; (c) $\sqrt{\Gamma} = 0.2$, $d/L = 0.08$; and (d) $\sqrt{\Gamma} = 0.5$, $d/L = 0.1$.

In this case, the labyrinth does not exhibit long fingers as in the homogeneous case due to the proliferation of local spots. Indeed, the heterogeneities introduce local disturbances in the wavevector reflected in the widening of $S(k)$ [cf. blue curve and inset in the bottom panel of Fig. 4(b)]. When the heterogeneities are sufficiently intense ($\sqrt{\Gamma} = 0.2$) and correlated ($d/L = 0.08$), the perfect labyrinthine pattern loses its structure and blobs of vegetation or bare soil emerge [see Fig. 4(c)]. In this aridity level, the maximum of the structure factor \hat{k} lies outside w_h [cf. blue curve in the bottom panel of Fig. 4(c)]. We define this shift in \hat{k} as a transition from perfect labyrinths ($|\hat{k} - k_c| < w_h$) to *imperfect labyrinthine patterns* ($|\hat{k} - k_c| > w_h$). When further increasing the correlation and the intensity level of the heterogeneities ($\sqrt{\Gamma} = 0.5$ and $d/L = 0.1$), the labyrinthine pattern is almost completely lost. A few vegetated fingers coexist with homogeneous islands of vegetation and bare soil [see the top panel in Fig. 4(d)]. As seen in the bottom panel of Fig. 4(d), the peak of the structure factor exhibits a significant shift (from $\hat{k} = 0.9k_c$ to $\hat{k} = 0.55k_c$) toward the center of the spectrum. Moreover, the global Fourier spectrum loses its powdered ring shape [see the inset in the bottom panel of Fig. 4(d)]. In this regime, the spatial profiles

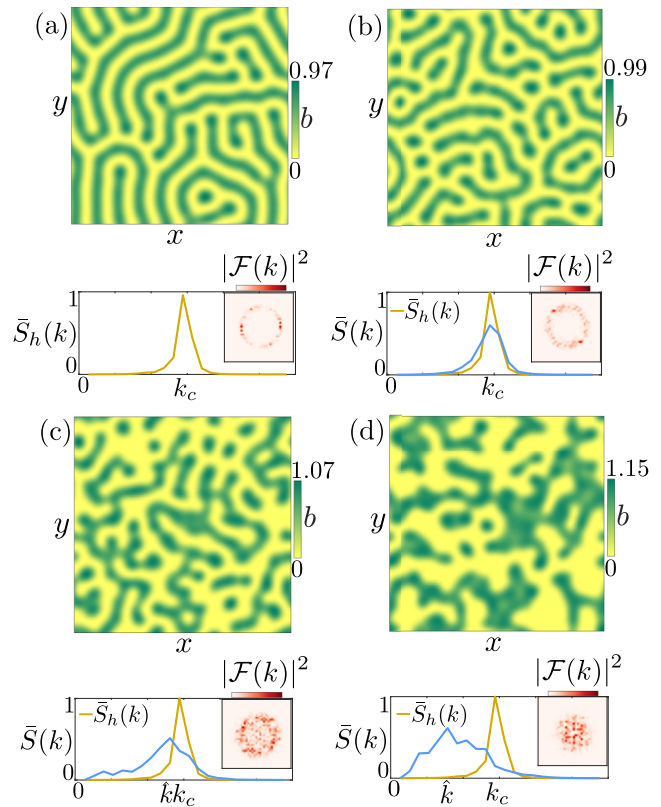


FIG. 4. Spatial characterization of the equilibria from Eq. (2) with $\kappa = 0.6$, $\nu = 0.011$, $\gamma = 0.5$, $\alpha = 0.125$, and $\eta = 0.075$. The top panels in each subfigure display the steady-state vegetated covers from the model equation (2) considering the aridity profiles $\eta(\mathbf{r})$ depicted in Fig. 3, respectively. The blue and yellow curves of the bottom panels indicate the normalized structure factor $\bar{S}(k) \equiv S(k)/S_h(k_c)$, and $\bar{S}_h(k) \equiv S_h(k)/S_h(k_c)$, respectively. $S_h(k)$ is the structure factor in the homogeneous case. The insets in the bottom panels correspond to the Fourier transform $|\mathcal{F}(k)|^2$ of the solutions from Eq. (2). The wavevector \hat{k} illustrates the maximum of $\bar{S}(k)$ when heterogeneities are present.

of the aridity and the biomass density are strongly correlated [see the lower panels of Fig. 3(d) and Fig. 4(d), respectively]. We have termed this spatial structure as *disordered self-organization*.

A phase diagram is generated using numerical simulations of Eq. (2), as shown in Fig. 5(a). The diagram depicts the existence and stability domains of three types of vegetation structures: perfect and imperfect labyrinths and disordered self-organization. We can see that perfect labyrinthine patterns can persist for different combinations of $\sqrt{\Gamma}$ and d/L . Given a minimum intensity level value $\sqrt{\Gamma}$ or degree of correlation d/L , the perfect labyrinths bifurcate to imperfect labyrinthine patterns. When heterogeneities are strong enough, the system exhibits disordered self-organization. We stress that the transition between different labyrinthinelike textures can be triggered solely by $\sqrt{\Gamma}$ or d/L [cf. dashed arrows in Fig. 5(a)]. For example, Fig. 5(b) show the variation of \hat{k}/k_c by fixing $d/L = 0.08$ and moving $\sqrt{\Gamma}$. The insets (i)–(iii) along the diagram illustrate the change in $\bar{S}(k)$ and \hat{k} as the biomass

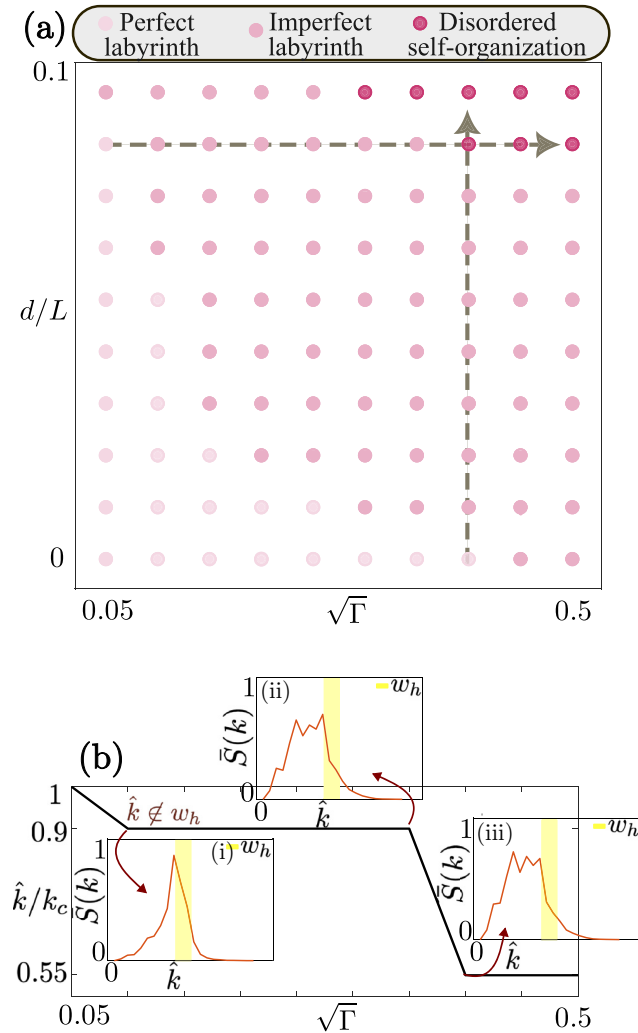


FIG. 5. Phase diagram of vegetation patterns in heterogeneous environments. (a) Phase diagram of the global spatial structure of Eq. (2) with $\kappa = 0.6$, $\nu = 0.011$, $\gamma = 0.5$, $\alpha = 0.125$, and $\eta = 0.075$ as a function of the intensity level $\sqrt{\Gamma}$ and the degree of correlation d/L . The different phases are perfect labyrinthine patterns ($\hat{k} \approx k_c$), imperfect labyrinthine patterns ($\hat{k} \approx 0.9k_c$), and disordered self-organizations ($\hat{k} \approx 0.55k_c$). The dashed gray arrows illustrate possible transition paths between the equilibria. (b) Transition triggered by changing the intensity of the heterogeneities $\sqrt{\Gamma}$ given a correlation $d/L = 0.8$ in the aridity distribution. The insets (i)–(iii) show the normalized structure factor $\bar{S}(k)$ and its peak position \hat{k} . The yellow rectangle depicts the characteristic wavevector range w_h of the labyrinth with $\Gamma = 0$.

departures from the perfect labyrinths. The transition between imperfect labyrinths and disordered self-organization [(ii) \rightarrow (iii)] resembles the disappearance of scurvy labyrinthine patterns in a variational Swift-Hohenberg model [10].

In what follows, we further numerically characterize the labyrinthinelike equilibria using local Fourier transforms. This statistical tool allows us to investigate the self-organization process at small spatial scales. Ideal labyrinthine patterns, for instance, are characterized by their local striped behavior. This feature can be extracted through the averaged

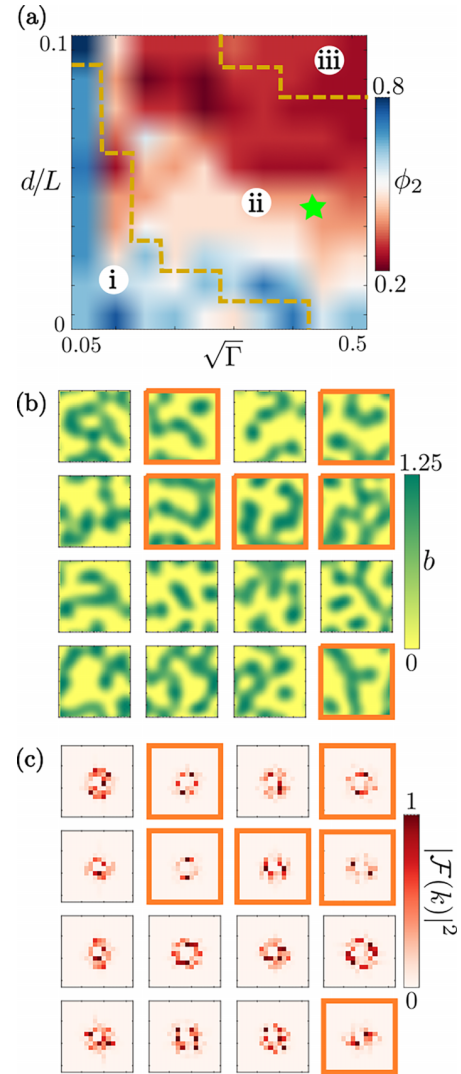


FIG. 6. Phase diagram of the local structure of labyrinthine patterns from Eq. (2) with $\kappa = 0.6$, $\nu = 0.0113$, $\gamma = 0.5$, $\alpha = 0.125$, and $\eta = 0.075$. (a) Colormap of the local two-mode fraction ϕ_2 for different intensity level Γ and correlation d/L of the heterogeneities $\xi(\vec{r})$. The segmented yellow lines separate the three regions of Fig. 5: (i) perfect labyrinthine patterns, (ii) imperfect labyrinthine patterns, and (iii) disordered self-organization. (b) Spatial division of a steady-state vegetation pattern, with $\sqrt{\Gamma} = 0.4$ and $d/L = 0.04$ (\star), in windows of size $2.3\lambda_c$. (c) Local Fourier transform $|\mathcal{F}(\vec{k})|^2$ of each window. The orange borders in (b) and (c) indicate that the local pattern fulfills the criteria of being dominantly a stripe.

windowed Fourier transform [10]. The procedure consists of dividing the labyrinthine patterns into N windows of size s , calculating each window's Fourier transform, and then performing a projective average in Fourier space. The result is a single wave mode (stripe) local Fourier spectrum. The critical step is to choose the adequate size s . It has to be small enough to lose the pattern's isotropy and sufficiently big to account for the labyrinth wavelength. Then, the safe choice is $s \approx 2\lambda_c$. Here, we compute the local Fourier transform of the patterns obtained from Eq. (2) in windows of size

TABLE I. Summary of the sensitivity analysis. The sensitivity indices $Si(\phi_2^{pi})$ and $Si(\phi_2^{id})$ are associated to the transition fractions ϕ_2^{pi} and ϕ_2^{id} , respectively.

	η	κ	ν	γ	α	s	th
Original value	0.085	0.6	0.01	0.5	0.125	$2.3\lambda_c$	0.8
$Si(\phi_2^{pi})$	0.10	0.09	0.11	0.07	0.14	0.16	0.26
$Si(\phi_2^{id})$	0.33	0.17	0.12	<0.01	0.23	0.11	0.21

$s = 2.3\lambda_c$ because L/s is an integer number. As a consequence of imperfect labyrinths and disordered self-organizations, the projective average process is not a good approach. To amend this, we introduce the three largest values of the local Fourier transforms $\mathcal{F}_1 \geq \mathcal{F}_2 \geq \mathcal{F}_3$. We define a local window to be dominantly a stripe if $\mathcal{F}_1 = \mathcal{F}_2$ (dominated by two peaks, i.e., a stripe) and $\mathcal{F}_3 \leq 0.8\mathcal{F}_1$. The threshold (th = 0.8), which takes into account the defects of the labyrinths, is selected to maximize the fraction $\phi_2 = N_s/N$ of the labyrinthine pattern under homogeneous conditions. N_s is the number of windows exhibiting stripes.

Figure 6(a) shows the fraction ϕ_2 for different combinations of the intensity level Γ and degree of correlation d/L of the heterogeneities. Additionally, the dashed yellow lines indicate the transitions related to the global spatial structure of the biomass density (see Fig. 5). We note that the transition from perfect labyrinths to imperfect labyrinths is marked by $\phi_2^{pi} = 0.61 \pm 0.06$. As well, imperfect labyrinths become disordered self-organizations when $\phi_2^{id} = 0.30 \pm 0.02$. Figures 6(b) and 6(c) illustrate the local structure and the windowed Fourier transform of an imperfect labyrinthine pattern with $N_s = 6$ as depicted by the orange squares. We note that the transitions in the $(\sqrt{\Gamma}, d/L)$ parameter space depend on the choices of $[\eta, \kappa, \gamma, \alpha, \nu]$. Hence, we highlight that a suitable model parametrization is needed for extending our classifications to natural landscapes.

To test the robustness of our predictions against modeling decisions, we have performed a sensitivity analysis by changing in $\pm 10\%$ the original values of the parameters chosen to observe labyrinths in Eq. (2), the window size s , and the threshold th. When varying the window length, we use the same number of windows N as in the original case by overlapping the windows or by not considering the boundaries of the simulation boxes. To evaluate the sensitivity, the simple sensitivity index $Si(h) = |1 - h_{\min}/h_{\max}|$ is used, where h_{\min} and h_{\max} are a model output when a parameter was decreased or increased, respectively [60]. Values closer to 1 indicate high sensitivity, while $Si(h) < 0.01$ means no sensitivity to variations. We consider the averaged fractions ϕ_2^{pi} and ϕ_2^{id} as model outputs with sensitivity indices $Si(\phi_2^{pi})$ and $Si(\phi_2^{id})$, respectively (see Table I). The transitions from perfect to imperfect labyrinths and imperfect labyrinths to disordered self-organizations are always observed when varying the parameters in Table I.

The sensibility analysis shows that ϕ_2^{id} is sensible to the mean aridity parameter η , which is related to the system being near the boundaries η_l and η_r (see Fig. 2). Additionally, this transition is highly affected by the spatial coupling parameter α and could be related to changes in λ_c . Table I suggests that

both ϕ_2^{pi} and ϕ_2^{id} are sensible to the threshold th, which can be attributed to a wrong counting of the N_s values.

V. DISCUSSION AND CONCLUSIONS

We have investigated the effect of heterogeneous conditions on a pattern-forming ecological model of semiarid and arid landscapes. We have considered a well-known model based on the relationship between the vegetation biomass and the facilitation-competition interactions operating within plants. We have further simplified the analysis by focusing on a reduced model, Eq. (2), and we have restricted our study to a single species that accounts for most of the biomass. Motivated by topographic variations along labyrinthine self-organization in Niger and Sudan, we have modeled the heterogeneities as a spatial-dependent aridity parameter. The spatial fluctuations act around a mean aridity value with a certain intensity level. These variations can be correlated with a given correlation length.

By increasing the intensity level and the correlation length of the aridity heterogeneities, we have shown evidence of imperfect labyrinthine patterns and disordered self-organizations. These equilibria of Eq. (2) qualitatively resemble the real labyrinthine-like vegetation patterns observed in satellite images of arid and semiarid landscapes. Furthermore, we have found that perfect labyrinthine patterns are persistent until a critical degree of heterogeneity is reached, where they become imperfect labyrinths. Further increasing the heterogeneities, the spatial structure of the imperfect labyrinth is eventually lost to a disordered self-organization, which is governed by the spatial distribution of the aridity. Based on the peak's position and width of the global structure factor, we have characterized the transitions between equilibria and built a phase diagram. A windowed Fourier transform is used to measure the departure from perfect labyrinthine patterns as a function of heterogeneities.

An interesting future research is the identification of perfect labyrinths, imperfect labyrinths, and disordered self-organizations in real ecosystems by applying the tools and modeling introduced here. To achieve this natural classification, on-site measurements in arid environments populated by labyrinthine-like vegetation patterns will be needed to validate the application of the reduced model, Eq. (2), and to verify if the model parameters are realistic or not. It will be crucial to determine the parameters η and α , as they significantly impact the transitions between labyrinthine-like vegetation patterns. For example, if the labyrinthine-like landscapes of Niger and Sudan (Fig. 1) are well described by model equation (2) and the parameters chosen are characteristic of these particular places, our classification could be applied by extending the local analysis presented here. In fact, our modeling can be used to identify the threshold th for the Sudan and Niger regions in Fig. 1. We hypothesize that these labyrinths are imperfect; that is, they are sustained by a minimum level of spatially correlated heterogeneity, and are the consequence of a combination of a symmetry-breaking instability and heterogeneous environmental conditions. Moreover, *in situ* observations of topography and resource distribution could reveal if a more complex way to incorporate heterogeneities

is needed or if our straightforward approach, based on the intensity level and degree of correlation, is sufficient and reasonable.

Our theoretical findings can be used with other modeling approaches to obtain more realistic labyrinthine patterns, such as reaction-diffusion systems where water dynamics is included explicitly [20,21]. Additionally, our classification can also be applied in different scientific contexts where labyrinths are experimentally observed. For example in fluid mechanics, liquid crystals, optics, biology, and chemistry [61–65], where the sources of heterogeneity are diverse (e.g., thermal fluctuations, experimental imperfections, boundary conditions, inhomogeneous forcing, material defects).

ACKNOWLEDGMENTS

The authors thank two anonymous referees whose constructive comments improve the presentation of this article. S.E.-A. acknowledges the financial support of ANID by Beca Doctorado Nacional 2020-21201376. D.P.-R. acknowledges the financial support of ANID National Ph.D. scholarship 2020-21201484. M.G.C. acknowledges the financial support of ANID–Millennium Science Initiative Program–ICN17_012 (MIRO) and FONDECYT Project No. 1210353. M.T. acknowledges support as a Research Director with the Fonds de la Recherche Scientifique FRS-FNRS, Belgium. We also acknowledge Wallonie-Bruxelles International (WBI).

-
- [1] G. Nicolis and I. Prigogine, *Self-Organization in Non-Equilibrium Systems* (Wiley, New York, 1977).
- [2] M. Cross and H. Greenside, *Pattern Formation and Dynamics in Non-Equilibrium Systems* (Cambridge University Press, New York, 2009).
- [3] J. D. Murray, *Mathematical Biology: I. An Introduction* (Springer, New York, 2002).
- [4] R. V. Solé and J. Bascompte, *Self-Organization in Complex Ecosystems. (MPB-42)* (Princeton University Press, Princeton, NJ, 2006).
- [5] A. M. Turing, The chemical basis of morphogenesis, *Philos. Trans. R. Soc. London, Ser. B* **237**, 37 (1952).
- [6] I. Prigogine and R. Lefever, Symmetry breaking instabilities in dissipative systems. II, *J. Chem. Phys.* **48**, 1695 (1968).
- [7] R. Hoyle and R. B. Hoyle, *Pattern Formation: An Introduction to Methods* (Cambridge University Press, Cambridge, UK, 2006).
- [8] T. Passot and A. C. Newell, Towards a universal theory for natural patterns, *Phys. D (Amsterdam, Neth.)* **74**, 301 (1994).
- [9] M. Le Berre, E. Ressayre, A. Tallet, Y. Pomeau, and L. Di Menza, Example of a chaotic crystal: The labyrinth, *Phys. Rev. E* **66**, 026203 (2002).
- [10] S. Echeverría-Alar and M. G. Clerc, Labyrinthine patterns transitions, *Phys. Rev. Res.* **2**, 042036(R) (2020).
- [11] R. E. Rosensweig, M. Zahn, and R. Shumovich, Labyrinthine instability in magnetic and dielectric fluids, *J. Magn. Magn. Mater.* **39**, 127 (1983).
- [12] K. J. Lee, W. McCormick, Q. Ouyang, and H. L. Swinney, Pattern formation by interacting chemical fronts, *Science* **261**, 192 (1993).
- [13] P. Oswald and P. Pieranski, *Nematic and Cholesteric Liquid Crystals: Concepts and Physical Properties Illustrated by Experiments* (CRC, Boca Raton, FL, 2005).
- [14] S. Park, Manipulating the sequences of block copolymer patterns on corrugated substrates, *Polymer* **180**, 121726 (2019).
- [15] A. Nakhoul, C. Maurice, M. Agoyan, A. Rudenko, F. Garrelie, F. Pigeon, and J.-P. Colombier, Self-organization regimes induced by ultrafast laser on surfaces in the tens of nanometer scales, *Nanomaterials* **11**, 1020 (2021).
- [16] P. Kavle, J. A. Zorn, A. Dasgupta, B. Wang, M. Ramesh, L.-Q. Chen, and L. W. Martin, Strain-driven mixed-phase domain architectures and topological transitions in $\text{Pb}_{1-x}\text{Sr}_x\text{TiO}_3$ thin films, *Adv. Mater.* **34**, 2203469 (2022).
- [17] W. Macfadyen, Soil and vegetation in British Somaliland, *Nature (London)* **165**, 121 (1950).
- [18] R. Lefever and O. Lejeune, On the origin of tiger bush, *Bull. Math. Biol.* **59**, 263 (1997).
- [19] O. Lejeune and M. Tlidi, A model for the explanation of tiger bush vegetation stripes, *J. Veg. Sci.* **10**, 201 (1999).
- [20] J. von Hardenberg, E. Meron, M. Shachak, and Y. Zarmi, Diversity of Vegetation Patterns and Desertification, *Phys. Rev. Lett.* **87**, 198101 (2001).
- [21] M. Rietkerk, M. C. Boerlijst, F. van Langevelde, R. HilleRisLambers, J. v. de Koppel, L. Kumar, H. H. Prins, and A. M. de Roos, Self-organization of vegetation in arid ecosystems, *Am. Nat.* **160**, 524 (2002).
- [22] V. Deblauwe, N. Barbier, P. Couteron, O. Lejeune, and J. Bogaert, The global biogeography of semi-arid periodic vegetation patterns, *Global Ecol. Biogeogr.* **17**, 715 (2008).
- [23] F. Borgogno, P. D’Odorico, F. Laio, and L. Ridolfi, Mathematical models of vegetation pattern formation in ecohydrology, *Rev. Geophys.* **47**, RG1005 (2009).
- [24] V. Deblauwe, P. Couteron, O. Lejeune, J. Bogaert, and N. Barbier, Environmental modulation of self-organized periodic vegetation patterns in Sudan, *Ecography* **34**, 990 (2011).
- [25] L. Mander, S. C. Dekker, M. Li, W. Mio, S. W. Punyasena, and T. M. Lenton, A morphometric analysis of vegetation patterns in dryland ecosystems, *R. Soc. Open Sci.* **4**, 160443 (2017).
- [26] O. Lejeune, M. Tlidi, and P. Couteron, Localized vegetation patches: A self-organized response to resource scarcity, *Phys. Rev. E* **66**, 010901(R) (2002).
- [27] M. Rietkerk, S. C. Dekker, P. C. De Ruiter, and J. van de Koppel, Self-organized patchiness and catastrophic shifts in ecosystems, *Science* **305**, 1926 (2004).
- [28] E. Meron, H. Yizhaq, and E. Gilad, Localized structures in dryland vegetation: Forms and functions, *Chaos* **17**, 037109 (2007).
- [29] P. Couteron, F. Anthelme, M. Clerc, D. Escaff, C. Fernandez-Oto, and M. Tlidi, Plant clonal morphologies and spatial patterns as self-organized responses to resource-limited environments, *Philos. Trans. R. Soc. A* **372**, 20140102 (2014).
- [30] M. Tlidi, E. Berríos-Caro, D. Pinto-Ramo, A. Vladimirov, and M. G. Clerc, Interaction between vegetation patches and gaps: A self-organized response to water scarcity, *Phys. D (Amsterdam, Neth.)* **414**, 132708 (2020).

- [31] M. G. Clerc, S. Echeverría-Alar, and M. Tlidi, Localised labyrinthine patterns in ecosystems, *Sci. Rep.* **11**, 18331 (2021).
- [32] M. Van Rooyen, G. Theron, N. Van Rooyen, W. Jankowitz, and W. Matthews, Mysterious circles in the Namib desert: Review of hypotheses on their origin, *J. Arid. Environ.* **57**, 467 (2004).
- [33] M. Tlidi, R. Lefever, and A. Vladimirov, On vegetation clustering, localized bare soil spots and fairy circles, *Lect. Notes Phys.* **751**, 381 (2008).
- [34] N. Juergens, The biological underpinnings of Namib desert fairy circles, *Science* **339**, 1618 (2013).
- [35] M. D. Cramer and N. N. Barger, Are Namibian “fairy circles” the consequence of self-organizing spatial vegetation patterning? *PLoS One* **8**, e70876 (2013).
- [36] C. Fernandez-Oto, M. Tlidi, D. Escaff, and M. Clerc, Strong interaction between plants induces circular barren patches: Fairy circles, *Philos. Trans. R. Soc. A* **372**, 20140009 (2014).
- [37] D. Escaff, C. Fernandez-Oto, M. G. Clerc, and M. Tlidi, Localized vegetation patterns, fairy circles, and localized patches in arid landscapes, *Phys. Rev. E* **91**, 022924 (2015).
- [38] S. Getzin, K. Wiegand, T. Wiegand, H. Yizhaq, J. von Hardenberg, and E. Meron, Adopting a spatially explicit perspective to study the mysterious fairy circles of Namibia, *Ecography* **38**, 1 (2015).
- [39] C. E. Tarnita, J. A. Bonachela, E. Sheffer, J. A. Guyton, T. C. Coverdale, R. A. Long, and R. M. Pringle, A theoretical foundation for multi-scale regular vegetation patterns, *Nature (London)* **541**, 398 (2017).
- [40] I. Bordeu, M. G. Clerc, P. Couteron, R. Lefever, and M. Tlidi, Self-replication of localized vegetation patches in scarce environments, *Sci. Rep.* **6**, 33703 (2016).
- [41] M. Tlidi, I. Bordeu, M. G. Clerc, and D. Escaff, Extended patchy ecosystems may increase their total biomass through self-replication, *Ecol. Indic.* **94**, 534 (2018).
- [42] M. Tlidi, M. Clerc, D. Escaff, P. Couteron, M. Messaoudi, M. Khaffou, and A. Makhoute, Observation and modelling of vegetation spirals and arcs in isotropic environmental conditions: Dissipative structures in arid landscapes, *Philos. Trans. R. Soc. A* **376**, 20180026 (2018).
- [43] S. Kéfi, M. Rietkerk, C. L. Alados, Y. Pueyo, V. P. Papanastasis, A. ElAich, and P. C. De Ruiter, Spatial vegetation patterns and imminent desertification in Mediterranean arid ecosystems, *Nature (London)* **449**, 213 (2007).
- [44] F. Meloni, G. M. Nakamura, C. R. Granzotti, and A. S. Martinez, Vegetation cover reveals the phase diagram of patch patterns in drylands, *Phys. A (Amsterdam, Neth.)* **534**, 122048 (2019).
- [45] P. Adler, D. Raff, and W. Lauenroth, The effect of grazing on the spatial heterogeneity of vegetation, *Oecologia* **128**, 465 (2001).
- [46] P. D’Odorico, F. Laio, and L. Ridolfi, Vegetation patterns induced by random climate fluctuations, *Geophys. Res. Lett.* **33**, L19404 (2006).
- [47] P. D’Odorico, F. Laio, A. Porporato, L. Ridolfi, and N. Barbier, Noise-induced vegetation patterns in fire-prone savannas, *J. Geophys. Res.* **112**, G02021 (2007).
- [48] T. E. Franz, E. G. King, K. K. Caylor, and D. A. Robinson, Coupling vegetation organization patterns to soil resource heterogeneity in a central Kenyan dryland using geophysical imagery, *Water Resour. Res.* **47**, W07531 (2011).
- [49] I. Rodriguez-Iturbe, Z. Chen, A. C. Staver, and S. A. Levin, Tree clusters in savannas result from islands of soil moisture, *Proc. Natl. Acad. Sci. USA* **116**, 6679 (2019).
- [50] K. Pal, S. Deb, and P. S. Dutta, Tipping points in spatial ecosystems driven by short-range correlated noise, *Phys. Rev. E* **106**, 054412 (2022).
- [51] P. Villa Martín, J. A. Bonachela, S. A. Levin, and M. A. Muñoz, Eluding catastrophic shifts, *Proc. Natl. Acad. Sci. USA* **112**, E1828 (2015).
- [52] M. Scheffer, S. Carpenter, J. A. Foley, C. Folke, and B. Walker, Catastrophic shifts in ecosystems, *Nature (London)* **413**, 591 (2001).
- [53] J. Greenwood, The development of vegetation patterns in Somaliland protectorate, *Geogr. J.* **123**, 465 (1957).
- [54] C. Montana, The colonization of bare areas in two-phase mosaics of an arid ecosystem, *J. Ecol.* **80**, 315 (1992).
- [55] B. Bookhagen and D. W. Burbank, Topography, relief, and TRMM-derived rainfall variations along the Himalaya, *Geophys. Res. Lett.* **33**, L08405 (2006).
- [56] O. Lejeune, M. Tlidi, and R. Lefever, Vegetation spots and stripes: Dissipative structures in arid landscapes, *Int. J. Quantum Chem.* **98**, 261 (2004).
- [57] D. Pinto-Ramos, S. Echeverría-Alar, M. G. Clerc, and M. Tlidi, Vegetation covers phase separation in inhomogeneous environments, *Chaos, Solitons & Fractals* **163**, 112518 (2022).
- [58] M. C. Cross and D. I. Meiron, Domain Coarsening in Systems Far from Equilibrium, *Phys. Rev. Lett.* **75**, 2152 (1995).
- [59] T. Galla and E. Moro, Defect formation in the Swift-Hohenberg equation, *Phys. Rev. E* **67**, 035101(R) (2003).
- [60] S. Echeverría, M. B. Hausner, N. Bambach, S. Vicuña, and F. Suárez, Modeling present and future ice covers in two antarctic lakes, *J. Glaciol.* **66**, 11 (2020).
- [61] J. Gollub, A. McCarriar, and J. Steinman, Convective pattern evolution and secondary instabilities, *J. Fluid Mech.* **125**, 259 (1982).
- [62] M. Seul and D. Andelman, Domain shapes and patterns: The phenomenology of modulated phases, *Science* **267**, 476 (1995).
- [63] Q.-X. Liu, P. M. J. Herman, W. M. Mooij, J. Huisman, M. Scheffer, H. Olf, and J. van de Koppel, Pattern formation at multiple spatial scales drives the resilience of mussel bed ecosystems, *Nat. Commun.* **5**, 5234 (2014).
- [64] A. Pandey, J. D. Scheel, and J. Schumacher, Turbulent superstructures in Rayleigh-Bénard convection, *Nat. Commun.* **9**, 2118 (2018).
- [65] Y. Soupart and P. Aguilera-Rojas (private communication).

Complements and perspectives on Part III

1. Reduced equation from reaction-diffusion models in the pattern forming regime

In chapter 5, we derived an imperfect pitchfork normal form with diffusive transport from two modeling perspectives of the biomass spatiotemporal evolution, which satisfies a scaling close to the critical point of a single eigenvalue crossing the imaginary axis. Differently, in chapter 6, an equation in a pattern forming regime is used; that is, when a Turing instability is possible at zero wavenumber. That is developed only from the integrodifferential types of models, leaving out the case of reaction-diffusion models. Employing a similar set of equations as Eqs. (18) of chapter 5, one can derive similar equations compared to Eq. (2) of chapter 6, which we remind here

$$\partial_t b = -\eta b + \kappa b^2 - b^3 + (d - \gamma b)\nabla^2 b - \alpha b\nabla^4 b. \quad (6.1)$$

Derivation from integrodifferential models

We first give a short derivation from the integrodifferential models. The normalized biomass $b(\mathbf{r}, t)$ considers nonlocal interactions, obeying the following interaction-redistribution model [74, 79], sometimes called interaction-redistribution model [79]

$$\partial_t b = b(1 - b)M_f[b] - \mu b M_c[b] + D\nabla^2 b, \quad (6.2)$$

where μ corresponds to the mortality to the natality rate of vegetation in the absence of interactions. The functions $M_f[b]$ and $M_c[b]$ model the facilitation and competition plant-to-plant interactions, respectively. These are two distinct sets of processes since they are influenced by various ecological factors, involve various functional structures, and take place over different spatial scales. The facilitative interaction takes place on the aerial structures of plants (L_f) and corresponds to the natural growth of vegetation through mutual shelter, seed production, dissemination, germination, and development of new shoots. On the other hand, competitive interactions between plants favor vegetation biomass decay by natural death due to resource competition and other effects. This interaction extends over a spatial range on the order of the size of the plant's roots (L_c). The third term corresponds to the seed dispersion mechanisms described by a simple random walk associated with Brownian motion, D is a phenomenological diffusion constant, and $\nabla^2 \equiv \partial_{xx} + \partial_{yy}$ is the Laplace operator acting on the plane (x, y) . However, plants and seeds do not diffuse randomly. We assume that a diffusion process governs seed dispersion for mathematical simplicity. The nonlocal functions are

equal to unity ($M_f = M_c = 1$) if plants have no facilitative and competitive interactions. In this limit, one recovers the Fisher-Kolmogorov-Petrovsky-Piskunov (FKPP) equation when $\mu < 1$, a well-known paradigm model for studying population dynamics [1].

The homogeneous steady state of Eq. [6.2] admits a critical point where the homogeneous solution $b = 0$ flips its stability as a function of μ . The nonlocal functions M_f and M_c are $M_{f,c}[b] = \exp\{\chi_{f,c} \int d\mathbf{r}' \phi_{f,c}(\mathbf{r}') b(\mathbf{r} + \mathbf{r}')\}$ with general kernels $\phi_{f,c}$. The onset of bistability is given by $\chi_f - \chi_c = 1$. At this critical point, the coordinates of the biomass density and mortality parameters are $b_c = 0$ and $\mu_c = 1$. We introduce a small parameter that measures the distance to the critical point as $\mu = 1 + \epsilon\eta$; then, the biomass density is written in terms of ϵ as $b = \epsilon^{1/2} A(\tau = \epsilon t, \mathbf{x} = \epsilon^{1/8} \mathbf{r}) + \dots$. We select the kernels such that $M_{f,c}$ can be expanded in series. We expand the integral terms as $M_f = 1 + \chi_f(A + \epsilon^{1/4} C_{2f} \nabla_{\mathbf{x}}^2 A + \epsilon^{1/2} C_{4f} \nabla_{\mathbf{x}}^4 A + \dots) + \chi_f^2(A + \dots)^2/2 + \dots$, where $2C_{2f} = \int dr d\theta r \phi_f(r) r^2 \cos^2 \theta$, $24C_{4f} = \int dr d\theta r \phi_f(r) r^4 \cos^4 \theta$, and the analogue follows for M_c . Assuming that both kernels are isotropic and inserting these expansions in Eq. [6.2], together with the conditions $\chi_f - \chi_c = 1 + \epsilon^{1/2} \kappa$, $\chi_c = C_{2f}/(C_{2c} - C_{2f}) - \epsilon^{1/4} \gamma/(C_{2c} - C_{2f})$, $D = \epsilon^{3/4} d$, and defining $\alpha = (C_{2f} C_{4c} - C_{2c} C_{4f})/(C_{2c} - C_{2f})$, one obtains to dominant order ($\epsilon^{3/2}$) the equation

$$\partial_{\tau} A = -\eta A + \kappa A^2 - A^3/2 + d \nabla_{\mathbf{x}}^2 A - \gamma A \nabla_{\mathbf{x}}^2 A - \alpha A \nabla_{\mathbf{x}}^4 A,$$

Which corresponds to Eq. [6.1] up to a rescaling of A and the parameters. Note that the derivation of the equation can be carried out without mentioning the kind of kernels utilized, provided that it admits a series representation [80].

Derivation from reaction-diffusion models

Differently, other types of model consider a soil water density field $w(\mathbf{r}, t)$ that couples to the biomass density $b(\mathbf{r}, t)$ [75, 76, 81–83]. An example from the literature that we simplify reads [83] (note that corresponds to Eq. (18) of chapter 6 when the carrying capacity of the logistic term is infinite)

$$\begin{aligned} \partial_t b &= w(1 + b\sigma)^2 b - \mu b + D \nabla^2 b, \\ \partial_t w &= p - lw - sw(1 + b\sigma)^2 b + \delta \nabla^2 w, \end{aligned} \tag{6.3}$$

where the source term p represents precipitation, a loss term $-lw$ accounts for evaporation, and μ models the biomass mortality rate. A water suction term by vegetation is modeled by $-sw(1 + b\sigma)^2 b$, where σ measures the shoot-to-root length ratio and the parameter s accounts for the water-uptake rate. The biomass diffusion is described by $D \nabla^2 b$ and the transport of water is described by simple diffusion $\delta \nabla^2 w$.

Linear analysis of equation [6.3] shows that the bare soil (full of water) state $(b, w) = (0, p/l)$ changes stability at the condition $p/l - \mu = 0$, transitioning from an attractor point to a hyperbolic point in the phase space of homogeneous states. The eigenvector of the slow unstable mode corresponds to $\mathbf{v} = (v_1, v_2) \propto (1, -sp/l^2)$. The critical linear operator at instability reads

$$L_c = \begin{pmatrix} 0 & 0 \\ -sp/l & -l \end{pmatrix},$$

and the kernel of the adjoint of L_c considering the euclidean norm corresponds to $\text{Ker}\{L_c\} = \{(1, 0)\}$.

Similar to the previous section, we propose an ϵ parameter quantifying how far we are from the instability as $p/l - \mu = -\epsilon\eta$. Then we propose the expansions $2\sigma p/l - sp/l^2 = \epsilon^{1/2}\kappa/v_1$, $D = \epsilon^{3/4}d$, $\delta = D + \epsilon^{1/4}\gamma l^3/(spv_1)$, and $(b, w) = (\epsilon^{1/2}Av_1, p/l + \epsilon^{1/2}Av_2 - \epsilon\gamma\nabla_{\mathbf{x}}^2A + \epsilon^{3/2}(v_2 + sv_1)(\gamma/l)A\nabla_{\mathbf{x}}^2A - \epsilon^{5/4}(\gamma/l)\nabla_{\mathbf{x}}^4A)$, where $A = A(\tau = \epsilon t, \mathbf{x} = \epsilon^{1/8}\mathbf{r})$. Inserting this, one finds at the dominant order plus the first stabilizing correction the following equation for A

$$\partial_{\tau}A = -\eta A + \kappa A^2 - \frac{3\sigma^2 v_1^2 p}{l} A^3 + d\nabla_{\mathbf{x}}^2 A - \gamma A\nabla_{\mathbf{x}}^2 A - \epsilon^{1/4}\frac{\gamma}{l}A\nabla_{\mathbf{x}}^4 A,$$

which, again, corresponds to Eq. [6.1] up to rescaling A and redefine the parameters. It is important to note that it explicitly depends on ϵ in this case. Modifications of the model to find a proper scaling (equation independent of ϵ) are possible and are currently being proposed; our future objective is to unveil which class of equations can be generally reduced to Eq. [6.1].

2. Exact equivalence of vegetation models in specific cases

One motivation to derive the normal form of the instabilities occurring in different population dynamics models is to have a framework to unify them despite all the different approaches in the literature. Some equations exist for which there is an equivalence between an integrodifferential and a reaction-diffusion model. Consider the set of equations

$$\begin{aligned}\partial_t b &= \gamma w b - b^2 - \mu b + D\nabla^2 b, \\ \epsilon\partial_t w &= p - lw - b + \delta\nabla^2 w.\end{aligned}\tag{6.4}$$

This model is purely of theoretical interest and does not model actual physical processes occurring in the interaction of water and biomass. The limit of $\epsilon \rightarrow 0$ in equations 6.4 is called an *adiabatic* limit due to the variable w being instantly determined by the variable b . Let $w = p/l + W$, then we can solve

$$\frac{1}{\delta}b = (\nabla^2 - \frac{l}{\delta})W.$$

It is similar to a Helmholtz equation, for which the Green function is widely known; then, solving for W in terms of the inhomogeneity b is straightforward. For simplicity, consider a single spatial dimension; the solution is then (assuming the appropriate boundary conditions)

$$W = -\sqrt{\frac{1}{4l\delta}} \int e^{-\sqrt{\frac{l}{\delta}}|x-x'|} b(x', t) dx'.$$

Finally, replacing W in the equation for the biomass, one gets

$$\partial_t b = \gamma b \left(\frac{p}{l} - \sqrt{\frac{1}{4l\delta}} \int e^{-\sqrt{\frac{l}{\delta}}|x-x'|} b(x', t) dx' \right) - b^2 - \mu b + D\nabla^2 b.$$

We have found equivalence between an integrodifferential model and a reaction-diffusion set of equations in an adiabatic limit. Other types of kernels different than the exponential one

can be found with this method when modifying the water transport equation; it is important to note that the dimension of space also modifies the kernel. A similar calculation can be employed in a non-adiabatic case; then, the integral term will have both a spatial and a temporal part, and the resulting equation for the biomass will be both nonlocal in space and in time. This approach to compute reduced equations near critical points of the dynamics is yet to be explored in the future.

3. Heterogeneities in the regime of spots of vegetation

We have explored the regime of diffusive transport and moved to a general model of pattern formation. In chapter 6, we focused on studying the labyrinthine pattern and how it is affected by heterogeneous parameters. In this perspective, we analyze patterns of the *spot* type. Spotted patterns occur for higher mortality levels in the biomass field and correspond to periodic hexagonal arrays of circular spots of biomass; these spots can survive as localized structures [84] and create non-periodic structures according to their initial conditions and interactions over time. We employ the general model Eq. 6.1 in the presence of heterogeneities in the linear parameter as $\eta = \eta + \sqrt{\Gamma}\xi(\mathbf{r})$, ξ is obtained in the same form as described in chapters 5 and 6.

Numerical simulations of Eq. [6.1] with an inhomogeneous level of effective mortality η are performed using periodic boundary conditions. Figure 6.1 summarizes the results. As the mean η level is increased, a branch of vegetation patterns, symbolized by the orange color, emerges from spatial instability of the homogeneous cover (dotted black curve) in Fig. 6.1a). The average biomass density decreases as a function of η , reaching a state of patchy patterns. An example of the obtained pattern with a high density of patches emerging from this branch is shown in Fig. 6.1c). An entirely distinct branch of vegetation patterns with low biomass density is observed. It emerges from covers with low density of patches when the η parameter is decreased; we refer to the vegetation pattern in this branch as clustered patches of vegetation, with the average biomass density shown in Fig. 6.1a). An example of a pattern belonging to this branch is shown in Fig. 6.1d). The two branches form a hysteresis loop in which both vegetation patterns with a large and a small number of patches coexist for the same value η . Close to the point where the two branches with high and low biomass density meet, patches die off one by one until the system shows a gradual transition towards the bare state. Therefore, inhomogeneities can make vegetation cover more resilient to changes in environmental conditions.

To better analyze the difference between the two branches forming a large hysteresis loop, we use the Fourier transform to show whether both branches of solutions possess a characteristic wavenumber. Patterns in the upper branch show a clear characteristic wavenumber. Increasing the level of η to the point where the two branches of the solution meet leads to a random spatial distribution of patches whose positions are essentially uncorrelated. Close to this point, the characteristic wavenumber goes to zero, and the bare state becomes dominant. It has been shown that vegetation patches could increase the system biomass by a process called self-replication [84, 86], which activates depending on the η level and the patch size. In the extreme condition of high mortality, the patch self-replication process is inactive, and the patches can not invade the remaining space. However, by reversing the level of η , favorable regions due to inhomogeneities will allow self-replication locally; different from the

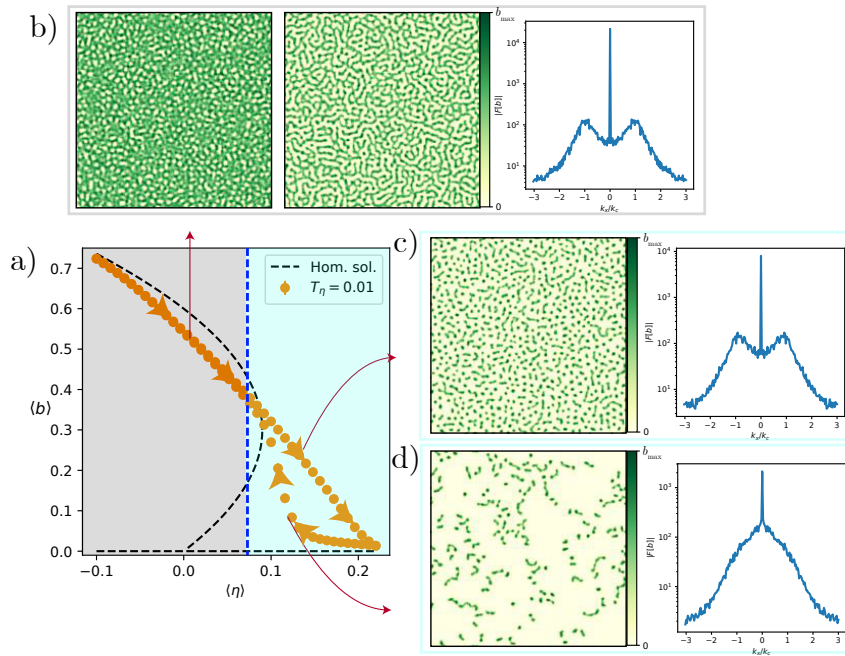


Figure 6.1: Numerical characterization of solution branches with heterogeneous parameters. Panel a) illustrates the bifurcation diagram for a path in the mean aridity parameter depicted by the orange arrows, insets show different examples of the vegetation mosaics in the diagram. Panels b) and c) show the spatial characterization of the two branches of patchy patterns for the upper branch, which transit from a labyrinthine pattern to a patchy pattern. d) shows the lower branch that emerges as the aridity parameter decreases. Parameters are $\kappa = 0.6$, $d = 0.02$, $\gamma = 0.5$, $\alpha = 0.125$.

self-replication process in homogeneous conditions, the inhomogeneous environment will not allow complete recovery. Indeed, in this regime, inhomogeneity has a twofold effect: I) the patches that reach the critical size due to favorable local η value self-replicate, increasing the biomass of their surroundings; II) the patches will reach spatial locations with unfavorable local η , stopping the self-replicating process and pinning the colonization front. These effects, when combined, lead to a *clustering phenomenon* of patches. By further decreasing the level of mortality, more patches will be able to develop a process of self-replication, increasing the pattern density until the two branches coincide again.

These characteristics of the equilibrium branches are being compared to actual spotted patterns observed in different continents. In addition, as the observation of one spotted pattern branch or the other depends on the history of parameters, we are analyzing the temporal evolution of the aridity levels in the spotted vegetation patterns observed. This would offer a possible explanation for the actual spatial distribution status of different spotted patterns in arid climates.

Conclusions

Our adventure analyzing the intriguing behaviors of nature, which could be described by dynamical systems of several kinds, can meet no end. Nature is vast, and its complexity is being slowly unveiled. In this dissertation, I tried to answer several questions which emerged thanks to the interaction with my advisor and peers, most of the time, out of curiosity.

I devoted a part of my studies to the theory of mechanical nonreciprocally coupled systems, helping to generalize their behavior in the presence of simple nonlinearities in part I of this dissertation. Nonreciprocal coupling in mechanical systems has direct implications in the isolation and conduction of energy, and nonreciprocal response has been developed in several metamaterials with unique properties; Our findings show that in nonlinear systems, nonreciprocal coupling controls the relative stability of states through propagation mechanisms, namely, fronts. The dynamic of a front into the unstable state was unveiled when the system has a nonreciprocal coupling; convective instabilities could stabilize a high energy state or a self-assembled pattern of fronts into the stable state. The velocity of fronts into the unstable state and fronts into the stable state is theoretically obtained, unveiling the role of nonreciprocal coupling in the propagation of states.

This dissertation proposes a experimental setup, the liquid crystal light valve with translational optical feedback, where the different behaviors observed are being contrasted with the theoretical findings; this opens several avenues for future research to be developed. What happens if we create a lattice of points in the LCLV instead of a chain? What is the result of rotating the feedback loop instead of translating it? Those are some open questions that encourage more theoretical and experimental efforts in the matter, with the basis for their research found in this dissertation.

Nonreciprocal coupling could also be understood in the context of fields, or infinite dimensional systems, as seen in part II of this dissertation. In the LCLV experiment, a translational feedback mimics a nonreciprocal coupling; When writing the discretized equations one obtains a non-symmetric adjacency matrix (and nonlinear coupling terms also). A field interacting with itself at each point but shifted in space a fixed distance $\delta\mathbf{r}$ can be understood as a nonlocal coupling, with a highly asymmetric kernel; we learned that a natural system that could be modeled by a dynamical system with nonlocal coupling correspond to the distribution of a biomass population. We predicted that patterns in a system under nonreciprocal coupling may display a decaying density of defects in the downstream direction, and large scale vegetation patterns showed to be an interesting natural system exhibiting stripe patterns with defects. Motivated by the challenges of our times, we dedicated good time to investigate models of vegetation biomass spatiotemporal evolution, and how environmental changes could drive different bifurcations in the biomass cover. In this context, we estab-

lished how the distribution of defects in a pattern of vegetation biomass could warn of its state; unfortunately, models suggest that the operating regime found in the communities of *Tillandsia Landbeckii*, exhibiting stripe patterns in the north of Chile, is the last one before an imminent collapse happens if the mortality rate of these plants increases (which may do if environmental conditions change).

We adopted the idea that based on the spatial properties of the biomass cover, such as the size of patches, the pattern wavelength, the defects, and more, one could deduce information of the biomass status. To theoretically predict the different patterns of vegetation cover and their properties, the heterogeneity in the dynamical system parameters is introduced as a fundamental ingredient. The heterogeneity in the parameters is capable of generating new type of patterns not predicted by the previous theories; these new patterns exhibit similar properties as the ones observed in natural vegetation cover such as the patch size, the spatial spectral power density, the dominant wavevector, and the pair correlation functions discussed in part III of this dissertation. Moreover, we established how these properties will change against environmental conditions affecting the biomass, particularly the mortality rate. The different models present in the literature, such as two-variable (or more) reaction-diffusion models, or integrodifferential equations of a single variable were addressed; we showed that these different perspectives can be unified when analyzing close to bifurcation points. These findings set ground for the development of more specialized theoretical tools that can be used to monitor and predict the behavior of one of the most complex systems of nature, numerous living beings interacting that form the vegetation biomass cover seen from planes or the space.

Bibliography

- [1] Murray, J. D., *Mathematical biology II: Spatial models and biomedical applications*, vol. 3. Springer New York, 2001.
- [2] Cross, M. C. y Hohenberg, P. C., “Pattern formation outside of equilibrium,” *Reviews of modern physics*, vol. 65, no. 3, p. 851, 1993.
- [3] De Gennes, P.-G. y Prost, J., *The physics of liquid crystals*. No. 83, Oxford university press, 1993.
- [4] Residori, S., “Patterns, fronts and structures in a liquid-crystal-light-valve with optical feedback,” *Physics Reports*, vol. 416, no. 5-6, pp. 201–272, 2005.
- [5] Aranson, I. S. y Tsimring, L. S., “Patterns and collective behavior in granular media: Theoretical concepts,” *Reviews of modern physics*, vol. 78, no. 2, p. 641, 2006.
- [6] Borgogno, F., D’Odorico, P., Laio, F., y Ridolfi, L., “Mathematical models of vegetation pattern formation in ecohydrology,” *Reviews of geophysics*, vol. 47, no. 1, 2009.
- [7] Coulais, C., Sounas, D., y Alù, A., “Static non-reciprocity in mechanical metamaterials,” *Nature*, vol. 542, no. 7642, pp. 461–464, 2017.
- [8] Brandenbourger, M., Locsin, X., Lerner, E., y Coulais, C., “Non-reciprocal robotic metamaterials,” *Nature Commun.*, vol. 10, no. 1, pp. 1–8, 2019.
- [9] Zheng, Z., Hu, G., y Hu, B., “Collective directional transport in coupled nonlinear oscillators without external bias,” *Physical Review Letters*, vol. 86, no. 11, p. 2273, 2001.
- [10] Alvarez-Garrido, F., Clerc, M., y Gonzalez-Cortes, G., “Transition to spatiotemporal intermittency and defect turbulence in systems under translational coupling,” *Physical review letters*, vol. 124, no. 16, p. 164101, 2020.
- [11] Shankar, S., Souslov, A., Bowick, M. J., Marchetti, M. C., y Vitelli, V., “Topological active matter,” *Nature Reviews Physics*, vol. 4, no. 6, pp. 380–398, 2022.
- [12] Braun, O. M. y Kivshar, Y. S., *The Frenkel-Kontorova model: concepts, methods, and applications*. Springer Science & Business Media, 2013.
- [13] Tamaševičiūtė, E., Tamaševičius, A. V., Mykolaitis, G., Bumelienė, S., y Lindberg, E., “Analogue electrical circuit for simulation of the duffing-holmes equation,” *Nonlinear Analysis: Modelling and Control*, vol. 13, no. 2, pp. 241–252, 2008.
- [14] Jackson, E. A., *Perspectives of Nonlinear Dynamics: Volume 1*, vol. 1. CUP Archive, 1989.
- [15] Remoissenet, M., *Waves called solitons: concepts and experiments*. Springer Science & Business Media, 2013.

- [16] Arnold, V. I., Ordinary differential equations. Springer Science & Business Media, 1992.
- [17] Anosov, D. V., Arnold, V. I., y Anosov, D., Dynamical systems I: ordinary differential equations and smooth dynamical systems. Springer, 1988.
- [18] Guckenheimer, J. y Holmes, P., Nonlinear oscillations, dynamical systems, and bifurcations of vector fields, vol. 42. Springer Science & Business Media, 2013.
- [19] Elphick, C., Tirapegui, E., Brachet, M., Coulet, P., y Iooss, G., “A simple global characterization for normal forms of singular vector fields,” *Physica D: Nonlinear Phenomena*, vol. 29, no. 1-2, pp. 95–127, 1987.
- [20] Bowick, M. J., Fakhri, N., Marchetti, M. C., y Ramaswamy, S., “Symmetry, thermodynamics, and topology in active matter,” *Physical Review X*, vol. 12, no. 1, p. 010501, 2022.
- [21] Scheibner, C., Souslov, A., Banerjee, D., Surówka, P., Irvine, W. T., y Vitelli, V., “Odd elasticity,” *Nature Physics*, vol. 16, no. 4, pp. 475–480, 2020.
- [22] Tlidi, M., Bataille-Gonzalez, M., Clerc, M., Bahloul, L., Coulibaly, S., Kostet, B., Castillo-Pinto, C., y Panajotov, K., “Isolas of localized structures and raman-kerr frequency combs in micro-structured resonators,” *Chaos, Solitons & Fractals*, vol. 174, p. 113808, 2023.
- [23] Pismen, L. M., Patterns and interfaces in dissipative dynamics, vol. 30. Springer, 2006.
- [24] Clerc, M. G., Petrossian, A., y Residori, S., “Bouncing localized structures in a liquid-crystal light-valve experiment,” *Physical Review E*, vol. 71, no. 1, p. 015205, 2005.
- [25] Van Saarloos, W., “Front propagation into unstable states,” *Phys. Rep.*, vol. 386, no. 2-6, pp. 29–222, 2003.
- [26] Aronson, D. G. y Weinberger, H. F., “Multidimensional nonlinear diffusion arising in population genetics,” *Advances in Mathematics*, vol. 30, no. 1, pp. 33–76, 1978.
- [27] Fisher, R. A., “The wave of advance of advantageous genes,” *Annals of eugenics*, vol. 7, no. 4, pp. 355–369, 1937.
- [28] Kolmogorov, A., Petrovskii, I., y Piskunov, N., “A study of the equation of diffusion with increase in the quantity of matter, and its application to a biological problem,” *Byul. Moskovskogo Gos. Univ.*, vol. 1, pp. 1–25, 1937.
- [29] Benguria, R. y Depassier, M., “Validity of the linear speed selection mechanism for fronts of the nonlinear diffusion equation,” *Physical review letters*, vol. 73, no. 16, p. 2272, 1994.
- [30] Benguria, R. y Depassier, M., “Variational characterization of the speed of propagation of fronts for the nonlinear diffusion equation,” *Communications in mathematical physics*, vol. 175, pp. 221–227, 1996.
- [31] Benguria, R. y Depassier, M., “Speed of fronts of the reaction-diffusion equation,” *Physical review letters*, vol. 77, no. 6, p. 1171, 1996.
- [32] Rajaraman, R., “Some non-perturbative semi-classical methods in quantum field theory (a pedagogical review),” *Physics Reports*, vol. 21, no. 5, pp. 227–313, 1975.
- [33] Fife, P. C. y McLeod, J. B., “The approach of solutions of nonlinear diffusion equations to travelling front solutions,” *Archive for Rational Mechanics and Analysis*, vol. 65,

- pp. 335–361, 1977.
- [34] Diehl, H., Kroll, D., y Wagner, H., “The interface in a ginzburg-landau-wilson model: Derivation of the drumhead model in the low-temperature limit,” *Zeitschrift für Physik B Condensed Matter*, vol. 36, no. 4, pp. 329–333, 1980.
 - [35] Bausch, R., Dohm, V., Janssen, H., y Zia, R., “Critical dynamics of an interface in $1+\varepsilon$ dimensions,” *Physical Review Letters*, vol. 47, no. 25, p. 1837, 1981.
 - [36] Haudin, F., Elías, R., Rojas, R., Bortolozzo, U., Clerc, M., y Residori, S., “Driven front propagation in 1d spatially periodic media,” *Physical review letters*, vol. 103, no. 12, p. 128003, 2009.
 - [37] Álvarez-Socorro, A. J., Castillo-Pinto, C., Clerc, M. G., González-Cortés, G., y Wilson, M., “Front propagation transition induced by diffraction in a liquid crystal light valve,” *Optics Express*, vol. 27, no. 9, pp. 12391–12398, 2019.
 - [38] Alfaro-Bittner, K., Castillo-Pinto, C., Clerc, M., González-Cortés, G., Jara-Schulz, G., y Rojas, R., “Front propagation steered by a high-wavenumber modulation: Theory and experiments,” *Chaos: An Interdisciplinary Journal of Nonlinear Science*, vol. 30, no. 5, p. 053138, 2020.
 - [39] Alfaro-Bittner, K., Clerc, M., García-Ñustes, M., y Rojas, R., “ π -kink propagation in the damped frenkel-kontorova model,” *EPL (Europhysics Letters)*, vol. 119, no. 4, p. 40003, 2017.
 - [40] Alfaro-Bittner, K., Clerc, M., Rojas, R., y García-Ñustes, M., “Traveling wave into an unstable state in dissipative oscillator chains,” *Nonlinear Dyn.*, vol. 98, no. 2, pp. 1391–1402, 2019.
 - [41] Flach, S. y Kladko, K., “Perturbation analysis of weakly discrete kinks,” *Physical Review E*, vol. 54, no. 3, p. 2912, 1996.
 - [42] Kladko, K., Mitkov, I., y Bishop, A., “Universal scaling of wave propagation failure in arrays of coupled nonlinear cells,” *Physical review letters*, vol. 84, no. 19, p. 4505, 2000.
 - [43] Swift, J. y Hohenberg, P. C., “Hydrodynamic fluctuations at the convective instability,” *Physical Review A*, vol. 15, no. 1, p. 319, 1977.
 - [44] Echeverría-Alar, S. y Clerc, M., “Labyrinthine patterns transitions,” *Physical Review Research*, vol. 2, no. 4, p. 042036, 2020.
 - [45] Clerc, M., Coulibaly, S., Del Campo, F., Garcia-Nustes, M., Louvergneaux, E., y Wilson, M., “Recurrent noise-induced phase singularities in drifting patterns,” *Physical Review E*, vol. 92, no. 5, p. 050902, 2015.
 - [46] Del Campo, F., Haudin, F., Rojas, R., Bortolozzo, U., Clerc, M., y Residori, S., “Effects of translational coupling on dissipative localized states,” *Physical Review E*, vol. 86, no. 3, p. 036201, 2012.
 - [47] Aranson, I. S. y Kramer, L., “The world of the complex ginzburg-landau equation,” *Reviews of modern physics*, vol. 74, no. 1, p. 99, 2002.
 - [48] Chaté, H. y Manneville, P., “Phase diagram of the two-dimensional complex ginzburg-landau equation,” *Physica A: Statistical Mechanics and its Applications*, vol. 224, no. 1-2, pp. 348–368, 1996.
 - [49] Matsuoka, C. y Nozaki, K., “Vortex dynamics of the complex ginzburg-landau equation,”

- Journal of the Physical Society of Japan, vol. 61, no. 5, pp. 1429–1432, 1992.
- [50] Chuang, I., Turok, N., y Yurke, B., “Late-time coarsening dynamics in a nematic liquid crystal,” *Physical review letters*, vol. 66, no. 19, p. 2472, 1991.
 - [51] Yurke, B., Pargellis, A., Kovacs, T., y Huse, D., “Coarsening dynamics of the xy model,” *Physical Review E*, vol. 47, no. 3, p. 1525, 1993.
 - [52] Kudo, K. y Kawaguchi, Y., “Coarsening dynamics driven by vortex-antivortex annihilation in ferromagnetic bose-einstein condensates,” *Physical Review A*, vol. 91, no. 5, p. 053609, 2015.
 - [53] Cuevas-Maraver, J., Kevrekidis, P. G., y Williams, F., “The sine-gordon model and its applications,” *Nonlinear systems and complexity*, vol. 10, 2014.
 - [54] Wu, Q., Xu, X., Qian, H., Wang, S., Zhu, R., Yan, Z., Ma, H., Chen, Y., y Huang, G., “Active metamaterials for realizing odd mass density,” *Proceedings of the National Academy of Sciences*, vol. 120, no. 21, p. e2209829120, 2023.
 - [55] Sounas, D. L., Caloz, C., y Alu, A., “Giant non-reciprocity at the subwavelength scale using angular momentum-biased metamaterials,” *Nat. Commun.*, vol. 4, no. 1, pp. 1–7, 2013.
 - [56] Matías, M. y Güémez, J., “Transient periodic rotating waves and fast propagation of synchronization in linear arrays of chaotic systems,” *Physical review letters*, vol. 81, no. 19, p. 4124, 1998.
 - [57] Chen, Z., Peng, Y., Li, H., Liu, J., Ding, Y., Liang, B., Zhu, X.-F., Lu, Y., Cheng, J., y Alù, A., “Efficient nonreciprocal mode transitions in spatiotemporally modulated acoustic metamaterials,” *Science advances*, vol. 7, no. 45, p. eabj1198, 2021.
 - [58] Bender, C. M. y Orszag, S. A., *Advanced mathematical methods for scientists and engineers I: Asymptotic methods and perturbation theory*, vol. 1. Springer Science & Business Media, 1999.
 - [59] Schlichting, H. y Gersten, K., *Boundary-layer theory*. Springer, 2016.
 - [60] Van Kampen, N. G., *Stochastic processes in physics and chemistry*, vol. 1. Elsevier, 1992.
 - [61] Deissler, R. J., “Noise-sustained structure, intermittency, and the ginzburg-landau equation,” *Journal of statistical physics*, vol. 40, pp. 371–395, 1985.
 - [62] Saleh, B. E. y Teich, M. C., *Fundamentals of photonics*. John Wiley & sons, 2019.
 - [63] Neubecker, R., Oppo, G.-L., Thuring, B., y Tschudi, T., “Pattern formation in a liquid-crystal light valve with feedback, including polarization, saturation, and internal threshold effects,” *Physical Review A*, vol. 52, no. 1, p. 791, 1995.
 - [64] Clerc, M., Nagaya, T., Petrossian, A., Residori, S., y Riera, C., “First-order fréedericksz transition and front propagation in a liquid crystal light valve with feedback,” *The European Physical Journal D-Atomic, Molecular, Optical and Plasma Physics*, vol. 28, pp. 435–445, 2004.
 - [65] Hatsugai, Y., “Chern number and edge states in the integer quantum hall effect,” *Physical review letters*, vol. 71, no. 22, p. 3697, 1993.
 - [66] Hoyle, R. B., *Pattern formation: an introduction to methods*. Cambridge University

Press, 2006.

- [67] Zhu, Y., Chen, H., Fan, J., Wang, Y., Li, Y., Chen, J., Fan, J., Yang, S., Hu, L., Leung, H., *et al.*, “Genetic diversity and disease control in rice,” *Nature*, vol. 406, no. 6797, pp. 718–722, 2000.
- [68] Franz, T. E., King, E. G., Caylor, K. K., y Robinson, D. A., “Coupling vegetation organization patterns to soil resource heterogeneity in a central kenyan dryland using geophysical imagery,” *Water resources research*, vol. 47, no. 7, 2011.
- [69] Gandhi, P., Werner, L., Iams, S., Gowda, K., y Silber, M., “A topographic mechanism for arcing of dryland vegetation bands,” *Journal of The Royal Society Interface*, vol. 15, no. 147, p. 20180508, 2018.
- [70] McGrath, G. S., Paik, K., y Hinz, C., “Microtopography alters self-organized vegetation patterns in water-limited ecosystems,” *Journal of Geophysical Research: Biogeosciences*, vol. 117, no. G3, 2012.
- [71] Rodriguez-Iturbe, I., Chen, Z., Staver, A. C., y Levin, S. A., “Tree clusters in savannas result from islands of soil moisture,” *Proceedings of the National Academy of Sciences*, vol. 116, no. 14, pp. 6679–6683, 2019.
- [72] Murray, J. D., *Mathematical Biology: I. An Introduction*, Third Edition. Springer, New York, NY, 2002.
- [73] Thiery, J., d’Herbès, J.-M., y Valentin, C., “A model simulating the genesis of banded vegetation patterns in niger,” *Journal of Ecology*, pp. 497–507, 1995.
- [74] Lefever, R. y Lejeune, O., “On the origin of tiger bush,” *Bulletin of Mathematical biology*, vol. 59, no. 2, pp. 263–294, 1997.
- [75] Klausmeier, C. A., “Regular and irregular patterns in semiarid vegetation,” *Science*, vol. 284, no. 5421, pp. 1826–1828, 1999.
- [76] von Hardenberg, J., Meron, E., Shachak, M., y Zarmi, Y., “Diversity of vegetation patterns and desertification,” *Physical review letters*, vol. 87, no. 19, p. 198101, 2001.
- [77] Gilad, E., von Hardenberg, J., Provenzale, A., Shachak, M., y Meron, E., “Ecosystem engineers: from pattern formation to habitat creation,” *Physical Review Letters*, vol. 93, no. 9, p. 098105, 2004.
- [78] Sun, G.-Q., Li, L., Li, J., Liu, C., Wu, Y.-P., Gao, S., Wang, Z., y Feng, G.-L., “Impacts of climate change on vegetation pattern: Mathematical modelling and data analysis,” *Physics of Life Reviews*, 2022.
- [79] Tlidi, M., Lefever, R., y Vladimirov, A., “On vegetation clustering, localized bare soil spots and fairy circles,” en *Dissipative Solitons: From Optics to Biology and Medicine*, pp. 1–22, Springer, 2008.
- [80] Tlidi, M., Berríos-Caro, E., Pinto-Ramo, D., Vladimirov, A., y Clerc, M. G., “Interaction between vegetation patches and gaps: A self-organized response to water scarcity,” *Physica D: Nonlinear Phenomena*, vol. 414, p. 132708, 2020.
- [81] Rietkerk, M., Boerlijst, M. C., van Langevelde, F., HilleRisLambers, R., de Koppel, J. v., Kumar, L., Prins, H. H., y de Roos, A. M., “Self-organization of vegetation in arid ecosystems,” *The American Naturalist*, vol. 160, no. 4, pp. 524–530, 2002.
- [82] Gilad, E., von Hardenberg, J., Provenzale, A., Shachak, M., y Meron, E., “A mathemat-

- ical model of plants as ecosystem engineers,” *Journal of Theoretical Biology*, vol. 244, no. 4, pp. 680–691, 2007.
- [83] Fernandez-Oto, C., Tzuk, O., y Meron, E., “Front instabilities can reverse desertification,” *Physical review letters*, vol. 122, no. 4, p. 048101, 2019.
- [84] Bordeu, I., Clerc, M. G., Couteron, P., Lefever, R., y Tlidi, M., “Self-replication of localized vegetation patches in scarce environments,” *Scientific reports*, vol. 6, no. 1, pp. 1–11, 2016.
- [85] Rietkerk, M., Dekker, S. C., De Ruiter, P. C., y van de Koppel, J., “Self-organized patchiness and catastrophic shifts in ecosystems,” *Science*, vol. 305, no. 5692, pp. 1926–1929, 2004.
- [86] Tlidi, M., Bordeu, I., Clerc, M. G., y Escaff, D., “Extended patchy ecosystems may increase their total biomass through self-replication,” *Ecological indicators*, vol. 94, pp. 534–543, 2018.

